# UNIVERSITÀ DEGLI STUDI DELL'AQUILA
**DIPARTIMENTO DI INGEGNERIA INDUSTRIALE DELL'INFORMAZIONE E DI ECONOMIA**


Dottorato di Ricerca in Ingegneria Industriale, dell'Informazione e di Economia

Curriculum Ingegneria Meccanica, Energetica e Gestionale

XXXVII ciclo

Titolo della tesi

Advanced characterization of components made by Material Extrusion process

SSD ING-IND/16 Tecnologie e Sistemi di Lavorazione


Dottorando

Silvia Ilaria Scipioni

Coordinatore del corso

Prof.ssa Katia Gallucci

Tutor

Prof. Francesco Lambiase


a.a. 2023/2024

# Table of contents

List of figures ..... IV

List of tables ..... X

Abstract ..... 1

Preface ..... 3

Chapter 1 – Additive Manufacturing processes ..... 7

Introduction ..... 7

1.1 Steps of additive manufacturing process ..... 8

1.2 Classification of Additive Manufacturing processes ..... 10

1.2.1 Binder jetting ..... 12

1.2.2 Powder bed fusion ..... 14

1.2.3 Directed Energy Deposition ..... 17

1.2.4 Sheet Lamination ..... 21

1.2.5 Vat Polymerization ..... 23

1.2.6 Material jetting ..... 25

1.2.7 Material extrusion ..... 28

1.3 Mechanical characterization of plastic components ..... 34

1.3.1 Tensile test ..... 35

1.3.2 Compression test ..... 38

1.3.3 Flexural behavior ..... 39

1.3.4 Shear test ..... 42

Chapter 2 – Characteristics of thermoplastic materials ..... 43

2.1 Amorphous and semi-crystalline polymers ..... 43

2.1.1 Influence of temperature on the bonds between polymer chains in semi-crystalline polymers ..... 45

2.2 Thermal characterization of polymeric materials ..... 46

2.2.1 Differential Scanning Calorimetry (DSC) ..... 46

2.2.2 Thermogravimetric Analysis (TGA) ..... 51
2.2.3 Dynamic Mechanical Analysis (DMA) ..... 53
2.3 Thermoplastics materials used in material extrusion process ..... 56
Chapter 3 – Characterization of components made by Material extrusion process ..... 60
3.1 Mechanical characterization by traditional testing ..... 60
3.2 Limitations of traditional mechanical characterization ..... 64
3.2.1 Anisotropic behavior ..... 65
3.2.2 Interlayer adhesion ..... 66
3.2.3 Porosity ..... 70
3.3 Final remarks ..... 72
Chapter 4 – Advanced mechanical characterization and process monitoring ..... 75
4.1 Analysis of density and presence of porosity in Material extrusion components ..... 75
4.1.1 Introduction ..... 76
4.1.2 Materials and methods ..... 77
4.1.3 Determination of density ..... 83
4.1.4 Mechanical behavior of the samples ..... 89
4.1.5 Morphological analysis ..... 100
4.2 Interlayer adhesion ..... 105
4.2.1 Introduction ..... 105
4.2.2 Materials and methods ..... 106
4.2.3 Specimens preparation and mechanical test ..... 112
4.2.4 Fracture surface analysis ..... 123
4.2.5 Infrared analysis ..... 124
4.2.6 DMA and DSC analysis ..... 127
4.3 Artifacts introduced by different manufacturing strategies in material extrusion components ..... 130
4.3.1 Introduction ..... 130
4.3.2 Materials and methods ..... 131

4.3.3 Mechanical behavior ..... 138
4.3.4 Optical analysis ..... 144
4.3.5 Geometrical artifacts ..... 148
4.3.6 Thermal analysis ..... 151
Chapter 5 – Results analysis and Discussion ..... 156
5.1 Impact of porosity on mechanical properties ..... 156
5.2 Influence of process parameters on the interlayer fracture toughness ..... 161
5.3 Impact of manufacturing strategies on mechanical properties ..... 164
Chapter 6 – Conclusions and future works ..... 169
List of symbols ..... 176
List of acronyms ..... 177
References ..... 179

# List of figures

Fig. 1 – Workflow of additive manufacturing processes ..... 8
Fig. 2 – Schematization of binder jetting machine [22] ..... 12
Fig. 3 – Schematization of Powder Bed Fusion machine [13] ..... 15
Fig. 4 – Schematization of Directed Energy Deposition machine [43] ..... 17
Fig. 5 – Schematization of Sheet Lamination machine [53] ..... 21
Fig. 6 – Schematization of Vat Polymerization machine [55] ..... 23
Fig. 7 – Schematization of Material Jetting machine [21, 62] ..... 26
Fig. 8 – Schematization of Material Extrusion machine [19, 21] ..... 29
Fig. 9 – Dimensions of the test specimens [93] ..... 36
Fig. 10 – Stress-strain curve [93] ..... 38
Fig. 11 – Compression Test Specimen for materials with a thickness less than 3.2 mm [94] ..... 39
Fig. 12 – Specimen and loading nose usable during the test [95] ..... 40
Fig. 13 – DSC curve ..... 49
Fig. 14 – TG curve (green) and DTG curve (red) of $Mn(CH_3CO_2)_2.4H_2O$ heated up to 900°C in air [116] ..... 52
Fig. 15 – Storage modulus (E') and tan δ of PVC and Polycarbonate [117] ..... 55
Fig. 16 – Analyzed printing parameters ..... 60
Fig. 17 – Anisotropy determined by the bonding difference between successive layers and adjacent filaments ..... 65
Fig. 18 – Two different ways of fracture when specimen is subject to a tensile test in Z-direction ..... 69
Fig. 19 – Cross section of material extrusion components made by SEM at 100x and 500x magnification to study porosity ..... 70
Fig. 20 – Schematics of the build orientation of the sample during the printing: vertical (a) and horizontal (b) ..... 78
Fig. 21 – Schematic of the sample and the indenter during flat indentation test ..... 79
Fig. 22 – Schematic of the adopted equipment to perform thermomechanical compaction ..... 79
Fig. 23 – Experimental equipment and sample orientation during the indentation test (a); schematic of the force displacement curve recorded during loading (red) and unloading (blue) phases (b) ..... 81
Fig. 24 – Normalized stress curve recorded during instrumented flat indentation test ..... 82
Fig. 25 – Influence of the extrusion multiplier and printing orientation on the density of the samples of the first experimental campaign ..... 83

Fig. 26 – Cross section on vertically printed samples of the first experimental campaign printed with different extrusion multiplier ..... 84
Fig. 27 – Influence of the extrusion multiplier on the density of the samples of the second experimental campaign ..... 84
Fig. 28 – Influence of the extrusion multiplier and thermomechanical compaction on the density of the samples of the third experimental campaign ..... 85
Fig. 29 – Cross sections of the samples produced under different processing conditions ..... 85
Fig. 30 – Cross section of the samples made by SEM analysis at 8x magnification (a) and 100x magnification (b) ..... 86
Fig. 31 – Image analysis of mesostructure features (voids): a) original image; b) identified voids; c) distribution of void area and d) distribution of major axis length. (Extrusion multiplier EM=96%) 86
Fig. 32 – Normal dimensions of voids produced under different deposition conditions and compaction ..... 87
Fig. 33 – External surfaces of the samples produced under different processing conditions: (a) EM=96%; (b) EM=100%; (c) EM=104%; (d) compacted ..... 88
Fig. 34 – Surface analysis performed on two samples: a) printed with extrusion multiplier set to 104% and; b) compacted. Virtual profile of the samples c) EM=104% and d) compacted ..... 89
Fig. 35 – Influence of the extrusion multiplier on the slope measured during indentation tests on samples printed in (a) D = 4 mm and (b) D = 2 mm on horizontally printed samples ..... 90
Fig. 36 – Influence of the extrusion multiplier on the slope measured during indentation tests on samples printed in (a) D = 4 mm and (b) D = 2 mm on vertically printed samples ..... 90
Fig. 37 – Correlation of the slopes measured during indentation tests and the density on (a) horizontally printed and (b) vertically printed samples ..... 91
Fig. 38 – Overall correlation between the slope measured the indentation tests on horizontal and vertical samples during loading (E1) and unloading (E2) phases ..... 91
Fig. 39 – Force–displacement curves recorded during the compression tests of samples printed with different extrusion multipliers ..... 92
Fig. 40 – Influence of the a extrusion multiplier and b density on the yield strength measured through compression tests ..... 92
Fig. 41 – Load–displacement curves recorded during the indentation tests of samples printed with different extrusion multipliers ..... 93
Fig. 42 – Influence of the extrusion multiplier on the normalized force determined through indentation tests performed on the a–c top surface and b–d bottom surface ..... 94

Fig. 43 – Influence of the sample density on the yielding condition measured by indentation tests performed on the a, b upper and c, d lower sample surface ..... 95
Fig. 44 – Correlation between the a yield strength (measured through the compression tests) and b the normalized force (measured through the indentation tests) ..... 95
Fig. 45 – Macrograph of a sample before and after compression tests ..... 96
Fig. 46 – Stress-strain curves of the samples produced under different processing conditions ..... 96
Fig. 47 – Stress-strain curves recorded during the compression tests of the samples produced under different processing conditions (both strain rate and manufacturing process) ..... 97
Fig. 48 – Compressive Yield Strength of the samples ..... 98
Fig. 49 – Empirical model developed to describe the influence of the density of the samples and the strain rate ..... 99
Fig. 50 – Surface reconstruction of a vertical printed sample (a); topography of the analyzed surface area (b); virtual cross section of the surface (c) ..... 101
Fig. 51 – Surface reconstruction of a horizontal printed sample (a); topography of the analyzed surface area (b); virtual cross section of the surface (c) ..... 101
Fig. 52 – Macrograph of surfaces of sample made with EM=99%: (a) upper; (b) bottom and EM=104%: (a) upper; (b) bottom ..... 102
Fig. 53 – 3D maps of the upper and lower surfaces on samples produced with EM=99% and EM=104% ..... 103
Fig. 54 – Relative dimension between filaments and applied load ..... 107
Fig. 55 – Various steps of the execution of the printing process of the DCB specimens including the supporting U-shape (a), the placement of the Polyimide tape (b) and the finalization of the specimen (c) ..... 108
Fig. 56 – Schematic of the sample produced by printed spacers without the release film ..... 109
Fig. 57 – Main dimensions of the samples used in the experimentations ..... 110
Fig. 58 – Relative direction between deposited filaments and applied load and different types of specimens printed via the MatEx process: (a) cross-ply specimen (following layers oriented at 0/90°) and (b) angle-ply specimen (following layers oriented at±45°) ..... 112
Fig. 59 – Picture of the sample during DCB test with the equipment required ..... 113
Fig. 60 – Identification of the change in compliance starting from the load-crosshead displacement curve (a) and definition of the Δ factor for calculating the critical energy release rate (b) ..... 114
Fig. 61 – The Load-Crosshead Displacement curves of representative specimens of each category (a) and the Crack Length-Crosshead Displacement ratio obtained by the experimental campaign (b) 115

Fig. 62 – The average critical energy release rate calculated with the beam and modified beam theory ..... 116
Fig. 63 – The R-curves for the specimens of the mode I fracture toughness tests..... 116
Fig. 64 – Load-crosshead displacement charts obtained from the 0–90 specimens tested related to the test matrix, with several extrusion multipliers (EM). The transparent curves represent the initial crack opening, while the sharper curves correspond to the stable propagation phase. For each testing condition, just two curves S1 and S2 were reported ..... 117
Fig. 65 – Load-crosshead displacement charts obtained from the±45° specimens tested related to the test matrix. The transparent curves represent the initial crack opening, while the sharper curves correspond to the stable propagation phase ..... 118
Fig. 66 – Fracture surface of specimens produced with varying the extrusion multiplier (a) EM=96%, (b) EM=100%, and (c) EM=104%..... 119
Fig. 67 – Influence of the process parameters (extrusion multiplier and deposition speed) on GIc using diferent deposition strategies: (a) 0/90° and (b) ±45° ..... 120
Fig. 68 – Fractured surface analysis of a sample made by using the polyimide film: a) Stereoscopic image; b) 3D Reconstruction and c) virtual cross section ..... 122
Fig. 69 – Fractured surface analysis of a sample made with nested spacers: a) Stereoscopic image; b) 3D Reconstruction and c) virtual cross-section ..... 122
Fig. 70 – The zone of the stable crack propagation observed with SEM..... 123
Fig. 71 – Fracture surface observed through optical microscopy of samples made under reference deposition conditions: (a) v=1000 mm/min, EM=100%; (b) v=1000 mm/min, EM=104%; (c) v=2000 mm/min, EM=100%; (d) v=2000 mm/min, EM=104% ..... 124
Fig. 72 – (a) Temperature distribution measured during deposition and (b) temperature variation with time measured at the measurement point. Samples made with a pause time of 60 s to account for the time required for the Polyimide placement ..... 125
Fig. 73 – (a) IR temperature maps acquired during the deposition of the samples, (b) temperature history at the measurement point (on the top surface of the sample) under different deposition conditions, and (c) temperature history during the deposition of a single layer ..... 126
Fig. 74 – DMA analysis conducted on the specimens obtained with different EMs: (a) Storage moduli and (b) tan d ..... 127
Fig. 75 – (a) DSC analyses and (b) ATR spectra for the specimens obtained with different EMs. The analyses of the filament are also reported for comparison..... 128
Fig. 76 – SEM micrographs obtained with two magnifications, ×250 (a, b) and ×1000 (c, d), for the parts obtained with 100 and 104 EM, after the delamination test..... 129

Fig. 77 – Schematic of the adopted printing strategies: direct print of a) vertical, b) horizontal samples, and c) horizontal with longitudinal filaments. Plaque print and cut of d) vertical plaque and e) horizontal plaque ..... 132
Fig. 78 – Schematic of the sample produced using different approaches: a) direct sample printing, b) rectangular box printing. c) extraction (through abrasive waterjet cutting) of tensile samples from the rectangular box. ..... 134
Fig. 79 – Schematic of the sample produced using different approaches: a) direct sample printing, b) extraction (through abrasive waterjet cutting) of tensile samples from the rectangular box ..... 136
Fig. 80 – Annealing thermal cycle ..... 136
Fig. 81 – Influence of the deposition conditions on the density of the samples ..... 138
Fig. 82 – Influence of the deposition conditions on the Young's modulus (a) and on the yield stress (b) of the samples ..... 139
Fig. 83 – Stress-strain curves of different samples produced with direct sample printing and cutting with two thicknesses ..... 140
Fig. 84 – Mechanical characteristics of the samples produced using different manufacturing strategies ..... 141
Fig. 85 – Side view of the samples at low and higher magnifications ..... 142
Fig. 86 – Stress-strain curves of different samples produced with direct sample printing and cutting one ..... 143
Fig. 87 – Mechanical characteristics of the samples produced using different manufacturing strategies ..... 144
Fig. 88 Porosities in direct printed vertical samples V1 (a), in corresponding "extracted" samples (b) and in direct printed horizontal samples H1 (c) with a zoom on their distribution ..... 145
Fig. 89 – SEM image of the intralayer fracture of a specimen made by direct printing ..... 146
Fig. 90 – Cross sections of (a) directly printed and (b) cut samples ..... 146
Fig. 91 – Dimensional characterization if interlayer voids produced on samples made by direct printing and cutting ..... 147
Fig. 92 – Cross section of (a) directly printed sample and (b) cut sample. (SECT. AA-Direct print and SECT. BB-Cut from the box) ..... 147
Fig. 93 – Fracture surfaces of cut samples under (a) annealing and (b) as printed conditions ..... 148
Fig. 94 – 3D analysis of the fracture surfaces showing (a) directly printed sample and (b) cut sample both under "as printed condition" ..... 149
Fig. 95 – Fracture surfaces observed through SEM of (a) directly printed and (b) cut from the box samples both after annealing ..... 150

Fig. 96 – DSC curves of the samples produced through different deposition and post-processes conditions ..... 150
Fig. 97 – IR maps recorded at different deposition times during 3D printing of a single sample ... 152
Fig. 98 – IR maps recorded at different deposition times during 3D printing of four samples (two samples are behind the shown ones) ..... 152
Fig. 99 – IR maps recorded at different deposition times during 3D printing of the plate ..... 153
Fig. 100 – Thermal history measured at the actual printing layer during the sample deposition using three strategies: (a) direct printing of one sample, (b) direct printing of four samples, and (c) printing of a plate ..... 154
Fig. 101 – Infrared pictures acquired during deposition of (a) direct sample printing and (b) box printing for sample cutting; (c) Thermal history recorded during deposition of direct samples and box ..... 155
Fig. 102 – (a) Schematic of the different material flow conditions arising during the deposition of subsequent shells as moving from the outside perimeter shells towards the core of the layer and (b) during the deposition of subsequent layers; (c) uneven porosity distribution in the central zone ... 158
Fig. 103 – Schematic of the loaded shells tested during indentation tests on (a) vertically and (b) horizontally printed samples ..... 159
Fig. 104 – Effect of the strain rate (during the compression tests) on the distribution of the voids 161
Fig. 105 – Higher magnification of a printed sample showing smaller voids in contact with the building plate ..... 161
Fig. 106 – Schematic of the deposition of directly printed vertical samples (V1 type) (a) with a zoom on main artifacts in directly printed samples (b) ..... 164
Fig. 107 – Artifacts affecting the interlayer deposition in directly printed samples ..... 167

# List of tables

Table 1 – Specimens dimensions ..... 35
Table 2 – Designations for speed oh the testing ..... 37
Table 3 – Most commonly used thermoplastics in material extrusion process [121] ..... 56
Table 4 – Critical temperatures of thermoplastic materials for material extrusion process ..... 59
Table 5 – Literature papers that investigate mechanical properties of thermoplastics components made by material extrusion ..... 61
Table 6 – Selected printing parameters value ..... 78
Table 7 – Full factorial experimental plan of the third experimental campaign ..... 82
Table 8 – Density and relative densities calculated according to different manufacturing conditions ..... 88
Table 9 – Characteristic dimensions of the specimens used for ASTM D5528 tests, ..... 110
Table 10 – Characteristics of the four specimens produced by material extrusion process ..... 111
Table 11 – Test matrix with factors and assumed levels ..... 112
Table 12 – Main deposition parameters ..... 132
Table 13 – Levels of the first full factorial experimental plan ..... 133
Table 14 – Test matrix summarizing the experimental conditions used for the second experimental campaign ..... 134
Table 15 – Main deposition parameters of the third experimental campaign ..... 135
Table 16 – Test matrix summarizing the experimental conditions used for the experimental investigation ..... 137
Table 17 – Measurement of enthalpies and crystallinity of the samples produced through different deposition and post-processes conditions ..... 150
Table 18 – Difference of the density and mechanical behavior of samples made by direct printing (V1, H1, and HL1) and extraction method (V2, H3, and H2) ..... 165

# Abstract

This work aims to carry out a detailed investigation into the characterization methods of components made by Material Extrusion (MatEx) process. There are several articles in the literature that analyze the influence of process parameters on mechanical properties of MatEx components. However, traditional characterization methodologies are used, and these are not specifically developed for parts made by Material Extrusion process. Due to the layer-by-layer production mode, these components have some specific characteristics that are difficult to evaluate by classical mechanical characterization tests. Thus, advanced characterization of components made by Material Extrusion process has been conducted. Appropriately designed test methodologies have been developed for the mechanical evaluation of such components. Through these tests, the possibility to evaluate some characteristics of components with a high impact on their mechanical properties has arisen. Investigations on the presence of porosity, inter-laminar adhesion, and the impact of the size of manufactured components on their mechanical properties were conducted. Local characterization tests, tests for laminar structures, and process monitoring were the key tools used to evaluate these properties. The selected process parameters during the printing stage and the manufacturing strategies of the samples have been found to have a very high impact on the mechanical properties of the components. From the analysis of the obtained results, it was determined that careful characterization of components produced by material extrusion was needed, through tests specifically designed for such parts.

# Preface

The following work addresses the ever-increasing need to make functional components through Additive Manufacturing processes. Nowadays, in many high-tech industries, including aerospace and biomedical, demand for components that combine high mechanical properties with low weight is increasing; this demand is also usually correlated with production batches of only a few units or, at the limit, even unit size. One of the additive manufacturing technologies that succeeds in meeting these needs is Material Extrusion process (MatEx). This process produces components by heating a filament, which, when extruded through a nozzle, allows the component to be made layer-by-layer. This is a relatively simple process, and because of this, it has become very popular both domestically and in the industrial field.

In the industrial field, however, especially in aerospace, biomedical, and automotive areas, components made by the MatEx process need careful characterization before they can be used in the required applications. Such characterization is carried out through conventional techniques. However, Material Extrusion components have characteristics and peculiarities strongly related to the production process, which, through traditional characterization, are not adequately considered. Layer-by-layer production, in fact, creates some specific issues in these components that should be considered when evaluating mechanical properties. Firstly, MatEx components present many porosities that reduce the load-bearing area and induce severe stress concentration, leading to higher stress. The presence and the dimension of the porosities are not easily predictable since they depend on the selected process parameters and the geometry and complexity of the component. Moreover, the distribution of these porosities is not uniform within the element. Another limitation of MatEx components concerns their anisotropic behavior, which involves different fracture mechanisms when the components are loaded along or perpendicular to the growing direction. Given what has been said so far, the need arises to characterize components produced by the Material Extrusion process using methodologies and procedures that can account for the issues highlighted. Thus, this work aims to provide suitable methods for the advanced characterization of components made by Material Extrusion process.

The first three chapters concern the state of the art. In the first chapter, a detailed description of additive manufacturing processing is provided, with emphasis on the Material Extrusion process. In addition, an overview of traditional characterization tests suitable for plastic

materials was given. The second chapter focused on the description of polymeric materials. Characteristics of thermoplastic materials were analyzed, highlighting the differences between amorphous and semi-crystalline polymers. Tests for thermal characterization of polymers were described, and the most common thermoplastic materials used in the Material Extrusion process were outlined. Finally, in the third chapter, an overview of the mechanical characterization by traditional testing of components made by the MatEx process was given, and the limitations of these methods were explained.

On the other hand, chapters four, five and six propose advanced methodologies and techniques for characterizing components made by the Material Extrusion process. Specifically, the studies conducted for this thesis produced eight papers. Three of these papers focus on the analysis of density and porosity in MatEx components. Flat indentation instrumented tests and compression tests were carried out to realize these studies. The papers produced on this topic are listed below.

- Lambiase, F., Scipioni, S. I., & Paoletti, A. (2022). Determination of local density in components made by fused deposition modeling through indentation test. *The International Journal of Advanced Manufacturing Technology*, *122*(3), 1467-1478.
- Lambiase, F., Scipioni, S. I., & Paoletti, A. (2023). Mechanical characterization of FDM parts through instrumented flat indentation. *The International Journal of Advanced Manufacturing Technology*, *125*(9), 4201-4211.
- Scipioni, S. I., & Lambiase, F. (2023). Yielding and post-yielding behavior of FDM parts under compression stress at different strain rates. *The International Journal of Advanced Manufacturing Technology*, *128*(3-4), 1199-1211.

Two other papers have studied the interlaminar adhesion of these components. Double cantilever beam tests were conducted, and the influence of process parameters was analyzed. A new kind of sample that embeds the "3D printed" nested spacers is proposed. The two studies are the following:

- Stamopoulos, A. G., Scipioni, S. I., & Lambiase, F. (2023). Experimental characterization of the interlayer fracture toughness of FDM components. *Composite Structures*, *320*, 117213.
- Lambiase, F., Liparoti, S., Pace, F., Scipioni, S. I., & Paoletti, A. (2024). A multidisciplinary approach to investigate the influence of process parameters on

interlayer adhesion in material extrusion additive manufacturing. *The International Journal of Advanced* Manufacturing Technology, 133(11), 5553-5570.

Lastly, the influence of two different manufacturing conditions on mechanical properties was investigated through compression and tensile tests. Some specimens were produced directly by the Material Extrusion process at their final dimensions. At the same time, the second approach involved manufacturing larger components (plates or boxes) from which samples were subsequently extracted by waterjet cutting to attain the desired final dimensions. The studies listed below also involved a high-performance polymer used in aerospace applications.

- Scipioni, S. I., & Lambiase, F. (2023). Error introduced by direct 3D printing of compression samples of PLA made by FDM process. *The International Journal of Advanced Manufacturing Technology*, *129*(9), 4355-4368.
- Lambiase, F., Scipioni, S. I., Pace, F., & Paoletti, A. (2024). Unraveling the main issues of direct sample printing and sample cutting from a sheet of tensile test samples for characterization of Material Extrusion components. The International Journal of Advanced Manufacturing Technology, 132(5), 2991-3003.
- Scipioni, S. I., Pace, F., Paoletti, A., & Lambiase, F. (2024). Mechanical characterization of FDM components made of polyaryletherketone (PAEK) for aerospace applications: a comparison of direct printing and box-cut sample manufacturing strategies. *The International Journal of Advanced Manufacturing Technology*, *134*(11), 5615-5629.

Thus, chapter four describes all the activities conducted; chapter five explains the analysis and discussion of the results; eventually, in chapter six, the thesis's conclusions and future works are reported.

# Chapter 1 – Additive Manufacturing processes

## Introduction

Additive manufacturing, also known as 3D printing, has transformed the way components are produced, positioning itself in opposition to more common techniques, like milling or casting. The ISO ASTM 52900 standard [1] has defined additive manufacturing (AM) as: "the process of joining materials to make parts from 3D model data, usually layer upon layer, as opposed to subtractive manufacturing and formative manufacturing methodologies." The first AM process was developed around 1980, with the creation of the first stereolithography machine. Initially, these were processes intended for prototyping rather than actual production, hence the name rapid prototyping. Subsequently, this family of technologies was used for rapid tooling, until the end of the first decade of the 2000s in which the spread of these processes increased dramatically [2]. The increase in the diffusion of this family of processes is related to different reasons, all of which can be attributed to market demands, like greater customization of products, complex geometries, shorter lead times [3], and additive manufacturing processes succeed in meeting these new requirements. The production of a part by these processes is often called "free-form fabrication", as they give the possibility to realize structures with very complex shape; this aspect is so far from conventional manufacturing processes, where some geometries cannot be realized at all [4]. A further advantage of these processes lies in the possibility of creating multi-material structures, which are particularly required for all those applications in which are required different mechanical features with weight reduction of the structures [5].

At the core of the operation of AM processes there is the "layer-by-layer" production, which allows the finished component to be made by overlapping multiple layers. The part to be fabricated will be discretized by a certain number of layers: increasing the number of layers, the thickness of each layer will reduce; thus, improving the discretization of the geometry to be fabricated [4]. All processes that are part of this family are characterized by a similar production cycle. It will then proceed with a section dedicated to the description of the various phases of the production process.

## 1.1 Steps of additive manufacturing process

In this section, all the phases of the production process that are necessary to produce components by additive manufacturing processes will be analyzed; Fig. 1 shows the generic workflow of additive manufacturing processes.

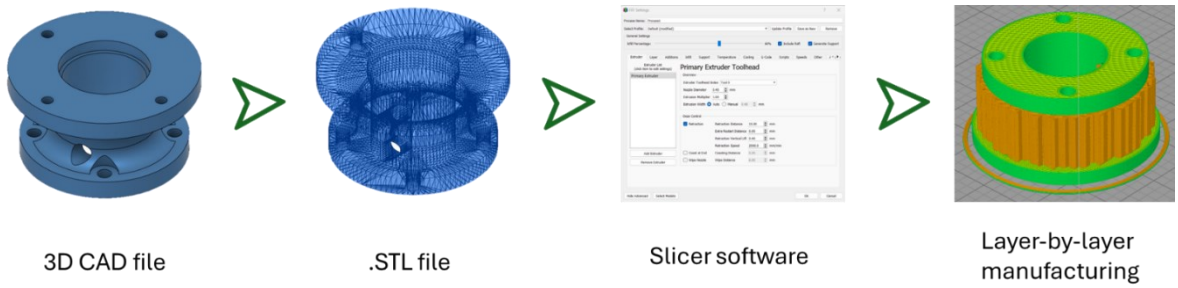



*Fig. 1 – Workflow of additive manufacturing processes*

The first step consists in the realization of the virtual model with a professional CAD software [4, 6, 7]; this represents the phase of the design, where it is relevant to realize the model considering that the component will be made by additive manufacturing. During the design of a component to be made by additive manufacturing, in fact, the possible need to insert supports must be taken into account, which will impact both the production time, and the amount of material used and therefore the cost; designing the component with these two aspects in view allows the presence of supports to be minimized. Reverse engineering equipment can be also used for this step; machines are scanners that use UV lights to emit from the source and receive back the target object. Reverse engineering is particularly used in high-precision industries: this is the case, for example, in the biomedical sector, where fully customized prostheses are made by scanning the patient and thus creating a perfectly tailored product [8, 9]. The design of the parts can also be supported by topology optimization [10] that is mathematical process that optimizes material layout and structure for a defined set of rules set by the designer. The goal is to maximize part performance by mathematically modelling and optimizing factors such as external forces, load conditions, boundary conditions, constraints, and material properties within the design envelope. Structures designed by topological optimization have complex geometries, as the weight of the component is minimized by removing material from the part to be produced, but ensuring the required mechanical properties; for this reason, it is very complicated to realize that parts by traditional manufacturing processes and additive manufacturing could be the answer to this limitation [11]. This method to design components, where is generally

used a finite element method to evaluate mechanical performance, is commonly used in automotive and aerospace industries [12].

The next stage of the manufacturing process concerns the conversion of the CAD model into .STL file format [4, 6]. STL is the acronym for Standard Triangulation Language [6] or Standard Tessellation Language [13]: this means that each surface of the component being realized is discretized by using triangles; increasing the number of triangles with which each surface is discretized increases the level of detail with which the component will be realized, improving its discretization. In this file format are removed all the CAD attribute, like textures and colors [14], making it suitable for ASCII and binary representation [15]. After the conversion is done, it is possible to transfer the file to machine.

Now the most critical stage begins, which is related to the choice of process parameters. In this step every single process parameter can be set, and this will have a strong impact on the features of the manufactured component. To do this, the .STL file has to be uploaded to a "slicer" software [6, 13]. There are several slicers available, some associated with specific additive manufacturing machines, others more general and suitable for different machines. All slicers, however, allow the possibility of choosing the printing parameters: starting from the orientation of the part on the printing table, up to the printing speed [16]. Depending on the chosen process, then, it is possible to set different parameters, which will be analyzed in the next sections. In this phase, it is also possible to insert supports or not, depending on the specific needs related to the geometry of the piece and the chosen process [17]. Regardless of the technology used, it is at this stage that the actual slicing of the part takes place: the geometry is "sliced" in a direction parallel to the printing table, giving rise to the layers that will be created during the production process. A very key parameter concerns the thickness of the individual layers: this will impact the surface finish of the part produced. Reducing the thickness of each layer will increase the number of them and consequently the duration of the production cycle, but this will lead to a better surface finish and geometry discretization. The output of this step is a G-code file, that is imported to machine [6].

After setting all process parameters, it is possible to proceed with the steps that concern the real production of the part [4, 13]. Layer-by-layer production is achieved during this step, but this phase can vary depending on the selected technology. Once the printing phase is complete, the component must be removed from the machine, taking care not to damage it.

At this point, it starts a series of optional steps, that can be enclosed in the post-processing operation [4, 7, 13]. The operations to be carried out during the post-process are strictly linked to the type of technology chosen; the only one common to all of them consists in removing the supports, that can be done by mechanical or chemical methods [17].

There are two main categories of post-processes, which are those of thermal type and those of mechanical type [18]. The choice of the post-process to carry out depends on the production process chosen and the improvement to be achieved through the treatment. To improve tolerance and surface finishing, for example, it can be done machining post-processing; to improve residual stresses, a thermal post-treatment can be performed [13]. Anyway, the choice is strictly linked to the chosen production process and to the specific application that the manufactured component will have to perform.

Now the part is ready to be used for its specifical application.

## 1.2 Classification of Additive Manufacturing processes

There are several classifications in the literature for additive manufacturing processes. Some authors classify the processes according to the form of raw materials input. Bahnini I. et al. [19] categorize the processes just into liquid-based and powder-based; in the first group they include both processes in which polymerization of the resin in a liquid state occurs, like stereolithography or digital light processing, as well as those processes in which they start with a filament that is melted and then solidified again, like fused deposition modeling. The second group, on the other hand, includes both processes in which powders are melted or sintered and processes in which powders are bonded using a binder. Abdulhameed O. et al. [3] divide the processes into three categories:

- Solid raw materials input.
- Liquid raw materials input.
- Powder raw materials input.

In [7] there is another classification based on the type of raw materials input that is more specific; they categorize the state of starting materials in liquid, paste, powder and solid sheet; in the first group there are processes like stereolithography, in the second group it is possible to find fused deposition modeling, in the third group powder bed fusion and in the last group laminated object manufacturing.

Other authors [2] still make a classification based on material, but not on the form of raw material, but rather on the type. In this sense, there are some processes suitable only for

polymeric materials, in turn listed as semicrystalline polymers, amorphous polymers and thermosets, that are, for example, material extrusion or material jetting and other processes, like directed energy deposition or sheet lamination, are appropriate for metals. Ferraris E. et al. [20] investigate all additive manufacturing processes suitable for ceramic materials; in this case, all these processes use ceramic in powder form, so it is possible to classify them in direct or indirect processes. In direct processes the ceramic powder is sintered or melted to achieve the shape of the final part, while during indirect processes there is a binder which allows the creation of required geometry.

Another way to classify these processes [21] is according to the baseline technology; in this classification, additive manufacturing processes are divided into laser-based processes, extrusion processes, material jetting, adhesive processes and electron beam processes.

A classification of these processes based on the use of three distinct parameters will be now proposed:

- Form of raw material input
- Layer creation technique
- Type of material input

In this way it is possible to assign each process to a specific set of three parameters, uniquely identifying it.

The ISO ASTM 52900 [1] classifies additive manufacturing processes into seven categories, defined as follows:

- Binder jetting: “process in which a liquid bonding agent is selectively deposited to join powder materials”.
- Powder bed fusion: “process in which thermal energy selectively fuses regions of a powder bed”.
- Directed energy deposition: “process in which focused thermal energy is used to fuse materials by melting as they are being deposited”.
- Sheet lamination: “process in which sheets of material are bonded to form an object”.
- Vat polymerization: “process in which liquid photopolymer in a vat is selectively cured by light-activated polymerization”.
- Material jetting: “process in which droplets of build material are selectively deposited”.
- Material extrusion: “process in which material is selectively dispensed through a nozzle or orifice”.

Below it will proceed by analyzing all additive manufacturing processes, following the classification made by the ISO ASTM 52900 [1].

### 1.2.1 Binder jetting

Binder jetting is an additive manufacturing technique that employs a liquid binding agent selectively deposited onto a powder bed to form solid structures layer by layer. This process allows the production of parts using a variety of materials, including metals, ceramics, and polymers, with relatively high precision and low production costs [22, 23]. Fig. 2 shows the schematization of the process.

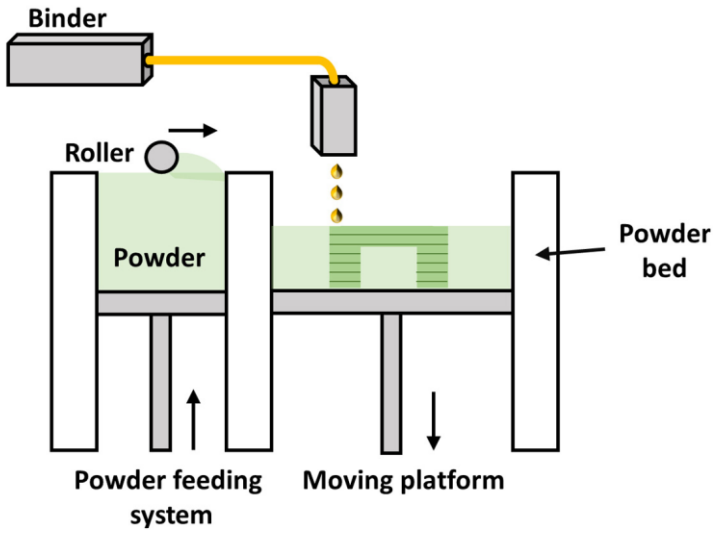



*Fig. 2 – Schematization of binder jetting machine [24]*

The machine has two chambers, one for the construction of the component and another one where the material is in the form of powders. The process begins with the distribution of a thin layer in the range of 50-100 μm [25] of powder material over the build platform. This is typically achieved using a roller or a blade to ensure uniform thickness and packing density. To create the layer, a printhead moves across the powder bed, selectively depositing droplets of a liquid bender, according to the data of the 3D model; the binder acts as an adhesive, bonding the powder particles together to form a cross-sectional layer of the part. Once a layer is completed, the build platform is lowered by one layer thickness, and a new layer of powder is spread from the other chamber through a roller, over the previous layer. The binder deposition process is repeated, allowing the successive layers to bond with each other.

After the completion of the printing process, it is obtained the “green part”, which is not the final product. Due to the fragility of the component, initial curing is required, typically achieved by placing the build platform in a furnace for variable durations and temperatures, which depend on factors such as section thickness, height, excess powder volume, and binder type. A typical curing regimen involves heating for 6–10 hours at 200–260 °C [13]. Post-curing, the part is extracted from the powder, cleaned, and any excess metal powder is recycled. To enhance the mechanical properties of the green metal part, a secondary process, usually sintering, is employed. Sintering serves to reduce porosity, increase density, and improve mechanical properties. This process typically involves two thermal cycles within a furnace, generally conducted in an inert atmosphere. The first cycle, known as the de-binding phase, involves the evaporation of the binder at temperatures ranging from 175 to 450 °C [26]. Subsequently, the 'brown' part undergoes a final densification cycle at elevated temperatures. During this cycle, atomic motion facilitates the reduction of surface area and energy as the temperature is elevated to approximately 80% of the metal's melting point. At lower temperatures, densification is minimal, with only slight atomic movement and no significant shrinkage. As the temperature increases, weak forces promote particle cohesion via grain boundary and volumetric diffusion, leading to mass movement and the formation of necks between particles, resulting in a densification of 2–3% [26]. During the intermediate stage, further temperature increases cause necks to merge, transforming and shrinking tubular pores, achieving 92–93% of the theoretical density. In the final stage, as the maximum furnace temperature is reached, grain growth accelerates, reducing tubular pores to isolated grain boundary pores. Achieving this level of densification typically requires sintering in a vacuum [13]. Generally, the final sintered part has a smaller volume than the original green part, though the mass remains constant. One of the main advantages of binder jetting is its resulting surface roughness, which is around Ra 6 μm after post-processing. Tumble polishing can further improve the finish to approximately Ra 1.25 μm [27].

The versatility of binder jetting systems lies in their compatibility with a broad spectrum of materials; it is possible to realize components using metals, ceramic and polymers. Initially, the process was intended to be used for the production of metal parts, but nowadays using binder jetting process is possible to realize components also made by ceramics and polymers. Common metals used include stainless steel, bronze, and titanium. Metal parts often require post-processing steps like sintering and infiltration to achieve full density and optimal

mechanical properties. Regarding ceramics materials, this is one of the few processes suitable for making parts with alumina, silica or zirconia, that are used for high-temperature applications due to their excellent thermal and mechanical properties [20]. Polymers application are less commons, due to the fact that polymers are rarely produced as powders, even if polymer powders can be used, primarily for prototyping and low-load applications [22].

Binder jetting owes its popularity to its various advantages. One of them is the material versatility that distinguishes it, as there are few more additive manufacturing processes capable of working with metals, ceramics and polymers. Another advantage of this process lies in the ability to make components without the use of external energy sources, such as lasers; this allows binder jetting to have low costs compared to other processes; additionally, binder jetting is a powder bed process, so it means that there no need for support structures and the possibility to reuse powder [13]. Scalability is another feature of this process, as it is suitable for both small-scale and large-scale production runs. On the other hand, limitations of binder jetting are the need to expose manufactured parts to extensive post-processing and the inferior mechanical properties that components may exhibit compared to those produced by other additive manufacturing powder bed processes, like selective laser melting or electron beam melting [22].

Main applications of this process are in medical and pharmaceutics [28] field, like the fabrication of patient-specific implants and prosthetics [29], but also in some specific electronic application [30, 31].

### 1.2.2 Powder bed fusion

Powder Bed Fusion (PBF) is a class of additive manufacturing (AM) processes that utilize thermal energy to selectively fuse regions of a powder bed. These processes are highly significant in the production of complex, high-resolution components in a variety of materials, but it finds its greatest applications in the field of metallic materials; in fact, these processes are the most diffused for metal components printing [32]. PBF processes, whose process scheme is shown in Fig. 3, involve spreading a thin layer of powder material, generally in the range of 20-200 μm [33], over a build platform. A high-energy source, typically a laser or electron beam, then selectively melts or sinters the powder according to the cross-sectional geometry of the part being manufactured. Once a layer is completed, the

build platform is lowered, and a new layer of powder is spread [34]. After every layers is completed, the chamber is gradually lead to ambient temperature to avoid thermal shock and the part is removed from the powder bed [13].

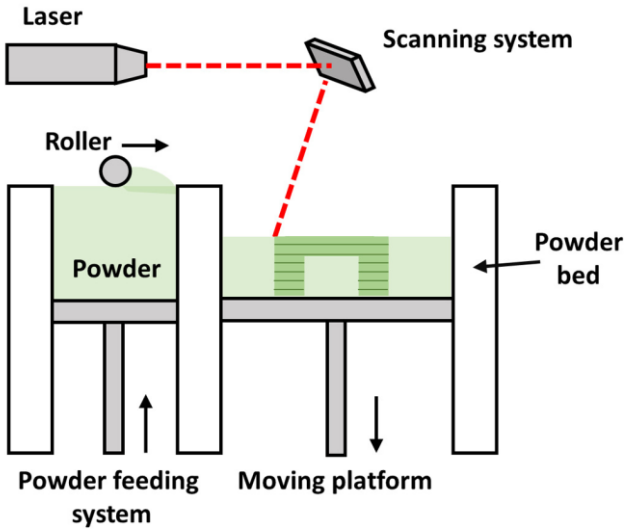



*Fig. 3 – Schematization of Powder Bed Fusion machine [24]*

Powder Bed Fusion processes include three different technologies, distinguished by the energy source used [13]. Selective Laser Sintering (SLS) utilizes a laser to sinter powders, while Selective Laser Melting (SLM) involves the complete melting of powders using a laser. SLM often refers to processes that achieve full melting, resulting in highly dense parts; SLM machines are equipped with high powdered lasers between 200 and 500 W, and the precision is dependent on the spot size, in the range of 20–500 µm, depending on the machine specifications [13].

On the other hand, Electron Beam Melting (EBM) employs an electron beam as the energy source to melt metal powders in a vacuum environment. This process is particularly effective for titanium and other high-performance alloys, often used in aerospace and medical applications.

PBF processes are versatile, accommodating a wide range of materials. Common materials include:

- Metals: Titanium alloys, aluminum alloys, stainless steels, and nickel-based superalloys are prevalent in SLM and EBM processes, providing high strength and thermal resistance [35].

- Polymers: Nylon (polyamide) and its composites are extensively used in SLS, offering good mechanical properties and flexibility [36].
- Ceramics: Zirconia and alumina powders are utilized in PBF for applications requiring high hardness and thermal stability [37].

The quality and properties of PBF-manufactured parts are highly dependent on process parameters, including laser/electron beam power, scanning speed, layer thickness, and powder characteristics. Optimization of these parameters is crucial to minimizing defects such as porosity, warping, and residual stresses. There are some parameters that are strictly connected to the laser and others that refer to building conditions. Laser power, scan speed and scan spacing belong to the first group, while in the second one there are layer thickness and powder bed temperature [36]. Laser Power, scan speed and scan spacing influence the energy input into the powder bed, affecting the melting and solidification dynamics. Excessive power can lead to overheating and part distortion, while insufficient power may result in incomplete fusion. Regarding building conditions, thinner layers enhance the resolution and surface finish but increase the build time; conversely, thicker layers reduce the build time but may compromise the part's detail and accuracy.

Powder characteristics also influence the quality of the parts. Particle size distribution, shape, and flowability are critical factors that influence layer uniformity and packing density. Spherical particles are preferred for their superior flow characteristics and packing efficiency [38].

Considering these parameters, it is possible to define the three-dimensional energy density, using eq. 1 [36], that considers also the effect of layer thickness.

$$Energy\ density\ = \frac{Laser\ Power}{Scan\ speed\ * Scan\ spacing\ * Layer\ thickness} \qquad eq.\ 1$$

The energy density is a crucial parameter in these processes: it is important that it reaches sufficient value to increase sufficiently the temperature of powder, but if it is too high this leads to an excessive powder melting, with a possible degradation and deterioration of mechanical properties [39].

Applications of PBF span various industries, thanks to its advantages, like the ability to fabricate complex geometries with internal features, undercuts, and lattice structures,

without any support. This is a crucial aspects in aerospace and automotive industries, in which is pivotal to realize lightweight and high-strength components, such as turbine blades and structural parts [40]. Another advantage refers to the material efficiency that enables great material utilization and the possibility to recycle powders. Through these processes it is also possible to achieve high levels of customization, that are ideal for producing custom implants and prosthetics tailored to individual patient anatomy in biomedical industry [36].

Despite its advantages, powder bed fusion processes, faces some challenges; it is often required a post-processing stage [41], to achieve desired surface finish and mechanical properties, adding time and cost. Parts made by these processes cannot be excessive in scale [42], as they are limited to the working cube of the machinery, as well as being characterized by high residual stress. Finally, powder handling involves health and safety risks [43].

### 1.2.3 Directed Energy Deposition

Directed Energy Deposition (DED) involves the focused delivery of energy and material to a substrate or build platform to create or repair parts layer by layer. The process typically uses a high-energy beam, such as a laser, electron beam, or plasma arc, to melt material that is simultaneously deposited. DED processes are suitable only for conductive material and it can be in the form of wire or powder, and the energy source is directed at a precise location to create the desired geometry [44]. Fig. 4 shows the schematization of DED.

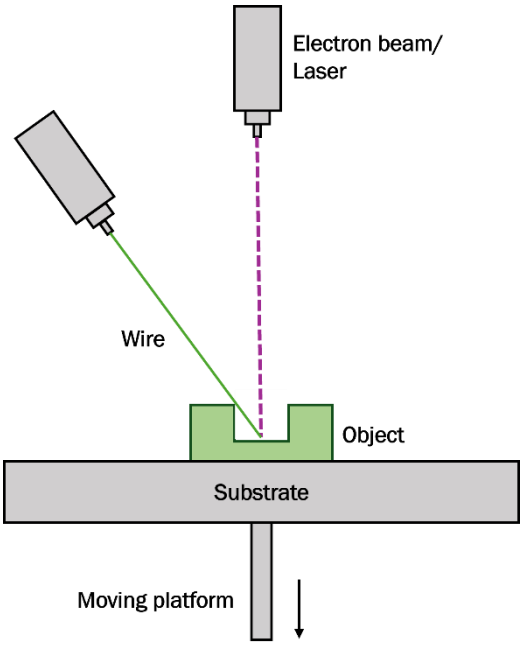



*Fig. 4 – Schematization of Directed Energy Deposition machine*

The Key Components of the process are [44, 45]:

- Energy source: it provides the necessary heat to melt the material; it could be a laser, electron beam, plasma, or electric arc.
- Deposition head and material feedstock: material can be delivered in powder, or wire form to the melt pool created by the energy source; during the process, molten pool is formed by melting the previous layer and the feedstock in and around the spot of the energy source. There are two different ways to provide material; in the first one, the material is fed coaxial to the energy source, while in the second one occurs an off axis (or lateral) feeding.
- Control system: manages the movement and coordination of the deposition head and substrate, typically through computer numerical control (CNC).

Thus, DED processes can be categorized according to the type of energy source and the type of feedstock; powder-based systems are the most common and they are usually used with laser as the energy source. These systems are more accurate than wire-based systems, but they have a lower deposition rate and they are less suitable for building large size components [45].

The main differences between deduction processes that employ powders and those that use wire are:

- Typical layer thickness: layer thickness using powder is in the range of 200-500 mm, while in wire-based system layer thickness is in the range of 1000-3000 mm.
- Minimum feature size: this parameter is strictly connected to the layer thickness; powder-systems provide an accuracy of about 700 mm, that is much more accurate than wire-based system.
- Deposition rate: wire-based system achieve high levels of deposition rate, non-comparable with any other additive manufacturing processes, up to 9 kg/h [46].

During the process there is a heat accumulation due to multi-layer deposition, and that can change the microstructure and then mechanical properties of the printed components. Between subsequent layers, a minimum level of metallurgical bonding is required, which can be quantified using eq. 2, that describes a parameter called dilution, denoted by “D”:

$$D = \frac{d}{d + h} \qquad \textit{eq. 2}$$

where “d” is the depth of the melt pool below the actual deposition level and “h” is the height of the material that is being deposited. High value of “h” means high flow rate or low energy input. The optimal value of dilution relates to the optimal value of penetration. Low value of penetration means a lack of fusion with the substrate, while high levels lead to perforation of the substrate. There is an optimal level for penetration, allowing for dilution levels between 10% and 30%, which results in a good metallurgical bonding [45].

The mechanical properties of components made by DED processes are strongly influenced by microhardness; since this is a process in which the material is melted, the size of the crystalline grains undergoes changes during the process, and this leads to different mechanical properties depending on the areas being analyzed. The microhardness values exhibit variation along the build direction because of changes in microstructure. Specifically, microhardness is elevated near the initial and final layers of the build, while being comparatively lower in the central layers. This variation is attributable to the cyclic thermal history characteristic of the Directed Energy Deposition (DED) process. In the central layers, there is an accumulation of heat, leading to diminished microhardness values [47]. It is possible to observe an increase in hardness and a refinement of microstructure with an increase in substrate thickness, as a greater substrate mass functions as an efficient heat sink. Conversely, increasing the substrate temperature results in decreased hardness due to a reduction in thermal gradients and cooling rates, which can induce a coarser microstructure. Additionally, an extended interlayer dwell time is associated with increased hardness, due to the presence of steeper thermal gradients [48]. Post-processing techniques, such as heat treatment or aging, may offer more effective control over hardness compared to alterations in DED process parameters [49].

DED excels in repair applications, allowing for the restoration of worn or damaged components. This capability reduces waste and extends the lifecycle of expensive parts, such as turbine blades, die and molds. DED systems can be scaled to accommodate large parts, making them suitable for applications in industries such as automotive, aerospace, and shipbuilding, where large components are common. The advantage in repairing by DED instead of traditional techniques, is that it is possible to make more accurate deposition, with concentrated and focused laser [50]. The directed delivery of material minimizes waste, as

only the required amount of material is deposited. This efficiency is particularly beneficial when working with expensive or scarce materials.

### *Powder production processes*

Powder production is a critical aspect of additive manufacturing, particularly for processes such as powder bed fusion (PBF), directed energy deposition (DED), and binder jetting. The quality and properties of the powder directly influence the mechanical properties, surface finish, and dimensional accuracy of the printed parts. Atomization is the most common method for producing metal powders used in additive manufacturing. There are four main types of atomization techniques [51]:

- Gas atomization: a molten metal stream is disintegrated into fine droplets using a high-velocity gas stream (usually inert gases like nitrogen or argon). The droplets solidify into spherical particles. This process allows the production of highly spherical particles with good flowability and packing density and it is suitable for a wide range of metals but requires high gas consumption and energy.

- Water atomization: it uses high-pressure water jets to break up the molten metal, so it is more cost-effective than gas atomization. On the other hand, water atomization produces irregularly shaped particles and is not suitable for reactive metals due to potential oxidation.

- Centrifugal atomization: molten metal is dropped onto a rapidly rotating disc, which throws the metal outward, forming droplets that solidify into powders. It produces spherical particles and is ideal for small-scale production, but it is limited to metals with low melting points.

- Plasma atomization: metal wires are fed into a plasma torch, where they are melted and atomized into fine droplets. This process produces highly spherical and pure powders with minimal contamination, but it is also characterized by high energy consumption and high equipment costs.

Other processes used for powder production are electrolysis and reduction of oxides. In the first one process [52], metallic ions are deposited from a solution onto a cathode and then they are mechanically removed to form a powder; this process allows the production of high-

purity powders with controlled composition, but it is limited to specific metals, and it can be expansive due to the required equipment. Reduction of oxides [53] includes that metal oxides are reduced to metallic powders using reducing agents like hydrogen or carbon monoxide. Through this process high-purity powders at relatively low cost can be realized, but it is not suitable for all metals and may require post-processing to achieve desired properties.

Powder production is a crucial aspect for additive manufacturing process in which material raw is in form of powder, because it has significant implications for the quality and cost of manufactured parts. Understanding the various production methods and their impact on powder properties is essential for optimizing AM processes. The dimensions of powders directly impact the layer thickness during additive manufacturing process [25], and consequently the mechanical properties and surface finish of manufactured components.

### 1.2.4 Sheet Lamination

Sheet Lamination is an additive manufacturing technique characterized by the sequential stacking and bonding of sheets of material to form three-dimensional objects. It encompasses methods such as Laminated Object Manufacturing (LOM) and Ultrasonic Additive Manufacturing (UAM). Unlike other AM processes that typically involve the melting or sintering of powders, sheet Lamination uses a laminate of material sheets, which are cut and bonded layer by layer [54]. Fig. 5 shows a schematic of sheet lamination process.

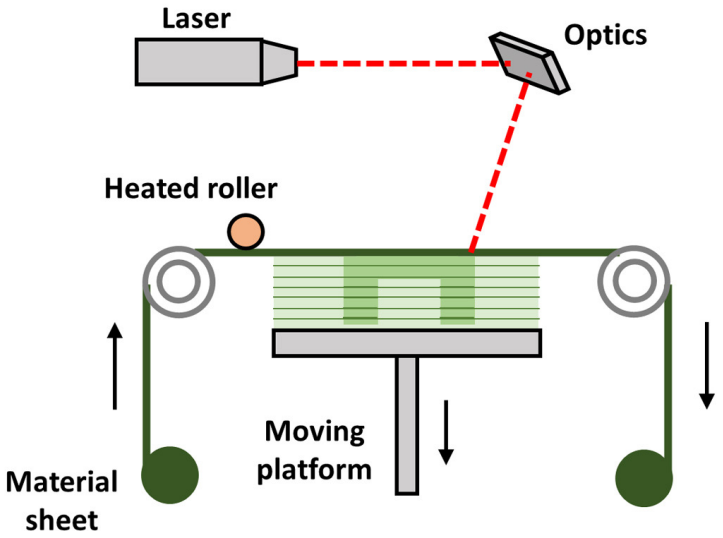



*Fig. 5 – Schematization of Sheet Lamination machine [24]*

Laminated Object Manufacturing employs materials such as paper, plastic, or metal foils coated with an adhesive on one side. The materials are typically supplied in rolls or sheets. The process can be implemented through two different methods. It is possible to cut each sheet to the desired cross-sectional shape, using a laser or blade, and then each sheet is bonded to the previous layer using and adhesive. This method is called “Form-then-bond-process”. On the other hand, there is the “Bond-then-form-process”. Here, after positioning each sheet, a heated roller passes across the sheet and melts the coating, causing a bond between subsequent layers. After each layer has been bonded and the final height of the component has been reached, it proceed with cutting by a laser [4]. In both types of methods, after the build process, unneeded sections are removed, revealing the final part. Post-processing may include surface finishing, infiltration, or painting, depending on the material and application requirements.

In the Ultrasonic Additive Manufacturing process thin metal foils are used, typically aluminum, copper, or titanium with a thickness in range of 100-500 μm, to realize the final part. This process leverages ultrasonic welding to bond metal foils. During the process, a sonotrode moves along the length of the foil. Each foil is held closely in contact with the previous layer due to the normal force applied by the sonotrode. The rotating sonotrode oscillates at a constant 20 kHz frequency and with an amplitude set by the user. After depositing a foil, another foil is deposited above it. This procedure is repeated until each layer is placed [4]. Ultrasonic transducers induce high-frequency vibrations that create localized frictional heating and plastic deformation at the interface of the metal sheets, bonding them without melting. After each layer is bonded, a CNC machining step can be used to create required geometries [55].

The advantages of this process involve low energy consumption: if compared to melting-based processes, sheet lamination requires less energy as it generally operates at lower temperatures. The process also permits the embedding of sensors, electronics, and fibers during the build, facilitating the production of functional and composite parts in composite fabrication and electronics components [4]. Sheet lamination offers distinct advantages in energy efficiency and multi-material integration; although the technique faces challenges in terms of surface finish and mechanical strength, ongoing research and development continue to expand its capabilities and application areas.

### 1.2.5 Vat Polymerization

Vat polymerization is one of the earliest and most widely used additive manufacturing techniques. It is primarily based on the principle of photopolymerization, where light is used to cure liquid photopolymer resin into solid parts. Fig. 6 shows one of the two different processes belonging to vat polymerization [56]:

- Stereolithography (SLA): the light used to cure liquid is a laser.
- Digital Light Processing (DLP): there is a projector that enables photo-polymerization.

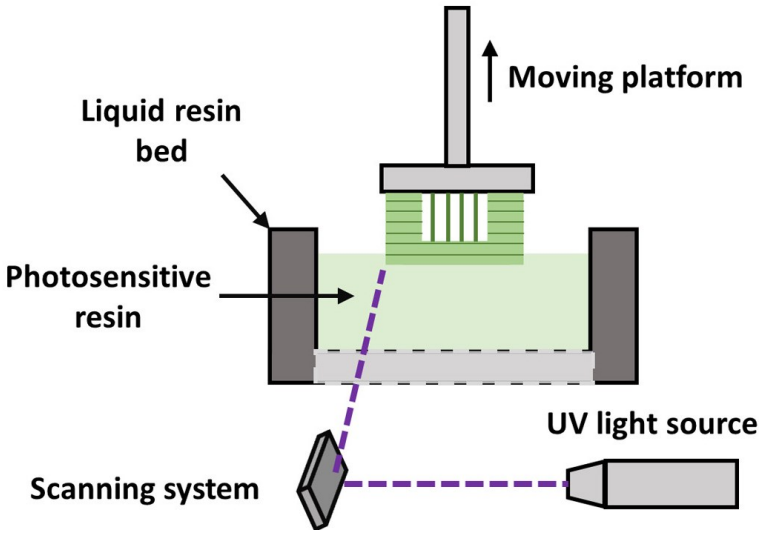



*Fig. 6 – Schematization of Vat Polymerization machine [24]*

The main difference between these two technologies lies in the way of polymerization. During the SLA process, each individual dot of each layer is cured individually, due to an UV laser; on the other hand, during DLP, using a projector, the polymerization of the entire layer is done at one time. Thus, DLP method offers higher printing speed [57]. Regardless of which method is used, the production of a component using vat polymerization consists of the following steps [4]:

1. Preparation: A 3D model is designed using CAD software and then sliced into thin layers. These slices are sent to the vat polymerization machine for processing.
2. Liquid resin: The machine contains a vat filled with liquid photopolymer resin, which is sensitive to light, typically ultraviolet.

3. Polymerization: a light source selectively exposes the resin to light based on the cross-sectional shape of the first layer. This exposure allows curing the resin in the specified shape.
4. Layer-by-layer construction: the build platform either lowers (top-down approach) or rises (bottom-up approach) to allow a new layer of liquid resin to cover the previously cured layer. The process repeats, with each layer being cured and adhered to the layer below it until the entire object is formed.
5. Post-processing: once the object is fully printed, it is removed from the vat and may require post-curing to enhance mechanical properties. Additional post-processing steps like washing to remove excess resin, and sanding or coating for surface finishing, could be necessary.

A crucial process parameter is layer thickness. This parameter determines the resolution and surface quality and the build time. In fact, thinner layers result in higher resolution, and this allows to realize accurate features but increase build time. The duration for which the resin is exposed to light represents the exposure time and it affects the degree of polymerization and mechanical properties of the part.

Vat polymerization can produce complex geometries with fine details and smooth surfaces. The accuracy of the printed part is determined by the resolution of the printer's light source. In SLA printers, XY resolution, defined as the minimum feature size that can be reproduced, is defined by the diameter of the laser spot; in DLP it is determined by the pixel size of the projector. On the other hand, the Z- axis resolution determines the layer thickness, that can be modified by changing material or printer [58]. Layer thickness that can be achieved by these processes is less than 50 mm, ensuring that very fine detail and features can be realized and offering superior surface finishes compared to other additive manufacturing processes [59].

Another advantage of vat polymerization lies in the variety of usable materials. A wide range of photopolymer resins is available, including those with specific properties such as high strength, flexibility, or biocompatibility. Additionally, it is possible to create multi-material structures [60], very useful in biomedical applications, for the realization of tissue construct, to better emulate biological systems.

Due to the precision and the accuracy of vat polymerization, it is typically limited to small build volumes compared to other AM processes, generating size constraints. During the process, it is also often required to insert very intricate support structures, to tilt components in the building chamber. These supports need to be removed post-printing and this operation adds time and complexity to the entire process, that also need in any case post-curing and cleaning steps. As for the costs, photopolymers are more expensive than other polymers and they are sensitive to light and temperature, requiring careful handling and storage. The equipment also consists of several parts characterized by high cost, such as the handling system and the lighting source.

Vat polymerization finds its applications in all those fields in which high level of detail is required [57]; in medical and dental industries it is used for producing dental models, customized patient implants and surgical guides, owing to its precision and biocompatible materials [61]. In aerospace and automobile industries [62], it is used to create functional parts and lattice structures with high strength and low weight. In jewelry it allows the creation of intricate and customized designs and patterns.

In summary, vat polymerization is a versatile and precise additive manufacturing process well-suited for applications requiring high detail and smooth surface finishes. However, it is important to consider its high cost and post-processing requirements when selecting it for specific applications.

### 1.2.6 Material jetting

Material Jetting (MJ) is an advanced additive manufacturing technology that builds objects layer by layer by precisely depositing droplets of material, which subsequently harden to form a solid. This technique is analogous to inkjet printing, but instead of ink, materials such as photopolymers, metals, or wax are used [63]. MJ is renowned for its ability to create highly detailed, multi-material, and multi-color parts [19], making it a popular choice for prototyping, tooling, and in some cases, end-use products.

Material Jetting can utilize a variety of materials, depending on the application:

- Photopolymers: These are the most commonly used materials in MJ. They are light-sensitive resins that solidify when exposed to UV light. Photopolymers are ideal for creating highly detailed and smooth surfaces, making them popular for prototyping.
- Waxes: Waxes are used primarily in the jewelry industry and for investment casting. They can easily melted away after the part is created.
- Metals: Metal material jetting is still in a developmental stage but holds significant promise for high-precision applications. It typically involves the deposition of metal droplets, which are later sintered or fused.
- Multi-Material Options: MJ allows for the combination of different materials within a single build, enabling parts with varied mechanical properties or multiple colors.

The process begins with the selective deposition of droplets from a print head onto a build platform; the print head moves in a controlled manner, guided by a digital design file (usually a CAD model). After deposition, the material is solidified by a curing process. For photopolymers, this typically involves ultraviolet (UV) light curing. For metals, the droplets may solidify through cooling or further post-processing steps. The print head continues to deposit material, building the object layer by layer. Each layer is solidified before the next one is deposited. After the object is fully formed, post-processing may be required. This can include cleaning off excess material, removing support structures, or additional curing. Fig. 7 shows a schematization of the process [63].

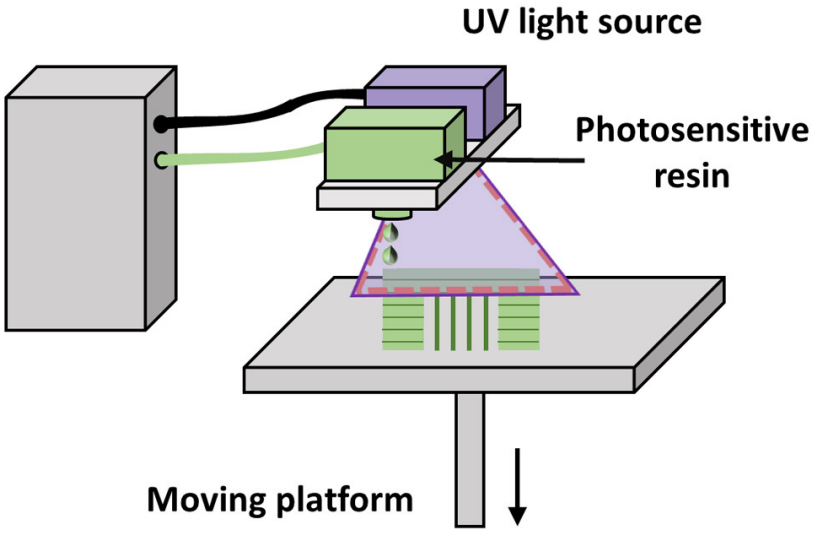



*Fig. 7 – Schematization of Material Jetting machine [24]*

Material Jetting offers excellent dimensional accuracy and fine feature resolution, making it ideal for producing complex geometries with high precision and smooth surface quality.

Furthermore, using this process is possible to print with multiple materials and colors simultaneously, allowing for parts with intricate designs and functional gradients. Compared to other AM technologies, material jetting systems are often easier to operate and maintain, with fewer material handling requirements; finally, material jetting is an efficient process with minimal material waste, as the material is deposited only where needed.

However, material jetting has some limitations, including [63]:

- Material Limitations: although the process could be versatile, it is limited by the range of materials available, particularly in comparison to technologies like Stereolithography (SLA) or Selective Laser Sintering (SLS).
- Support Structures: MJ often requires the use of support structures for overhanging features, which need to be removed in post-processing. The removal of these supports can be labor-intensive and might affect surface quality.
- Mechanical Properties: Parts produced via material jetting may have inferior mechanical properties compared to those made by other methods such as SLS or Direct Metal Laser Sintering. This limits their use in load-bearing applications.
- Cost: The cost of MJ systems and materials can be higher than other AM technologies, which might be prohibitive for some users.

Material Jetting is used, nowadays, across various industries for different applications. Most relevant applications of the processes concern prototyping and rapid tooling; in prototyping, MJ is widely used for creating high-fidelity prototypes, especially in industries like consumer electronics, automotive, and aerospace, where detail and surface finish are crucial. Regarding tooling applications, with this process it is possible to create molds and other tooling components, especially when fine detail is needed.

Material Jetting is a powerful additive manufacturing process that excels in producing highly detailed, multi-material, and multi-color parts. While it has certain limitations in terms of material properties and cost, its advantages make it an invaluable tool for specific applications, particularly in prototyping and tooling fields. As technology evolves, it is likely to play an increasingly important role in the broader landscape of additive manufacturing.

### 1.2.7 Material extrusion

Material Extrusion (MatEx) is a widely used additive manufacturing process that builds parts layer by layer through the deposition of material. This process is most commonly associated with Fused Deposition Modeling (FDM) or Fused Filament Fabrication (FFF), both of which use thermoplastic materials extruded through a heated nozzle. The simplicity, versatility, and accessibility of the Material Extrusion process have made it one of the most popular techniques in both industrial and consumer-grade 3D printing.

Fig. 8 depicts schematization of the material extrusion. During the process the material, usually in the form of a filament, being fed into the extrusion head. The filament is pushed into a heated nozzle where it is melted; the molten material is extruded through a small nozzle onto the build platform. The extrusion head is guided by a digital design file (usually a CAD model), which dictates the path of the nozzle. The material is deposited layer by layer according to the design. As the material is deposited, it cools and solidifies, forming the first layer of the object. The build platform then moves down (or the nozzle moves up), and the next layer is deposited on top of the previous one. This process repeats until the entire object is constructed [19, 21]. Once the object is fully printed, post-processing may be necessary. This can include the removal of support structures, surface finishing, or thermal treatment to improve mechanical properties.

There are mainly three types of material extrusion machines [63]; in cartesian fused deposition modeling, the extrusion head travels within XY plane, while build platform travels in Z direction. In the second type, the printing bed is stationary, and the movements in XYZ are entrusted to the printed head; these cases machines are polar type. Finally, when the extrusion head can travel in all printing environments, machines are called delta printers.

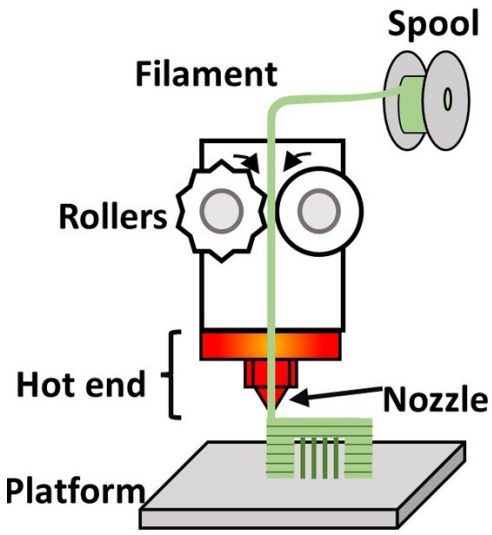



*Fig. 8 – Schematization of Material Extrusion machine [24]*

Material Extrusion typically uses thermoplastic polymers, but advancements have expanded the range of materials to include composites and even metals. Common materials include [2, 63, 64]:

- Thermoplastics: Polylactic acid (PLA), for example, is a biodegradable plastic derived from renewable resources like corn starch or sugarcane. It is easy to print with and is one of the most commonly used materials in FDM/FFF. Another thermoplastic widely used is Acrylonitrile Butadiene Styrene (ABS), that is a petroleum-based plastic known for its toughness and impact resistance. It requires a heated bed and controlled environment to prevent warping.
- High-performance thermoplastics: these polymers are characterized by a processing temperature higher than 250 °C [65]; they are engineered to withstand elevated temperatures without compromising their mechanical integrity, making them suitable for demanding environments where conventional polymers may falter. Their high glass transition temperatures and resistance to thermal degradation equip them for applications where thermal stability is paramount. Industries such as aerospace, automotive, and electronics benefit from high-performance thermoplastics ability to maintain structural integrity under extreme conditions [66].
- Composite materials [67]: it is possible to use fiber reinforced materials, such as carbon fiber or glass fiber reinforced filaments. The first one, combines a thermoplastic matrix with carbon fiber strands, providing enhanced strength and

stiffness. Similar to carbon fiber composites, glass fiber reinforced materials offer improved mechanical properties, particularly in terms of stiffness and heat resistance.

- Elastomers: Thermoplastic elastomers (TPEs) like TPU (Thermoplastic Polyurethane) are used for parts that require flexibility and durability, such as gaskets, seals, and flexible components.
- Metal-Filled Filaments: metal powders embedded in a thermoplastic matrix can be extruded and later processed to remove the plastic binder, leaving behind a metal part. This process, however, requires sintering to achieve full density.

Thus, material extrusion can handle a wide range of materials, from standard thermoplastics to high-performance composites and flexible materials; this is one of the greatest advantages of this process. Additionally, the technology is relatively inexpensive compared to other AM processes, both in terms of equipment and material costs [54], making it accessible for a broad range of users; machines are generally user-friendly, with straightforward setup and operation, making them suitable for both professionals and hobbyists. Material Extrusion can be also used for a wide range of part sizes, from small, intricate components to large, industrial-scale parts: printers are characterized by an inherent scalability, as well as the process allows for the easy creation of custom parts, making it ideal for prototyping and small-batch production.

Due to the advantages just listed, material extrusion is employed across a variety of industries for numerous applications. One of the most common uses of Material Extrusion is in rapid prototyping, where engineers and designers create functional prototypes to test form, fit, and function. However, advancements in materials have enabled the production of functional, end-use parts, particularly in industries like automotive, aerospace, and consumer goods. The ability to quickly produce custom tools, fixtures, and jigs makes material extrusion also invaluable in manufacturing environments where custom setups are often required. Material Extrusion is finally used to create custom medical devices, such as prosthetics, orthotics, and surgical guides, due to its ability to produce patient-specific parts quickly and affordably [8, 68].

Despite the advantages just discussed, there are also limitations related to this process; first, parts produced via material extrusion often exhibit anisotropic properties, meaning their mechanical strength varies depending on the direction of the layers [69]. The interlayer bonding is typically weaker than the intralayer strength [70]. Moreover, the layer-by-layer

deposition process often results in a visible "stair-stepping" effect, leading to a rough surface finish. Post-processing, such as sanding or chemical smoothing, is often required to achieve a smooth surface [18]. The accuracy of parts produced by Material Extrusion can be affected by factors such as material shrinkage, warping, and the precision of the extrusion system [71]. This can limit its use in applications requiring high dimensional accuracy. Complex geometries may require support structures to prevent overhangs from collapsing during the building process. These supports need to be removed afterward, which can be labor-intensive and may leave marks on the final part.

Material Extrusion is a versatile and accessible additive manufacturing process with broad applications in prototyping, tooling, and end-use part production. While it has some limitations, such as anisotropy and surface finish quality, ongoing advancements in materials and process technologies continue to expand its capabilities. As technology evolves, Material Extrusion is expected to play an increasingly important role in both industrial and consumer manufacturing.

### *Material Extrusion processes application fields*

The material extrusion process, due to the explained advantages, has found various applications over the years. The main areas of application include fields where components with a high level of detail, materials with low weight but high mechanical properties and a strong level of customization are required.

The aerospace industry demands materials that can withstand extreme conditions and stringent requirements [72, 73]. Material extrusion printed parts find applications in aerospace for lightweight structural components, such as brackets, mounts, and interior cabin parts. Using materials such as high-performance polymers or fiber-reinforced filaments, is possible to produce parts with high strength-to-weight ratio and excellent thermal and chemical resistance, making them suitable for demanding aerospace environments. These components provide a balance between performance and weight, contributing to fuel efficiency and overall safety. The aerospace industry demands high-performance materials and precision engineering, making material extrusion process a valuable tool for various applications. In prototyping and design validation, this process is extensively used for creating prototypes of aerospace components, including airfoils, cabin parts, and engine components. These prototypes allow the validation of designs, test fit and form, and through them it is possible to conduct aerodynamic testing at a fraction of the cost and time required

for traditional manufacturing methods [74]. Furthermore, tooling and fixtures customization is a critical step in aerospace manufacturing. Material extrusion process allows for the rapid production of lightweight, durable jigs, fixtures, and assembly tools. This capability speeds up the manufacturing process and reduces costs, particularly for small production runs or custom projects. Regarding end-use parts, MatEx process is increasingly being used to manufacture custom interior components for aircraft, such as seat frames, tray tables and overhead bin parts; the ability to produce these parts on-demand helps reduce inventory and allows for greater customization, in a sector where parts are often produced in low volumes, offering a cost-effective solution for manufacturing custom parts without the need for expansive tooling [75].

As well as the aerospace industry, also the automotive industry has widely adopted material extrusion for both prototyping and end-use applications [75]; using this process is possible to create quick iteration and validation of designs and this can accelerate the development process and ensures the performance of critical components. Material extrusion printed parts serve as functional prototypes for components like dashboards, grilles and engine components. These prototypes allow for design verification, fit testing, validation of designs, and even functional testing under actual operating conditions, before mass production. This accelerates the product development cycle and reduces the costs associated with traditional prototyping. With advancements in materials, material extrusion process is now being used to produce end-use parts for vehicles. This includes low-volume production runs of custom or specialty parts, such as brackets, housings, and even exterior panels. Similar to aerospace, this process is used to produce custom interior components such as air vents, control knobs, and panels. These parts can be produced quickly and customized for specific vehicle models or customer preferences. Material extrusion process gives the possibility to realize customized tooling, jigs and fixtures [76] used in the assembly line faster than other processes; tools are crucial for positioning, holding, and aligning components during assembly, improving efficiency, and reducing production times. Finally, with a view to the lightening of structures to improve fuel efficiency and performance, MatEx allows to produce lightweight parts, often incorporating lattice structures that maintain strength while reducing material usage.

In the biomedical field [9, 77], material extrusion process has opened up new possibilities for patient-specific solutions and medical devices, especially using materials like PEEK an

PEI that are characterized by biocompatibility. The medical field benefits from customized implants that match patient anatomy, reduce rejection risk, and enable faster recovery. MatEx-printed PEEK implants offer biocompatibility, which is critical for successful medical applications. This process is widely used to create anatomical models for pre-surgical planning and education. Models, based on patient-specific imaging data (e.g., CT or MRI scans), allow surgeons to better understand complex cases, practice procedures, and improve surgical outcomes [78]. It is also possible to produce custom prosthetics and orthotics tailored to individual patients. This includes limb prostheses, orthotic braces, and cranial implants [71]. The use of biocompatible materials ensures that these devices are safe for long-term use.

In all the fields described, material extrusion process gives some essential advantages, including:

- Customization: FDM allows for the production of highly customized parts, tailored to specific requirements in aerospace, automotive, and biomedical applications.
- Cost-Effectiveness: FDM is particularly cost-effective for low-volume production and prototyping, which is crucial in industries where custom or small-batch production is common.
- Rapid Turnaround: The ability to quickly produce parts and prototypes accelerates the development cycle, enabling faster innovation and response to market demands.
- Material Versatility: The availability of advanced thermoplastics, composites, and biocompatible materials expands the range of possible applications across these industries.

Material extrusion process plays a crucial role in the aerospace, automotive, and biomedical fields due to its ability to produce customized, cost-effective, and functional parts. While it has some limitations, ongoing advancements in materials and technology continue to expand their capabilities, making it an increasingly valuable tool across these industries. As MatEx technology evolves, it is likely to see even broader adoption in both prototyping and end-use production, particularly in applications that benefit from customization and rapid turnaround.

## 1.3 Mechanical characterization of plastic components

Additive manufacturing processes have fundamentally changed the way components are made [4], especially regarding plastic materials, enabling the creation of complex geometries and custom components with minimal material waste. As this technology advances, understanding the mechanical properties of the resulting plastic materials becomes increasingly crucial [79, 80]. Mechanical characterization serves as a fundamental aspect in evaluating the performance, reliability, and applicability of these materials in various industrial sectors.

Mechanical characterization encompasses a range of tests and analyses that quantify the mechanical behavior of materials under different conditions. For plastic materials produced through additive manufacturing, these properties can vary significantly depending on factors such as the type of polymer used [81], the chosen printing process, the processing parameters [82-84], the orientation of the printed layers [85], and post-processing treatments [86]. Key mechanical properties of interest typically include tensile strength [87], compressive strength [88], elasticity, hardness, and fatigue life [89], among others.

The layer-by-layer fabrication process inherent to additive manufacturing introduces anisotropy in the mechanical properties of printed plastics [90]. Unlike conventionally manufactured materials, where properties are often more homogeneous, the mechanical response of AM plastics can be highly directional. This anisotropy is influenced by the bonding between layers, the cooling rate, and the potential presence of voids or defects during the printing process. Thus, characterizing the mechanical properties of these materials is not only essential for quality control, but also for optimizing design and process parameters to achieve the desired performance. Moreover, the wide variety of polymers used in additive manufacturing [79, 91], from thermoplastics like polylactic acid (PLA) and acrylonitrile butadiene styrene (ABS) to more advanced materials such as polyetheretherketone (PEEK), necessitates a comprehensive approach to mechanical characterization. Each material exhibits distinct mechanical behaviors, which are further influenced by the specific additive manufacturing technique employed.

Thus, the mechanical characterization of plastic materials in additive manufacturing is a vital step in ensuring that the printed components meet the required performance criteria for their intended applications. By understanding the mechanical properties, it is possible to better

predict the behavior of these materials under various operational conditions, leading to more reliable and efficient use of additive manufacturing technologies in industries ranging from aerospace to biomedical applications [8, 72, 92, 93]. In this section the main mechanical tests dedicated to plastic materials components will be analyzed.

### 1.3.1 Tensile test

The procedure to be followed, with all the information and guidelines, regarding how to conduct the test on plastics materials, is described in the ASTM D638 standard [94]. This standard can be applied for the determination of the tensile properties of unreinforced and reinforced plastics; it is applicable for dumbbell-shaped specimens with thickness up to 14 mm. The specimens shall respect the dimensions shown in Table 1.

*Table 1 – Specimens dimensions (referred to Fig. 9) [94]*

*Specimen Dimensions for Thickness, T (mm)*

| *Dimensions* | 7 or under | | Over 7 to 14 | 4 or under | | Tolerances |
|---|---|---|---|---|---|---|
| | Type I | Type II | Type III | Type IV | Type V | |
| *W* | 13 | 6 | 19 | 6 | 3.18 | ±0.5 |
| *L* | 57 | 57 | 57 | 33 | 9.53 | ±0.5 |
| *WO* | 19 | 19 | 29 | 19 | 9.53 | +3.18 |
| *LO* | 165 | 183 | 246 | 115 | 63.5 | No max |
| *G* | 50 | 50 | 50 | 25 | 7.62 | ±0.13 |
| *D* | 115 | 135 | 115 | 65 | 25.4 | ±5 |
| *R* | 76 | 76 | 76 | 14 | 12.7 | ±1 |
| *RO* | | | | 25 | | ±1 |

Fig. 9 shows the five types of specimens available for the test:

- Type I: it is the preferred type of specimen and when it is possible, it shall be used. The thickness is 7 mm or less and it is the only one type usable for reinforced composites.
- Type II: it can be used when, after testing type I specimens, the failure doesn't occur in the narrow section.
- Type III: this type of specimen is suitable for testing material with thickness in the range of 7 mm and 14 mm.

- Type IV: it is used for testing nonrigid plastic with a thickness up to 4 mm.
- Type V: it shall be used when there is limited material with a thickness of 4 mm.

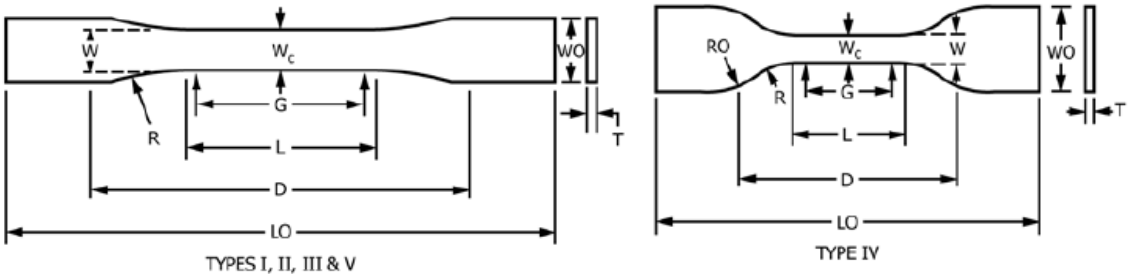



*Fig. 9 – Dimensions of the test specimens [94]*

The testing machine shall be equipped with a traveling crosshead that moves at a constant speed and with a fixed or stationary member. The specimen is held by grips between the two members; grips could be fixed, if they are rigidly attached to the members, or self-aging, and in this case, they can move freely so that the load axis application matches with the axis of the specimen. If grips are fixed it is necessary to align the axis of the specimen as far as possible with the direction of the applied load. During the test the total tensile load carried by the test specimen is shown due to a load-indicating mechanism that shall be free of inertia and shall indicate the load with an accuracy of ±1% or less. To determine the modulus of elasticity it is possible to use an extensometer that automatically and continuously records data with a maximum strain error of 0.0002 mm/mm. For isotropic materials, it is necessary to test at least five specimens for each sample, while for anisotropic materials shall be tested five specimens normal to and five parallel with the axis of anisotropy. The speed of the test is strictly dependent on the type of plastics and specimens used; in Table 2 the possible values are reported. If the speed is not specified it shall be used the lowest speed for the specimen geometry used which gives rupture in a time ranging from 0.5 minutes to 5 minutes.

After tests are finished and after collecting all data, it is possible to determine the stress-strain curve, that is depicted in Fig. 10, and the following quantities can be determined:

- Tensile strength ($\sigma$): it is calculated by dividing the maximum load by the average original cross-section of the specimen, as shown in eq. 3; tensile strength is expressed in Newton per square meters.

$$\sigma = \frac{W}{A_0} \qquad \textit{eq. 3}$$

- Percent elongation (%El): the procedure to calculate this quantity is shown in eq. 4 and eq. 5; it represents the change in gage length relative to the original specimen length expressed as a percent. It can be calculated also at yield point and break point.

$$\varepsilon = \frac{\Delta L}{L_0} = \frac{L - L_0}{L_0} \qquad \textit{eq. 4}$$

$$\%El = (\frac{L - L_0}{L_0}) * 100 = \varepsilon * 100 \qquad \textit{eq. 5}$$

- Nominal strain at break ($\varepsilon_U$): it is calculated by dividing the change in grip separation at the point of rupture by the original grip separation and multiplying by 100, as shown in eq. 6.

$$\varepsilon_U = \left(\frac{L_U - L_0}{L_0}\right) * 100 \qquad \textit{eq. 6}$$

- Modulus of elasticity (E): it is calculated by extending the initial linear portion of the load-extension curve and dividing the difference in stress corresponding to any segment of the section.
- Secant modulus: it is calculated at designated strain by dividing the nominal stress by the designated strain.

*Table 2 – Designations for speed oh the testing*

| *Material type* | *Specimen type* | *Speed of testing (mm/min)* |
|---|---|---|
| *Rigid and semirigid* | I, II, III, IV | 5±25%<br>50±10%<br>500±10% |
| | V | 1±25%<br>10±25%<br>100±25% |
| *Nonrigid* | III, IV | 50±10%<br>500±10% |

For each series of tests, the arithmetic means of all values obtained and the standard deviation for the quantity in question shall be calculated.

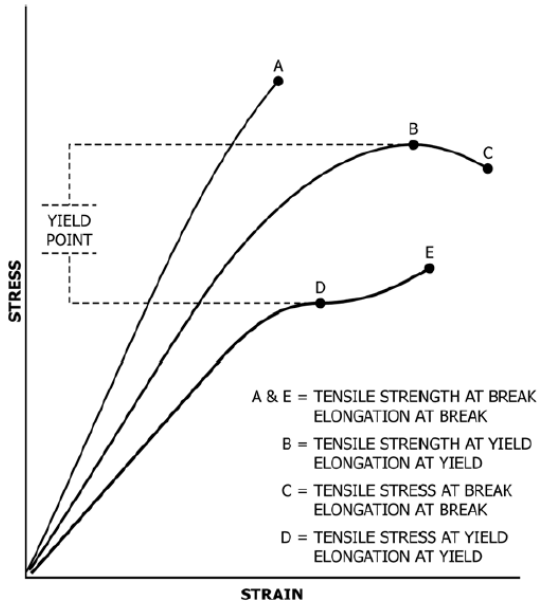



*Fig. 10 – Stress-strain curve [94]*

### 1.3.2 Compression test

The ASTM D695 standard [95] describes how to perform compression test of unreinforced and reinforced rigid plastics, including high-modulus composites. Compression test provides information about compressive behavior and properties of plastics, including modulus of elasticity, yield stress, deformation beyond yield point, and compressive strength.

The standard test specimen shall be in the form of right cylinder or prism. The specimen size shall be such that the height is twice the main dimension of the base. When the standard specimens cannot be obtained due to the thickness of the material, less than 6.4 mm, alternative specimens shall be used:

- For materials with a thickness less than 3.2 mm, a specimen conforming to that shown in Fig. 11 shall be used.
- For materials with a thickness in the range of 3.2 mm and 6.4 mm, the specimen used for strength measurements shall consist of a prism having a cross section of 12.7 mm by the thickness of the material and a length of 12.7 mm.

The testing machine shall be capable to control the crosshead movement at a constant rate due to a drive mechanism, with a standard speed that shall be 1.3 +- 0.03 mm/min. It is equipped with a load indicator capable of showing the total load applied on the specimen with an accuracy of 61% of the maximum indicated value of the test or more; this mechanism shall be free of inertia. There is also a compressometer that can automatically record the distance between two fixed points on the specimen at any time during the test. The load is

applied by a compression tool constructed in such a way as to apply the load axially within 1:1000 through flat surface parallel to each other within 0.025 mm in a plane normal to the vertical loading axis.

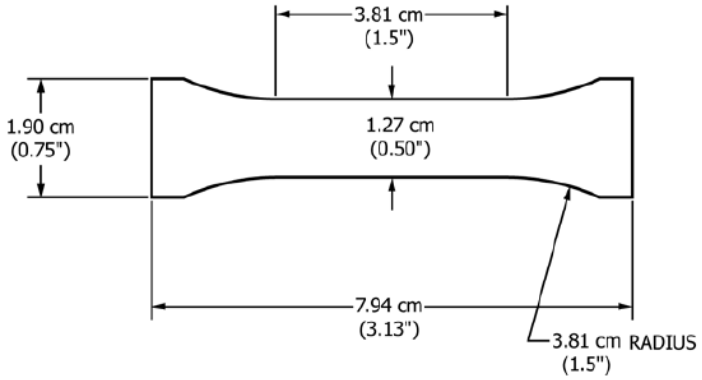



*Fig. 11 – Compression Test Specimen for materials with a thickness less than 3.2 mm [95]*

For isotropic materials, at least five specimens shall be tested for each sample, while for anisotropic materials it is necessary to test five specimens normally and five parallel with the axis of anisotropy.

After tests are completed, the following quantities can be determined:

- Compressive strength: it is calculated by dividing the maximum compressive load by the initial cross-sectional area of the specimen.
- Compressive yield strength: it is computed as the previous strength but calculate in the yield point.
- Offset yield strength: it is the stress at which the stress-strain curve departs from linearity by a specified percent of deformation.
- Modulus of elasticity: it is calculated drawing a tangent to the initial linear portion of the deformation curve, selecting a point on this and dividing the compressive stress at this point by the corresponding strain.

For each series of tests, it shall be calculated the arithmetic mean of all values obtained and the standard deviation for the quantity considered.

### 1.3.3 Flexural behavior

The ASTM D790 standard [96] provides the procedure to determine flexural proprieties of unreinforced and reinforced plastics; using this method it is not possible to determine flexural strength for those materials that do not break within the 5% strain limit, because

here it is used a three-point loading system, while for those materials it is necessary a four-point loading system, that can be found in ASTM D6272 standard [97].
This test follows two different procedures depending on the type of material to be tested:

- Procedure A: shall be used for the determination of flexural properties for materials that break at small deflections. The strain rate is 0.01 mm/mm/min.
- Procedure B: it is adapted for the measurement of flexural strength only as it is characterized by a higher standard deviation than comparable data obtained by using Procedure A. The strain rate is higher than that used in the previous procedure, and it is 0.10 mm/mm/min.

Fig. 12 shows the specimen, that is a prismatic bar with rectangular cross section, placed on two supports and loaded by a loading nose located in the middle of the two supports. The loading nose shall have a cylindrical surface, with a radius that shall be 5+- 0.01 mm, unless otherwise specified. When other dimensions are used, the radius shall be between 3.2 mm and a value that is four times specimen depth. The specimens' dimensions shall be as follows:

- If the thickness of the specimen is higher than 1.6 mm, the support span shall be 16 times the depth of the beam and the specimen shall be long enough to allow an overhang that is sufficient to prevent the specimen from slipping through the support. If the test is flatwise, the depth of the specimen and its thickness shall be equal, while, if the test is edgewise, the depth of the specimen shall not exceed the width, which shall be equal to the thickness of the sheet.
- If the thickness of the specimen is lower than 1.6 mm, the length shall be 50.8 mm and the width 12.7 mm; specimen shall be tested flat on a 25.4 mm support span.

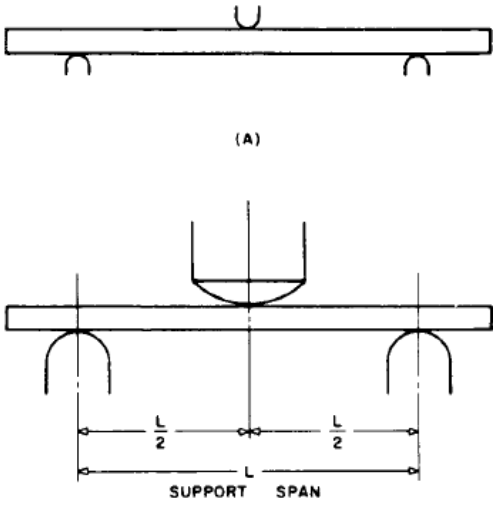



*Fig. 12 – Specimen and loading nose usable during the test [96]*

The testing machine shall be equipped with a deflection measuring device and shall operate at a constant rate of crosshead with an error in the load measuring system less than 61% of the maximum load; the load indicating mechanism shall be free of inertia. The machine shall have enough stiffness to ensure that the total elastic deformation of the system does not exceed 1% of the total deflection of the specimen during the test. It is possible to use micrometers for measuring thickness and width of the specimen; micrometers shall discriminate at least 0.025 mm. In the case of isotropic material, it shall be tested five specimens or more for each sample; on the other hand, for anisotropic materials, it is necessary to test at least five specimens for the flatwise condition and five specimens for the edgewise condition.

Once the test is completed, it is possible to determine the following quantities:

- Flexural stress: it is possible to calculate at any point of the load-deflection curve, multiplying three times the load by the support span and dividing the resulting quantity by two times the square of the depth of beam testing multiplying by the width of beam tested; it shall be use eq. 7:

$$\sigma_f = \frac{3 * P * L}{2 * b * d^2} \qquad \textit{eq. 7}$$

- Flexural strength: it is the maximum flexural stress supported by the specimen during the test.
- Flexural offset yield strength: it is calculated on the point in which the stress-strain curve deviates by a given strain from the tangent to the initial line portion of the curve.
- Flexural stress at break: it is calculated according to eq. 7 at the point of break.
- Stress at a given strain: it is calculating by eq. 7 by setting P equal to the load corresponding to the desire deformation.
- Flexural strain: it is “the nominal fractional change in the length of an element of the outer surface of the test specimen at midspan, where the maximum strain occurs”; it can be calculated using eq. 8, where D represents the maximum deflection of the center of the beam:

$$\in_f = \frac{6 * D * d}{L^2} \qquad \textit{eq. 8}$$

- Tangent modulus of elasticity: it is the ratio between stress and its corresponding strain within the elastic limit.

- Secant modulus: it is calculated dividing stress by strain at any point of the stress-strain curve.
- Chord modulus: it is calculated between two selected points, using eq. 9:

$$E_f = \frac{\sigma_{f2} - \sigma_{f1}}{\epsilon_{f2} - \epsilon_{f1}} \qquad \textit{eq. 9}$$

The arithmetic means of all values obtained and the standard deviation shall be calculated.

### 1.3.4 Shear test

The ASTM D732 standard [98] provides all the information and the procedure to determine the shear strength of plastics materials with a thickness in the range of 1.27 mm and 12.7 mm.

The specimen shall be a disk with a diameter of 50.8 mm or a square with 50 mm side. A hall 11 mm in diameter shall be drilled at the center of the specimen and the upper and lower surfaces shall be parallel to each other. The test is conducted with a constant crosshead speed of 1.27±0.30 mm/min, due to a drive mechanism that imparting uniform and controlled velocity. The testing machine is also equipped with a mechanism that indicates the load carried by the test specimen free from inertia, with an accuracy of ±1% at least. The shear tool is a punch that permits the specimen to stay rigidly clamped both to the stationary and the movable block, to avoid its deflection. It is also necessary to equip the testing machine with a micrometer that can measure the thickness of the specimen. For each sample material, a minimum of five specimens shall be tested.

The shear strength is the maximum load required to shear the specimen divided by the sheared area, with the rupture of the specimen such that the moving portion of the load fixture has completely cleared the stationary portion.

# Chapter 2 – Characteristics of thermoplastic materials

Polymeric materials can be divided into two categories, which are thermoplastics and thermosets [99]. Thermoplastics are a key class of materials used extensively in additive manufacturing [100] due to their re-shapeable nature and properties. They soften when heated and harden when cooled: this is a reversible process that allows for multiple cycles of melting and solidification, which is particularly advantageous in additive manufacturing processes [63]. This reversible process is possible due to the molecular structures of thermoplastics, that consists of long and short carbon chains that work independently. On the other hand, thermoset materials cross-linked polymers, and this characteristic does not allow them to be remolded when heated, instead they undergo thermal degradation [99].

Thermoplastics typically exhibit the following thermal behavior [101], that will be more detailed in the next section:

- Glass transition temperature ($T_g$): this is the temperature range over which the polymer transitions from a hard, glassy material to a softer, rubber state. For some thermoplastics, this is the critical temperature that determines their working temperature range.
- Melting temperature ($T_m$): this is the temperature at which the crystalline regions of the polymer melt. In amorphous polymers, a distinct melting point is not observed, but a gradual softening occurs instead.

Thermoplastics in additive manufacturing offer a wide range of mechanical properties and thermal behaviors, making them suitable for various applications, from prototyping to functional parts. Their thermal behavior is critical in determining the quality and mechanical performance of printed objects, especially in processes like material extrusion. Understanding these properties and behaviors is essential for optimizing additive manufacturing processes and achieving desired material performance [102].

## 2.1 Amorphous and semi-crystalline polymers

Amorphous and semi-crystalline polymers exhibit distinct structural characteristics that significantly influence their physical properties and applications. Amorphous polymers lack a long-range ordered structure, resulting in a disordered arrangement of polymer chains. This

disordered state leads to specific thermal and mechanical properties, such as lower density and higher flexibility compared to their semi-crystalline counterparts. In contrast, semi-crystalline polymers possess both crystalline and amorphous regions, where the crystalline regions exhibit regular chain arrangements, while the amorphous regions are disordered. The interplay between these two phases is critical in determining the overall material properties, including tensile strength, elasticity, and thermal stability [103, 104]. The thermal properties of amorphous and semi-crystalline polymers differ markedly, which affects their processing and performance in applications. For instance, the glass transition temperature ($T_g$) is a key parameter for amorphous polymers, marking the transition from a hard and relatively brittle state to a more rubber-like state upon heating. Semi-crystalline polymers, on the other hand, exhibit both glass transition temperature and melting temperature, with the latter being associated with the crystalline phase. The presence of crystalline regions in semi-crystalline polymers contributes to their higher tensile strength and modulus, as these regions can effectively bear loads and provide structural integrity [105]. Additionally, the mechanical properties of semi-crystalline polymers can be enhanced by optimizing the ratio of crystalline to amorphous phases, which can be tailored through processing techniques such as injection molding and selective laser sintering [103, 105]. Moreover, the morphology of these polymers plays a crucial role in their performance. In semi-crystalline polymers, the presence of tie chains that connect the crystalline and amorphous phases can enhance toughness and ductility, allowing for better energy absorption during deformation [106]. In contrast, amorphous polymers tend to exhibit higher resistance to mechanical strain due to their disordered structure, which allows for more significant chain mobility [107].

The choice between amorphous and semi-crystalline polymers depends on the specific application and it is often dictated by the required balance of properties. Amorphous polymers are favored for applications requiring transparency and flexibility, while semi-crystalline polymers are preferred for their strength and thermal stability [108]. Understanding the fundamental differences in structure and properties between these two types of polymers is essential for the development of advanced materials tailored for specific applications.

The properties and characteristics of amorphous and semi-crystalline polymers are fundamentally influenced by their structural arrangements. Amorphous polymers are characterized by their disordered chain arrangement, leading to unique thermal and mechanical properties, while semi-crystalline polymers exhibit a combination of crystalline

and amorphous regions that enhance their strength and stability. The interplay between these structural features is critical in determining the suitability of these materials for various applications.

### 2.1.1 Influence of temperature on the bonds between polymer chains in semi-crystalline polymers

The influence of temperature on the bonds between polymer chains in semicrystalline polymers is a critical aspect that affects their mechanical properties, thermal behavior, and overall performance in various applications. As temperature increases, the mobility of polymer chains generally increases, leading to changes in the interchain interactions and bonding characteristics. At elevated temperatures, semicrystalline polymers undergo significant changes in their amorphous and crystalline phases. The glass transition temperature is a crucial threshold; below $T_g$, the polymer chains are relatively immobile, resulting in a rigid and brittle state. Above $T_g$, the chains gain mobility, transitioning to a more flexible, rubbery state, which allows for enhanced interchain interactions and bonding [101]. This increased mobility facilitates the rearrangement of polymer chains, enabling them to accommodate stress and strain more effectively, thereby improving the material's toughness and ductility [109]. The crystalline regions in semicrystalline polymers are particularly sensitive to temperature changes. As the temperature approaches the melting temperature, the crystalline domains begin to soften, leading to a decrease in the density of interchain hydrogen bonds and van der Waals forces that stabilize the crystalline structure [110]. This phenomenon can result in a marked decrease in the mechanical strength of the material as the crystalline regions become less effective at bearing loads [111]. Conversely, the amorphous regions, which are more flexible, can absorb energy and deform under stress, contributing to the overall toughness of the polymer [112].

Moreover, the presence of nanoparticles within semicrystalline polymers can further influence the temperature-dependent behavior of polymer chains. For instance, the incorporation of nanoparticles can enhance the interfacial interactions between the polymer matrix and the nanoparticles, leading to improved mechanical properties at elevated temperatures. The increased surface area of nanoparticles, such as aluminum oxide, can create additional bonding sites for polymer chains, enhancing their mobility and facilitating better load transfer between the matrix and the filler [113]. Temperature also plays a role in the crystallization process of semicrystalline polymers. During cooling, the rate of

crystallization is influenced by the mobility of the polymer chains; higher temperatures allow for more rapid chain movement, which can lead to more efficient packing of chains into crystalline structures. However, if the cooling rate is too rapid, it can result in a higher fraction of amorphous regions, which may affect the overall mechanical properties of the material [114]. In summary, temperature significantly influences the bonds between polymer chains in semicrystalline polymers by affecting their mobility, interchain interactions, and the balance between amorphous and crystalline phases. Understanding these temperature-dependent behaviors is essential for optimizing the performance of semicrystalline polymers in various applications.

## 2.2 Thermal characterization of polymeric materials

Thermal characterization of polymeric materials is crucial for understanding their properties, stability, and performance in various applications. Thermal analysis measures the effects of energy exchange between the material and the environment that result in a change in the interaction existing in the mass of the specimen under investigation. Differential Scanning Calorimetry (DSC), Thermogravimetric Analysis (TGA), and Dynamic Mechanical Analysis (DMA) are three key analytical techniques used to evaluate the thermal behavior and properties of polymers. DSC analysis, which is widely used in many areas of research, development and quality control, makes it possible to study any phenomenon involving a change in the heat capacity of a material, exploring a wide range of temperatures and requiring small amounts of sample. TGA analysis, mainly used in the study of thermal and thermo-oxidative stability and related degradation mechanisms, is also a popular technique and uses small sample quantities. It measures changes in the weight of a material as a function of temperature and/or time in a controlled atmosphere environment. In DMA analysis, periodic stress is applied to the specimen, and the resultant strain is measured; this provides information on the mechanical characteristics of the material.

### 2.2.1 Differential Scanning Calorimetry (DSC)

The ASTM D3418 [115] standard defines the methodology to be followed to perform DSC analysis. DSC measures the heat flow into or out of a polymer sample as a function of temperature or time. It identifies thermal transitions such as glass transition temperature ($T_g$), melting temperature ($T_m$), crystallization temperature ($T_c$), and heat capacity changes. Differential scanning calorimetry is one of the most widely used analytical techniques for

the characterization of polymers and polymeric materials in general, food and pharmaceuticals, biological macromolecules such as proteins, etc., because of the simplicity with which the test can be performed and the amount of information it can provide. A DSC calorimeter measures the heat fluxes associated with the thermal transitions that occur in a sample when it is heated or cooled, if the test is performed in dynamic condition, or maintained at a constant temperature, in isothermal conditions, in a controlled manner. This allows the determination of the temperature or the temperature range during any transitions that occur in the sample, like melting processes or crystallization, and to quantify the energies associated with them. To be able to measure heat flux, since it is not an absolute quantity, it is necessary to have a benchmark sample; when the benchmark sample is thermally stressed similarly to the sample on which the test is conducted, the first sample will respond differently, providing a differential signal. The differential measurement is important both from a theoretical and practical point of view because the resulting signal can be studied independently of all those thermal effects external to the system that affect the two samples equally, allowing to obtain in output the behavior proper to the material under examination. In the specific case of polymers and polymeric materials in general, DSC calorimetry under dynamic conditions allows mainly to determine mainly the following variables:

- Glass transition temperature ($T_g$).
- Melting temperature ($T_m$).
- Crystallization temperature ($T_c$).
- Melting enthalpy ($\Delta H_m$) and crystallization enthalpy ($\Delta H_c$).
- Degree of crystallinity ($\chi_c$), in semi-crystalline polymers.

By means of DSC analysis under isothermal conditions, on the other hand, it is possible to perform thermal stability tests and to study the kinetics of crystallization and phase transitions, as far as this does not result in a change in the mass of the sample under examination.

To perform DSC analysis, there are two types of DSC instruments:

- Power (or energy) compensating calorimeter: it is equipped by two separate heating elements, one for the sample under test and one for the benchmark sample, consisting of an empty crucible, usually made of aluminum. Both elements are heated (or

cooled) and a compensating power is established between them to maintain the previously programmed heating (or cooling) rate. This power is a measure of the changes in enthalpy or heat capacity of the sample relative to the benchmark sample.

- Heat flow calorimeter: there is a single furnace where there is placed a copper-nickel alloy plate that provides or removes heat from the sample and the reference. One or more temperature sensors detect the temperature of individual crucibles, thereby measuring the temperature difference between the sample and the benchmark, which is then converted into equivalent energy.

Curves generated during DSC analysis report a signal expressed in mW as a function of temperature or time. The area subtended by the curve represents the energy involved in the transition and is normally converted by the instrument to J/g from the signal in mW, given the scan rate and the mass of the sample under investigation. To quantify the area of a peak (A), it is possible to use eq. 10, where m is the mass of the sample, ΔH the enthalpy change associated with the transformation, λ the thermal conductivity of the sample, and g an instrumental geometric factor.

$$A = \frac{m * \Delta H}{\lambda * g} \qquad \textit{eq. 10}$$

DSC calorimetry does not provide absolute quantities, so instrument calibration is always necessary. Temperature calibration is performed with a standard sample, that is typically high-purity indium, or benzoic acid, tin, or zinc, that has a sharp and well-defined melting temperatures in the range to be explored. Substances with known enthalpies of fusion, determined with adiabatic calorimeters, are used for calorimetric peak calibration. As a reference standard for estimating the specific heat of a material, substances that do not exhibit transitions over a wide temperature range should be used, such as sapphire. Usually, the accuracy of a DSC measurement is 1-2°C on temperature values and 5-10% on enthalpy values.

Using DSC measurements, the specific heat at constant pressure ($C_p$) of a material can be determined. To obtain this quantity, three DSC traces must be compared, which are the thermogram of a benchmark, that one of the samples under test, and that one of the empty sample holder. Knowing the scan rate used, that is represented by ratio of temperature variation and time ΔT/t, and the volume of the areas subtended by the thermograms, that

corresponds to the flow of heat q/t, in the area between two chosen temperatures, it is possible to find the heat supplied divided by the temperature increment, i.e., the value of $C_p$, characteristic of the material. eq. 11 $C_p$ shows ‘s calculation.

$$c_p = \frac{\frac{q}{t}}{\frac{\Delta T}{t}} = \frac{q}{\Delta t} \qquad \textit{eq. 11}$$

At the glass transition temperature there is a change in specific heat ($\Delta C_p$), detectable as a jump and a change in slope of the DSC curve; Fig. 13 shows DSC curve. The glass transition is a second-order transition involving a discontinuity in the second derivative of Gibbs free energy with respect to temperature. Conventionally, the measurement of $T_g$ is made by drawing two lines that ideally continue the baseline before and after the transition and the tangent to the point of maximum slope of the curve. The value of the glass transition temperature of a given material depends on its molecular and microstructural nature. In particular, the more flexible the polymer chain is, the lower the value of $T_g$ will be; conversely, all factors that increase the rigidity of the polymer chain led to an increase in $T_g$. The blending with other polymers or the presence of additives are all factors that influence the value of the glass transition temperature.

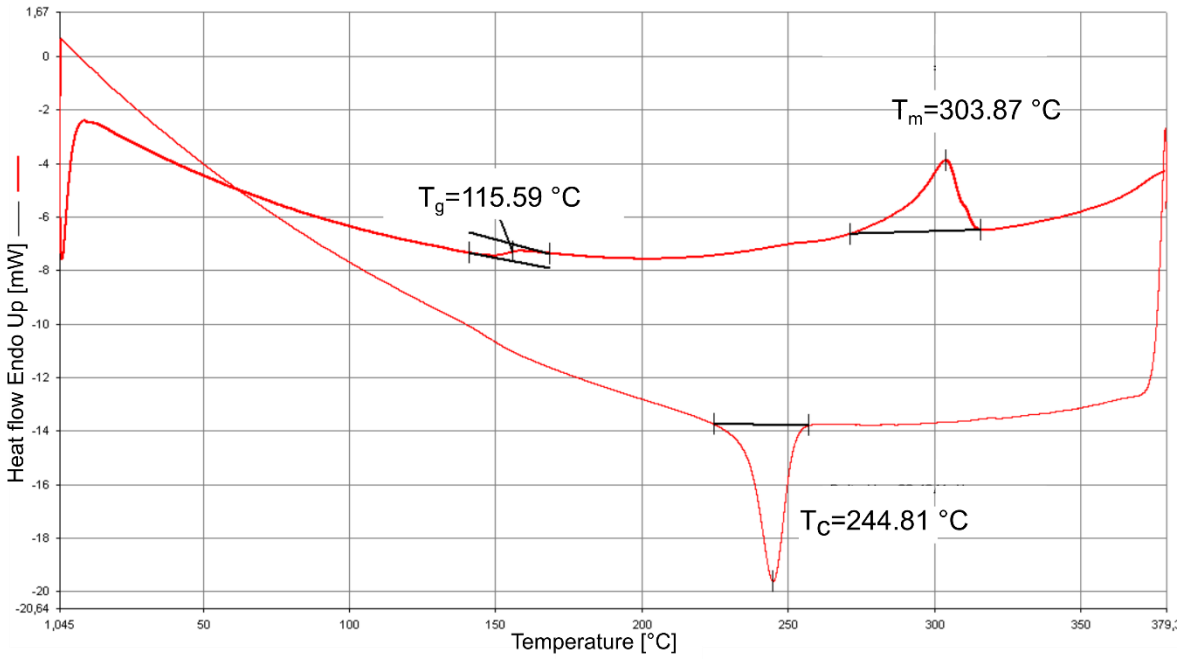



*Fig. 13 – DSC curve*

From the experimental value of $\Delta C_p$ measured at the glass transition, the degree of crystallinity ($\chi_c$) of a polymer can be calculated if the specific heat gain of the totally amorphous sample ($\Delta C_{pa}$) is known, according to the eq. 12.

$$\chi_c = 1 - \frac{\Delta c_p}{\Delta c_{pa}} \qquad \textit{eq. 12}$$

The melting temperature ($T_m$) of a semicrystalline polymer corresponds to the state transition of the crystalline phase to the viscous liquid phase. Although in this case it is a first-order transition, with latent heat absorption, it occurs in certain temperature range, because polymers are not monodispersed but always exhibit a distribution of molecular weights. The presence of defects along the polymeric chain contributes to further widening the melting temperature range of polymers. In DSC analysis, $T_m$ is usually denoted as the peak value of the melting endotherm. In addition to the nature of the material, this value is influenced by both the conditions under which the crystals were formed and the heating rate.

Similar reasoning can be made for the opposite phase transition, that is crystallization. The crystallization temperature ($T_c$) that is measured by DSC analysis is the temperature that corresponds to the point of minimum exotherm value in the temperature range at which crystallization occurs. The crystallization temperature depends strongly on the cooling rate: the higher this rate, the lower the observed $T_c$.

Another way to determine the degree of crystallinity of a polymer expects to know its enthalpy of melting. The enthalpy of a material is the energy required for the transition from one given temperature to another. Specifically, the enthalpy of fusion ($\Delta H_m$) is the heat required to bring a mole of substance from the crystalline state to the liquid or liquid-viscous state in the case of polymers, conversely, the enthalpy of crystallization ($\Delta H_c$) is the heat produced in the opposite transition. Using the DSC calorimeter from a simple area measurement of the melting peak or crystallization peak it is possible to measure the latent heat associated with the transition. Knowing the enthalpy of fusion of the polymer, it is possible to estimate its latent heat by relating it to the enthalpy of fusion of a perfect crystal free of defects ($\Delta H_m^0$), as shown in eq. 13:

$$\chi_c = \frac{\Delta \mathrm{H}_m}{\Delta H_m^0} \qquad \textit{eq. 13}$$

DSC calorimetry, as described so far, measures the amounts of energy absorbed, in endothermic phenomena, or released, in exothermic phenomena, by a given sample during

experiments under continuous heating or cooling (dynamic conditions) or at constant temperature (isothermal conditions). The advantages of this analysis mainly concern the non-destructiveness of the test, and the small amount of material required to perform the test, which is about 5 mg.

### 2.2.2 Thermogravimetric Analysis (TGA)

Thermogravimetric analysis (TGA) [116] consists of recording the change over time in the weight of a sample subjected to a programmed temperature scan. TGA analysis provides information on thermal stability, decomposition temperatures, and the amount of volatile components or fillers. The measurement is made with a microbalance, which is sensitive to changes in mass due to gas development or absorption, while the sample is placed in a furnace that allows for temperature and atmosphere control. With reference to polymeric materials, information obtainable by thermogravimetry concerns thermal stability, thermo-oxidative stability, composition in the case of multicomponent systems, and stability in corrosive or reactive atmospheres. Any chemical or structural changes that do not involve mass changes are not detectable by TGA analysis, just as direct information on the degradation products and thus the mechanisms of degradation cannot be obtained.

Thermogravimetric tests in the dynamic mode are typically carried out by varying the temperature with fixed scan rates at 10 or 20 °C/min in a flow-controlled gas atmosphere. The test result is a thermogram showing the temperature or time in the abscissa and the mass change expressed as an absolute value or percentage in the ordinate; Fig. 14 shows ax example of the thermogram. This thermogram is called thermal decomposition curve or TG curve; derivative or DTG curve is also often reported, which allows for better evidence of changes in sample weight. From the TG curve, the polymer degradation temperature can be determined. It is generally defined as the initial onset temperature, $T_{onset\text{-}i}$; sometimes other temperatures are also indicated such as the temperature at which 10% degradation of the material occurs, $T_{10\%}$, the temperature at which 50% degradation of the material occurs, $T_{50\%}$, and the onset temperature of end of degradation, $T_{onset\text{-}f}$. Another temperature, which is usually calculated to define degradation, is the temperature of maximum degradation rate ($T_{vmax}$) determined as the minimum point of the curve in DTG derivative and thus corresponding to the inflection point of the TG curve.

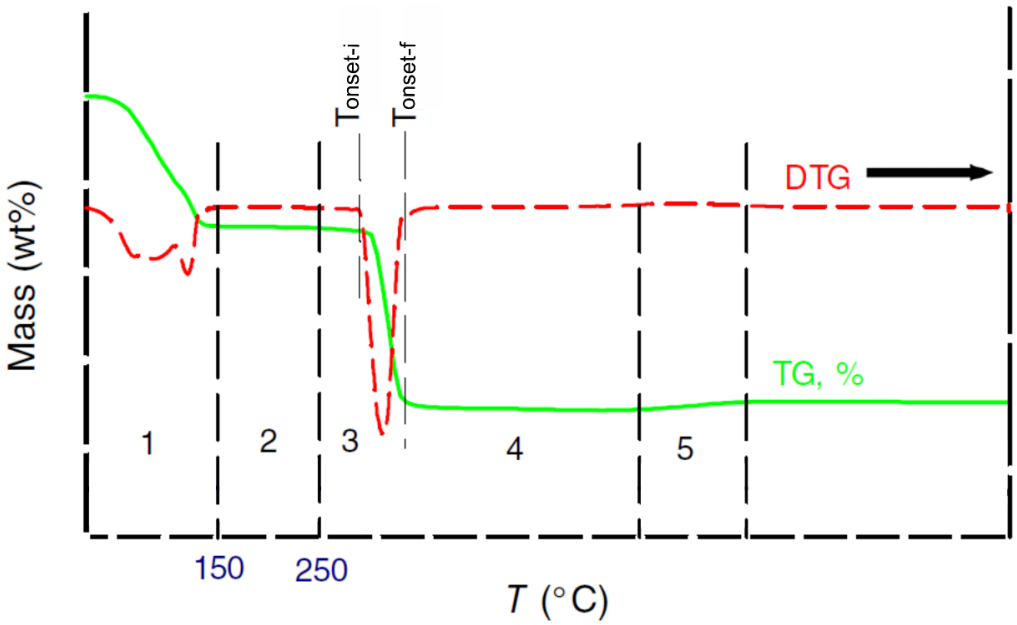



*Fig. 14 – TG curve (green) and DTG curve (red) of $Mn(CH_3CO_2)_2.4H_2O$ heated up to 900°C in air [117]*

The instrumentation required to conduct TGA analysis involves the use of an extremely precise balance, in which the sample is heated progressively from room temperature even to over 1000 °C, with programmable ramps in temperature and in controlled gas flow. The main components are:

- Analytical balance with sensitivity on the order of μg or $\mu g \times 10^{-1}$.
- Crucible sample holder.
- Furnace, programmable with temperature from 25 to 1500°C.
- Purge gas flushing system, programmable in terms of both flow and type of gas, capable of ensuring an inert or reactive atmosphere and heat diffusion at every point.
- Computer for instrument control, data acquisition and display.

The balance consists of two arms, in which the one where the sample under analysis is inserted is placed inside the furnace. Depending on the mechanism for measuring weight change, the thermobalance can be of two types:

- "Null point" mechanism balance: it involves a sensor determining the deviation from the equilibrium position (null point) of the sample and activating a servomechanism to correct this deviation. This is the most used type of mechanism because it allows the sample to remain in the same position within the furnace whatever the weight changes.

- Deflection balance with rod, cantilever, torsion or spring mechanism: in this case, the deflection from the equilibrium point due to weight variation is measured by different mechanisms.

In either instance, calibration with certified weights is required to associate the change in position or the force required to cancel it with the change in weight. A thermocouple is placed inside the furnace, usually made of refractory material, which records the actual temperature trend of the sample over time. This thermocouple, usually made of chrome/aluminum alloy, is calibrated using standard samples. The purge gas flushing system allows management and programming of the type of gas, inert or reactive, and the flow of the same.

It is important to note that the thermogram resulting from a thermogravimetric measurement is highly dependent on the analytical conditions set, specifically: sample weight and shape, temperature scan rate, type and flow of the purge gas, and system pressure conditions. Therefore, it is advisable to make the determination in duplicate or triplicate (weighing as similar an amount of sample as possible for the repeats) and express the result as an average of the data, especially when analyzing samples characterized by low homogeneity (mixtures, composites).

### 2.2.3 Dynamic Mechanical Analysis (DMA)

Dynamic Mechanical Analysis (DMA) [118, 119] is a technique that involves applying stress or strain to a sample and analyzing its response to determine phase angle and deformation data. Specifically, DMA involves applying a variable sinusoidal stress to a material and measuring the resulting sinusoidal strain. For materials that are purely elastic, the phase difference between the stress and strain sine waves is 0°, so they are in phase. For purely viscous materials, this phase difference is 90°. However, most real-world materials, such as polymers, are viscoelastic, showing a phase difference somewhere between these two extremes. This phase difference, along with the amplitudes of the stress and strain waves, is used to calculate fundamental material parameters such as viscosity, transition temperatures, stress relaxation, impact resistance, and morphology.

There are two main methods for conducting DMA: the forced frequency approach, where a signal is applied at a constant frequency, and the free resonance approach, where the material

is perturbed and allowed to undergo free resonance decay. Most DMA instruments use the forced frequency method, while the torsional braid analyzer uses the free resonance method. Both methods are highly sensitive to the motion of polymer chains and are powerful tools for identifying transitions in polymers. Additionally, DMA allows rapid scanning of a material's modulus and viscosity as a function of temperature, strain, or frequency. The key components of a DMA instrumentation include:

- The drive motor, which applies the sinusoidal deformation force to the sample.
- The drive shaft support and guidance system, which transfers the force from the drive motor to the clamps holding the sample.
- The displacement sensor, which measures the deformation of the sample under the applied force.
- The temperature control system (furnace).
- The sample clamps.

A typical DMA procedure involves the following steps:

1. Preparing a sample in the form of a thin strip or disk.
2. Applying a controlled oscillatory strain or stress to the sample while the temperature is either ramped or held constant.
3. Measuring the resulting stress or strain and calculating the storage modulus, loss modulus, and tan δ.

DMA measures the viscoelastic properties of materials, including storage modulus (E'), loss modulus (E''), and loss tangent (tan δ), providing information about their stiffness, damping, and transitions such as the glass transition temperature ($T_g$). Fig. 15 shows the storage modulus and the loss tangent of two different polymeric materials. The storage modulus indicates the material's stiffness by representing the elastic or stored energy component. The loss modulus represents the viscous or dissipated energy component, indicating the material's damping characteristics. The loss tangent (tan δ), which is the ratio of the loss modulus to the storage modulus, gives insights into the material's damping properties and the degree of viscoelasticity. The $T_g$ is identified by a peak in either the loss modulus or the tan δ curve, which signifies a significant change in the material's viscoelastic behavior. Besides $T_g$, DMA can detect other thermal transitions related to local molecular motions or side-chain relaxations within the polymer structure. These secondary relaxations provide

insights into molecular mobility and segmental dynamics. DMA also allows for variation in the frequency of applied oscillating stress or strain. The viscoelastic properties of a material are frequency-dependent; higher frequencies generally lead to a higher storage modulus and a lower tan δ, suggesting a stiffer material response.

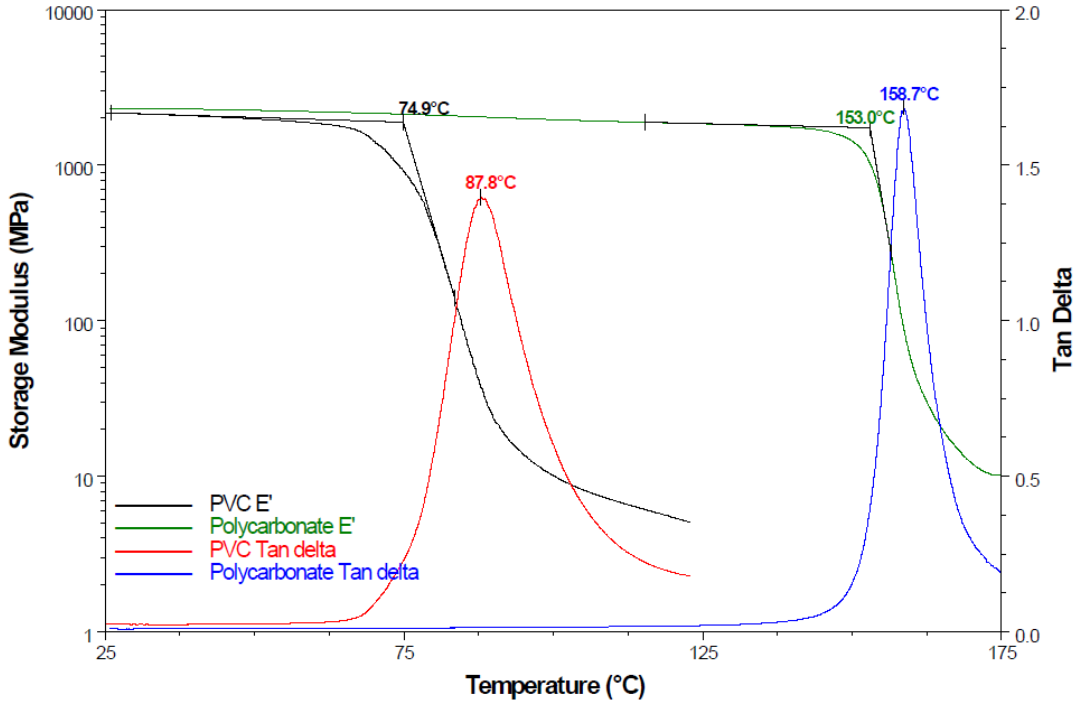



*Fig. 15 – Storage modulus (E') and tan δ of PVC and Polycarbonate [118]*

Polymeric materials, due to their viscoelastic nature, exhibit behavior that depends on both time and temperature during deformation. The Time-Temperature Superposition (TTS) principle [120] is used to analyze and process this type of data. This method can be applied to the data from DMA multifrequency experiments to create master curves, which predict the long-term mechanical behavior of polymers from short-term data by shifting curves obtained at various temperatures along the time or frequency axis. This approach is particularly valuable for predicting the long-term performance of materials under different environmental conditions. The basis of TTS is that molecular relaxation or rearrangement processes in viscoelastic materials occur faster at higher temperatures and that there is a direct relationship between time (frequency of measurement) and temperature. Therefore, these processes can be observed over shorter time periods by conducting measurements at elevated temperatures and then shifting the resulting data to lower temperatures. This shifting results in a master curve that can predict the material properties at a specific end-use temperature over a broad time scale.

Therefore, in summary, Differential Scanning Calorimetry is primarily used to study thermal transitions like $T_g$, $T_m$, and $T_c$. Thermogravimetric Analysis provides information about thermal stability, decomposition temperatures, and the composition of materials. Dynamic Mechanical Analysis characterizes the mechanical properties of polymers as a function of temperature, frequency, and time, revealing details about viscoelastic behavior and glass transition. Together, DSC, TGA, and DMA provide a comprehensive understanding of the thermal, chemical, and mechanical behavior of polymeric materials.

## 2.3 Thermoplastics materials used in material extrusion process

Material extrusion process works by extruding a continuous filament of thermoplastic material through a heated nozzle; precisely because of the deposition mode of the material, it is necessary that the filament can be extruded, softening when heated to temperatures higher than glass transition temperature. A significant factor in the success and proliferation of FFF is the use of thermoplastic materials, which are polymers that become moldable at elevated temperatures and solidify upon cooling. Thermoplastics materials used in material extrusion exhibit a wide range of properties, from flexibility and toughness to resistance to high temperatures and chemicals. The selection of material depends on the application requirements such as mechanical strength, thermal resistance, chemical stability, and environmental exposure [63, 121]. Table 3 reported the most commonly used thermoplastics in material extrusion process.

*Table 3 - Most commonly used thermoplastics in material extrusion process [122]*

| | *General-purpose* | *Engineering grade* | *Ultra-performance* |
|---|---|---|---|
| *Semi-crystalline* | PLA | Polyamide | PEEK, PAEK |
| *Amorphous* | ABS, ASA, PETG | PC, TPU | PEI |

Polylactic acid (PLA) is one of the most popular materials used in FFF due to its ease of use, low cost, and biodegradability. It is a thermoplastic aliphatic polyester derived from renewable resources like cornstarch or sugarcane, biodegradable under industrial compositing conditions, making it an environmentally friendly choice. This material is a semi-crystalline thermoplastic, characterized by low glass transition temperature (around 60-65°C) and a melting point of 150-160°C. It is commonly used for applications that include prototyping, concept modeling and low-stress application, due to its low impact resistance and flexibility, while having high tensile strength, around 50 MPa, and a tensile modulus of

about 2300 MPa [63]. Parts made with PLA are not suitable for high-temperature or high-stress environments. Also in the general-purpose applications, there is Acrylonitrile Butadiene Styrene (ABS), that is a durable thermoplastic known for its toughness and impact resistance. It is made from acrylonitrile, butadiene, and styrene monomers, providing a good balance between mechanical properties and processability. It has a higher glass transition temperature (around 105 °C) than PLA, making it more heat-resistant, but it is characterized by lower tensile strength and modulus, that are respectively of about 20 MPa and 1600 MPa [63]. ABS can be post-processed with acetone vapor to achieve a smooth surface finish. An alternative to ABS is represented by acrylonitrile styrene acrylate (ASA), that has similar mechanical properties that ABS, but a higher environmental stability and ultraviolet resistance, making it appropriate for applications in harsher environmental conditions [123]. Polyethylene Terephthalate Glycol (PETG) is a copolymer of PET modified with glycol, which enhances its printability and transparency. It is known for combining the advantages of both PLA and ABS; it has higher impact resistance than PLA and comparable strength to ABS and it is also characterized by a good chemical resistance [124]. Its glass transition temperature is around 80 °C, making it suitable for application like medical components and mechanical parts without deformation. PETG is susceptibility to moisture absorption, so pre-drying of filament is often necessary to prevent print quality issues.

Concerning those polymers used for more engineering applications, there is Polyamide (or nylon) in the group of semi-crystalline thermoplastics, and Polycarbonate (PC) and Thermoplastics Polyurethane (TPU) among amorphous polymers [122]. Polyamide is a versatile, durable, and flexible material that is highly valued in industrial applications. It is known for its high strength, flexibility, and wear resistance. It has a high tensile strength, of about 40 MPa and it is characterized by an elevate abrasion and impact resistance [63]. Glass transition temperature of polyamide is lower than other materials (about 60°C), but it requires higher print temperature, typically range from 240-260 °C. This material has a hygroscopic nature, and a heated bed is necessary to prevent warping, but despite this, it finds great applications in functional prototypes, mechanical parts and applications requiring toughness and flexibility. Polycarbonate (PC) is a strong, durable thermoplastic known for its impact resistance, heat resistance, and optical clarity. It is widely used in engineering and industrial applications, also for those that required high heat resistance; its temperature glass transition is around 120 °C and it requires high printing temperature, of about 250 °C. Tensile strength of PC is around 50 MPa [125]. Thermoplastic Polyurethane (TPU) is a flexible,

elastic thermoplastic that belongs to the polyurethane family. It is known for its rubber-like flexibility and durability, making it a unique material for FFF. Due to its high elasticity, it requires low print speeds and extruding temperature of about 220 °C to minimize its viscosity [126]. TPU has high elasticity, abrasion resistance, and tensile strength of about 45 MPa, making it suitable for mechanical parts and medical devices.

Ultra-performance thermoplastics are characterized by a processing temperature requirements higher than 250 °C [65]; they are engineered to withstand elevated temperatures without compromising their mechanical integrity, making them suitable for demanding environments where conventional polymers may falter. Their high glass transition temperatures and resistance to thermal degradation equip them for applications where thermal stability is pivotal. Industries such as aerospace, automotive, and electronics benefit from high-performance thermoplastics ability to maintain structural integrity under extreme conditions [72, 93]. Polyaryletherketone (PAEK) is a broader family of semi-crystalline thermoplastics [127], including PEEK, PEKK (Polyetherketoneketone), and others. Polyether Ether Ketone (PEEK) is a semi-crystalline thermoplastic with an excellent thermal stability, due to its glass transition temperature around 140 °C and its melting point of about 340 °C. Realizing components in PEEK by material extrusion process requires machine in which nozzle can reach high temperature, around 400 °C [81], and they should be equipped with heated build chambers; it is necessary to maintain temperature at a constant value up to 250 °C to guarantee proper layer adhesion. Polyetherimide (PEI), commonly known by its trade name Ultem, is an amorphous thermoplastic with high thermal resistance and excellent mechanical strength. Its glass transition temperature is around 180 °C, so it requires nozzle temperature of 300-400 °C and heated oven temperature of about 180 °C [128]. PEI exhibits good dimensional stability, flame retardancy, and chemical resistance like PEEK, but it is less expensive than it. This material could be dried before printing to avoid printing defects like bubbling or poor surface finish.

High-performance thermoplastics are commonly used to realize parts with high mechanical strength, but low weight, with a high strength-to-weight ratio, chemical resistance and thermal stability. Specialized high-temperature 3D printers are needed to handle these materials and precise control over printing temperatures, bed temperatures, and cooling rates is essential to achieve optimal mechanical properties and avoid defects. Annealing may be necessary to relieve internal stresses and improve crystallinity and mechanical properties.

Material extrusion components realized with these materials can find their application in aerospace, automotive and biomedical fields [71, 72, 77, 92].

Thermoplastics used in the material extrusion process offer a wide range of properties that cater to various applications from prototyping to end-use parts. Each material presents unique challenges and advantages, which must be carefully considered when choosing a filament for a specific application.

Table 4 shows the critical temperatures of the thermoplastic materials analyzed.

*Table 4 – Critical temperatures of thermoplastic materials for material extrusion process*

| | *Glass transition temperature (°C)* | *Extrusion temperature (°C)* | *Bed temperature (°C)* | *Chamber temperature (°C)* |
|---|---|---|---|---|
| *PLA* | 60 | 190-210 | 25-80 | - |
| *ABS* | 105 | 220-260 | 90-110 | - |
| *PETG* | 80 | 220-250 | 60-80 | - |
| *Polyamide* | 60 | 240-260 | 70-110 | - |
| *PC* | 120 | 250-270 | 80-110 | 70-80 |
| *TPU* | 70 | 210-230 | 25-60 | - |
| *PEEK* | 140 | 380-410 | 90-150 | 120-180 |
| *PEI* | 180 | 350-400 | 90-130 | 120-180 |

# Chapter 3 – Characterization of components made by Material extrusion process

Mechanical characterization of components produced through material extrusion process is essential for understanding their performance in practical applications. This characterization is influenced by numerous factors, including the choice of material, process parameters, and environmental conditions [81, 129, 130]. The mechanical characterization of components produced through material extrusion process is essential for understanding their performance in practical applications. Mechanical characterization involves evaluating key mechanical properties such as tensile strength, flexural strength, impact resistance, and fatigue behavior [128, 131, 132]. Understanding how these properties are influenced by the process parameters, such as printing temperature, layer thickness, raster configuration, and build orientation [87, 133], is essential for optimizing the manufacturing process and achieving desired performance outcomes. This section aims to provide a comprehensive review of the mechanical characterization techniques employed in the study of thermoplastics materials components made by material extrusion process.

## 3.1 Mechanical characterization by traditional testing

There are several papers in the literature that investigate the mechanical properties of thermoplastics components with respect to printing parameters. Some examples of such papers are given in

Table 5, while Fig. 16 shows some of the analyzed printing parameters.

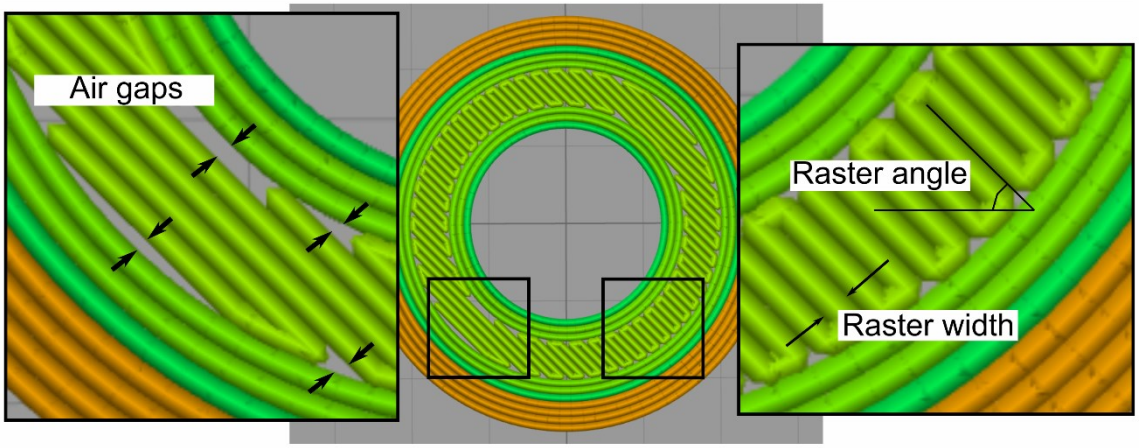



*Fig. 16 – Analyzed printing parameters*

Regarding the process parameters, the most analyzed are the orientation of the part on the printing plane, the raster angle, and the nozzle temperature. The most analyzed mechanical properties, on the other hand, concern the behavior of polymers subjected to tensile tests.

*Table 5 – Literature papers that investigate mechanical properties of thermoplastics components made by material extrusion*

| *Process parameters* | *Tensile behavior* | *Compressive behavior* | *Flexural behavior* | *Shear behavior* |
|---|---|---|---|---|
| *Air gap* | [87, 128, 132] | [128] | [128, 132] | [132] |
| *Raster width* | [85, 87, 128] | [128] | [128] | |
| *Raster angle* | [81, 85, 87, 128, 129, 132-136] | [128, 133, 135] | [128, 129, 132-135] | [132] |
| *Build orientation* | [82, 84, 85, 89, 128, 129, 132-134, 137-140] | [128, 133, 141] | [128, 129, 132-134, 137, 142] | [82, 132] |
| *Layer thickness* | [81, 130, 133, 143, 144] | [133] | [133, 142] | |
| *Infill percentage* | [81, 82, 129, 130, 143] | | [129] | [82] |
| *Printing speed* | [81, 129, 130, 133, 143, 144] | [93, 133, 145] | [93, 129, 133, 142] | [145] |
| *Nozzle temperature* | [130, 133, 136, 139, 143, 144] | [93, 133] | [93, 133, 142] | |
| *Platform temperature* | [133, 143] | [133] | [133] | |
| *Chamber temperature* | [136, 138] | | | |

Mechanical characterization of high-performance thermoplastics components is critical given the demanding applications in which such components are used [8, 92]. Fischer et al. [89] investigated the influence of the build orientation of ULTEM specimens on the printing plane, on the mechanical properties evaluated by tensile test, analyzing tensile strength and

elongation at break. Byberg et al. [128] studied the influence of four process parameters, namely air gap, raster width, raster angle and build orientation, on the mechanical properties through tensile, compression and bending test. Among the four process parameters analyzed, it was found that the most influential parameter was the build orientation, determining that the printing direction that gives the best results is the edge direction. Forès-Garriga et al. [132] and Padovano et al. [137] came to the same conclusion. In the former research, the influence of build orientation, raster angle and air gap on tensile, flexural and shear strength was evaluated. In [137], the influence of the orientation of the component on the printing plane by tensile and bending tests is evaluated; the vertical printing condition was determined to be the worst for the mechanical properties obtained, both for flexural properties and for tensile properties. Zaldivar et al. [84] also evaluated the influence of the build orientation on the printing plane by tensile test. Gebisa et al. [87] varied air gap, raster angle, and raster width values during the printing process, determining that raster angle is the most impactful process parameter among the three analyzed on the mechanical properties evaluated by tensile test; it was found that as the parameter varied from 0° to 90°, the tensile strength ranged from 87 MPa to 30 MPa. Shelton et al. [138] determined the influence of build orientation and chamber temperature on tensile properties. They demonstrated that the mechanical strength of the specimens was highly dependent on the envelope temperatures, by varying more than 20% between the lowest and the highest level of the printing parameter. In the research analyzed up to now the thermoplastic material used for the realization of the specimens was polyetherimide (PEI); other researchers have carried out their analysis on specimens made also by PEEK. Kaplun et al. [85] studied the influence of build orientation on tensile strength. They demonstrated that this parameter directly affected the mechanical behavior in both materials tested, and they showed that the edge orientation of the sample performing the best in mechanical properties. Ding et al. [139] demonstrated the influence of nozzle temperature on tensile strength; by varying temperature from 360 °C to 420 °C, the density of both PEEK and PEI increases, determining better mechanical characteristics.

Pulipaka et al. [143] investigated the influence of nozzle temperature, platform temperature, infill percentage, layer thickness, and print speed on mechanical characteristics of PEEK specimens through tensile test. They found that tensile properties are all impacted by infill percentage, while other printing parameters impact singularly on specific characteristics: ultimate tensile strength is significantly impacted by the temperature of both nozzle and

platform, and by layer thickness. Nozzle temperature also shows a significant effect on the elastic modulus.

Arif et al. [134] investigated the influence of build orientation and raster angle on tensile and flexural behavior; they determined the best combination of these two printing parameters to achieve the best mechanical properties. Zhao et al. [136] made PEEK specimens by varying nozzle and chamber temperature, and raster angle to evaluate their impact on the tensile properties. The results show that nozzle temperature and chamber temperature have a close relationship with the mechanical properties, but also raster angle have a significant influence on the tensile properties, due to the different degree of interfacial adhesion strength determining by different fabrication angles. Also in [135] the influence of raster angle on mechanical properties is investigated; raster angle results in having strong impact on the mechanical strength of PEEK specimens. Wang et al. [93] performed compression and bending tests to evaluate the influence of three different printing parameters on mechanical properties. Among the three parameters analyzed, that are nozzle diameter, nozzle temperature and printing speed, the first one resulted the most influent; anyway, different combinations of parameters provide different characteristics in terms of compression and bending strength. Nozzle diameter of 0.2 mm is recommended for better bending modulus. A combination of a 0.4 mm nozzle diameter, 430 ◦C nozzle temperature and printing speed of 5 mm/s provides the highest bending strength and the most compact samples; meanwhile, increasing nozzle diameter the best compression properties and denser samples can be achieved.

Analyzing how the mechanical properties of components made by material extrusion process vary as process parameters change, is also necessary in the case of other thermoplastic materials. Regarding PLA, in [82], [133] and [140] the effect of build orientation on the printing plane is analyzed. Gonobadi et al. [82] studied the influence of build orientation and infill density through tensile and shear tests. Results show that mechanical properties vary as a function of process parameters, especially the build orientation. Anisotropy was found when comparing the on-edge and upright orientations of specimens; the tensile strength of on-edge specimens is 55% higher than that one obtained in the upright orientation samples. Same results are shown in [140], where it is determined that the horizontal specimens have the highest ultimate tensile strength level; for vertical specimens the ultimate tensile strength is about 58% lower. Cojocaru et al. [133] investigated the influence of layer thickness, printing speed, printing temperature, build platform temperature, build orientation and raster

angle on mechanical behavior evaluated by tensile, compressive and flexural tests. The mechanical properties decrease with increases in the specimen positioning angle relative to the build platform; also in this case, upright printed specimens have lower mechanical strength compared to horizontally specimens. Chalgam et al. [142] carried out three-point bending tests to characterize the influence of build orientation, layer thickness, nozzle temperature and printing speed on the mechanical properties of PLA samples. They determined that the best mechanical properties are achieved when printed parameters are the following: a horizontally orientation, a layer thickness of 0.3 mm, a nozzle temperature of 190 °C, and a printing speed of 90 mm/s.

Others research study the influence of printing parameters by varying materials used during the material extrusion process. The influence of five different printing parameters are studied in [129], in which their effects are analyzed on four thermoplastics: PLA, ABS, Polyamide, PEEK and PC. The effect of layer thickness, infill density, printing speed, build orientation, and raster angle on mechanical properties, through tensile and flexural tests is investigated. The results show the same trend regardless of material choise. Young's modulus of the components printed with 100% infill density was found to be the highest; when infill density decreases, the strength of the printed objects also reduces. The maximum tensile strength was obtained with build orientation of 0° relative to printing plane. Algarni et al. [81] conduct their analysis on PLA, ABS, PETG and PEEK; they evaluated tensile strength, compressive strength and flexural strength by varying layer thickness, raster width, infill percentage, raster angle, and build orientation. Among all printing parameters analyzed, they determined that the most influential one is the infill percentage on all mechanical properties. Printing speed mainly has more impact on flexural strength, while elongation at break is significantly affected by raster angle. Finally, the influence of build orientation on ABS samples through compression test is investigated in [141]. This study also found that the print direction is a pivotal parameter influencing mechanical properties and that the highest value of the modulus of elasticity results when specimens are printed horizontally.

## 3.2 Limitations of traditional mechanical characterization

The material extrusion process, as already explained, involves making components by overlapping successive layers of material [4]. This way of making parts is profoundly different from traditional manufacturing processes, whether by molding, injection, or tool machining. In the mechanical characterization of parts made by material extrusion, therefore,

certain inherent characteristics of the process must be considered, which deserve special attention in the evaluation of mechanical properties. The main issues related to this type of part production will be analyzed below.

### 3.2.1 Anisotropic behavior

The primary issue with material extrusion components is their inherent anisotropy [146-148], arising from the layer-by-layer deposition process. During printing, each layer is extruded in a predetermined pattern and bonds with the underlying layer. The bonding between subsequent layers is typically weaker than the strength of adjacent filaments within a single layer, leading to a reduction in mechanical properties when loads are applied perpendicular to the build direction. Fig. 17 shows a schematic of how layers are arranged in the growth direction and how adjacent filaments are disposed in the extrusion direction.

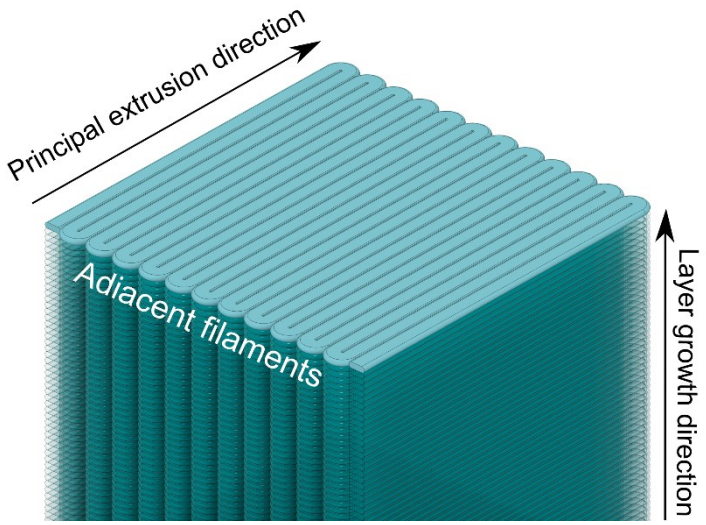



*Fig. 17 – Anisotropy determined by the bonding difference between successive layers and adjacent filaments*

This anisotropy manifests in several mechanical aspects, including:

1. Tensile Strength [82]: Tensile strength is highest along the filament deposition direction (XY plane) due to the continuous and uninterrupted polymer chains. However, tensile strength significantly decreases in the Z-direction, that is normal to the layers, where the mechanical properties are governed by interlayer adhesion. The weak interlaminar bonds act as potential fracture initiation points under tensile loading, leading to premature failure in the Z-direction.
2. Flexural Strength [149]: Similar to tensile properties, flexural strength exhibits anisotropic behavior. While components show good resistance to bending forces

applied parallel to the layers, within the XY plane, their performance is significantly reduced when the force is applied perpendicular to the layers. This is due to the limited interlayer fusion, which acts as a critical failure point under flexural loading.

3. Fatigue Resistance [89]: The anisotropic behavior also affects the fatigue performance of FDM components. The stress concentration at the interlayer boundaries results in crack initiation sites that propagate under cyclic loading, particularly in the Z-direction. As a result, the fatigue life of FDM components can be significantly shorter when loaded along directions that rely heavily on interlayer adhesion.

There are some printing parameters during the material extrusion process that influence the degree of anisotropy in the printed parts. First, the build orientation has a direct impact on mechanical properties [128]. Components printed with their major load-bearing surfaces aligned in the XY plane tend to exhibit higher strength and stiffness compared to those printed in the Z-direction, where the layers are stacked perpendicularly to the applied load [82]. Raster angle can also affect the anisotropy of the printed part [136]; the orientation of the deposited filaments plays a critical role in determining the strength and stiffness in the XY plane. To mitigate the effects of anisotropy in material extrusion components, different strategies can be employed. It is possible to optimize printing parameters that most impact anisotropy, like build orientation and raster angle. Another way to reduce anisotropy is through post or pre-processing techniques [150, 151], that can help in improving interlayer bonding and reduce the resulting effects of anisotropy. For example, annealing can promote further polymer chain diffusion across layer interfaces, thereby increasing mechanical strength [152]. The incorporation of fibers [153, 154], like carbon or glass fibers, into the filament material can enhance stiffness and strength in the XY plane while also improving the mechanical performance in the Z-direction, as the fibers can bridge the weak interlayer regions.

### 3.2.2 Interlayer adhesion

In the material extrusion process, its layer-by-layer nature introduces challenges related to interlayer adhesion, which significantly impacts the mechanical properties, structural integrity, and performance of the printed parts. Interlayer adhesion refers to the bonding between successive layers of extruded thermoplastic material. Poor adhesion between layers

results in weakened mechanical strength, increased anisotropy, and can lead to premature failure of the printed components. Causes of possible reduced interlaminar adhesion may include:

1. Thermal gradient and cooling rate [155]: interlayer adhesion is governed by the thermal bonding that occurs between a newly extruded layer and the previously deposited one. A critical issue arises when the previously deposited layer cools too quickly before the next layer is extruded. If the temperature of the previously printed layer drops below the glass transition temperature ($T_g$) of the material, poor bonding occurs due to insufficient polymer diffusion across the layer interface. The rapid cooling, combined with insufficient heat transfer from the newly deposited material, prevents proper bonding and leads to weak interfaces between layers.
2. Inadequate nozzle temperature [143]: the extrusion temperature is a key parameter affecting interlayer bonding. If the nozzle temperature is too low, the filament is not adequately heated, resulting in reduced polymer chain mobility and poor fusion between layers. This compromises the molecular entanglement necessary for strong adhesion. Conversely, excessive nozzle temperatures can lead to material degradation or oozing, which can also affect layer quality.
3. Material shrinkage and residual stresses [156]: thermoplastic materials typically exhibit shrinkage as they cool. In the material extrusion process, this shrinkage is non-uniform, especially in materials like ABS, which have high thermal expansion coefficients. Differential cooling rates between layers can introduce residual stresses that cause delamination or warping, which further exacerbates interlayer adhesion issues. Residual stress can pull layers apart, reducing the contact area available for bonding and increasing the likelihood of layer separation during mechanical loading.
4. Build Orientation [85]: the anisotropic nature of material extrusion parts is largely attributed to poor interlayer adhesion. When the build orientation is such that the primary load is applied perpendicular to the layers, in the Z-direction, the mechanical properties are dominated by interlayer adhesion. In contrast, parts loaded along the XY plane, parallel to the layers, experience better strength and stiffness because of the continuous nature of the filament deposition within each layer. The weak interlaminar bonding in the Z-direction is a primary cause of anisotropy in FDM parts.

5. Inconsistent layer deposition [133]: the deposition rate and the layer thickness can affect the contact between successive layers. If the layer height is too large relative to the nozzle diameter, or if the extrusion rate is inconsistent, gaps and voids can form between layers, leading to weak interlayer bonding. Additionally, inconsistencies in layer alignment or overlapping filaments can create discontinuities in the material, further reducing interlayer strength.
6. Surface roughness and incomplete contact [143]: the surface of a previously printed layer often exhibits micro-roughness due to the nature of the extrusion process, particularly when printing with large nozzle diameters or high layer heights. This uneven surface can limit the contact area between the newly extruded material and the previous layer. Without sufficient contact, there is less opportunity for molecular diffusion, leading to weak adhesion. Moreover, contaminants or oxidation on the surface of previously deposited layers can also inhibit effective bonding.

A poor interlayer adhesion can strongly impact mechanical properties of parts; in fact, one of the leading causes of anisotropic mechanical behavior in material extrusion printed parts is connected to this issue. The tensile and flexural strengths of these components are significantly lower in the Z-direction compared to the XY plane due to weak bonding between layers [157]. The Z-direction, where bonding is weakest, typically exhibits reduced strength and stiffness compared to the XY plane, where the filament is deposited continuously within a single layer. As a result, cracks can propagate more easily between layers under tensile or flexural loads, leading to premature failure of the part. Fig. 18 shows two specimens with a different fracture mode: in the first one an intra-layer fracture occurs, while in the second one it is possible to observe an inter-layer fracture.

Under mechanical loading, particularly when subjected to bending, shear, or impact forces, poor interlayer adhesion can lead also to delamination [135] or separation between adjacent layers. This failure mode is critical, especially in load-bearing applications, where the separation of layers can rapidly propagate through the structure and cause catastrophic failure. Poor interlayer bonding also affects the fatigue performance [89] of material extrusion parts. Under cyclic loading, interlayer defects such as voids, incomplete bonding, or weak interfaces act as initiation points for crack propagation. Repeating stress cause cracks to form and propagate along the layer interfaces, reducing the fatigue life of the part, particularly in the Z-direction. Finally, another common problem in material extrusion

components is related to the warping-phenomena, which is often exacerbated by poor interlayer adhesion [158]. Differential shrinkage during cooling can cause layers to contract unevenly, resulting in warping or distortion of the part. This not only affects the aesthetic and dimensional accuracy but also compromises the mechanical integrity of the component.

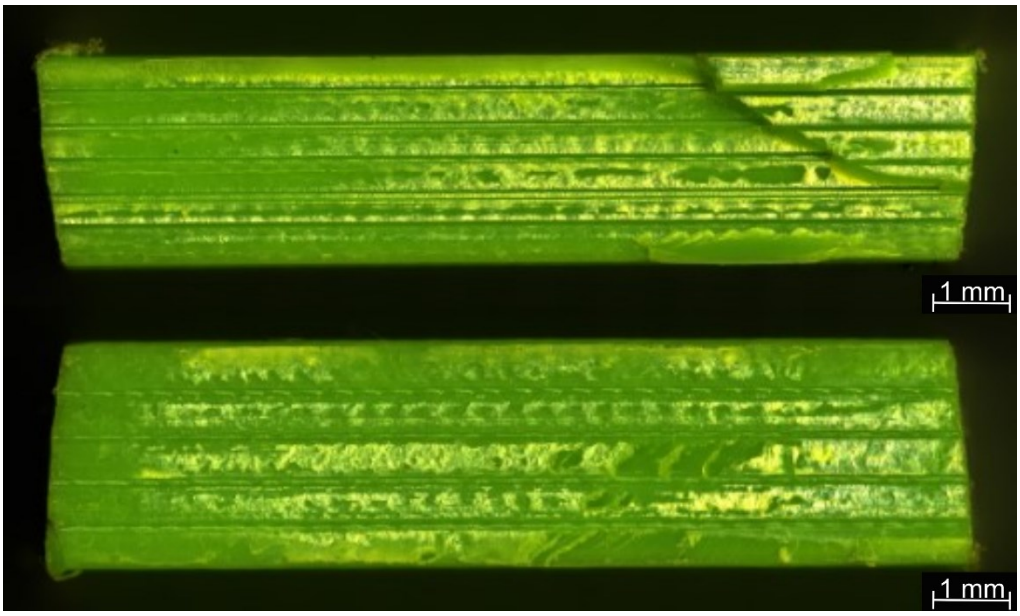



*Fig. 18 – Two different ways of fracture when specimen is subject to a tensile test in Z-direction*

There are some strategies that can improve interlayer adhesion by appropriately varying printing parameters. One of the most effective ways to improve interlayer adhesion is by optimizing the nozzle and bed temperatures [133, 136]. Keeping the previously deposited layer close to its glass transition temperature by maintaining adequate build plate heating ensures better thermal fusion with the newly deposited layer. Additionally, using higher extrusion temperatures promotes better polymer chain diffusion between layers. Another possible is by adjusting print speed and layer thickness [129, 143]. Slower print speeds allow for more consistent deposition and better contact between layers, enhancing bonding. Reducing the layer height can also improve interlayer adhesion, as thinner layers ensure that each newly deposited layer has sufficient contact with the previous one, allowing for better bonding. It is also possible to use adhesion promoters or primers. Applying these materials to the build plate or as surface treatments [159] between layers can improve the bonding of subsequent layers. This is especially useful for advanced thermoplastics with higher glass transition temperatures, which are more difficult to bond through conventional thermal means. To further improve interlayer adhesion, post-processing techniques such as annealing can be used [160]. Annealing allows the part to be heated uniformly, promoting further

diffusion of polymer chains across the layer interfaces. This can enhance the mechanical strength and reduce the anisotropy associated with poor interlayer bonding. Emerging technologies like ultrasonic welding [161] or laser-assisted layer bonding can also be applied to enhance interlayer adhesion [162]. These techniques involve applying additional energy to the interface between layers to promote better fusion without reprinting the entire part.

### 3.2.3 Porosity

Porosity is a critical issue in parts produced by material extrusion, leading to decreasing mechanical, thermal, and functional properties [163]. Unlike traditional manufacturing processes, the layer-by-layer deposition introduces voids, gaps, and internal defects, resulting in parts with porosity levels that can compromise their structural integrity and performance. Fig. 19 shows the presence of porosity in material extrusion components.

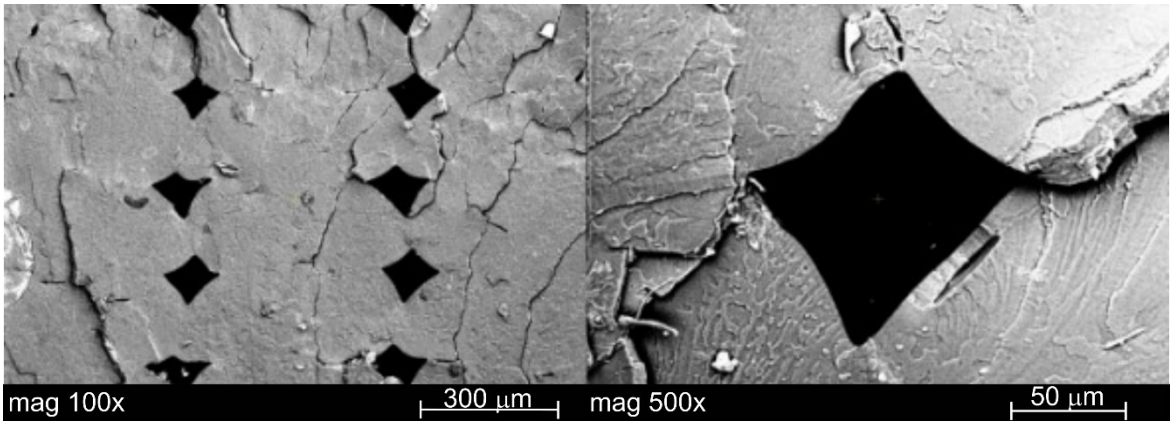



*Fig. 19 – Cross section of material extrusion components made by SEM at 100x and 500x magnification to study porosity*

These defects arise due to a combination of process parameters, material properties, and thermal dynamics during the printing process. One of the primary causes of porosity in material extrusion printed parts is the insufficient fusion between adjacent layers [135]. The process involves extruding thermoplastic material layer-by-layer, and the bonding between layers depends on the degree of heat transfer and pressure at the interface. If the material cools too rapidly or insufficient heat is applied, incomplete fusion occurs, leaving microscopic voids between layers. These voids contribute to anisotropy and significantly weaken the part's strength, particularly in the Z-direction. Another possible reason that can increase the presence of porosity is represented by an insufficient filament overlap [87]. The deposition of filament in material extrusion follows a specific raster pattern with adjacent lines of filament laid side by side. Insufficient overlap between these lines can result in gaps

between filaments, which manifest as internal porosity. This is influenced by factors such as extrusion width, nozzle diameter, and layer height. If the filament lines do not overlap adequately, it leads to incomplete filling of the part volume, leaving air pockets between deposited strands.

Porosity can also arise from inconsistent or improper extrusion flow [81]. This can be caused by fluctuations in the extrusion temperature, nozzle clogging, or incorrect material feed rates. Inconsistent extrusion leads to irregular filament deposition, forming voids and gaps within and between layers. This effect is particularly pronounced in intricate geometries, where uneven flow can worsen the formation of voids. Another possible cause for the presence of porosity is inherent the thermal history of the components during printing [164]; the cooling behavior of thermoplastic materials can induce porosity, particularly at the boundary regions between different layers. Differential cooling rates can cause localized shrinkage, which pulls layers apart, reducing the overall density of the part. This phenomenon is more prevalent in materials such as ABS [156], which are prone to thermal warping. Shrinkage-induced porosity typically occurs near sharp edges, overhangs, or thin walls, where cooling is less uniform. Finally, material extrusion process allows for the control of infill density, which affects the overall material composition of the printed part [132]. While infill patterns such as hexagonal or grid structures are used to reduce material consumption and printing time, lower infill densities inherently introduce voids into the part. Although some voids are intentional in low-density infill patterns, inadequate bonding between infill and outer walls can exacerbate porosity, reducing the mechanical integrity of the part under load.

The presence of porosity may have effects on mechanical properties of printed components; first, porosity acts as stress concentrators within the part, leading to significant reductions in tensile and compressive strength. The presence of voids decreases the effective load-bearing area, leading to localized stress concentrations that initiate crack propagation, particularly under tensile loading conditions. In the case of compressive loads [81, 93], the internal porosity may cause premature buckling or crushing of the part. Parts with high porosity levels tend to exhibit brittle fracture behavior. Voids within the structure serve as nucleation sites for cracks, which can propagate rapidly under mechanical loading. This is especially problematic in impact or dynamic load conditions, where the presence of pores lowers the material's ability to absorb energy, causing sudden catastrophic failure. Also, the fatigue performance of material extrusion parts [165] is severely compromised by internal porosity.

Under cyclic loading, pores act as stress risers that accelerate crack initiation and growth, leading to early failure. The non-uniform stress distribution in porous regions weakens the part's resistance to repeated mechanical stresses, particularly in applications where cyclic loads are prevalent.

Different strategies can be employed to reduce porosity in material extrusion components, leading to improved mechanical performance and material integrity. It is possible to act on printing parameters, for example increasing the extrusion temperature [138] and adjusting the layer thickness and print speed [142] can enhance the fusion between filaments and layers. Higher nozzle temperatures allow for better wetting and diffusion of polymer chains between adjacent layers, reducing the formation of interlayer voids. Lowering print speed can also improve deposition consistency and reduce flow irregularities. Higher infill densities [69] can reduce the overall porosity within the part. While this increases material usage and print time, the increased part density significantly improves mechanical strength and reduces the number of internal voids. Enhancing the bonding between adjacent layers can mitigate the effects of porosity. Using heated build plates, enclosed build chambers, or controlled cooling environments can promote more uniform layer adhesion by minimizing thermal gradients that induce warping or shrinkage. Post-processing methods [160] such as resin impregnation, infiltration, or annealing can help to reduce porosity. Resin infiltration fills internal voids, improving mechanical strength and sealing capabilities, while annealing enhances the molecular diffusion between layers, promoting a denser internal structure.

## 3.3 Final remarks

Traditional characterization tests to evaluate the mechanical properties of components made by material extrusion are helpful in determining specific properties. However, to date there is no precise standard for determining the mechanical characteristics of parts made by additive manufacturing processes. As mentioned so far, these processes are by their nature very different from traditional manufacturing processes. The layer-by-layer mode of fabrication results in the occurrence of certain issues typical only of these technologies. Traditional characterization performed by tensile, compression, or flexural testing leads to ignoring three fundamental aspects that characterize components produced by material extrusion:

1. Anisotropic behavior

2. Interlayer adhesion
3. Presence of porosity

To consider these aspects and give them due emphasis, it is necessary to structure characterization methodologies and tests suitable for the issues being analyzed. For this reason, the next chapter will examine in detail the procedures developed for the advanced characterization of components made by material extrusion. This characterization involves three fundamental aspects. Firstly, different mechanical characterization tests will be analyzed [166-169]. In addition, the mode of production of the components was carefully analyzed. Substantial differences in the mechanical properties of components were found if they were directly printed with the desired dimensions or extracted from larger parts. These differences in mechanical properties were analyzed on both compression-tested [168] and tensile-tested specimens [170]. Careful process monitoring was also conducted within this analysis.

Regarding characterization tests, mainly two types were studied:

- Indentation test: is a nondestructive test aimed at evaluating the local characteristics of a component. It is a particularly suitable test for evaluating the mechanical characteristics of parts produced by material extrusion because it is able to determine the behavior of the material in a confined way compared to the classical compression test. This makes it possible to take into account the density of the component under test, which is strongly influenced by the presence of porosity. These porosities, moreover, are not uniformly distributed in the specimens, resulting in different mechanical characteristics.
- Double cantilever beam test [171]: this mechanical characterization test arises for the study of composite materials or the adhesion between two sheets. However, In the case of components made by material extrusion, this test is very useful for evaluating the interlayer adhesion between subsequent layers.

Instead, the printing process was monitored by means of a thermal analysis of the process [170, 172]. Using an infrared thermal camera, it is possible to reconstruct the thermal history of the component during the entire printing process. Thermal history allows for the reconstruction of the temporal trends of the temperature during the printing process. Knowing how the temperature of the sample produced varies permits to better understand

some behaviors characterizing the mechanical properties and the adhesion characteristics between successive layers.

# Chapter 4 – Advanced mechanical characterization and process monitoring

This chapter will present the activities suitable for the advanced characterization of components made by Material Extrusion. At present, there is no specific standard for the characterization of such components. Analysis of the existing bibliography revealed that traditional mechanical characterization tests are used; these tests were developed for other manufacturing processes and are now adapted to additive manufacturing technologies. As anticipated in the previous chapter, however, components made by material extrusion have common issues arising from the nature of the production process. These limitations cannot be considered through traditional mechanical characterization tests, and there is a risk of incorrectly assessing the mechanical properties of the component under investigation. Therefore, some testing methodologies and procedures specifically developed for components made by material extrusion will be discussed here. Through these methodologies, it has been possible to identify three macro areas of interest in studying mechanical properties. All components made by material extrusion have issues that have already been analyzed, such as the presence of porosity, anisotropic behavior, and interlaminar adhesion problems. With the testing procedures developed, it is possible to carefully examine these three areas and develop procedures capable of taking them into account and, if necessary, compensating for them. The impact that these issues have on mechanical properties and how to be able to highlight them will be analyzed here.

This chapter will, therefore, be divided according to the three macro-areas mentioned above. In the first paragraph, the influence of porosities on mechanical properties will be analyzed; the second paragraph will focus on the interlayer adhesion of components made by MatEx. Finally, in the third section of this chapter, two different manufacturing strategies will be described, and their influence on the mechanical properties of components will be accurately investigated. The procedures followed, the instrumentation and equipment used, and the characterization methods developed will be described. In addition, the importance of careful process monitoring of the thermal history of manufactured components will be highlighted, as it has proven to be crucial for understanding some phenomena related to the mechanical characteristics of components produced by material extrusion.

## 4.1 Analysis of density and presence of porosity in Material extrusion components

### 4.1.1 Introduction

The presence of porosities significantly affects the mechanical performance of components produced via additive manufacturing (AM) processes. Porosities reduce the effective load-bearing area and introduce high stress concentrations, thereby elevating the overall stress within the material. Additionally, porosities generated during the material extrusion process present greater challenges compared to other AM techniques. In the material extrusion process, the extruder diameter, which controls the size of the deposited filament, typically ranges from 0.3 to 0.6 mm. As a result, the size and distribution of porosities in this process are generally more problematic than in other plastic AM processes. Specifically, during extrusion, relatively low pressure is applied to the molten material as it flows from the nozzle to the substrate, in contrast to traditional manufacturing methods such as injection molding. This lower pressure hinders complete volume filling and the formation of adequate bonds with adjacent layers, resulting in the formation of continuous porosities throughout the component.

The formation of internal voids and the mechanism of inter-layer adhesion in material extrusion are better characterized by sintering rather than welding, leading to mechanical properties that differ significantly from those obtained through processes like injection molding [173, 174]. For semi-crystalline polymers, these disparities are further influenced by crystallization kinetics, which can inhibit bonding between adjacent filaments during deposition. Moreover, the presence of porosities influences the crystallinity of semi-crystalline polymers, such as polylactic acid (PLA), as noted in prior studies [175].

Unlike conventional manufacturing processes, material extrusion lacks standardization, as the deposition conditions, inter-filament adhesion, and the morphology of porosities are highly dependent on the tool path. Consequently, the mechanical properties of the component are sensitive to its geometry, complicating both the characterization of the material and the prediction of its behavior. This variability poses challenges for the development of representative test samples that accurately reflect the manufacturing conditions of the final part.

X-ray computed tomography (CT) is a reliable method for accurately characterizing porosities, providing detailed information on their location, distribution, and dimensions through the creation of a digital twin of the component [176]. However, the high cost and extended scanning times associated with CT limit its practicality for widespread use. Alternatively, non-destructive testing (NDT) methods, such as indentation tests, offer a more time-efficient approach for gaining insights into the local mechanical behavior of components. The application of NDT on actual parts would enhance the quality control of AM components. Previous research has demonstrated the effectiveness of indentation tests for evaluating the mechanical properties of metals and polymers [177], also produced by processes such as direct energy deposition [178] and binder jetting [179]. These tests have been successfully applied to materials with relatively small porosities, typically much smaller than those found in material extrusion parts, allowing the use of standard hardness indenters and nanoindentation techniques. However, these tools are not suitable for material extrusion components, where the porosity size often exceeds the dimensions of the indenter. In contrast to conventional mechanical tests (e.g., tensile or compression tests), NDT offers the added advantage of determining local material properties [180, 181], which is particularly critical for components with heterogeneous structures, such as those produced via material extrusion.

### 4.1.2 Materials and methods

Two different experimental campaigns were conducted to study specimens' behavior when they were subjected to indentation test. The first one [166] was conducted on parallelepiped-shaped specimens made of polylactide acid (PLA) produced by Fabbrix. The samples were 5 mm × 60 mm × 20 mm in dimensions, and they were realized using a commercial machine Creality Ender-6. This machine enables the selection of a wide range of parameters and deposition conditions. Table 6 shows the parameter used during the deposition process. The samples were filled using five perimetral shells with a fixed width of 0.5 mm.

The samples were produced by varying two process parameters:

- Extrusion multiplier: it is the amount of material flow during the deposition; five different extrusion multipliers were adopted (94%, 97%, 100%, 103%, and 106%) to produce specimens with different porosities.
- Deposition strategy: the samples were produced both vertically and horizontally, as Fig. 20 depicts.

*Table 6 – Selected printing parameters value*

| *Printing parameter* | *Selected value* |
|---|---|
| *Nozzle temperature* | 210 °C |
| *Platform temperature* | 60 °C |
| *Layer thickness* | 0.2 mm |
| *Nozzle diameter* | 0.4 mm |
| *Printing speed* | 4000 mm/min |
| *Infill percentage* | 100% |
| *Infill pattern* | Rectilinear |

Commercial software Simplify 3D was used to control all the deposition settings and to generate the GCODE used as input for the material extrusion machines. Three replicates were made for each deposition condition.

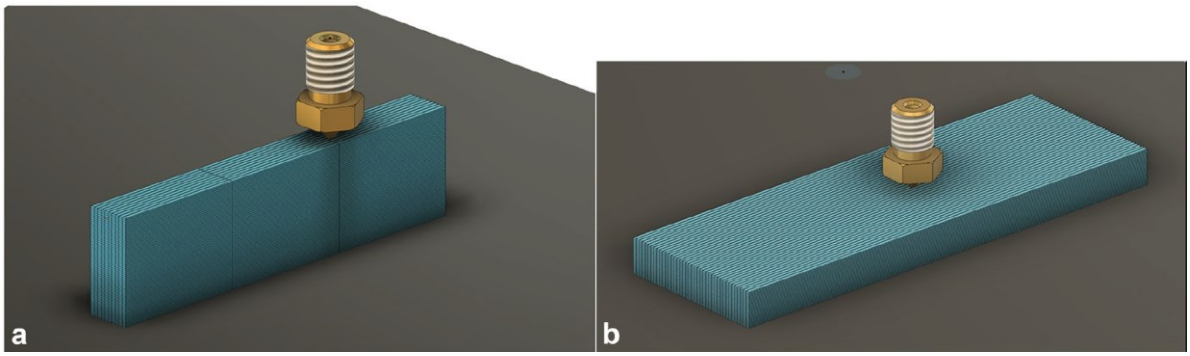



*Fig. 20 – Schematics of the build orientation of the sample during the printing: vertical (a) and horizontal (b)*

The second study [167] was conducted on cylindrical specimens 20 mm in diameter and 40 mm in height, according to ASTM 695 standards. These dimensions were selected to have the edge of the indenter to the sample border at least two times the diameter of the indenter, in order to limit the sample size effect, as shown in Fig. 21.

Samples were made also of PLA by Fabrix, using commercial machines Creality Ender 6, setting the printing parameters with the same values as the first experimental campaign, described in Table 6. In this campaign of experimental tests, the extrusion multiplier varied between 99 and 104%; four specimens were printed for each extrusion multiplier value. In addition to performing the indentation test, the compression test was also performed in the second testing campaign to find a correlation between the two tests.

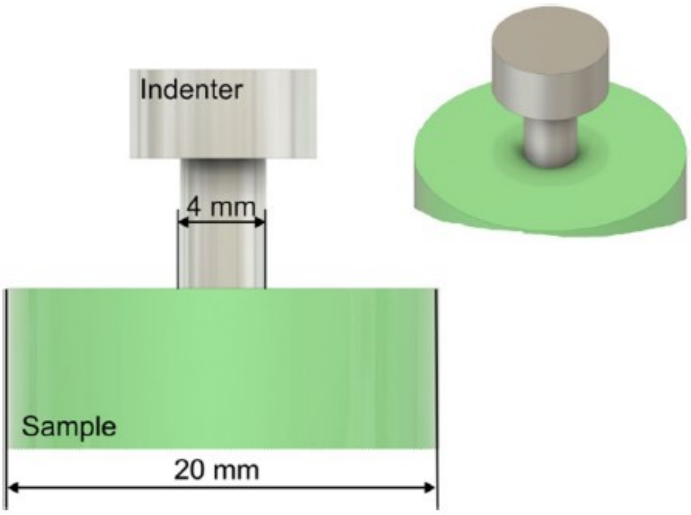



*Fig. 21 – Schematic of the sample and the indenter during flat indentation test*

A third campaign of experimental tests [169] was conducted to study the behavior of cylindrical specimens subjected to compression tests. Cylindrically shaped specimens of 15 mm in diameter and 15 mm in height were produced. The main deposition conditions are summarized in Table 6. The samples were produced by using four different material extrusion multipliers: 96%, 100%, and 104%. Then some specimens were subjected to thermomechanical compaction to further reduce the porosities and to achieve full-density samples. To this end, prototypal equipment was developed, showed in Fig. 22.

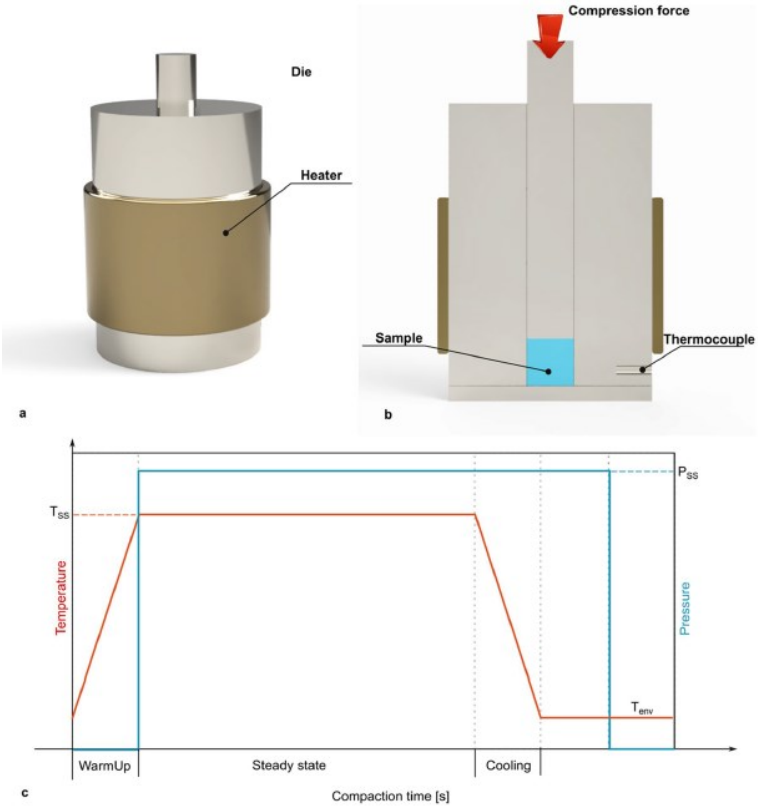



*Fig. 22 – Schematic of the adopted equipment to perform thermomechanical compaction*

The equipment involved a die with an inner diameter of 15 mm and a punch with the same diameter made by K720 steel by Bohler. An external heater and a K-type thermocouple were used to heat the die under control and to maintain a constant temperature of 120 °C. The heater and the thermocouple were connected to an external PID for temperature control. During the compaction tests, an external compression force of 1500 N was applied through a hydraulic press; this force corresponds to a pressure of almost 8.5 MPa.
All the samples, from the first, second and third experimental campaigns, were characterized after printing to determine the density of the components. To this end, the main dimensions were measured through a centesimal micrometer. Then, the weight of the samples was measured using a precision balance model XT1220M by Precisa. This enabled the estimation of the density of the samples and the influence of the extrusion multipliers on the density. A universal testing machine mode C43.50 equipped with a load cell with a full scale of 50 kN was adopted to conduct both instrumented indentation test and compression test.

Specimens of the first experimental campaign were characterized as follows. The specimen was positioned horizontally (with the 20 × 20 surface perpendicular to the indenter) on a compression plate, as shown in Fig. 23a. Two different cylindrical indenters were placed on the upper side of the sample, with diameters of 2 mm and 4 mm. Tests were conducted at a constant travel speed of 1 mm/min. The test was divided into two phases: the loading phase until the tool traveled for 0.6 mm through the sample thickness and the unloading phase, which involved a reverse tool direction. During the loading and the unloading phases, the force–displacement curves were recorded and then these curves were elaborated using an algorithm within the MATLAB 2021a environment. The algorithm identifies the linear path of the curves during both the two phases and identifies the slopes of each path, $E1$ and $E2$, respectively, as shown in Fig. 23b.
Specimens of the second campaign were subjected to flat indentation test and compression test. Tests were performed at a constant travel speed of 0.1 mm/min, using a flat-end cylindrical indenter with 4.0 mm diameter made of K720 high-strength steel by Bohler. To avoid contact-dependent trends, such as the non-coplanarity between the sample surface and the indenter flat face, a pre-load of 200 N was used. Instrumented indentation tests were performed on the upper and bottom surfaces of the specimen, imposing a maximum penetration depth of 2.0 mm.

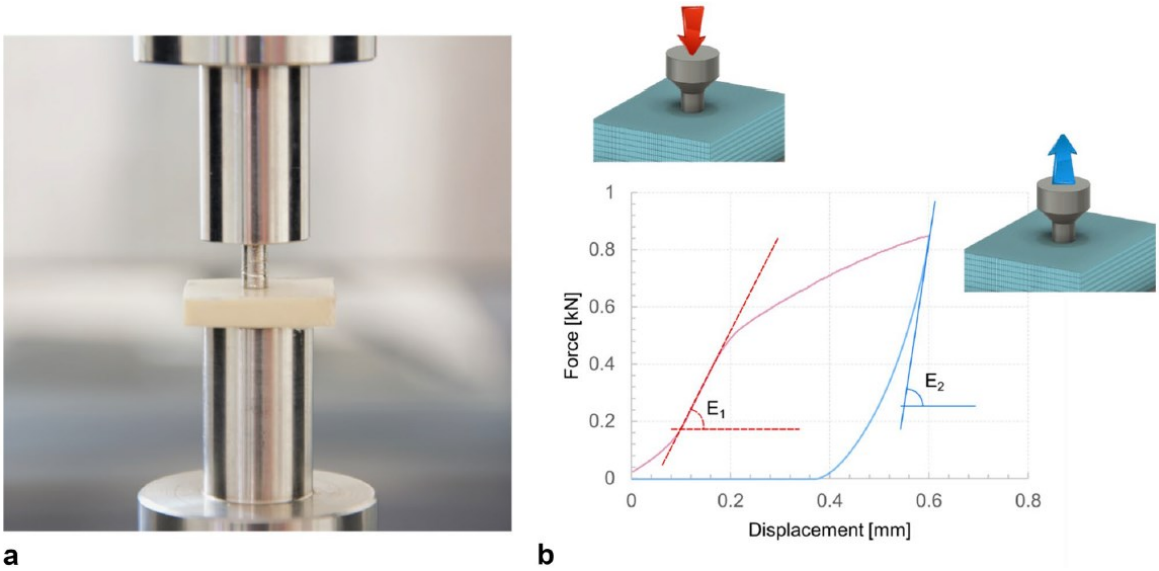



*Fig. 23 – Experimental equipment and sample orientation during the indentation test (a); schematic of the force displacement curve recorded during loading (red) and unloading (blue) phases (b)*

Load–displacement curves were recorded during the tests, and they were elaborated through an algorithm developed using MATLAB 2022b environment. During the indentation test, an uneven stress distribution is produced on the sample; consequently, the stress is not monodirectional, but it is due to both elastic and plastic deformation. In the first phase of the test, the elastic deformation is dominant; then, when a sufficient indentation is reached, plastic deformation is localized around the indenter edge [182]. Fig. 24 shows the trend of normalized stress as a function of the displacement of the indenter; to determine material's properties, in fact, the load was divided by the surface area of the flat indenter. The first part of the curve is almost linear due to the high elastic contribution. Increasing the penetration depth, the curve exhibits a plateau corresponding to a significant material flow. Due to this double behavior during the test, two approaches were followed to determine the onset of the yielding condition: the deviation from the linear regime, that represents the elastic limit, and the bitangent yield strength, as shown in Fig. 24. These values were determined automatically through a routine developed in MATLAB 2022b.

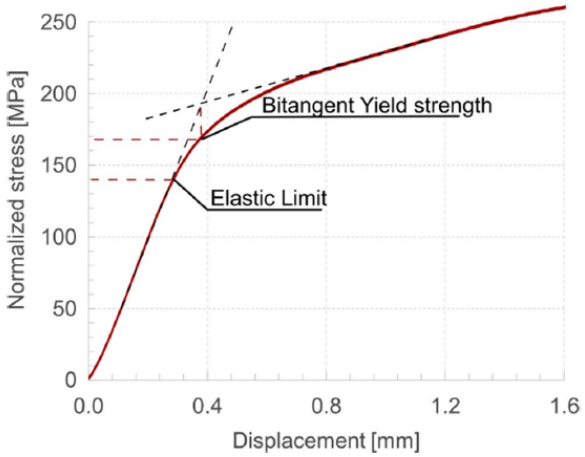



*Fig. 24 – Normalized stress curve recorded during instrumented flat indentation test*

Samples of the second experimental campaign were also subjected to compression test, to determine a correlation between two different tests. Compression tests were performed using MTS's Universal Testing Machine model C43.50 with a traverse speed of 1 mm/s, according to ASTM D695 standards. Even during the latter experimental campaign, compression tests were conducted. The tests were conducted under different strain rates, as shown in Table 7. For each deposition condition and testing condition, five replicates were performed.

*Table 7 – Full factorial experimental plan of the third experimental campaign*

| *Level* | *Extrusion multiplier (%)* | *Strain rate ($s^{-1}$)* |
|---|---|---|
| *I* | 96 | $5\times10^{-1}$ |
| *II* | 100 | $5\times10^{-2}$ |
| *III* | 104 | $5\times10^{-3}$ |
| *IV* | Compaction | $5\times10^{-4}$ |

Optical microscopy and SEM analysis was adopted to better understand the morphology of the samples before and after the mechanical tests. The samples were cross-sectioned following standard metallographic procedures and a metallographic microscope model DM5000 by LEICA was adopted to provide a better understanding of the mesostructural features and to investigate the presence of voids and porosities. The portions were molded into resin, and polished with fumed silica suspension 0.2 mm. Finally, the samples were treated in an ultrasonic bath to remove material from the porosities. To further investigate the differences among the surfaces of the samples produced with different extrusion multipliers, morphological analysis was performed through 3D surface reconstruction. To this end, a stereoscope model M205 by LEICA was adopted. The surfaces were subsequently analyzed using LEICA Map software for 3D reconstruction and analysis.

### 4.1.3 Determination of density

Fig. 25 shows the variation of the density of the samples of the first experimental campaign produced using different extrusion multipliers and printing orientations. The adoption of higher values of the extrusion multiplier raised the density of both vertical and horizontal samples. However, significant differences between the densities of samples printed with the same extrusion multiplier were observed on samples printed in horizontal and vertical directions, especially with lower values of the extrusion multiplier. Such difference tended to decrease with higher values of the extruder multiplier; then, a negligible difference was found for the extruder multiplier of 106%. The highest density reached by the printed samples was 1.195 g/mm$^3$. This value is almost 4.5% lower than the density of the original filament (1.25 g/mm$^3$).

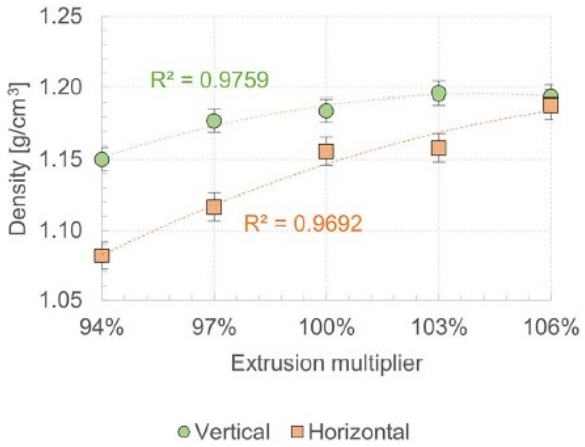



*Fig. 25 – Influence of the extrusion multiplier and printing orientation on the density of the samples of the first experimental campaign*

Fig. 26 depicts the cross-sections made on samples produced by different extrusion multipliers (EMs). The comparison of the cross-sections confirms a gradual reduction of the porosity dimension (darker regions) as the extruder multiplier increases. The porosities were diamond-like, as shown in the higher magnifications reported in Fig. 26. For EM = 94%, the average diagonal of the porosities was 180 mm, while for the samples made with EM = 103% and EM = 106%, the average diagonal was 85 mm. The analysis of the cross-section provided a better understanding of other defects. Samples made using a low extrusion multiplier (EM = 94%) showed a coalescence of porosities in different sample regions. In addition, several unconnected filaments were observed owing to the lower material flow. Such defects were not observed in samples made by higher extrusion multipliers (EM ≥ 97%). An uneven distribution of the porosities also characterized all the cross-sections. For

low extrusion multipliers, the variability of the porosity dimension led to the presence of coalescent porosities; on the other hand, in samples printed with higher extrusion multipliers, the outer shells generally showed smaller porosities than those observed in the central region.

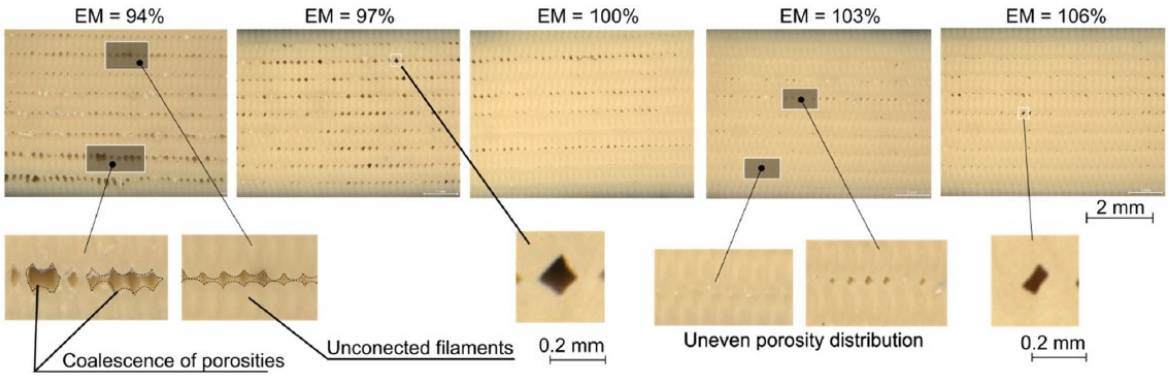



*Fig. 26 – Cross section on vertically printed samples of the first experimental campaign printed with different extrusion multiplier*

The influence of the extrusion multiplier on the density of the sample of the second experimental campaign is depicted in Fig. 27. Density shows linear growth with the extrusion multiplier, with values starting from 1.19 up to 1.23 g/cm$^3$, similar to the values shows in Fig. 25 for the same values of the extrusion multiplier.

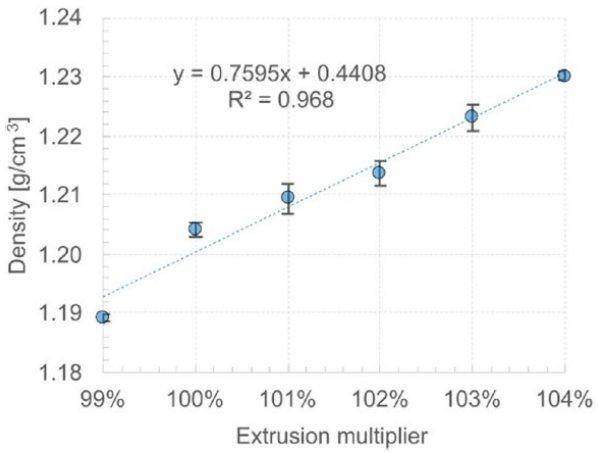



*Fig. 27 – Influence of the extrusion multiplier on the density of the samples of the second experimental campaign*

Regarding the third experimental campaign, Fig. 28 compares the densities of the samples produced with different extrusion multipliers (EMs) and those of samples produced through thermomechanical compaction. As can be inferred, increasing EM from 96 to 100% leads to an increase from 1.17 to 1.21 g/cm$^3$ (corresponding to 4% of the increase), while further increase leads to a minor increase in density of almost 2%. This density-saturation phenomenon was already observed in previous studies. The comparison of the density

achieved when using the highest extrusion multiplier (EM = 104%) and the thermomechanical compaction indicates that the adoption of EM =104% leads to a slightly lower density (almost 2% lower) as compared to thermomechanical compacted samples. In addition, the mean value of the density achieved by compacted samples corresponds to the density of the PLA reported by the filament manufacturer (1.25 g/cm$^3$). This indicates that the developed compaction process enabled to removal of almost all voids from the samples made by material extrusion process.

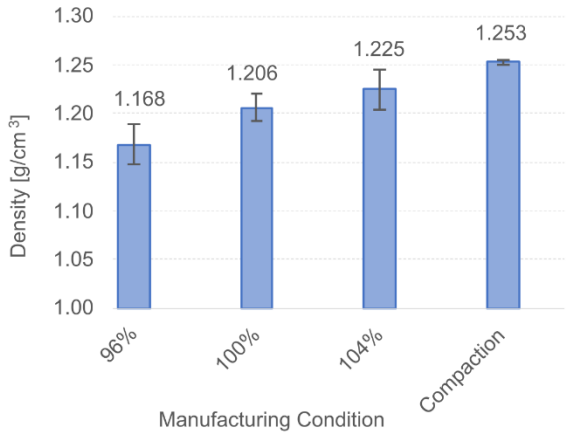



*Fig. 28 – Influence of the extrusion multiplier and thermomechanical compaction on the density of the samples of the third experimental campaign*

Optical microscopy and SEM analysis were adopted to observe the cross sections of the samples. Fig. 29 and Fig. 30 show the cross sections of the samples made under different processing conditions. Image analysis was performed to determine the porosity dimensions produced under different processing conditions.

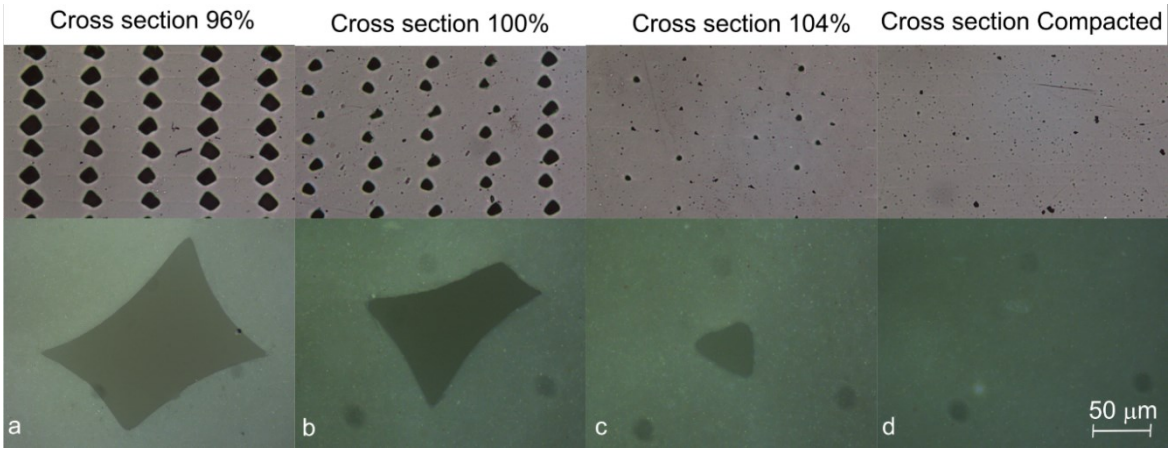



*Fig. 29 – Cross sections of the samples produced under different processing conditions*

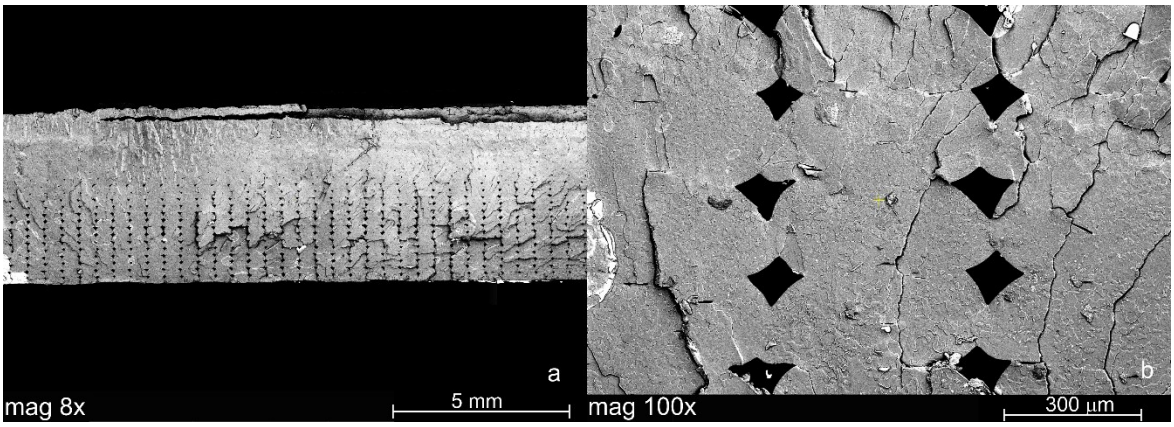



*Fig. 30 – Cross section of the samples made by SEM analysis at 8x magnification (a) and 100x magnification (b)*

Fig. 31 depicts void detection and statistical dimension characterization using a cross-sectional image of a sample produced with an extrusion multiplier of 96%. Starting from an image of the cross section (Fig. 31a), the software determines the presence of voids that are subsequently identified through different colors (Fig. 31b). Then, the dimension of the voids is determined as shown in Fig. 31c, d. The same procedure was followed to analyze the cross section of samples produced under different conditions (i.e., different extrusion multipliers and material extrusion/compaction process).

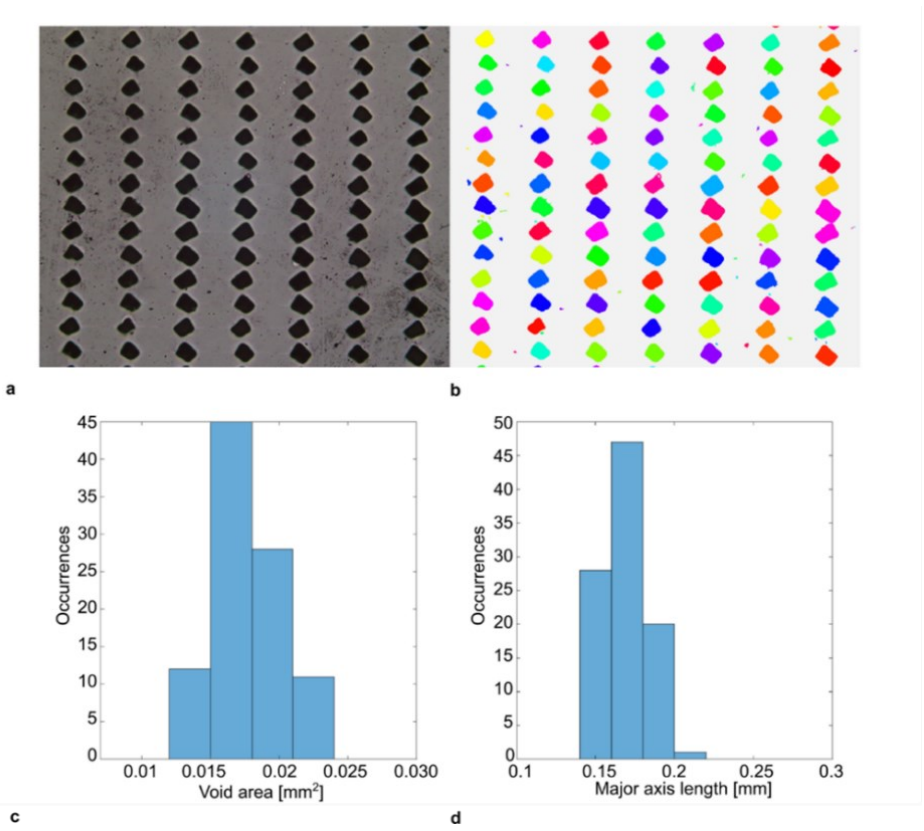



*Fig. 31 – Image analysis of mesostructure features (voids): a) original image; b) identified voids; c) distribution of void area and d) distribution of major axis length. (Extrusion multiplier EM=96%)*

When the extruder multiplier was set to 96%, the normal value of the major axis dimension was 170 mm. This value decreased to 125 mm (for EM = 100%) and to 65 mm (for EM = 104%). The voids almost disappeared for the compacted samples (the porosity with the highest major axis dimension was 20 mm). Similarly, the normal void area was determined for each condition. For EM = 96%, the normal value of the void area was 0.015 $mm^2$. This decreased to 0.01 $mm^2$ for EM = 100% and further reduced to 0.0025 $mm^2$ for EM = 104%.

The influence of the deposition conditions (and the adopted process) on the normal value of the characteristic dimension of the voids is depicted in Fig. 32. These results indicate that increasing EM involves significant reduction of the dimensions of inner voids. Increasing EM from 96 to 104% reduced the voids area to one-sixth from 15,000 $mm^2$ (for EM = 96%) to 2500 $mm^2$ (for EM = 104%). Both the cross sections and the quantitative measurement of voids indicated that thermomechanical compaction allowed to fulfill the inner voids almost completely.

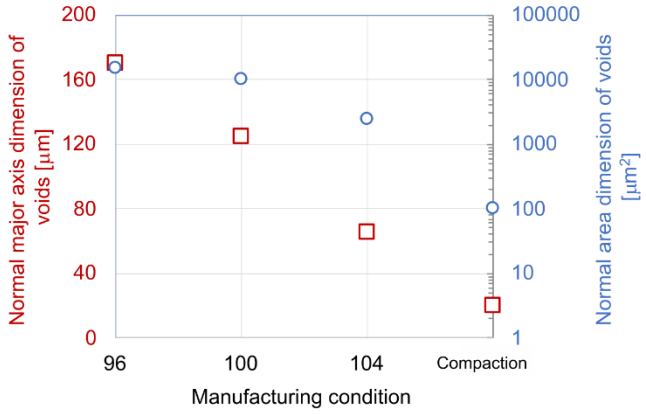



*Fig. 32 – Normal dimensions of voids produced under different deposition conditions and compaction*

Thus, the density of these samples was assumed as that of a real full density sample. Thus, the relative density $\rho_R$ calculated by normalizing the density of the sample $\rho_S$ by that of the full density sample ($\rho_{FD}$) was calculated for all conditions, according to eq. 14:

$$\rho_R = \frac{\rho_S}{\rho_{FD}} \qquad \textit{eq. 14}$$

The values of the relative densities of the samples produced using different extrusion multipliers are reported in

Table 8. Morphological analysis was also conducted on the samples to determine possible influence of the processing conditions on the surface appearance.

*Table 8 – Density and relative densities calculated according to different manufacturing conditions*

| *Manufacturing Condition* | *Density (g/cm$^3$)* | *Relative Density (%)* |
|---|---|---|
| *96%* | 1.17 | 93% |
| *100%* | 1.21 | 96% |
| *104%* | 1.23 | 98% |
| *Compaction* | 1.25 | 100% |

Fig. 33 shows the external surfaces of the samples made under different processing conditions and produced by MatExt and compaction tests.

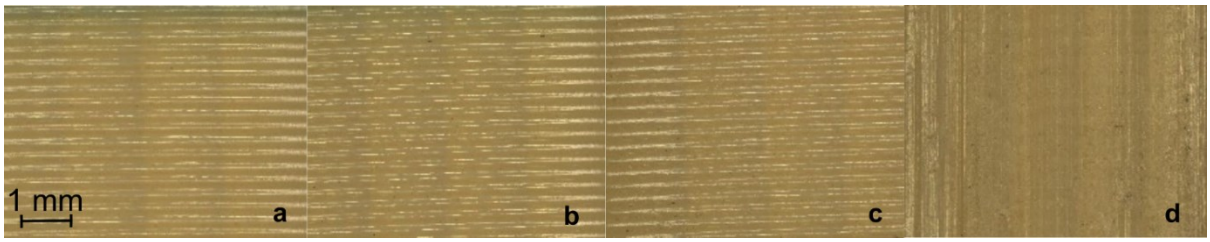



*Fig. 33 – External surfaces of the samples produced under different processing conditions: (a) EM=96%; (b) EM=100%; (c) EM=104%; (d) compacted*

The surfaces were subsequently analyzed using LEICA Map software for 3D reconstruction and analysis. Fig. 34a depicts the geometry of a sample produced by MatExt setting the extrusion multiplier to 104%, while Fig. 34b shows the surface of the compacted samples. As can be inferred, the sample produced through MatExt process shows typical features given by layer-by-layer deposition. On the other hand, the sample made by compaction shows a smoother geometry, as also shown in the virtual cross section, depicted in Fig. 34d.

This further indicates that the compaction experiments enabled for producing sufficient material flow to remove the mesoscale features (owing to the previous MatExt process) almost completely.

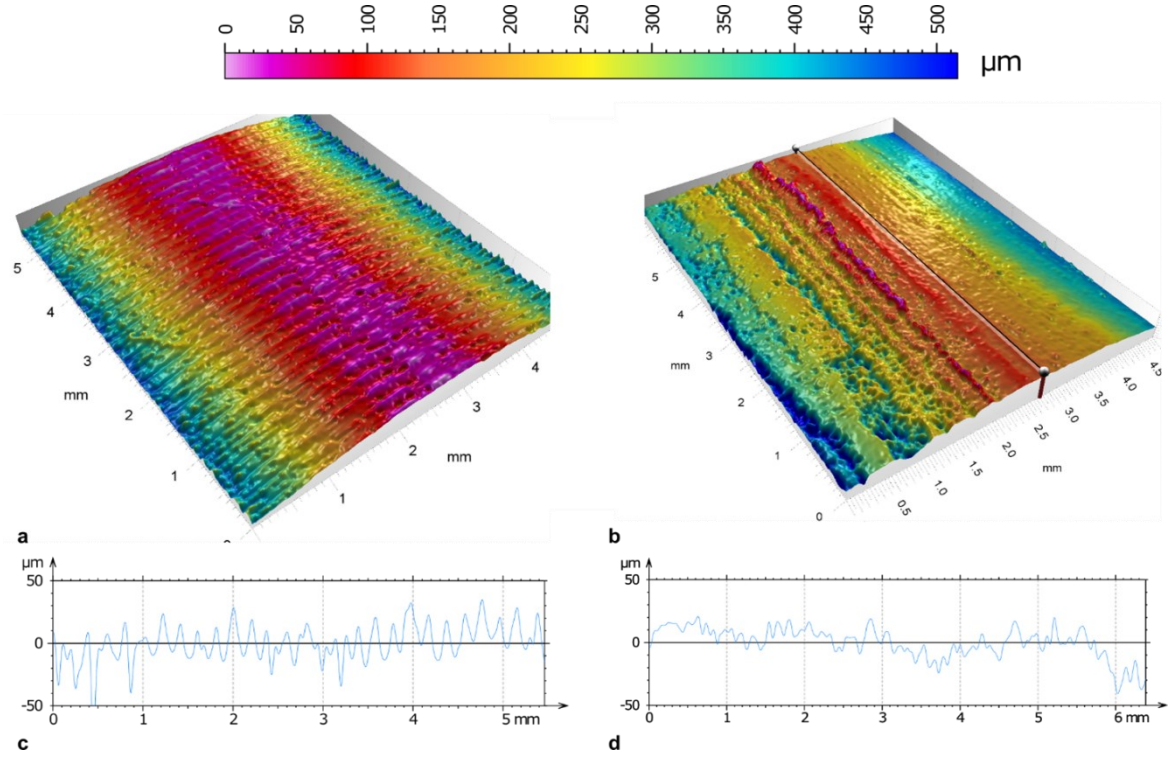



*Fig. 34 – Surface analysis performed on two samples: a) printed with extrusion multiplier set to 104% and; b) compacted. Virtual profile of the samples c) EM=104% and d) compacted*

### 4.1.4 Mechanical behavior of the samples

The first experimental campaign studied the behavior of the sample when they are subjected to a flat instrumented indentation test. Fig. 35a and b depict the influence of the extrusion multiplier on the slopes $E1$ and $E2$ (during the loading and unloading phases, respectively) measured through indentation tests using the two indenters ($D$ = 2 mm and $D$ = 4 mm, respectively) on samples printed horizontally. The trends indicate a linear increase in the slope with the extrusion multiplier. However, all the testing conditions (performed with the two indenters and during the loading or the unloading phases) indicated a saturation phenomenon. Indeed, the slopes determined on samples printed with the extrusion multiplier EM = 106% showed a negligible variation compared to those measured on samples printed with EM = 103%. Fig. 36a and b depict the trends of the slopes $E1$ and $E2$ measured (with indenter diameters $D$ = 2 mm and $D$ = 4 mm respectively) on samples printed in the vertical direction. In this case, the tests conducted with the tool diameter $D$ = 4 mm indicate a non-linear increase of the slopes with the extrusion multiplier characterized by a high coefficient of correlation. This non-linear behavior reflects that determined for the density (shown in Fig. 24). On the other hand, the slope measured through the smaller indenter ($D$ = 2 mm), as shown in Fig. 36b, was affected by higher uncertainty and dispersion (lower $R^2$ values).

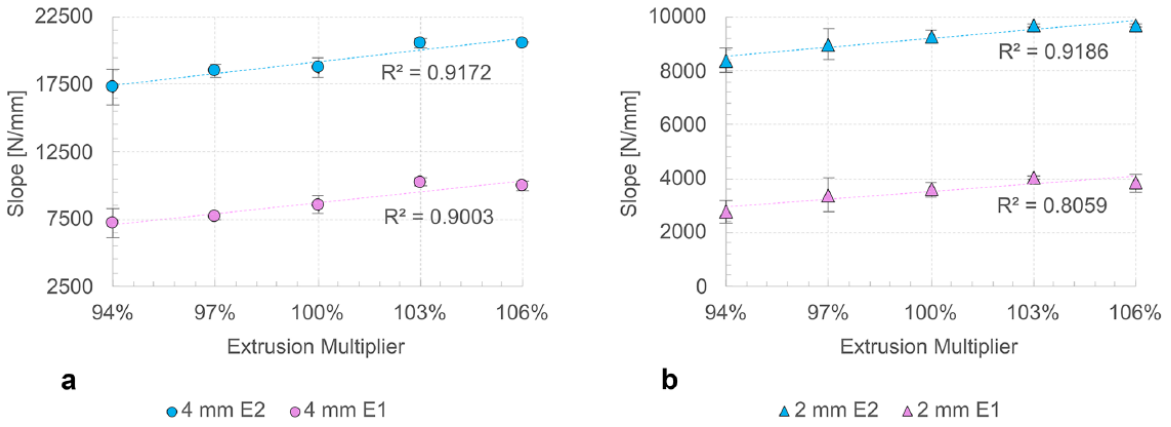



*Fig. 35 – Influence of the extrusion multiplier on the slope measured during indentation tests on samples printed in (a) D = 4 mm and (b) D = 2 mm on horizontally printed samples*

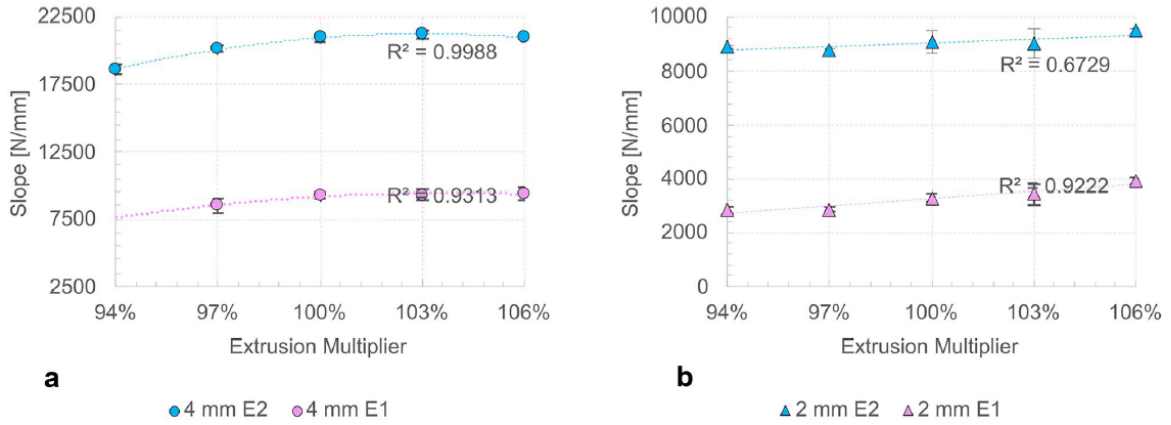



*Fig. 36 – Influence of the extrusion multiplier on the slope measured during indentation tests on samples printed in (a) D = 4 mm and (b) D = 2 mm on vertically printed samples*

Cross-correlation among the calculated slopes and the density measurements was performed to determine the best procedure and indenter diameter for density evaluation. Fig. 37a depicts the trends of the slopes $E1$ and $E2$ by different indenter diameters ($D = 2$ mm and $D = 4$ mm) for horizontal samples. The slope showed a high coefficient of correlation $R^2$ in all the testing conditions. The correlation between the slopes and the density for horizontally printed samples ranged between $R^2 = 0.917$ and $R^2 = 0.98$. Fig. 37b depicts the correlation between the slope and the density measured on samples printed vertically. In this case, adopting the indenter of $D = 4$ mm confirms a good correlation between the slope and the density; conversely, low values of $R^2$ for $D = 2$ mm indicate the limit of the smaller indenter for samples printed vertically. Fig. 37a and b indicate the possibility of correlating the slopes of indentation tests with density measurements performed on samples printed in the same direction, in horizontal and vertical directions, respectively. A further cross-correlation analysis was conducted to verify if a relationship can be established between the samples'

slopes and density regardless of the printing direction. This analysis was limited to the indenter with $D$ = 4 mm since the low values of the coefficient of correlation are shown in Fig. 37b.

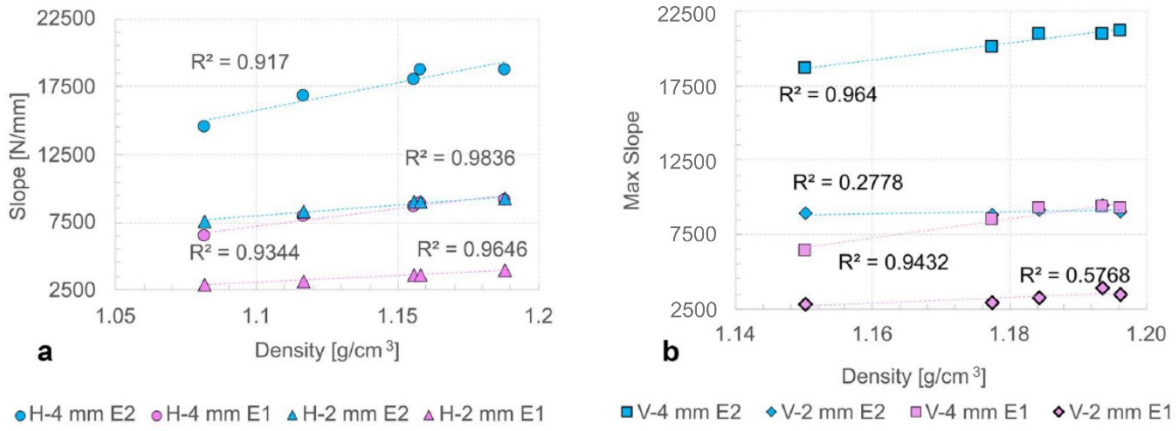



*Fig. 37 – Correlation of the slopes measured during indentation tests and the density on (a) horizontally printed and (b) vertically printed samples*

The relatively high values of the coefficient of correlation as reported in Fig. 38 ($R_2$≈0.90) indicate the reliability of such a general relationship between the slopes and the density of the samples.

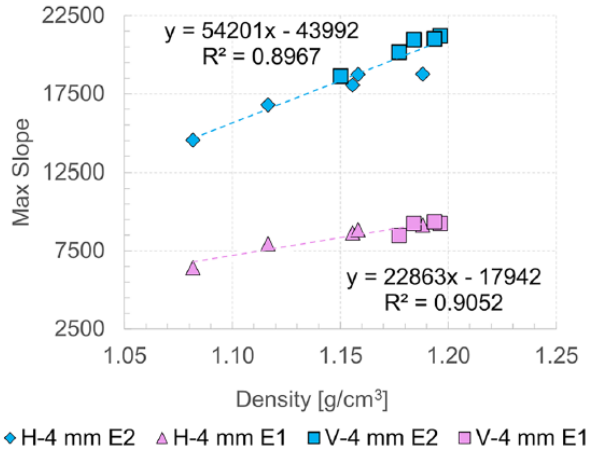



*Fig. 38 – Overall correlation between the slope measured the indentation tests on horizontal and vertical samples during loading (E1) and unloading (E2) phases*

Samples of the second experimental campaign were subjected to both indentation and compression tests. Fig. 39 compares the load-displacement curves recorded during the compression tests for samples achieved with different extrusion multipliers (i.e., 99%, 101%, and 104%). The higher the extrusion multiplier, the higher the stiffness and the peak load. This was due to the higher density of the samples produced with higher extrusion multipliers.

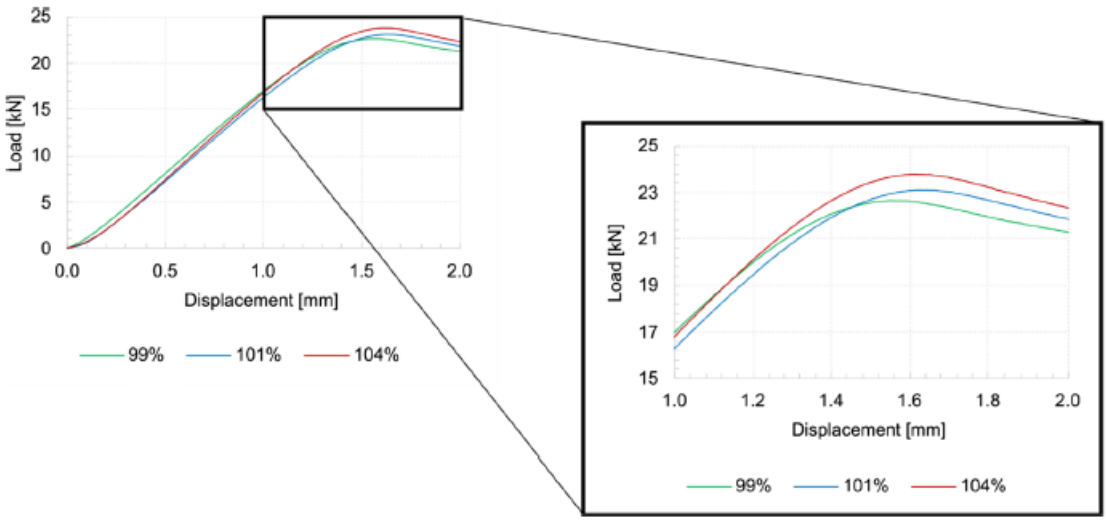



*Fig. 39 – Force–displacement curves recorded during the compression tests of samples printed with different extrusion multipliers*

The influence of the extrusion multiplier and density on the yield strength measured through the compression test are depicted in Fig. 40 a and b. The yield strength showed a linear increase versus both the extrusion multiplier and the density of the specimens. The specimens printed with a 99% extrusion multiplier showed yield strength of 71 MPa; increasing the value of the extrusion multiplier by 5% led to an increase of yield strength up to 75 MPa, corresponding to an increase of yield strength up to 5%.

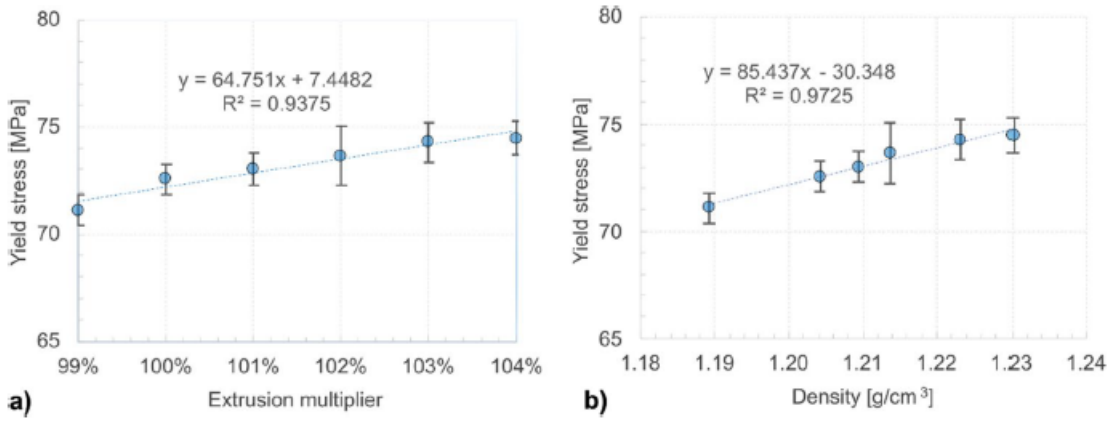



*Fig. 40 – Influence of the (a) extrusion multiplier and (b) density on the yield strength measured through compression tests*

Fig. 41 compares the load–displacement curves recorded during the indentation tests for samples achieved with different extrusion multipliers (i.e., 99%, 101%, and 104%). As for the compression tests, the higher the extrusion multiplier (and the density of the sample), the higher the load exerted on the sample during the indentation. From the observation of the curves, it emerges that the intersection of the tangents to the curves is reached in correspondence of displacement between 0.2 mm and 0.6 mm, as shown by the red rectangle

in Fig. 41. Thus, a maximum indentation depth of 0.8 mm could be enough to determine the yielding condition through indentation tests using the bitangent method, while 0.4 mm would be required if the elastic limit is preferred. As described above, each test's yielding condition was determined through a Matlab routine.

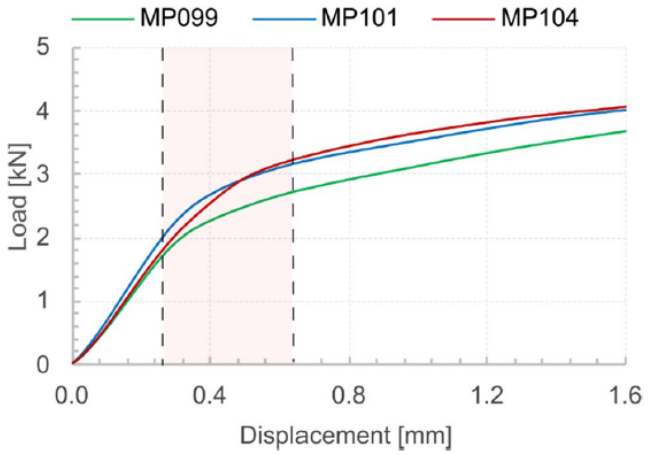



*Fig. 41 – Load–displacement curves recorded during the indentation tests of samples printed with different extrusion multipliers*

Fig. 42 a and b depict the influence of the extrusion multiplier on the normalized stress measured through indentation tests performed on the upper and lower sample surface using the two methods to detect the yielding onset. The normalized strength measured on the upper surface of the samples (Fig. 42a) increased almost linearly with the extrusion multiplier. The average yield strength for EM =99% was 102 N/mm$^2$, while the average yield strength for EM = 104% was 123 N/mm$^2$, corresponding to an increase of 21%. On the other hand, the normalized stress measured on the bottom surface of the specimens showed lower sensitivity to the extrusion multiplier during the indentation test. Indeed, the yield strength values hold almost constant. The average yield strength, calculated through the bitangent method, determined on the lower face of the specimens was equal to 152 MPa, and the standard deviation was 3 MPa. This indicated that the mechanical properties of the component surface in contact with the building plate are almost unaffected by the adopted extrusion multiplier and are much higher than those measured on the upper surface. Similar trends were found by adopting the elastic limit method. Indeed, the elastic limit increased significantly on the upper surface with the EM, while it showed lower sensitivity in the indentation tests performed on the bottom surface. Fig. 43a and b depict the normalized strength and the elastic limit as a function of sample density, respectively. The normalized strength grows linearly as a function of density. Similar trends can also be observed between the elastic limit and the density of the samples. In both cases, the coefficient of determination was relatively

high. For both the normalized strength and the elastic limit, $R_2 \cong 0.94$. On the other hand, both the normalized strength and the elastic limit measured on the bottom sample surface are almost unaffected by the average density of the sample. Thus, for each sample, the yield strength measured through compression tests was compared to the yield strength measured by indentation tests performed on the upper surface under the same deposition conditions.

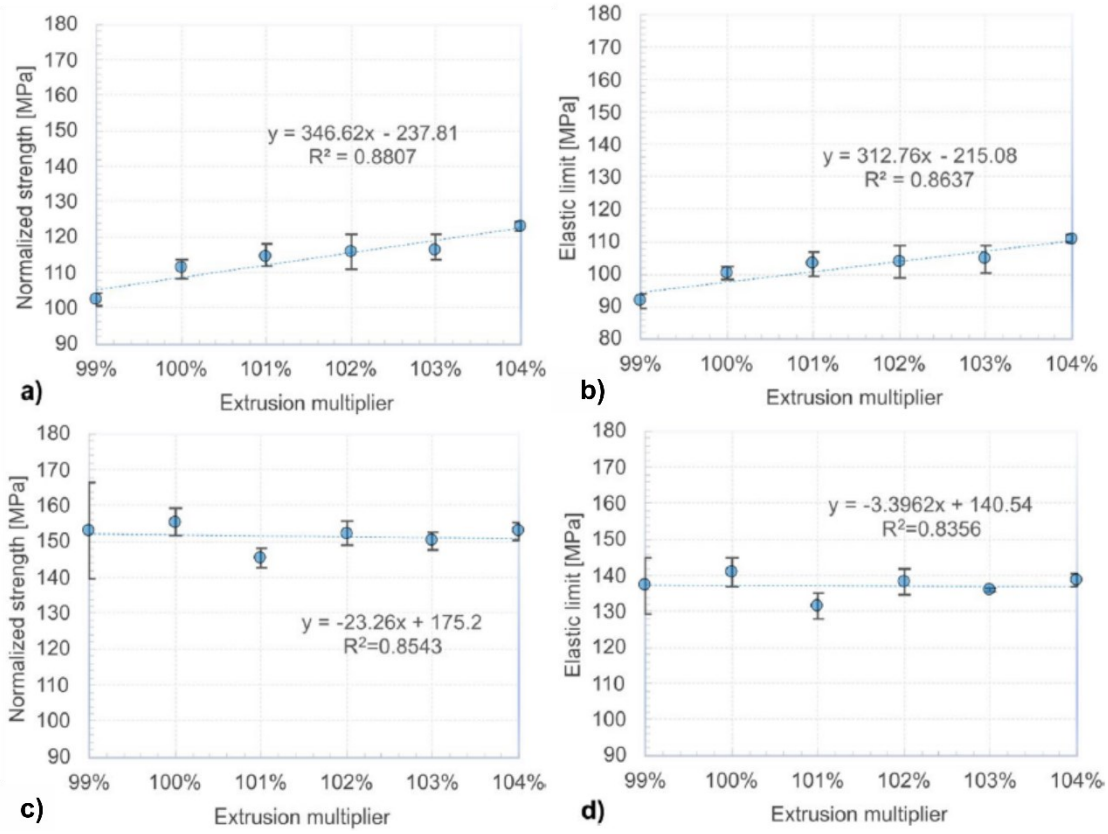



*Fig. 42 – Influence of the extrusion multiplier on the normalized force determined through indentation tests performed on the a, b upper surface and c, d lower sample surface*

Fig. 44 shows the correlation between the yield strength obtained through the indentation test and that obtained during the compression test. The correlation between the two yield strengths showed a linear trend, with a coefficient $R^2$ of 0.92. Similarly, the elastic limit (measured by the indentation test) and the yield strength (measured through the compression test) also showed a significant correlation since the coefficient of determination $R^2$ was 0.90. Thus, the established relationship (linear regression coefficients) can be exploited to convert the yielding condition measured through indentation tests to predict the compressive yield strength of the actual component on a specific location.

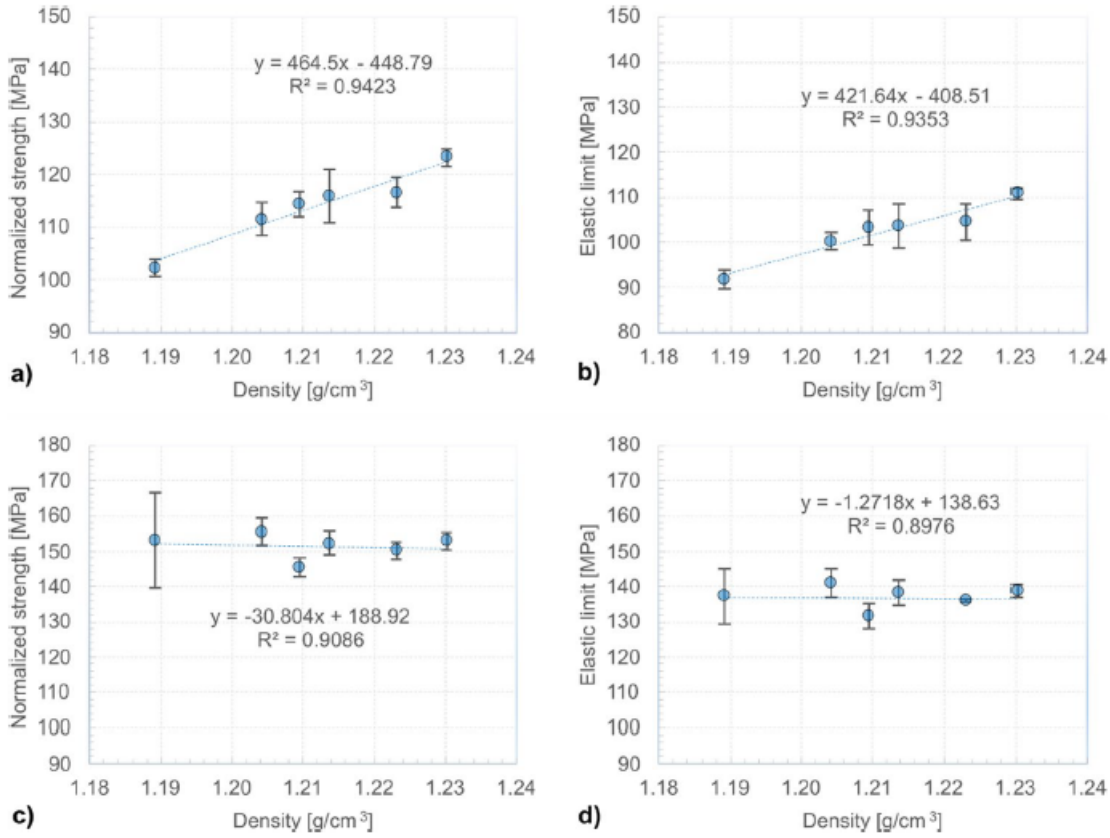



*Fig. 43 – Influence of the sample density on the yielding condition measured by indentation tests performed on the a, b upper and c, d lower sample surface*

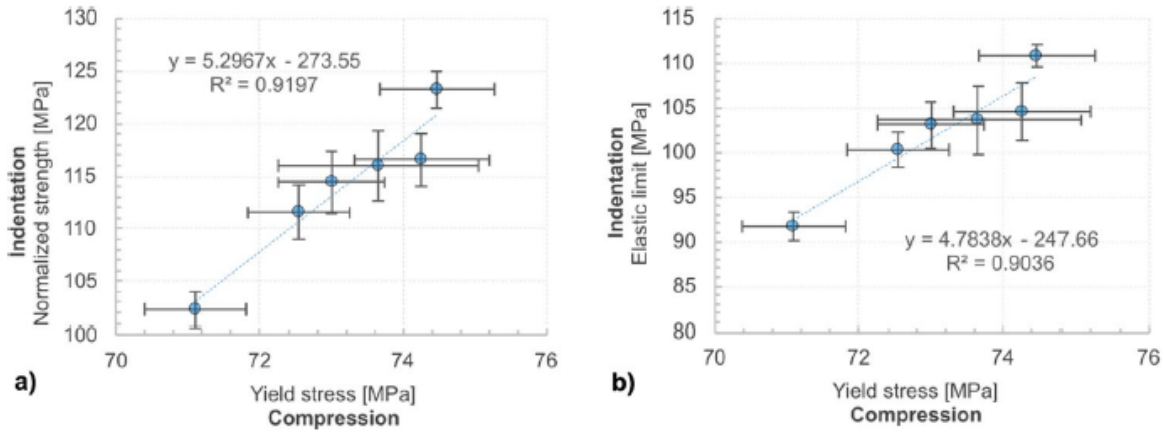



*Fig. 44 – Correlation between the (a) yield strength (measured through the compression tests) and (b) the normalized force (measured through the indentation tests)*

Concerning the latter experimental campaign, Fig. 45 shows a macrograph of a sample used in compression tests before and after the mechanical test. As can be observed, after the tests, the sample shows a barreling effect on the sides. This was achieved for all the samples irrespective of the processing conditions or the manufacturing process (MatExt or Compaction).

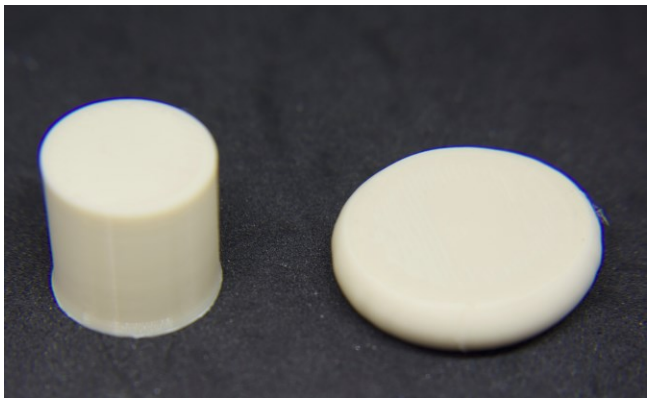


*Fig. 45 – Macrograph of a sample before and after compression tests*

The typical engineering stress-strain curve is depicted in Fig. 46. The engineering stress was calculated as the ratio of the load by the initial sample diameter and engineering strain was calculated as the ratio of the deformation by the initial sample height. The curve showed typical characteristics of compression tests on polymers [183, 184]. Indeed, they showed an elastic regime upon the onset of yielding (peak of the stress). Then, post-yielding behavior involving strain softening (stress drop) was observed. The stress held almost constant (steady state flow) upon the onset of the strain hardening (owing to molecular chains' alignment towards the loading path).

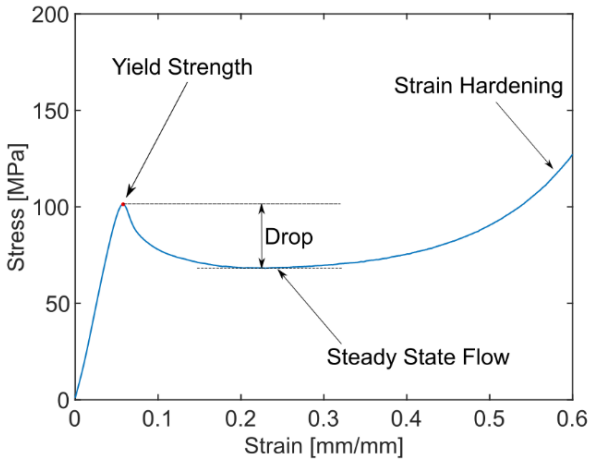



*Fig. 46 – Stress-strain curves of the samples produced under different processing conditions*

The influence of the manufacturing process (MatExt or compaction), the extrusion multiplier, and the strain rate on the yield strength, strain-softening, and strain-hardening behaviors can be retrieved from Fig. 47. As can be seen, increasing the material extrusion involvs higher stress which indicates a higher load-bearing capability of the material. The samples made by the compaction process showed the highest yield strength irrespective of

the strain rate. This was due to the higher relative density of compacted samples than MatExt samples.

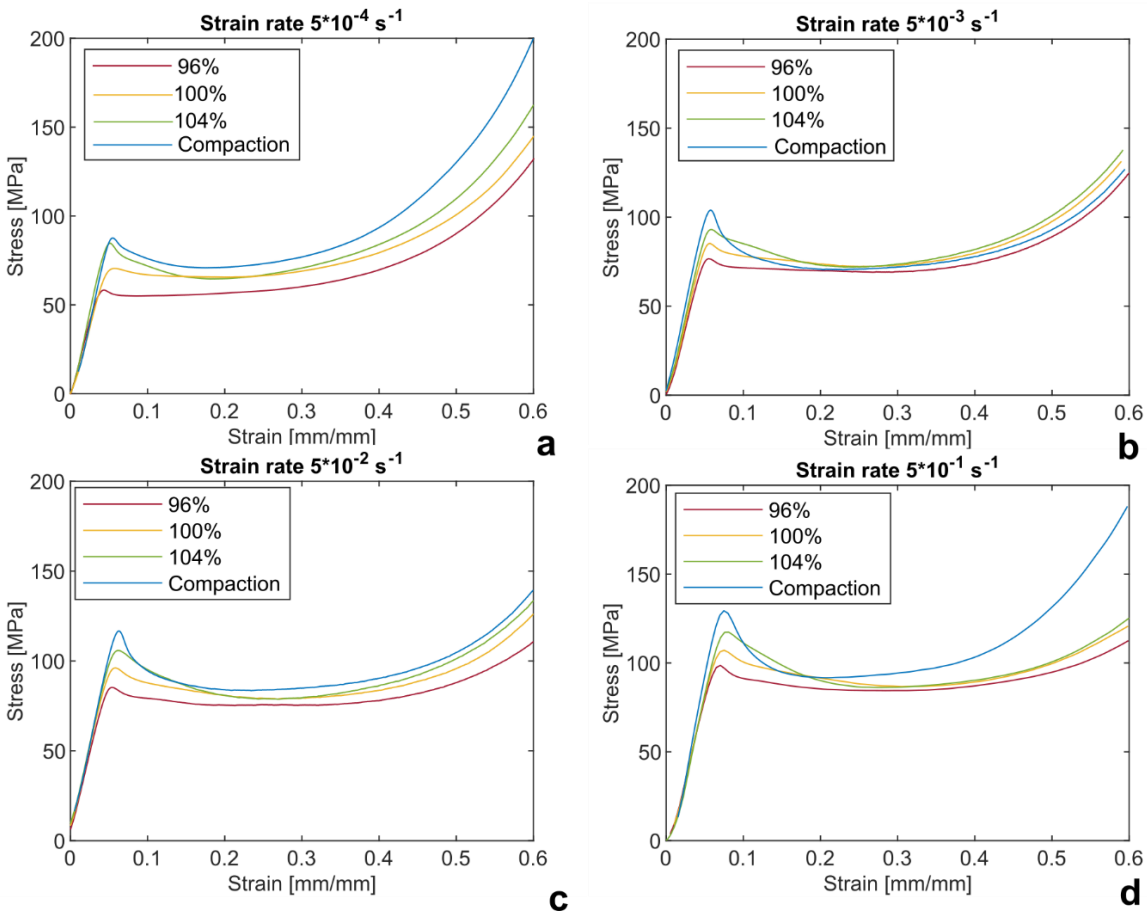



*Fig. 47 – Stress-strain curves recorded during the compression tests of the samples produced under different processing conditions (both strain rate and manufacturing process)*

However, a partial contribution was also provided by the aging of the polymer during compaction. The presence of aging was more evident from the analysis of the post-yielding behavior. Indeed, the strain softening behavior was more marked on the compacted samples as compared to MatExt samples, which were also strongly influenced by the extrusion multiplier. The compacted samples showed a severe strain softening with a stress drop from 117 MPa to 85 MPa after yielding (corresponding to 27%). Strain softening is commonly related to the aging of the polymer. Indeed, the thermomechanical compaction was performed at 120°C. Such temperature is well below the melting temperature of the PLA (almost 175°C). Thus, the steep drop as well as the narrow deformation involving such a drop indicates the occurrence of polymer aging. MatExt samples showed minor strain softening. These samples did not experience artificial aging owing to the thermal cycle of the compaction. Consequently, aging was limited to that developed during the MatExt

process. These samples showed a smoother reduction of the stress after yielding. Besides, the stress drops in these samples diminished by reducing the material multiplier. As an example, for EM=96% the stress reduced from 84 MPa (at yielding) to 77 MPa (corresponding to 8.3%). In these samples (EM=96%), the strain softening was almost imperceptible. However, if the true stress was plotted, the strain softening would be more marked (since the actual cross-sectional area of the sample is often larger than the initial cross-sectional area).

The influence of the process, processing conditions, and strain rate, on the yielding and post-yielding behavior of the samples recorded during the compression tests were further investigated by computing the yield strength, the strain softening drop, and the steady state flow, as reported in Fig. 48.

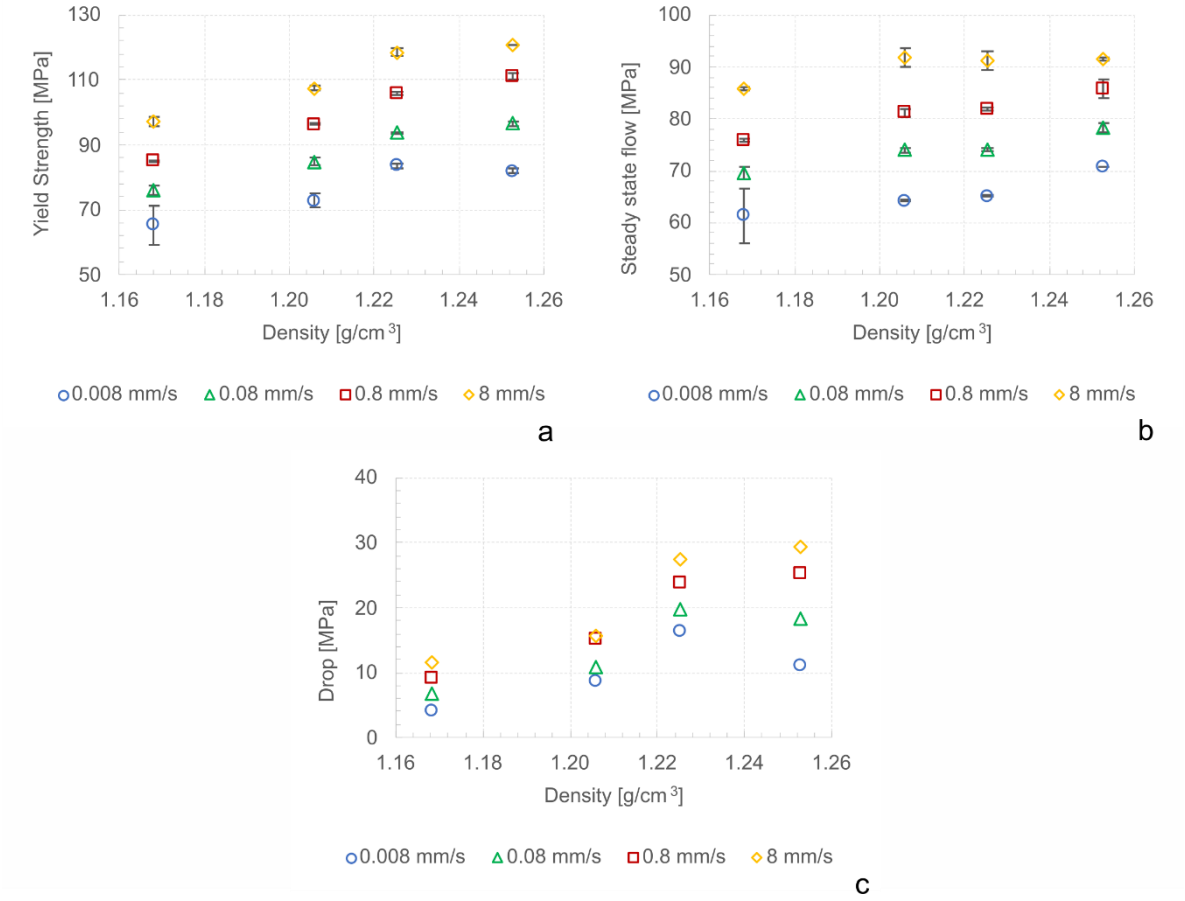



*Fig. 48 – Compressive Yield Strength of the samples*

As can be inferred, the compressive yield strength increased with the Extrusion multiplier. This was due to the higher density of the samples which showed higher load-bearing capability. In addition, even if the samples produced at 104% did not reach the density of

compacted ones, they showed close yield strength values as compared to those measured on compacted samples. Increasing the extrusion multiplier led to an increase in mechanical characteristics. The reduction of the dimensions of the void resulted in yield strength, steady-state flow, and strain hardening. However, the steady-state flow increases less than the yield strength; thus, a higher extrusion multiplier led to higher strain softening (post-yielding stress drop). This phenomenon may be due to a porosity distribution that is similar during deformation, irrespective of the value of the extrusion multiplier. The strain-softening drop in the compacted specimens was more localized, and this was due to the aging phenomenon. Indeed, the compaction process involved slow cooling from the steady compaction temperature (120°C). This also explains why the compacted specimens exhibited higher yield strength and drop at a steady state than the specimens with an extrusion multiplier of 104%, despite having very similar densities. Actually, the compacted specimens underwent thermal cycles at temperatures up to 120 °C.

Higher strain rates involved yield strength and steady-state flow increase. Similarly, the latter showed a lower increase than yield strength. Thus, higher strain rates led to higher strain softening (post-yielding drop) with greater localization of deformation in shear bands. As for strain hardening, this also increases as the strain rate increases. Strain hardening, however, occurs at higher strain values. Increasing the strain rate, therefore, postpones strain hardening. This phenomenon was related to the inversion of curves that occurs after steady-state flow, which leads curves with lower strain rates to grow faster than those with higher strain rates.

An empirical model was developed to describe the influence of the density of the samples and the strain rate. A linear fit model was developed, such as that reported in Fig. 49.

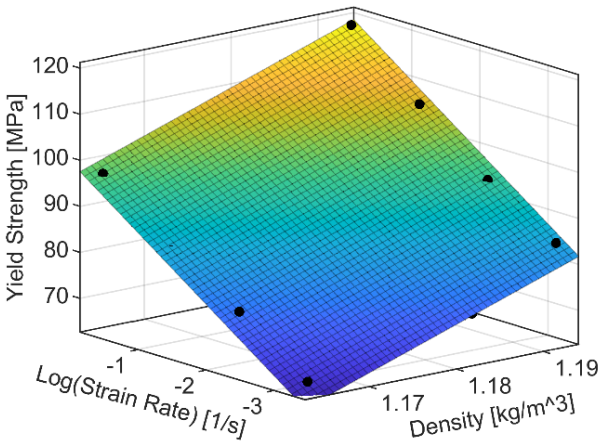



*Fig. 49 – Empirical model developed to describe the influence of the density of the samples and the strain rate*

The developed model, described by eq. 15 (where x represents density and y represents Log(Strain Rate)), showed a good fitting with the experimental data since the coefficient of determination $R^2$ was 0.984 and the adjusted coefficient of determination was 0.9805. Both values were very close to unity, indicating a good fitness of the developed model.

$$\sigma_y = -288.4 + 332.7 \cdot \rho + 11.14 \cdot \mathrm{Log}\,\dot{\varepsilon} \qquad \textit{eq. 15}$$

### 4.1.5 Morphological analysis

The surfaces to be tested during the indentation tests were analyzed for the specimens of the first experimental campaign to understand better possible causes that led to unreliable test results (especially for the smaller indenter). Fig. 50a depicts the 3D surface reconstruction of a sample printed in a vertical direction with the extrusion multiplier set to EM=100%. The deposited filaments can be clearly distinguished on the surface. The average distance between the filaments is 0.2 mm, corresponding to the layer height adopted in the 3D-printing deposition. Fig. 50c depicts a virtual cross-section of the surface which enables to determine better the irregularities of the external surface (that is tested during indentation tests of samples printed vertically). Red dots in Fig. 50c highlight the height of the external filaments. The height of the filaments is comprised between 8 and 30 μm; thus, the surface shows a variation of 22 μm in the surface that is in contact with the indenter. The total roughness $R_t$ value calculated as the difference between the peak surface and the bottom valley is 59 μm. This morphology is consistent with that shown in [185, 186]. The same analysis was performed on the top surface of the samples printed horizontally with an extrusion multiplier EM = 100%, as depicted in Fig. 51. Such surface was even less regular as compared to that observed on the vertical side shown in Fig. 50. Indeed, the maximum peak to valley height of the profile $R_z$ is 110 μm. Such a value corresponds to almost half of the layer thickness.

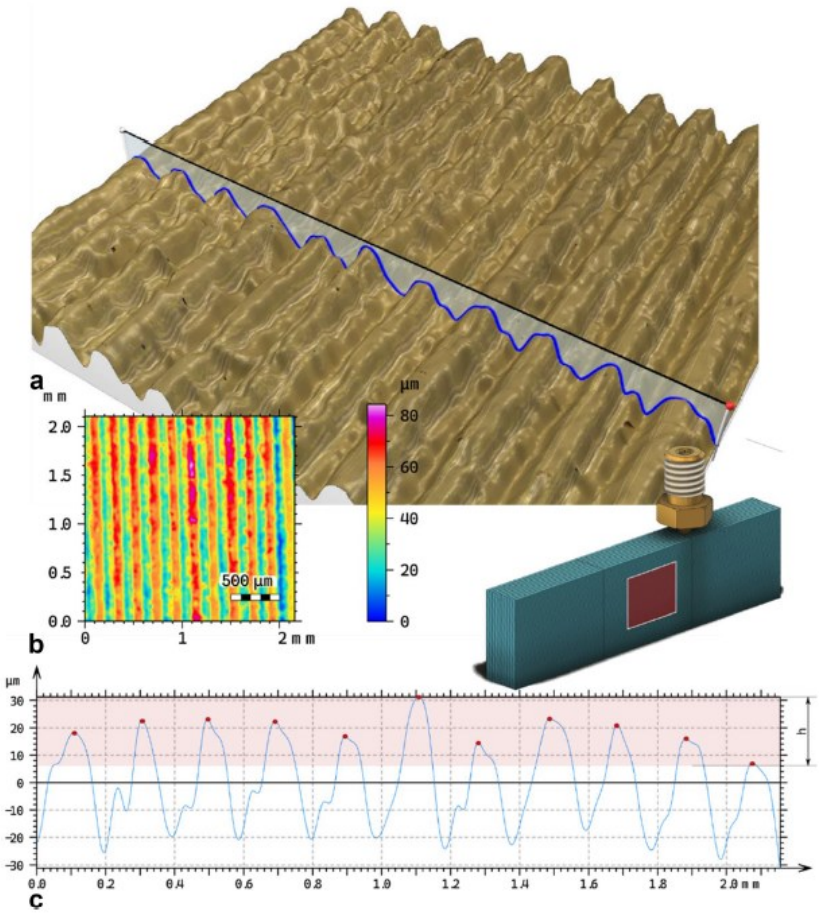



*Fig. 50 – Surface reconstruction of a vertical printed sample (a); topography of the analyzed surface area (b); virtual cross section of the surface (c)*

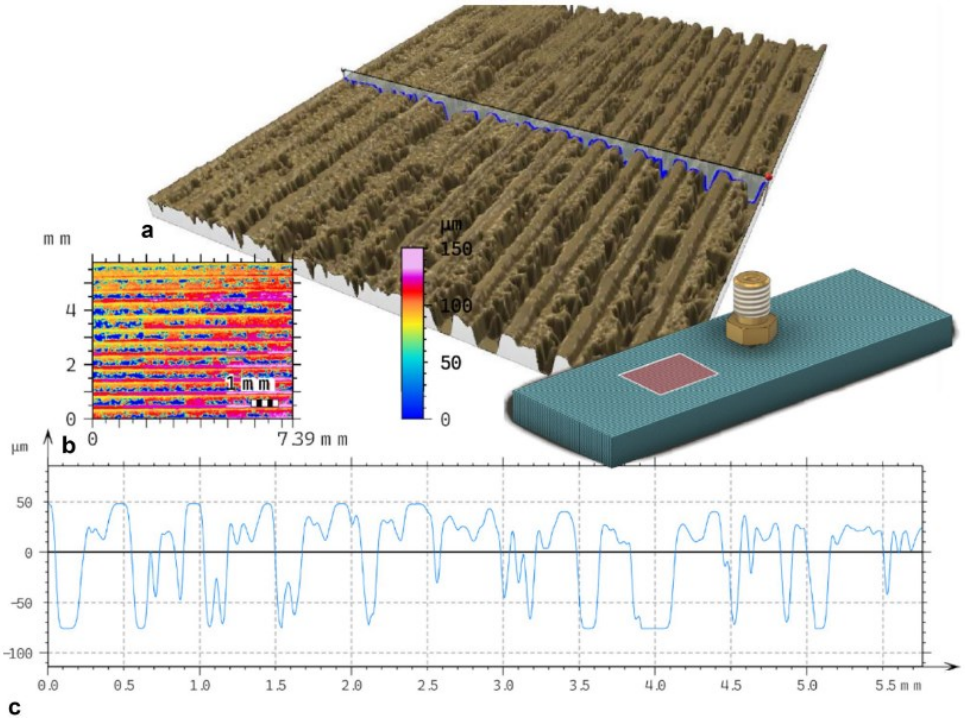



*Fig. 51 – Surface reconstruction of a horizontal printed sample (a); topography of the analyzed surface area (b); virtual cross section of the surface (c)*

Fig. 52 refers to the samples of the second experimental campaign and depicts the upper and bottom surfaces of samples produced with *EM* = 99% and *EM* = 104%. The upper surface of the sample made using *EM* = 99% (depicted in Fig. 52a) shows some unfilled regions in correspondence of the external shells and the internal infill. Adopting the same strategy with a higher extrusion multiplier, *EM*=104% (as shown in Fig. 52b) indicates that the surface is more regular without unfilled regions. Fig. 52 c and d depict the bottom surface of the samples with *EM*=99% and *EM*=104%, respectively. These surfaces were very similar, and no unfilled regions were detected regardless of the adopted extrusion multiplier. To further investigate the differences among the surfaces of the samples produced with different extrusion multipliers and through other EM, morphological analysis was performed through 3D surface reconstruction.

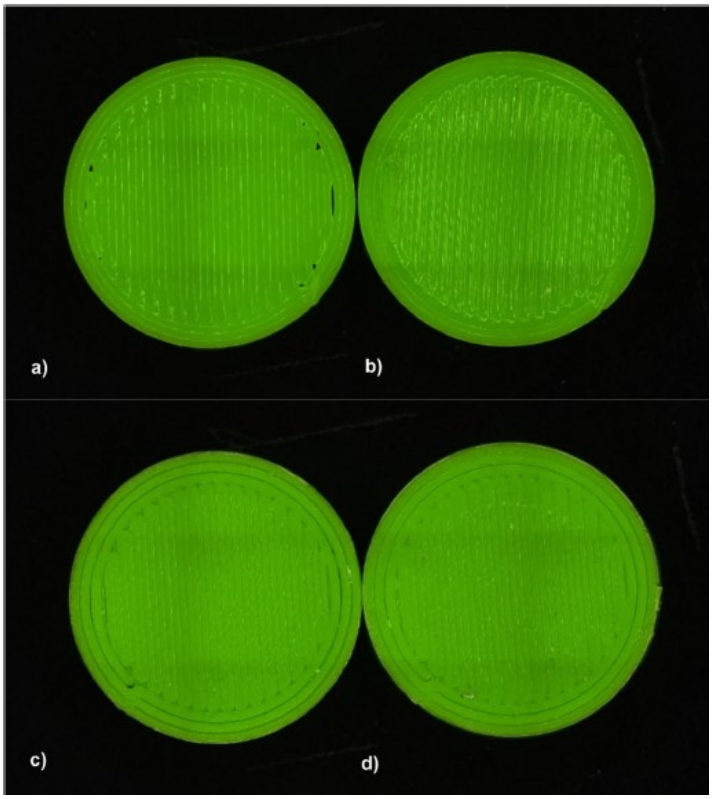



*Fig. 52 – Macrograph of surfaces of sample made with EM=99%: (a) upper; (b) bottom and EM=104%: (a) upper; (b) bottom*

Fig. 53 depicts the 3D maps of the reconstructed surfaces on two samples (*EM* = 99% and *EM* = 104%) on the upper and bottom surfaces (please note that all the maps have the same limits). The upper surface of the sample made with *EM* = 99% shows the presence of peaks and valleys indicative of the deposited direction. Indeed, the virtual cross-section shows a sinusoidal-like profile with an average amplitude of almost 400 μm. On the other hand, the upper surface of the sample made with *EM* = 104% shows a more uniform morphology, as

indicated by the virtual cross-section. These measurements indicate that the adopted extrusion multiplier strongly influences the morphology of the upper surface during the deposition and, consequently, the stiffness of the deposited layer.

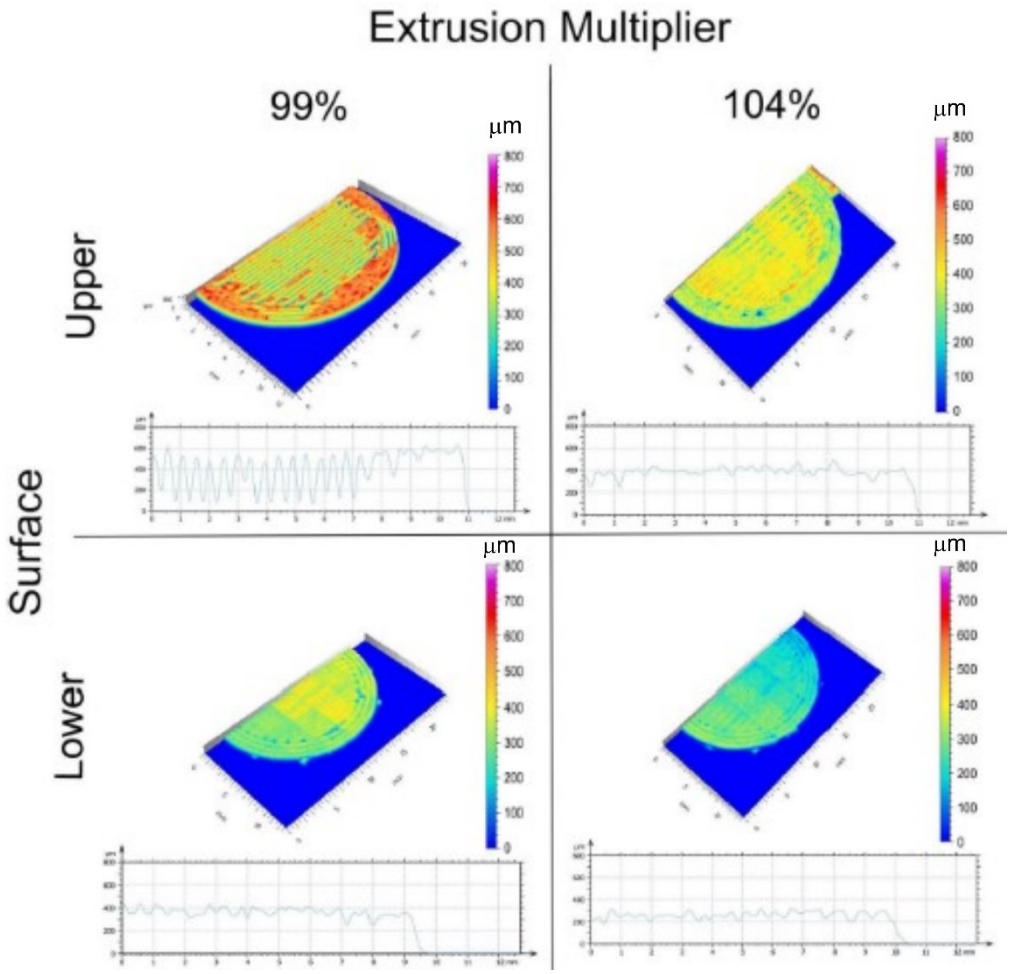



*Fig. 53 – 3D maps of the upper and lower surfaces on samples produced with EM=99% and EM=104%*

Otherwise, comparing the 3D maps of the bottom surface, it emerges that the adopted extrusion multiplier less influences the morphology of these surfaces. The above results indicate that the upper and bottom surfaces show different mechanical behavior owing to the different deposition conditions. Indeed, the bottom surface is produced by extruding material against the building plate; on the other hand, the upper surface is printed over previously deposited layers (which are much softer and can still be under a rubber-like state). During the material extrusion process, the building plate temperature was set at 60 °C. This temperature was above the glass transition temperature of the PLA (55 °C). This enabled the polymer's molecular chains close to the plate to rearrange during the entire printing process, providing a more "compact" chain distribution. On the other hand, the overlying layers' material rapidly cools down after being deposited. These layers do not have sufficient time

to let the polymer chains rearrange in a more compact form. This leads to uneven mechanical properties between the material in contact with the building plate and the overlying materials. The compression test averages such local differences, while the indentation test can discern such local behavior more easily.

## 4.2 Interlayer adhesion

### 4.2.1 Introduction

Most of the works aimed at characterizing the fracture toughness of additively manufactured components involve the testing standards developed for composite materials due to the similarities between their behavior. Among the most common tests there is mode I fracture toughness test; to perform this test, it shall be used a double cantilever beam (DCB) specimen. However, in almost all cases, the required pre-crack was achieved through the insertion of a film to be placed in the midplane for the produced specimen's production [187-192]. The film weakly adheres to the substrate and enables further deposition of the next layers. This methodology involved the deposition interruption to place the film, which also requires meticulous handling. Consequently, the release film may introduce some issues: indeed, the deposition process is paused and a longer time elapses before proceeding to the next layer of deposition. This involves a higher cooling of the substrate when depositing the next layer. Thus, the substrate undergoes higher cooling down compared to the normal deposition conditions. This leads to a thermal cycle alteration that may cause possible deviation in the interlayer mechanical properties [193]. In fact, the deposition temperature appears to be among the parameters that strongly influence the fracture toughness behavior of additively manufactured parts [194, 195]. In addition, the whole process requires the presence of an operator for placing the release film, a procedure that is susceptible to human errors and is more complicated in the case of high-temperature polymers. The aim of the first experimental campaign illustrated below is to overcome the above limitations by developing a new specimen, based on the well-established ones, that does not require the manual insertion of the release agent to produce the pre-crack. To this end, a new kind of sample that embeds the "3D printed" nested spacers is proposed. Double cantilever beam (DCB) specimens were produced and tested to capture the fracture toughness behavior for characterizing the material under mode I opening. This also enabled the comparison of the outcome of the testing campaign between the two kinds of samples. The comparison involved the critical energy release rate in mode I crack opening, the crack opening characteristics, the crack propagation path, and the phenomena that occurred while in testing. In addition, InfraRed (IR) Analysis was performed during the sample fabrication to capture possible differences in the thermal history caused by the insertion of the release film.

Although previous studies have contributed to understanding the micromechanics involved during interlayer adhesion, these studies were mainly focused on the fracture analysis. In some cases, a few studies investigated the thermal history during the deposition. This strongly influences the interlayer adhesion since it directly impacts the polymeric chain mobility. On the other hand, the interlayer adhesion is also strongly influenced by the formation (or pre-existence) of a crystalline phase that may hinder the mobility of the polymeric chains, and consequently, it could affect the interlayer adhesion. During the material extrusion process, the formation of interlayer bonding is achieved through molecular interdiffusion between the material being extruded and the underlying layer. However, different phenomena concur during deposition that makes extremely complex the understanding of the influence of the process parameters on the mechanical behavior. Indeed, the adoption of filaments with high crystalline percentage and process conditions involving high material flow may lead to incomplete melting of the crystalline phase [196, 197]. This could influence negatively interlayer adhesion. Similarly, deposition conditions have a direct influence on thermal history, which in turn influences the intermolecular entanglement between overlaying layers. A more comprehensive understanding of these interrelated phenomena occurring during the material extrusion process requires a broader and interdisciplinary analysis of the process as well as the components made by material extrusion. The second experimental campaign tries to fill this gap by using a multidisciplinary approach involving different methodologies. Particularly, the aim is to determine the influence of the deposition strategy, the deposition speed, and the material flow on the interlayer adhesion behavior. PLA was selected as a model material to limit the effect of warpage (more in general, part deformation) and analyze with a multidisciplinary approach the effect of printing conditions to the adhesion. First, experimental tests were conducted by recording thermal imaging through an IR thermal camera to monitor the temperature evolution during the deposition process. This enabled to better investigate the influence of the adopted process parameters on the thermal history. Additionally, extensive physical and chemical characterization were performed to investigate the influence of the involved processing parameters on the interlayer adhesion. Finally, optical and scanning electron microscopy (SEM) were involved to better analyze the fracture surface.

### 4.2.2 Materials and methods

The specimen considered for fracture toughness characterization was the classic DCB, whose geometry was designed according to the ASTM D5528 standard [198]. Considering

the prismatic double cantilever beam specimen of the corresponding standard, the filaments were aligned toward the length of the specimen as depicted in Fig. 54.

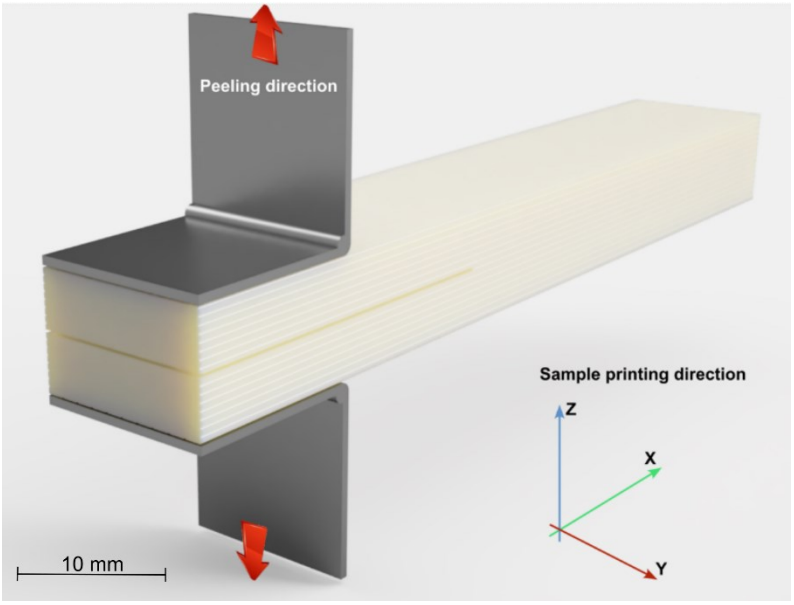



*Fig. 54 – Relative dimension between filaments and applied load*

The geometrical characteristics of the samples (e.g., the overall thickness, the distance between the midplane of each of the two substrates and the piano hinges as well as the pre-crack length) represent a key element for test suitability. These characteristics were defined, according to the corresponding standard as depicts in eq. 16:

$$t \leq \frac{h}{4} + 0.01\sqrt{\frac{0.0434h^3 + E_{11}}{G_{Ic}} + a^2} \qquad \textit{eq. 16}$$

Where $t$ refers to the distance between the loading block and the midplane of the first half of the specimen, $h$ is the specimen overall thickness, $E_{11}$ the elastic module in direction parallel to the filaments, $G_{Ic}$ the expected critical energy release rate and $\alpha$ the pre-crack length. The minimum overall thickness was determined through eq. 17 :

$$h \geq 8.28\sqrt[3]{\frac{G_{Ic}a_0^2}{E_{11}}} \qquad \textit{eq. 17}$$

while the pre-crack length is defined as follows in eq. 18:

$$\alpha_0 \leq 0{,}042\sqrt{\frac{h^3 E_{11}}{G_{Ic}}} \qquad \textit{eq. 18}$$

For the determination of the longitudinal Young modulus $E_{11}$ of the PLA of the same filaments, tensile tests were conducted according to ASTM D638 standards in ambient conditions and 1 mm/min crosshead speed using the MTS Criterion 43.50 testing machine. The measured modulus $E_{11}$ was 2.8, GPa with a relatively small standard deviation of ±X, a value that agrees with those reported in in past works where varies from 1.3 GPa [199] up to 3.3 GPa [189]. For the same material, the critical energy release rate, as seen in past works, varies from 0.8 [187] up to 3 kJ/m$^2$ [189]. Therefore, the minimum overall thickness, also depending on the abovementioned parameters and the crack length, was defined between 4.5 to 7.5 mm. Thus, the characteristic dimensions of the samples were defined considering the mechanical behavior of the Polylactic Acid (PLA) and the compliance with the suggestions of the corresponding testing standard [194] as reported in Fig 55. In this kind of test, the delamination grows from a pre-determined release film that is imposed as an initial pre-crack in the thickness midplane. In the case of composite materials, the corresponding standard [194] suggests the use of a very thin release agent with a thickness between 7 to 25 μm. To this end, some authors proposed the adoption of thin Polyimide films applied with the aid of an external support, as shown in Fig. 55 [188, 192]. The same approach was adopted in the present work for the specimens with release film, starting with the production of the specimen and the supporting jig for the Polyimide tape contemporaneously until the extruder reached the thickness midplane (Fig. 55a). Consecutively, a thin Polyimide tape was applied manually (Fig. 55b) and, after the meticulous inspection for absence of wrinkles in the region of the insert, the other half of the specimen was printed (Fig. 55c).

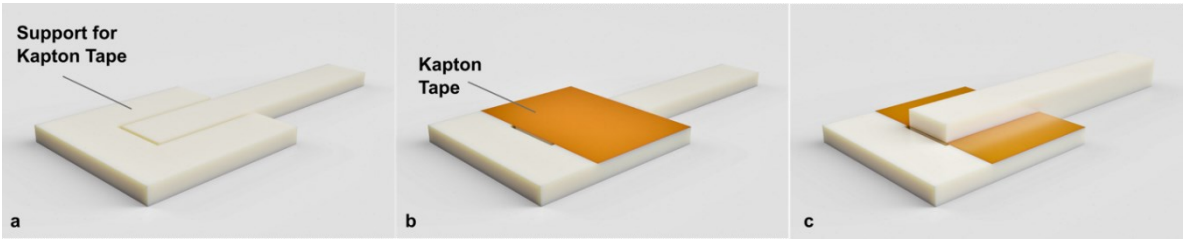



*Fig. 55 – Various steps of the execution of the printing process of the DCB specimens including the supporting U-shape (a), the placement of the Polyimide tape (b) and the finalization of the specimen (c)*

This approach would involve tremendously higher difficulties if applied for high temperature polymers printed within highly heated chambers. In addition, human induced errors would cause lower sample standardization. Thus, a new sample type was designed in the first experimental campaign of test [171] with the aim of avoiding any printing interruption and eliminating the possible variability induced by human interference. This involved a pre-

crack, of the same initial length as the one with the release film, created by a slot with a thickness of two layers of filaments, as seen in Fig. 56.

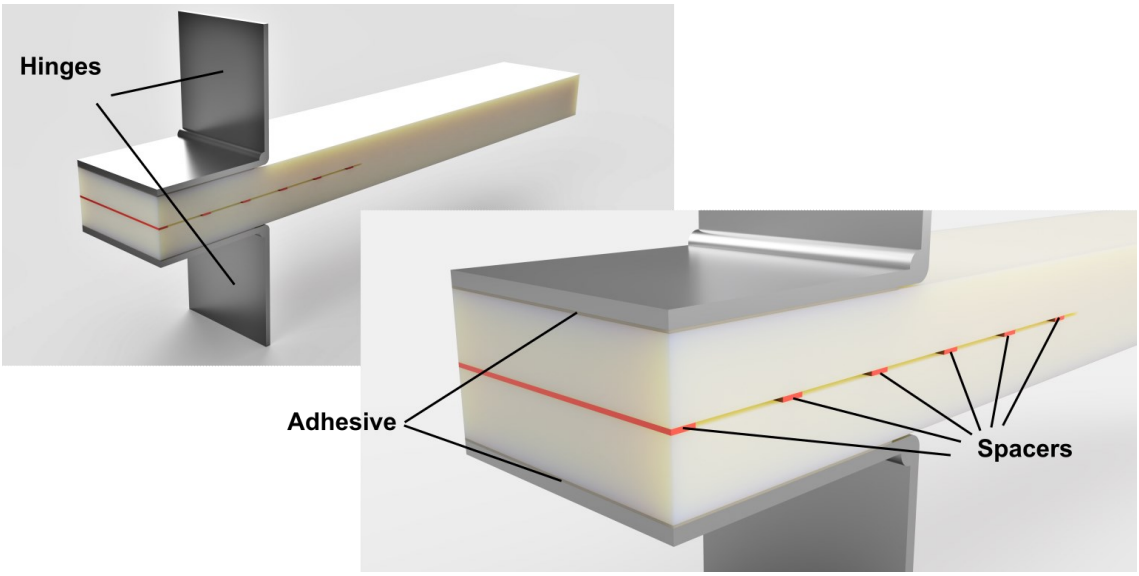



*Fig. 56 – Schematic of the sample produced by printed spacers without the release film*

The main difference between the proposed specimen and the DCB-based one seen in past works [199] is that the present one considers the advantages of the standardized DCB specimen, following the same principles regarding the overall dimensions, and a much thinner pre-crack. A critical aspect is feasibility, from the manufacturing point of view. The nested spacers serve to enhance the printing process of the specimen by maintaining the proper distance (and thus the thickness of the pre-crack) stable. Therefore, the presence of these supporting spacers contributes to the feasibility of the samples' printing. In addition, these nested spacers that are 3D printed as well as the rest of the specimen, are placed in a way to ensure the correct and stable pre-crack thickness and to avoid any adhesion between the two distinguished parts of the DCB specimen. Therefore, the nested spacers are designed also taking into consideration the feasibility of the printing process when such a small detail is required. They consist of 6 individual 3D printed columns, as seen in Fig. 56, in a finite distance between them to avoid any contact between the upper and lower part of the pre-crack region of the specimen while they are easy to remove manually before the testing procedure. Before the execution of the tests, the spacers were removed. The bending stiffness of the sample is dramatically affected by the overall specimen thickness. Apart from the definition of the minimum requirements based on the equations provided by the testing standard, a strong suggestion is the avoidance of significant bending deflections during the test. This is aimed at preventing flexure-induced failures or interference to the overall applied

load, correcting the geometrical characteristics of the specimen accordingly. Here two overall thicknesses (both complying with the requirements indicated by the testing standard) were considered. Consequently, the specimen types considered in the first and the second [172] experimental campaigns and the corresponding dimensions are reported in Table 9 and Fig. 57.

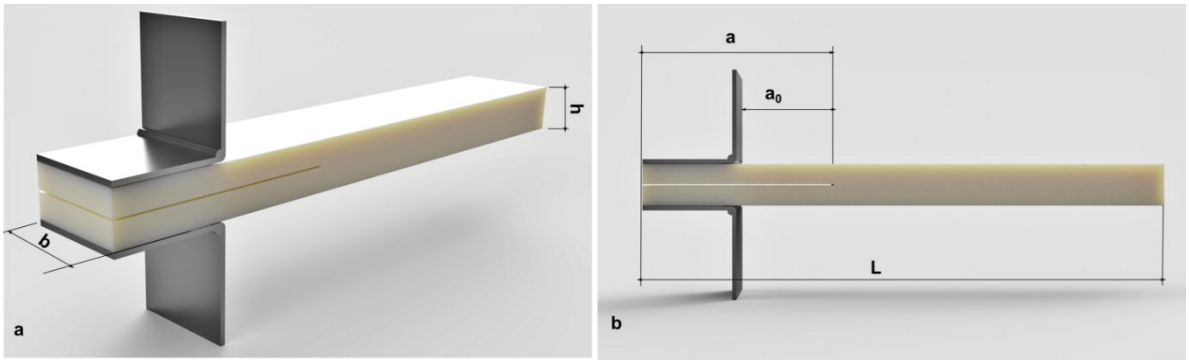



*Fig. 57 – Main dimensions of the samples used in the experimentations*

*Table 9 – Characteristic dimensions of the specimens used for ASTM D5528 tests*

| *Geometrical characteristics* | *Dimension (mm)* |
|---|---|
| *Length (L)* | 125 |
| *Width (b)* | 25 |
| *Pre-crack length (α)* | 55 |
| *Initial distance of the crack tip from the load axis ($\alpha_0$)* | 30 |

All the specimens were fabricated with Fabbrix PLA filaments (with diameter 1.75 ± 0.05 mm) using a commercial FFF machine model Ender-6 by Creality. This machine can be interfaced with the slicer Simplify 3D, which permits to set various parameters of the deposition characteristics and the architecture. The deposition conditions were as follows: the extruder temperature was set to 210 ◦C, while the bottom plate at 60 ◦C to avoid eventual distortions to the specimens and better adhesion to the building plate. Each filaments' layer thickness was set to 0.2 mm corresponding to 50% of the nozzle diameter (d = 0.4 mm). All the specimens were made to have the load line perpendicular to the printing plane. A rectilinear infill pattern aligned towards the X-axis of the FFF machine was adopted for the deposition strategy, i.e., with the filaments of each individual layer oriented according to the long side of the specimen. Specimens of the first experimental were printed with a deposition rate of 4000 mm/min and with extrusion multiplier set at 100%.

Specimens of the first experimental campaign [171] were produced by following the characteristics related to the deposition process listed in Table 10. Any external shell was adopted during the specimen fabrication to produce a homogeneous sample. A critical difference between the specimen types is the pause that was imposed in those incorporating a release film (Polyimide tape) compared to those with slot and removable spacers, as previously indicated in Table 10. In fact, the pause is necessary for applying the release film, interrupting the normal course of the 3D printing process.

*Table 10 – Characteristics of the four specimens produced by material extrusion process*

| *Specimen Type* | *Pre-Crack* | *Specimen thickness (h) (mm)* | *Pause During Printing* |
|---|---|---|---|
| *Polyamide/h=8* | Polyamide Film | 8 mm | Variable from 1 to 2 minutes |
| *Polyamide/h=16* | Polyamide Film | 16 mm | Variable from 1 to 2 minutes |
| *Spacers/h=8* | Spacers | 8 mm | - |
| *Spacers/h=16* | Spacers | 16 mm | - |

Specimens related to the second experimental campaign [172], on the other hand, were produced considering two distinct deposition strategies, resulting in the creation of two types of specimens:

1. 0/90° specimens: These specimens feature a raster angle of 0° in one consecutive layer and 90° in the subsequent layer, as depicted in Fig. 58a.
2. ±45° specimens: These specimens employ a deposition strategy with a±45° raster angle between consecutive layers, as shown in Fig. 58b.

The adoption of these two deposition strategies facilitates a comprehensive exploration of the influence of raster angle on specimen fracture toughness. This investigation aims to elucidate how different orientations affect mechanical behavior. Table 11 provides a summary of the test matrix detailing the variations in three key parameters throughout the MatEx process. For each test condition, four samples were manufactured, resulting in a total of 72 printed specimens.

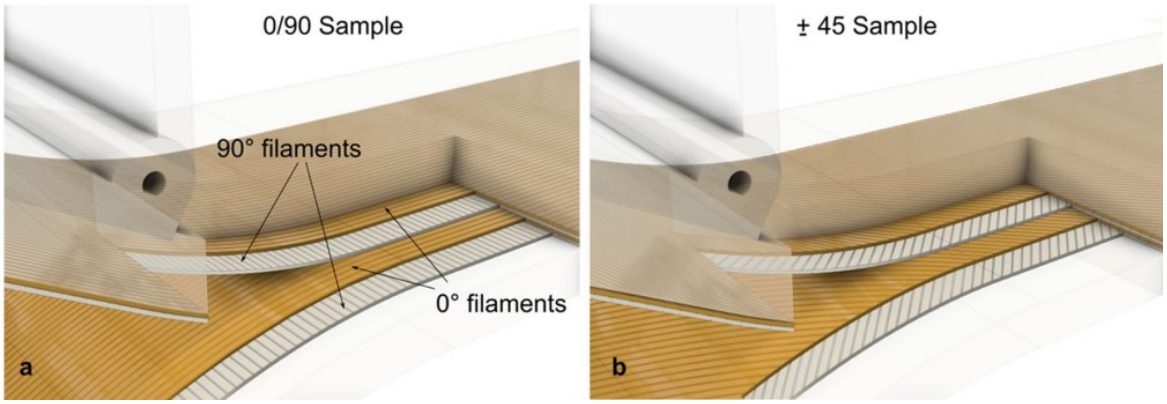



*Fig. 58 – Relative direction between deposited filaments and applied load and different types of specimens printed via the MatEx process: (a) cross-ply specimen (following layers oriented at 0/90°) and (b) angle-ply specimen (following layers oriented at±45°)*

*Table 11 – Test matrix with factors and assumed levels*

| *Level* | *Deposition strategy* | *Extrusion multiplier (%)* | *Deposition speed (mm/min)* |
|---|---|---|---|
| *I* | ±45° | 96 | 1000 |
| *II* | 0°/90° | 100 | 2000 |
| *III* | | 104 | 4000 |

### 4.2.3 Specimens preparation and mechanical test

A pair of steel piano hinges was bonded at the crack region of each of the specimens, as seen in Fig. 54, for applying the load required for opening the crack. The load line must be perpendicular to the surfaces of the specimens, promoting the transverse opening of the crack. To ensure this load condition, the two steel piano hinges were bonded to each specimen, following the protocol below:

1. Apply a neutralizing cleaning spray (WEICON cleaner) to improve the quality of the adhesion between the specimen surface and the hinges. This product is necessary to remove all the contaminant elements, like powder on both the surfaces of the specimen and the hinges.

2. White paint was applied to the specimen's side surface. Tick marks were marked every 5 mm each of them, starting from the crack tip (signed with 0) to determine the position of the crack front during the test were signed on this surface. In the first 5 mm starting from

sign 0, the marks were drawn 1 mm apart. This is crucial in the first part of the test as it will be explained in detail afterwards.

3. Subsequently, on the specimen's surfaces, at the hinge application area, the Primer WEICON P400 chloric is applied to prepare these surfaces before the application of glue.

4. A two-component toughened methacrylate adhesive system AralditeÆ 2022–1 was applied to both the surfaces in the hinge area through a constant dosage pistol with a mixing nozzle. This area is limited by the width of the specimens and a distance from the specimen's border (where the crack starts) of 30 mm. This adhesive is supplied by Huntsman Corporation (TX, USA).

5. To provide a correct adhesion between the hinges and the specimen, it was necessary to wait at least 24 h after the bonding at normal ambient condition of temperature as stated in the DIN EN 1465 standard [200].

The mechanical testing was executed using an MTS Universal Testing Machine, model C43.50, equipped with a 50 kN applied force capacity. For all the samples produced, great care during the first phase conforming to the requirements of the ASTM D5528 standards was taken. During this phase, the crack propagation was controlled by imposing a very slow traverse speed (1 mm/min), which aligns with the lowest velocity recommended by the corresponding standard. This permits to keep low the bias introduced in this phase while being within the limits prescribed by the test standard. To monitor the fracture tip, a Dino-Lite AM2111 travelling optical microscope with ×200 magnification, mounted on a movable base mechanism, was employed, as shown in Fig. 59.

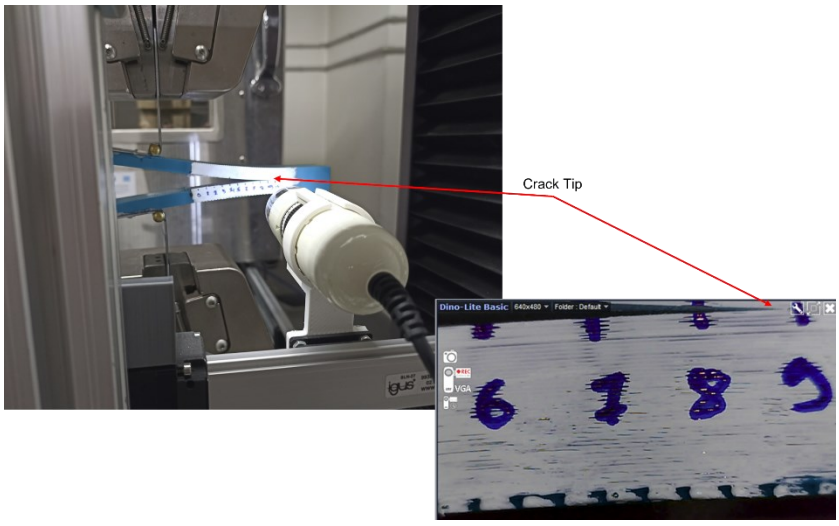



*Fig. 59 – Picture of the sample during DCB test with the equipment required*

The prescribed standard recommends splitting this mechanical test into two distinct phases. Specifically, the test was halted when the crack opening development, as recorded by the optical microscope, reached a value between 3 and 5 mm. As mentioned in the second step of the specimen setup, the distance between two consecutive marks in the initial 5 mm from the crack tip is 1 mm. Consequently, the specimen was completely unloaded at a crosshead speed of 8 mm/min. The objective of the first phase is to initiate the crack front and precisely determine the crack position. Additionally, it facilitates the elimination of any potential geometric imperfections introduced by the MatEx process. In the second phase, the test was resumed at a constant crosshead displacement speed of 1 mm/min. Throughout this stage, the load applied by the machine on the specimen was recorded alongside the corresponding value of the crosshead displacement and the crack tip position. These three values were logged each time a crack front progression of 5 mm was observed through the optical microscope. The critical energy release rate was determined using the VIS point technique. This method relies on visually identifying the initial crack motion through the microscope. Fig. 60a illustrates two typical load-crosshead displacement diagrams for the two deposition strategies. The transparent plot represents the first part of the test, while the sharper one corresponds to the crack propagation resulting from the movement of the mobile crosshead displacement. All the point-markers depicted on the propagation diagram signify a 5 mm increase in the crack length. The parameter Δ, depicted in Fig. 60b, represents the intercept of the linear regression curve between the cube root of C and the crack length that is the factor for calculating the critical energy release rate.

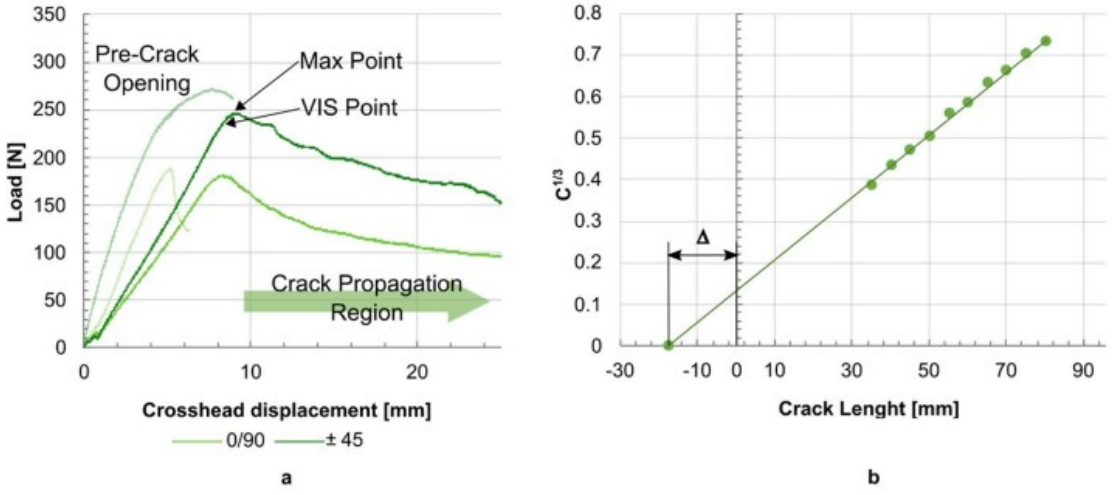



*Fig. 60 – Identification of the change in compliance starting from the load-crosshead displacement curve (a) and definition of the Δ factor for calculating the critical energy release rate (b)*

Thermal analysis was conducted using the infrared (IR) camera model E60 By Flir to investigate the thermal history during the deposition. The IR camera was strategically positioned along the elongated side of the sample, capturing the entire deposition process. Securely fixed to the frame of the 3D printer, the camera maintained its position as the hot-end moved horizontally, while the sample progressed vertically, offering a comprehensive view of the deposition process. A low acquisition frequency was adopted (1Hz); subsequently, the thermal history was analyzed through the software ResearchIR provided by Flir. Moreover, a post testing optical analysis was performed on the fractured surface to better investigate the morphology of the crack opening sides after the failure. In this context, a digital stereoscope model M205 by LEICA was adopted. The stereoscope was equipped with XYZ motorized axis and the software LEICA map that also enabled surface reconstruction over a wide observation window.

The applied Load-Crosshead displacement curves for each type of specimen of the first experimental campaign are reported in Fig. 61.

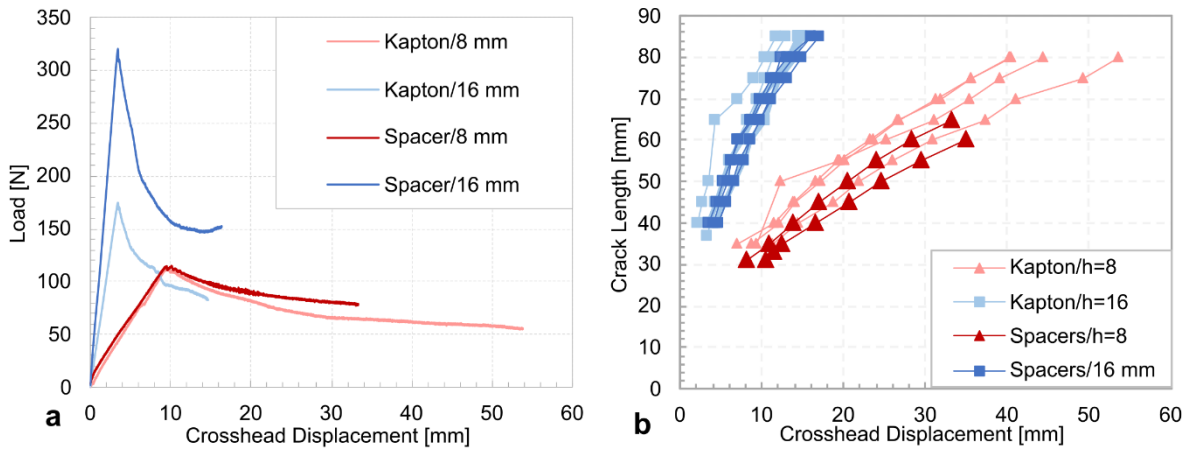



*Fig. 61 – The Load-Crosshead Displacement curves of representative specimens of each category (a) and the Crack Length-Crosshead Displacement ratio obtained by the experimental campaign (b)*

A good agreement between the specimen with release film and with spacers can be noticed for the case of the total thickness of 8 mm in terms of load-crosshead displacement. On the other hand, the difference between the specimens with release film and those with spacers can be observed for specimens with total thickness of 16 mm. Similar results between the specimens of 8 mm of thickness made with the release film and the spacer were observed in terms of crack length-crosshead displacement. However, the specimens of 16 mm, either those with release film or with spacers, appear to derive almost identical results in terms of machine crosshead displacement for opening the defined crack. In addition, a more stable

behavior was observed in terms of progressiveness of the crack growth with the increase of the applied machine crosshead displacement.

The average values of the critical energy release rate in both cases are reported in Fig. 62 along with the corresponding standard deviation. The corresponding values are consistent with those observed in similar works and materials of interest [187-189, 191].

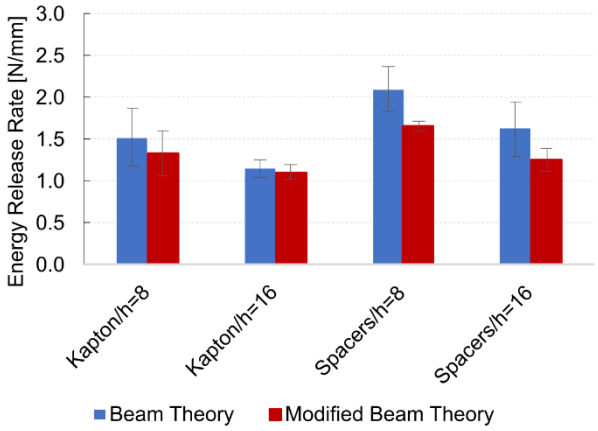



*Fig. 62 – The average critical energy release rate calculated with the beam and modified beam theory*

From the values obtained, it should be noted the lower difference between the $G_{IC}$ obtained with the beam and modified beam theory when the specimen thickness increased. In addition to that, there can be seen a difference between the specimens with release film and those with the slot pre-crack that is less evident when the critical energy release rate is calculated using the modified beam theory method. In Fig. 63 the R-curves of all the conducted tests are reported and are sorted into 2 groups, namely the samples with release film and those with slot and spacers.

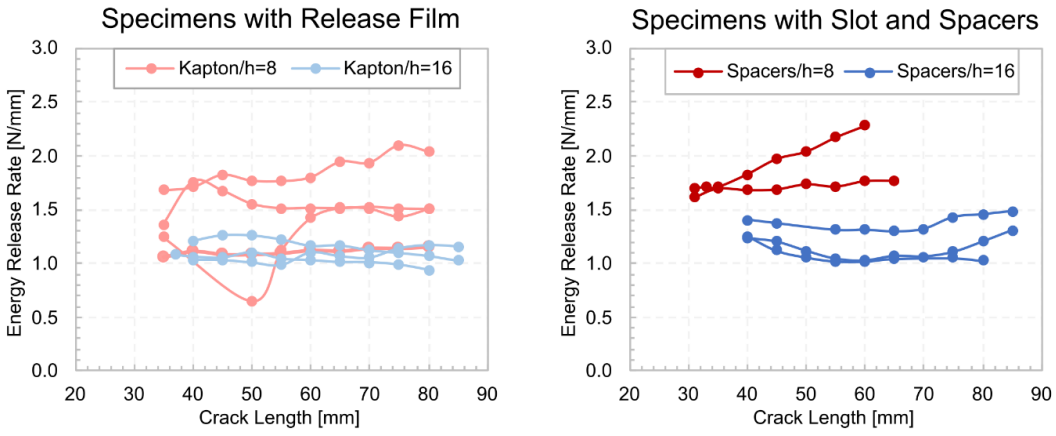



*Fig. 63 – The R-curves for the specimens of the mode I fracture toughness tests*

It can be observed that the difference between specimens with spacers and release film is lower while the overall thickness h increases. In fact, the specimen thickness appears to be a parameter that affects the results significantly. Indeed, specimens with 16 mm of thickness, presumably due to the higher bending stiffness, are less susceptible to bending deflections and provide more accurate measurements. In the same context, the energy release rate related to the crack propagation is lower compared to the critical one. This is consistent with previous works in the field of composite materials [199], only in the case where the specimen is less affected by bending deflections.

Regarding the second experimental campaign, Fig. 64 shows the load-crosshead displacement curves obtained from the mode I tests conducted on samples produced under different processing conditions.

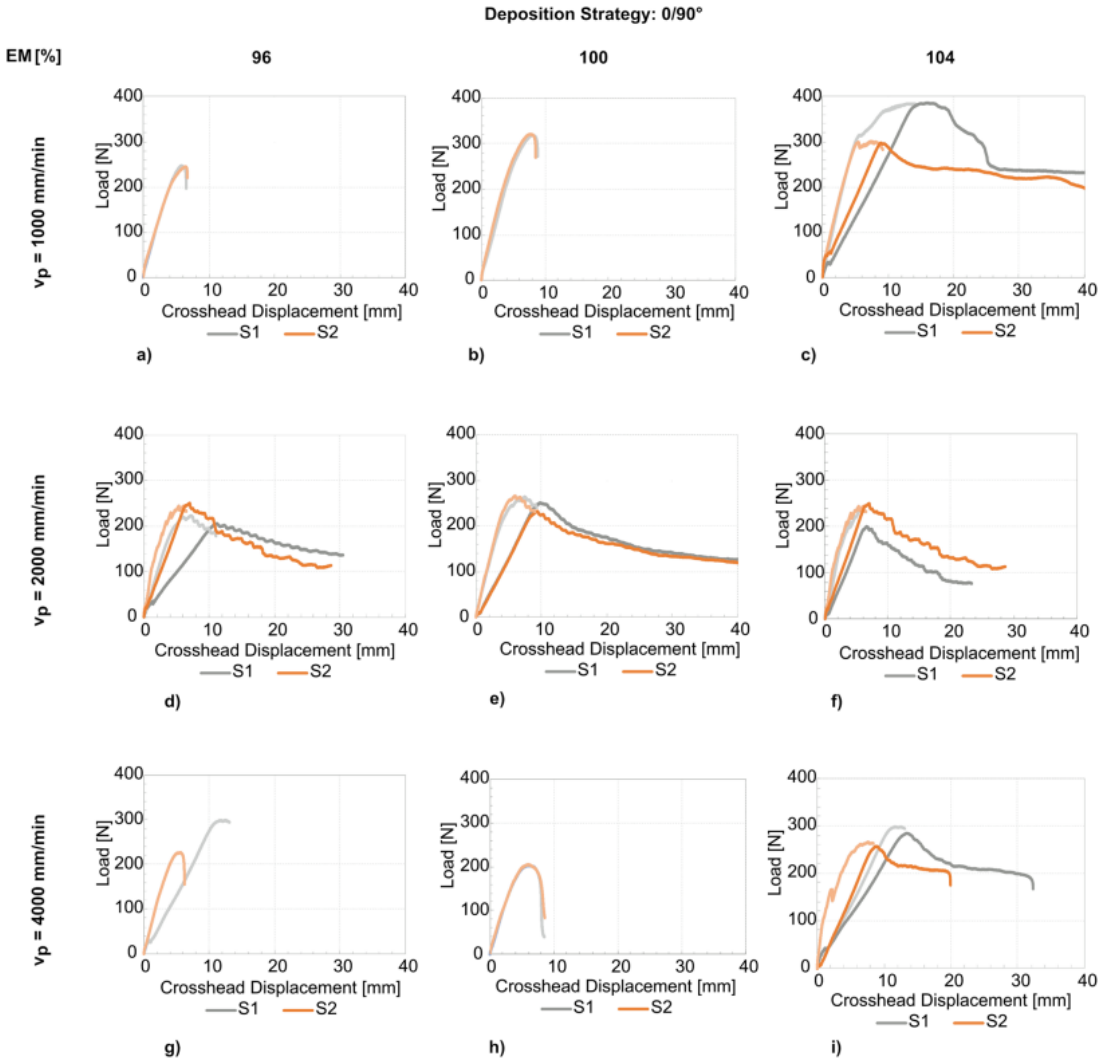



*Fig. 64 – Load-crosshead displacement charts obtained from the 0–90 specimens tested related to the test matrix, with several extrusion multipliers (EM). The transparent curves represent the initial crack opening, while the sharper curves correspond to the stable propagation phase. For each testing condition, just two curves S1 and S2 were reported*

The curves demonstrate two distinct behaviors primarily distinguished by the presence or absence of the crack propagation path. Only certain samples created with the 0/90° strategy lacked propagation, indicating poor interlayer adhesion and fracture toughness. Consequently, these samples exhibited null fracture toughness as the crack immediately propagated during the preliminary phase of the tests. Specifically, all samples created with the extrusion multiplier set to 104% showed the crack propagation path, irrespective of the deposition speed used. In contrast, under the lower extrusion multiplier conditions (i.e., EM =96% and EM =100%), the sole deposition speed that led to crack propagation was 2000 mm/min, while under the other conditions (1000 mm/min and 4000 mm/min), a brittle fracture behavior was observed. Conversely, all samples produced with the ±45° strategy exhibited a crack propagation path, highlighting the significant sensitivity of fracture toughness to the loading path, as depicted in Fig. 65.

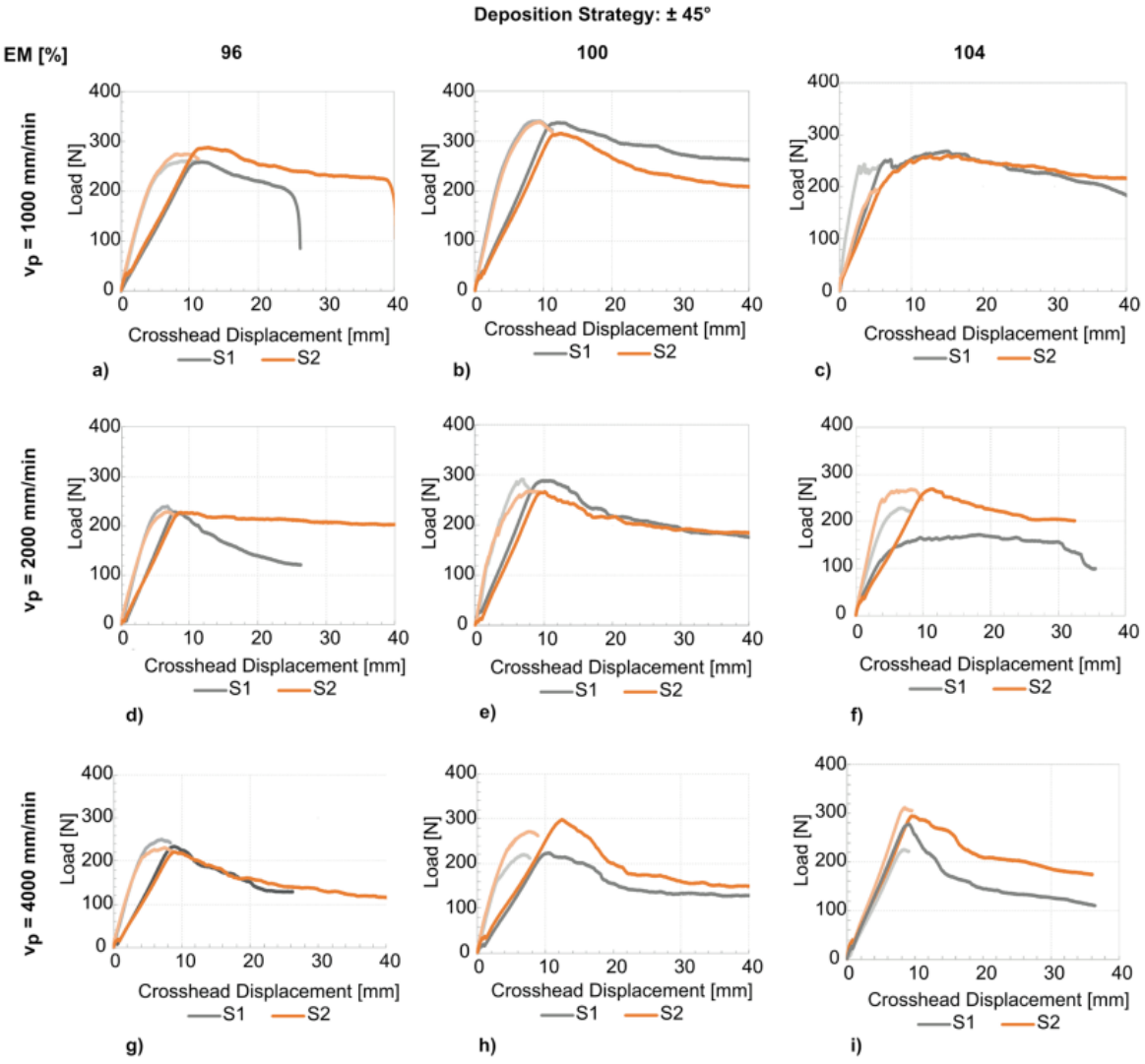



*Fig. 65 – Load-crosshead displacement charts obtained from the±45° specimens tested related to the test matrix. The transparent curves represent the initial crack opening, while the sharper curves correspond to the stable propagation phase*

Notably, the 0/90° samples revealed a substantial increase in fracture toughness with an increase in the extrusion multiplier from 96 to 104%. Additionally, the deposition speed significantly influenced the crack propagation behavior. Specifically, for EM =96% and EM = 100%, the adoption of the lowest (1000 mm/ min) and the highest (4000 mm/min) deposition speeds resulted in no fracture propagation. However, under the intermediate deposition speed (2000 mm/min), the crack propagation path was observed, regardless of the extrusion multiplier used. In the load-crosshead displacement curves of samples manufactured using the 0/90° strategy with a deposition speed of 2000 mm/min, an intriguing observation surfaced. Particularly, when the extrusion multipliers were set to lower values (EM =96% and EM =100%), the crack propagation path exhibited a distinct stepped decay pattern, depicted in the magnified illustration. This abrupt drop tended to diminish in samples printed with an EM of 104%, where the crack propagation displayed a smoother, more continuous decline. This behavior was attributed to the structural characteristics of the samples and the filament arrangement concerning the loading path. Samples created with lower extrusion multipliers demonstrated wider gaps between consecutive filaments, leading to a load drop as the crack traversed a filament perpendicular to the load (90° filaments), as can be noted in Fig. 66.

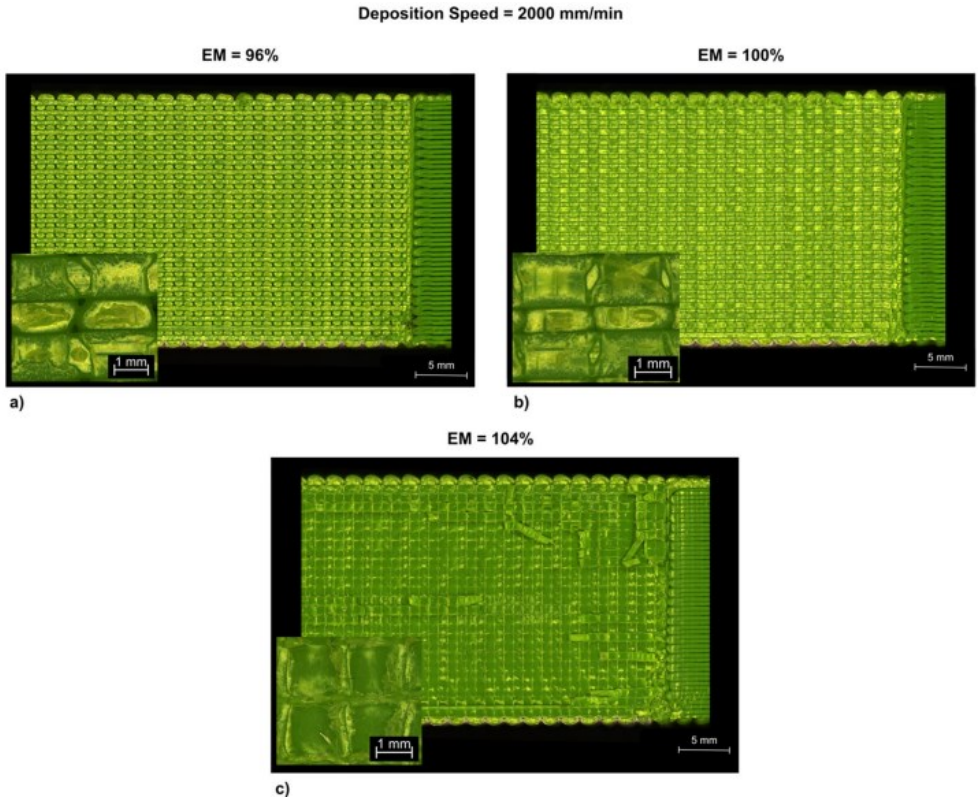



*Fig. 66 – Fracture surface of specimens produced with varying the extrusion multiplier (a) EM=96%, (b) EM=100%, and (c) EM=104%*

Conversely, an increase in the extrusion multiplier resulted in narrower gaps between filaments, fostering a more consistent load decay. Conversely, in the samples produced with the±45° strategy, the stepped pattern was consistently absent. Regardless of the deposition conditions, the crack opening exhibited a continuous decay in load. Indeed, in samples created with the±45° strategy, no filament was perpendicular to the crack propagation direction, enabling a more uniform load distribution along the filaments and preventing the stepped decay observed in the 0/90° samples.

Notably, the 0/90° specimens exhibited brittle behavior during the initial crack propagation in multiple samples, with some displaying out-of-plane crack propagation relative to the nominal direction introduced during the MatEx process. Consequently, this led to the inability to compute $G_{IC}$ and subsequent test failure in certain cases, as depicted in Fig. 67. In contrast, the ±45° deposition strategy induced increased plasticity during the initial crack displacement, likely owing to the path orientation between consecutive layers. Another key difference between the two specimen types is apparent in the crack propagation region depicted on the load-crosshead displacement charts in Fig. 64 and Fig. 65. As reported in [201], the ±45° samples exhibited a consistent release of fracture energy during the propagation phase, while the 0/90° samples showed load drops associated with crack propagation through consecutive filaments.

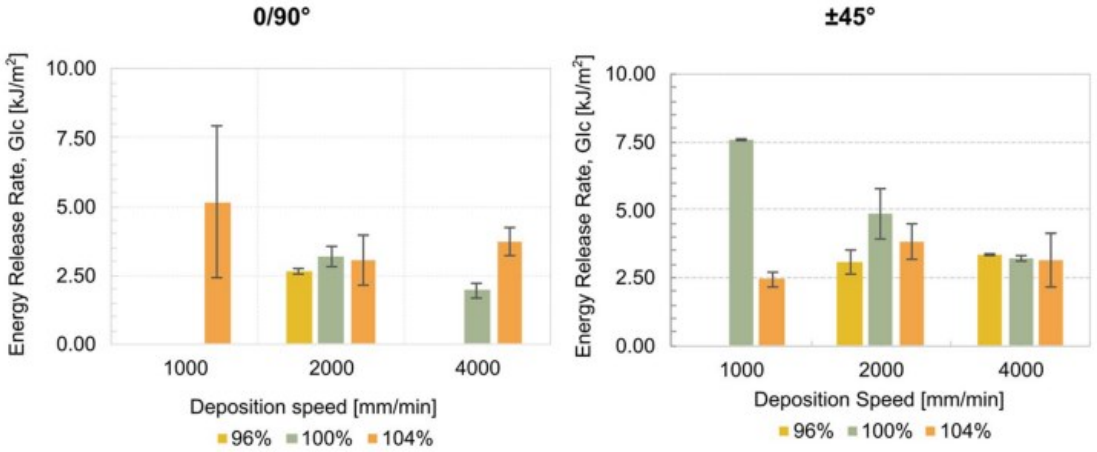



*Fig. 67 – Influence of the process parameters (extrusion multiplier and deposition speed) on GIc using diferent deposition strategies: (a) 0/90° and (b) ±45°*

In general terms, the crack propagation of the specimens of the first experimental campaign, was stable in most of the cases apart from fewer ones that presented an unexpected sudden crack growth. Three typical failure modes were obtained:

1. Stable crack propagation: it was the most frequently obtained, in which the crack was propagated smoothly between the midplane layers. This failure mode was present in most cases that the release film was implemented.
2. Unstable crack propagation: this failure mode was observed in the midplane in some rare cases where the release film as present.
3. Stable crack propagation with layer exfoliation: it was the most typical failure mode obtained by the specimens with slot and removable spacers. The difference between this failure and the first one is attributed mainly to the interface characteristics that are presumably altered by the interruption of the printing process that creates a weaker adhesion between the substrates of the midplane in the case of the specimens incorporating a release film.

The specimens demonstrating an unstable crack propagation may be divided into two distinct zones, namely the zone where the crack propagated gradually and a zone where the crack propagated rapidly. In Region A, an adhesive failure in the contact between the filament layers was observed while in Region B, a detachment of the two subsequent layers due to insufficient adhesion between them was present. Using the 3D reconstruction option of the stereoscope, the fractured zone of both kinds of specimens was captured and analyzed. In Fig. 68, the morphology of the specimen with release film and stable crack propagation is reported in terms of 3D reconstruction and virtual cross-section. Indeed, the morphology indicates an interlayer crack propagation in the same plane (midplane) without any implication and exfoliation of nearby layers. This fact is also supported by the variation of the height of the remaining filaments.

On the contrary, as seen in Fig. 69, in the case of the specimen with nested spacers, the crack was propagated in more than one plane, increasing the corresponding fractured area. In fact, there was observed a non-uniform fractured where two or three filament layers were exfoliated locally.

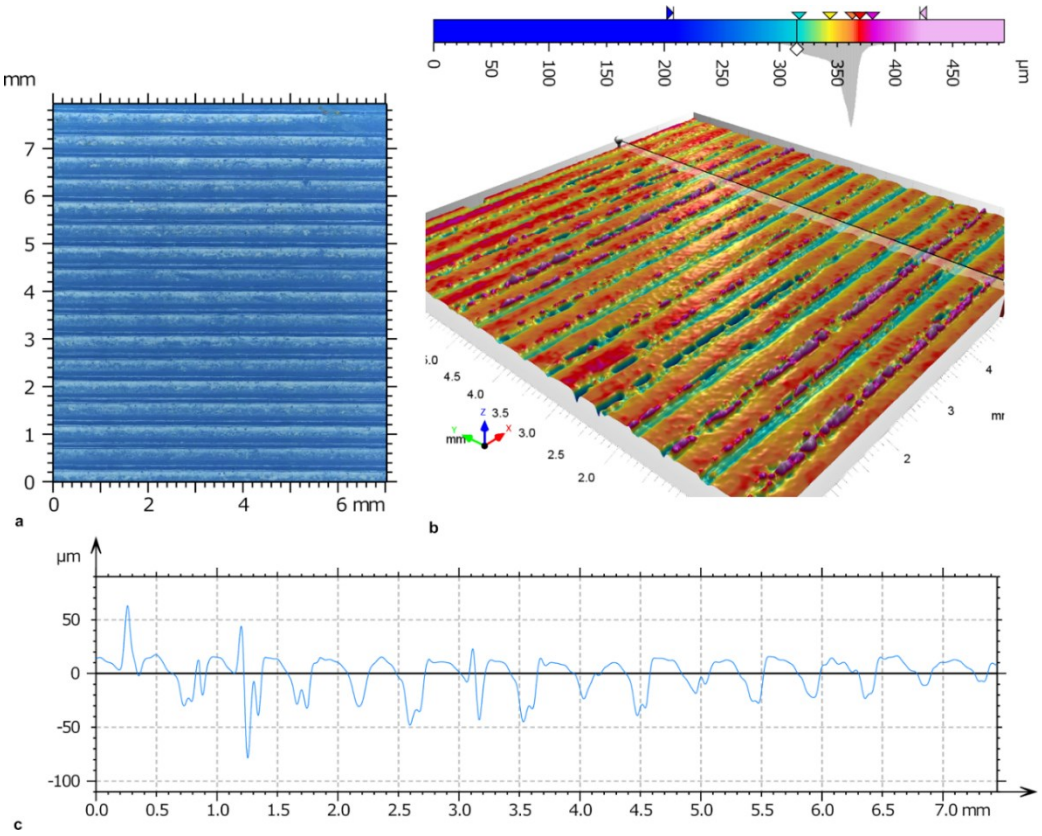



*Fig. 68 – Fractured surface analysis of a sample made by using the polyimide film: a) Stereoscopic image; b) 3D Reconstruction and c) virtual cross section*

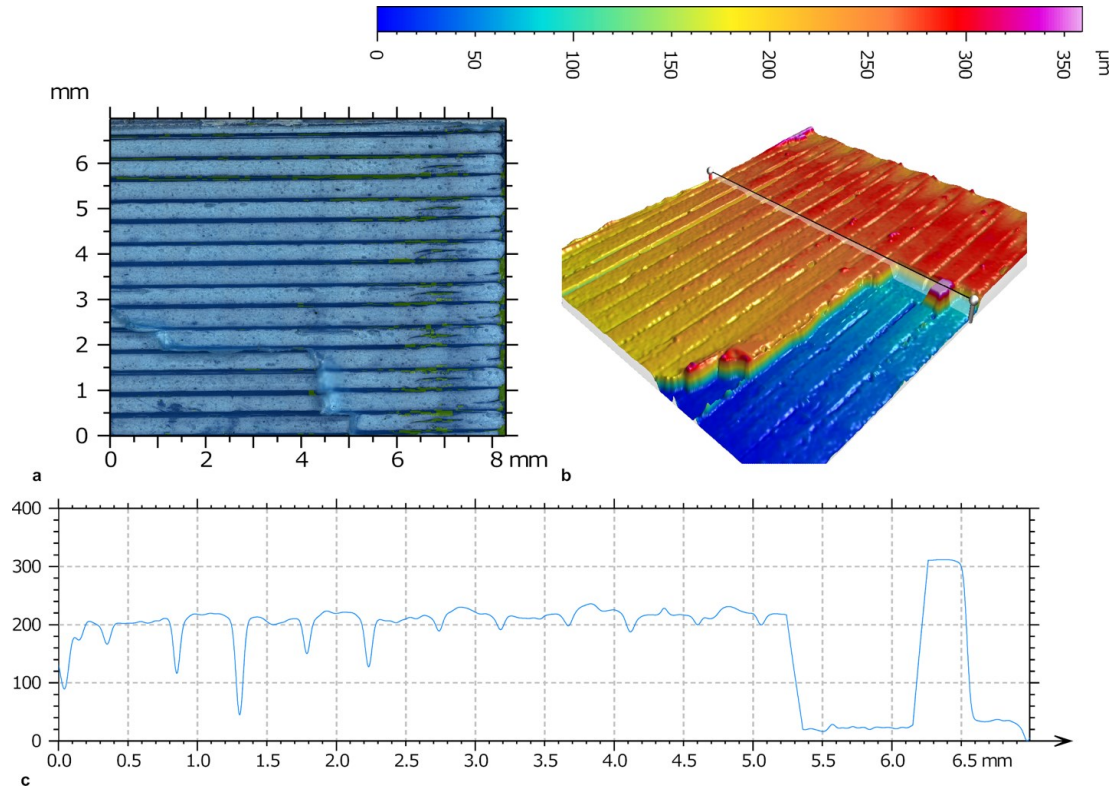



*Fig. 69 – Fractured surface analysis of a sample made with nested spacers: a) Stereoscopic image; b) 3D Reconstruction and c) virtual cross-section*

The effective area of the adhesion of the filaments was obtained by the analysis of SEM images. For the case of stable crack propagation (shown in Fig. 18) the percentage of adhesion can be defined as the ratio between the width of the effective contact (red line) and the distance of two consecutive filaments of the same layer (yellow line). The width of the contact zone of the substrate was found to be 223 ± 5 μm while the distance between the contact zones of two consecutive filaments was 480 ± 5 μm. Therefore, the effective adhesive ratio was 46.5% which corresponds to a typical stable crack propagation as the one of Zone A. On the contrary, in zone B the filaments were intact, indicating a lack of proper adhesion between the filament substrates.

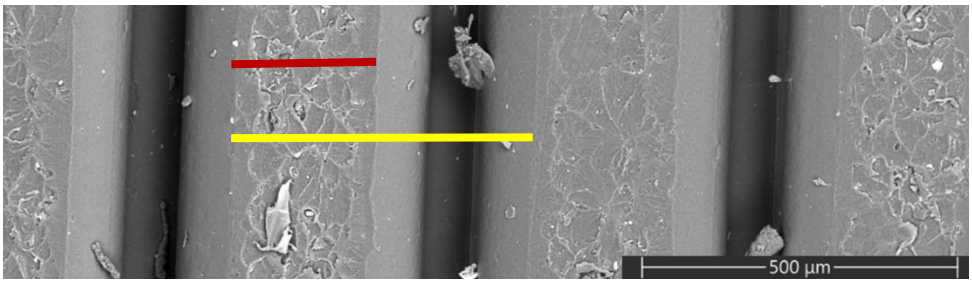



*Fig. 70 – The zone of the stable crack propagation observed with SEM*

### 4.2.4 Fracture surface analysis

The fracture surface analysis by optical microscope was conducted also for the specimens of the second experimental campaign, as depicted in Fig. 71, utilizing a LEICA M205A stereoscope.

Contrary to initial expectations, the increase in the extrusion multiplier did not yield a consistent rise in fracture toughness. The higher flow rate of extruded material was anticipated to enhance pressure and heat transfer on the underlying layers, thereby fostering improved interface adhesion. This was attributed to the more effective rearrangement of polymer chains between overlapping filaments in two consecutive layers. Surprisingly, specimens produced with an extrusion multiplier of 104% displayed weak adhesion, as clearly discernible in Fig. 71b and d. These images illustrate extensive areas where the initial crack propagates with a simple detachment between the two overlapping layers. Notably, the magnified images of the repetitive unit cell (RUC) indicate that the filaments deposited between successive layers remained largely intact, with only sporadic regions offering higher resistance to crack progression. These areas are distinguished by brighter regions compared to the original filament color, albeit visible only partially in the RUCs and the entire adhesion region in these two images. Conversely, the images show in Fig. 71a and c demonstrate that

the filaments of one layer were dragged by the overlying layer. These images reveal substantial damage not only at the interface but also internally within the single layer; this confirms the higher load-bearing capacity of these samples. In both the RUC and the overall view, these images appear notably brighter than those in Fig. 71b and d, likely owing to the superior resistance to defect propagation exhibited by components with an extrusion multiplier of 100%.

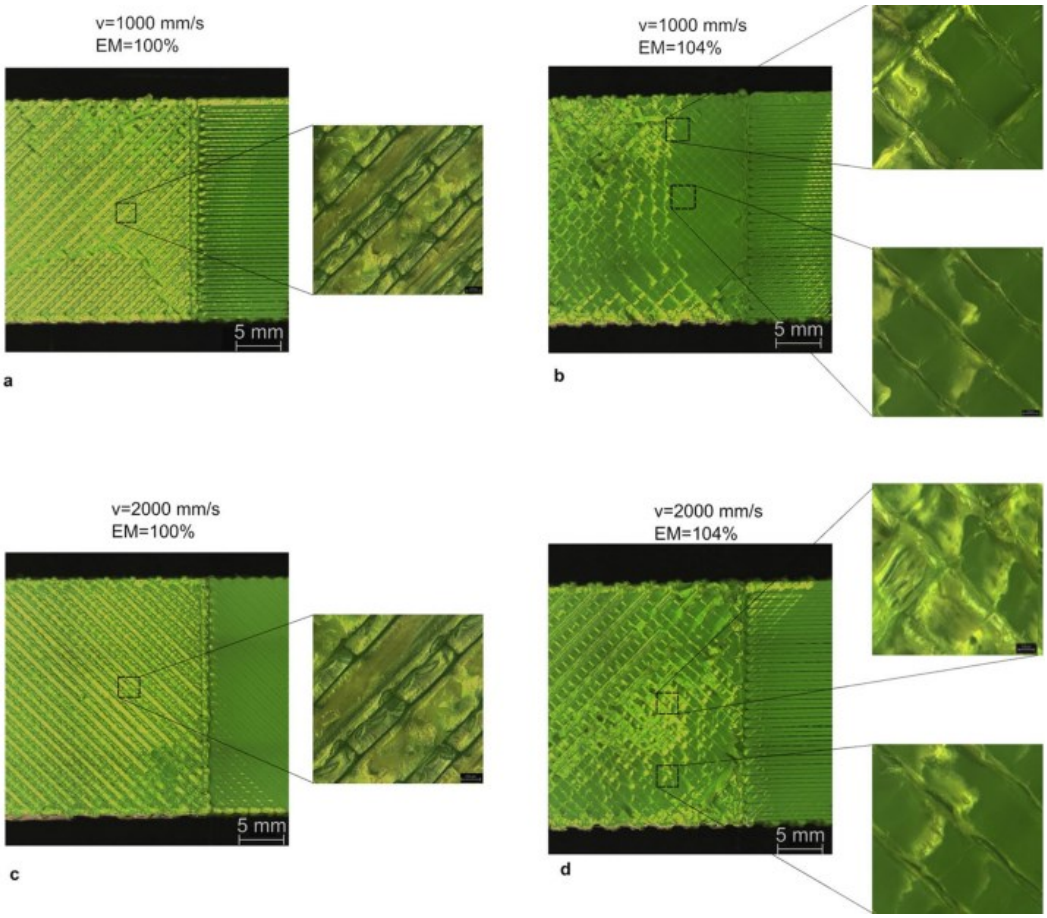



*Fig. 71 – Fracture surface observed through optical microscopy of samples made under reference deposition conditions: (a) v=1000 mm/min, EM=100%; (b) v=1000 mm/min, EM=104%; (c) v=2000 mm/min, EM=100%; (d) v=2000 mm/min, EM=104%*

### 4.2.5 Infrared analysis

Infrared analysis of the temperature was conducted during the deposition of the samples to better understand their thermal history. A measurement point region was focused to monitor the temperature variation during the deposition. The position of the measurement point was fixed on the deposition path for the specimens of the first experimental campaign, as Fig. 72a depicts. Consequently, the temperature measured shows a periodic trend. Indeed, when the nozzle extrudes material over the measurement point, the temperature trend shows a

peak, while it suddenly drops as the nozzle moves away, until the next layer deposition. The temperature history measured over the measurement point is depicted in Fig. 72b. to better distinguish between the temperature measured during each layer deposition, a Gaussian filter fixed at 500 samples was also adopted (red line). As can be inferred, as soon as the process was stopped for the insertion of the Polyimide tape, the temperature continues to decrease. Therefore, the minimum temperature reached before and after the pause (TN-1 and TN+1) were higher that the temperature reached by the layer where the Polyimide was placed (TN). Thus, the middle layer undergoes a thermal cycle that is different from that occurring during the normal deposition, leading to a lower healing of the polymer. It is worth noting that, during the tests performed by the adoption of the Polyimide tape, this "altered layer" is the one that is tested. On the other hand, this does not happen when the spacers are used since the pause time is not needed.

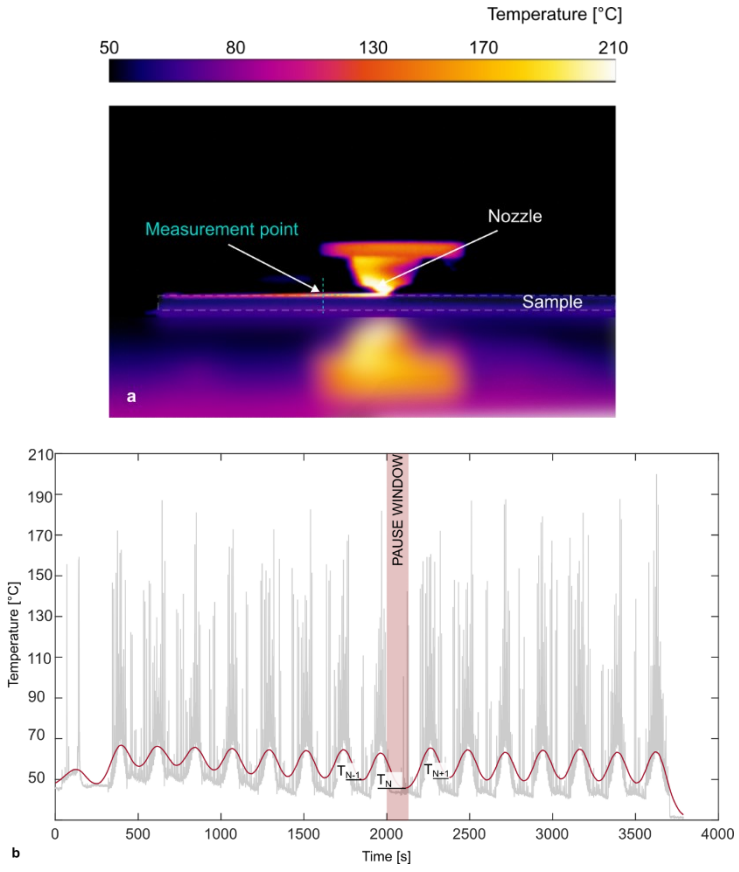



*Fig. 72 – (a) Temperature distribution measured during deposition and (b) temperature variation with time measured at the measurement point. Samples made with a pause time of 60 s to account for the time required for the Polyimide placement*

The infrared image acquired during printing of the samples of the second experimental campaign is depicted in Fig. 73a. To discern and quantify temperature variations between

samples produced under different processing conditions, a measurement point was designated on the upper surface of the sample. Fig. 73b compares the thermal histories recorded during two depositions at a constant speed of 1000 mm/min and an extrusion angle of ±45°. Temperature trends displayed peaks of approximately 210 °C as the hot-end traversed the measurement point, followed by a rapid decrease. Notably, these temperature peaks were consistent for both EM =100% and EM =104%. However, a significant discrepancy was observed in the substrate temperature. For EM =100%, the mean substrate (underlying layer) temperature was approximately 59 °C, while for EM =104%, it rose to almost 70 °C. A detailed examination of the temperature history during layer deposition is presented in Fig. 73c. It is evident that the use of a higher extrusion multiplier (EM =104%) resulted in a slower cooling rate and higher average temperature compared to the adoption of a lower extrusion multiplier (EM = 100%). This behavior can be attributed to the increased flow rate with higher EM values, consequently augmenting thermal inertia and leading to reduced cooling rates and elevated average temperatures, in contrast to the conditions observed with EM = 100%. However, it has to be pointed out that an increase in EM may lead to an incomplete melting.

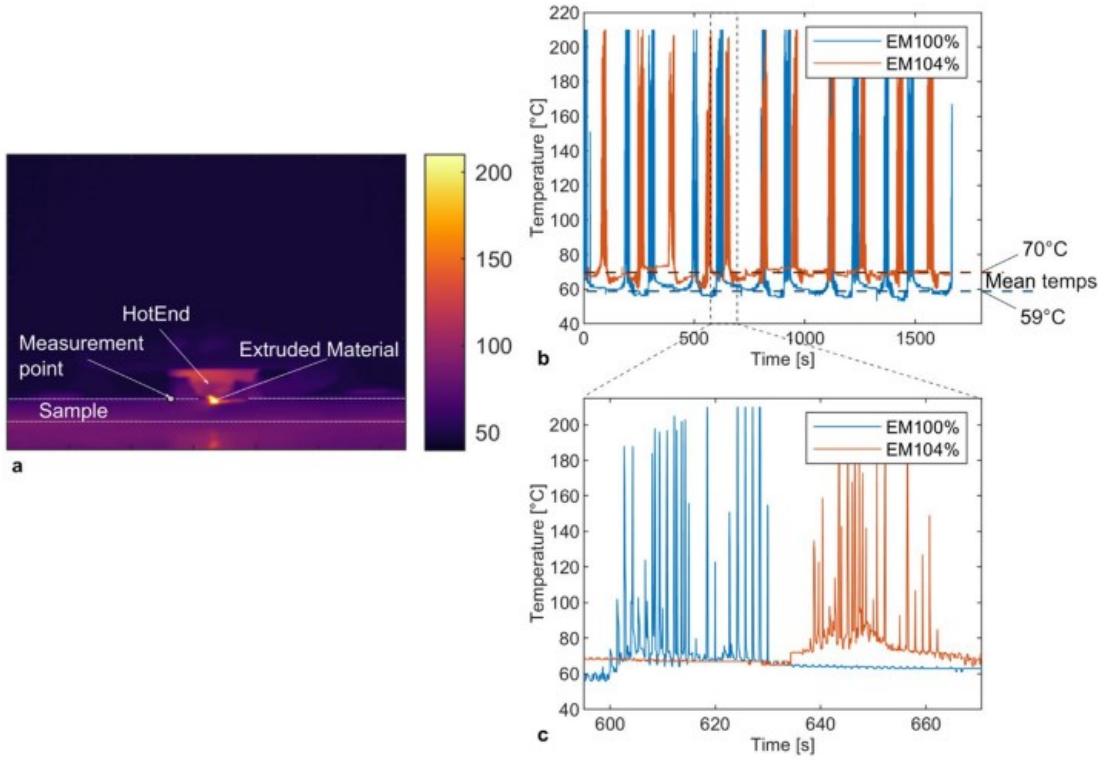



*Fig. 73 – (a) IR temperature maps acquired during the deposition of the samples, (b) temperature history at the measurement point (on the top surface of the sample) under different deposition conditions, and (c) temperature history during the deposition of a single layer*

### 4.2.6 DMA and DSC analysis

Samples of the second experimental campaign were subsequently further analyzed through additional techniques. Fig. 74 shows the DMA analyses conducted on the specimens obtained with different EMs, 100 and 104, in terms of storage modulus (a) and tan d (b), which represents the ratio between loss and storage modulus. The specimen obtained with EM=100% shows a slightly lower storage modulus (at the lower temperatures) and a higher glass transition temperature (see also the maximum value of tan d) than the specimen obtained with EM=104%. The storage modulus decreases when the temperature reaches the values of the glass transition; however, after the minimum, it increases again, due to the incoming crystallization. The specimen obtained with EM =100% shows a higher storage modulus increase; this may be due to a smaller crystallinity degree achieved during the deposition process. Conversely, the specimen obtained with EM=104% shows a smaller increase in the storage modulus after the minimum value, suggesting a higher crystallinity degree achieved during the deposition process. The higher values of the crystalline degree of the specimen obtained with EM=104% could be due to both slower cooling rate during deposition and the presence of nuclei due to incomplete melting.

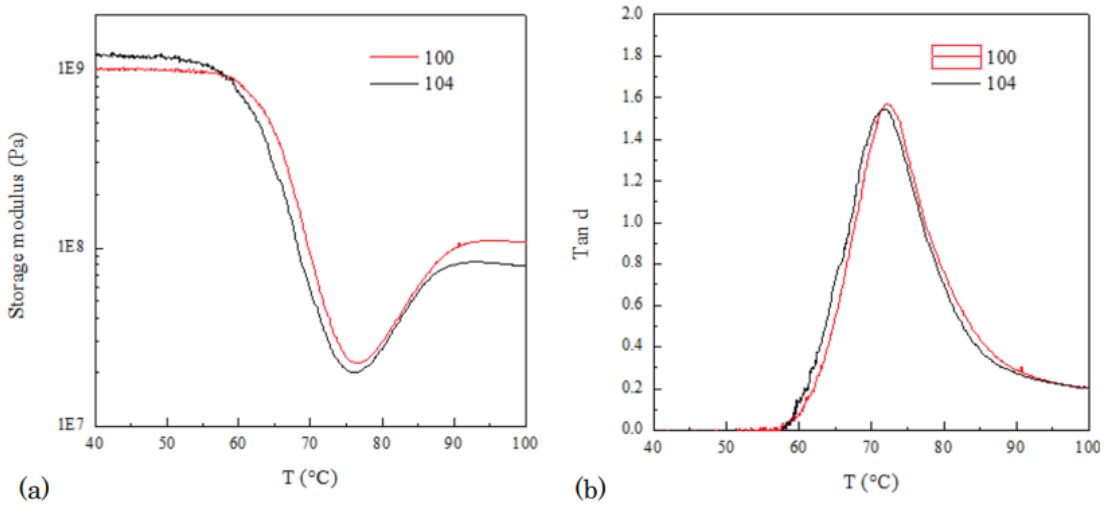



*Fig. 74 – DMA analysis conducted on the specimens obtained with different EMs: (a) Storage moduli and (b) tan d*

Fig. 75a, related to the calorimetric analyses of the 3D printed parts, confirms this assumption. The calorimetric analysis conducted on the filament revealed a high crystalline degree. The calorimetric analyses on 3D printed parts show, for both EMs, exothermic peaks ascribable to the cold crystallization arising during the analysis. Such an exothermic peak confirms that the fast cooling occurring during the process leads to the formation of mostly amorphous parts. Interestingly, the endothermic peak due to the melting moves toward lower

temperatures for the parts produced by MatEx. This could be ascribed to the formation of a different crystalline phase during the process [202]. DSC analyses essentially confirm what has been found by DMA analyses: the part obtained with EM=104% shows a higher crystalline degree than the part obtained with EM =100%. Fig. 75b shows the ATR spectra of 3D printed parts and the filament in the range 1300–1160 $cm^{-1}$. Two characteristic peaks can be detected: at 1210 $cm^{-1}$, related to C–O–C stretching vibration of the carbonyl group, characteristic of the crystalline phase, and 1270 $cm^{-1}$, characteristic of the amorphous phase [203].

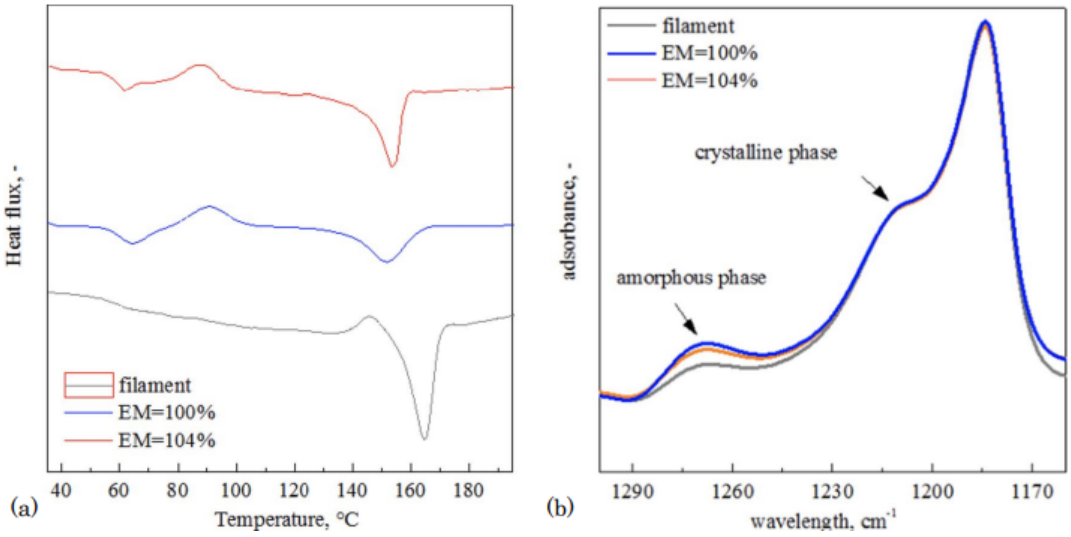



*Fig. 75 – (a) DSC analyses and (b) ATR spectra for the specimens obtained with different EMs. The analyses of the filament are also reported for comparison*

3D printed parts show higher intensity of the peak characteristic of the amorphous phase, consistently with those already observed from DSC analyses. Parts obtained with EM =100% show a higher amount of amorphous phase than the parts obtained with EM=104%. It must be noticed that ATR reveals information about the external part of the deposited layer, whereas DSC analysis is averaged on the whole specimen. Even if related to different areas of the deposited layer, the analyses are consistent and confirm that EM=104% leads to slightly higher crystallinity.

SEM analyses provide to investigate structures present in the part at the delamination (see Fig. 76). SEM micrographs clearly reveal that delamination induces the detachment of adjacent layers and that the extension of the detached area depends on the extrusion multiplier: for EM = 100%, a larger detached area was observed. Furthermore, the detached area of the part obtained with EM = 104% was smoother than the one observed for the part

obtained with EM =100% (compare Fig. 76a and b); this is a clear indication that the increase of EM to 104% led to weaker adhesion. Fig. 76d shows the presence of ordered structures, probably due to the presence of spherulites, on the surface of the deposited layers, such a finding is consistent with a higher crystallinity degree for the part obtained with EM =104%. Crossing the information provided by different analyses, it was hypnotized that for the part obtained with EM = 104%, the crystallization must occur before the polymer chain could diffuse at the interface between adjacent layers, hindering any additional diffusion. In the case of the part obtained with EM =100%, crystallization was slow enough to allow a significant polymer chain diffusion at the interface, leading to a stronger adhesion. The higher crystallinity degree of the parts obtained with EM =104% can be ascribed to the presence of small crystals already at the exit of the liquefier which makes the crystallization process faster, limiting, therefore, the rearrangement of polymer chains at the interface.

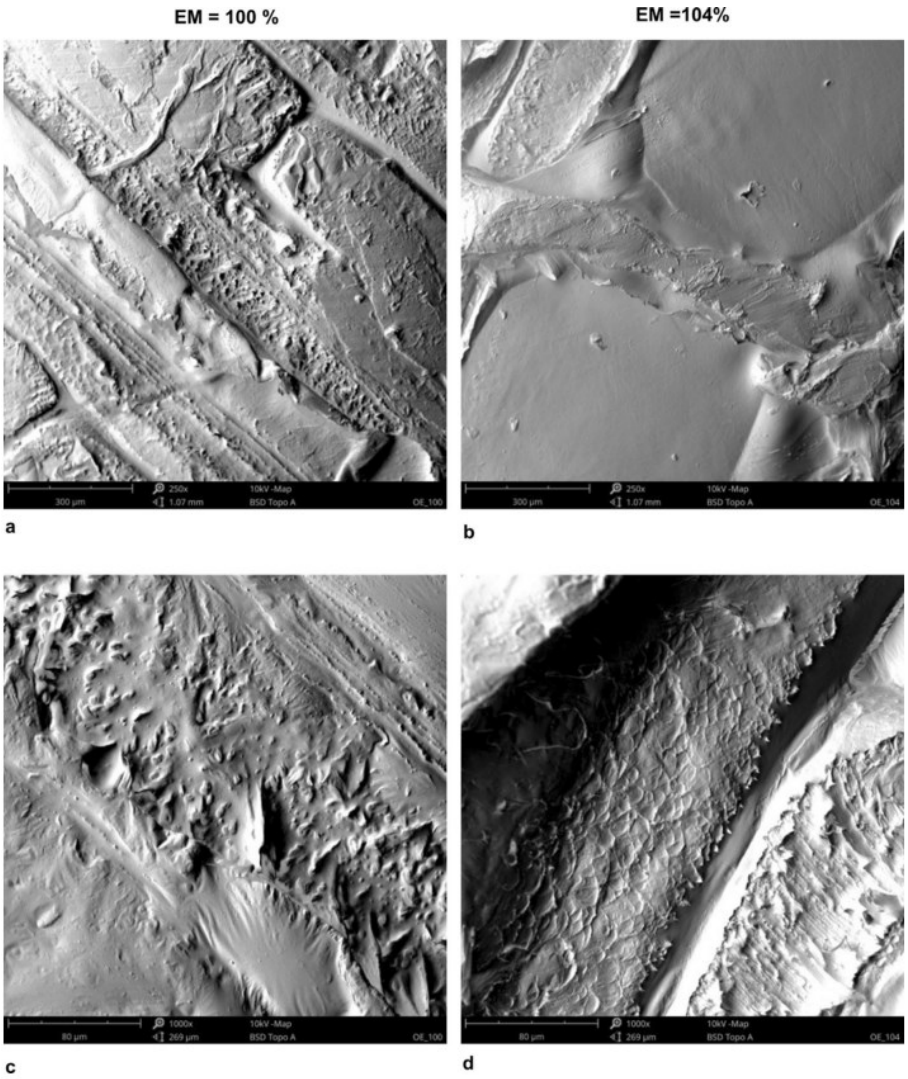



*Fig. 76 – SEM micrographs obtained with two magnifications, ×250 (a, b) and ×1000 (c, d), for the parts obtained with 100 and 104 EM, after the delamination test*

## 4.3 Artifacts introduced by different manufacturing strategies in material extrusion components

### 4.3.1 Introduction

Direct sample print is widely adopted to determine the mechanical behavior of an AM component [204-206]. The sample with all its features (e.g., dogbane for tensile tests) is produced. This method is favored for its simplicity, eliminating the need for additional machining prior to testing. However, this sample may show different behavior as compared to that of a larger component since the time between the deposition of consecutive layers could be highly different. Different interlayer time elapsed when using series or parallel deposition strategy. This indicates that the interlayer time should also be similar between the effective workpiece and the sample printing. The completion time for each layer is contingent on its dimensions, resulting in a lower interlayer time for directly printed samples compared to their larger counterparts. Thus, there are discrepancies in the thermal histories experienced by directly printed samples compared to those encountered by larger components.

Another potential artifact produced while direct printing a sample is represented by the effective deposition speed. Indeed, when small samples are produced, even though the same nominal rate is set, the acceleration and deceleration ramps may hinder reaching the set nominal speed owing to the small length of the sample. This may also lead to differences between the characteristics of a sample produced by direct print and "as extracted" from a component. Directly printed samples exhibit uneven filament distribution, particularly noticeable at the edges. This discrepancy arises from the lower hot end speed experienced at the edge due to deceleration and acceleration during directional changes.

Finally, as reported by several studies [207, 208], the mechanical behavior of printed samples is also sensitive to the distance from the building plate. In the material extrusion process [66, 83, 89, 136, 209], layers in contact with the building plate show higher density than overlying layers. In addition, as the building plate is typically kept at temperatures close or even higher to the polymer's glass transition temperature, aging may occur in these layers. This also alters the mechanical properties of these layers compared to those of the rest of the sample [207].

Since Additive manufacturing processes enable the production of very complex geometries, the mechanical characterization of the samples was performed by directly printing the

sample with the final geometry. However, the "deposition history" can be significantly different from that occurring during the production of a real (larger) component. Direct sample printing may introduce artifacts that can alter the mechanical properties of the component. Consequently, it may lead to underestimation or overestimation of the physical properties (e.g., density) and mechanical properties. On the other hand, the "classical" sample preparation demands more effort for sample extraction from a larger part and is more time-consuming. In pursuit of uncovering critical insights, an extensive experimental investigation was undertaken to discern and elucidate the differences and potential causal factors that could significantly impact the accurate assessment of the mechanical behavior of components fabricated via the material extrusion process. By adopting two different strategies, that are direct printing and extraction of the samples from a larger part, the aim is to provide a comprehensive understanding of how the manufacturing approach influences the mechanical properties, microstructure, and overall performance of components produced via Material Extrusion (MatEx). This knowledge is crucial for quality assessment of MatEx components that is mandatory, especially for the production of high-performance aerospace components.

### 4.3.2 Materials and methods

Two different materials were used to produced specimens required to conduct the following studies: for the first two experimental campaigns [168, 170] Polylactide acid (PLA) was used, while for the third experimental campaign [210] Polyaryletherketone (PAEK) was adopted.

Polylactide acid (PLA), provided by RS PRO was characterized by an initial diameter of 1.75 mm ± 0.02 mm. The samples were produced using a Creality Ender 6 commercial machine. Simplify 3D version 4.1.2 was used as slicing software. The critical deposition parameters are listed in Table 12.

The sample of the first experimental campaign were produced to be subjected to compression tests, according to ASTM D695 standard [95]. The samples were produced using two different approaches: direct printing and sample extraction (cut) from larger components (plate). The final dimensions of the samples used for compression tests were 12 mm × 12 mm × 48 mm. Three different orientations were tested, leading to (1) vertical samples (the loading direction corresponds to the material extrusion machine Z-axis), (2) horizontal samples with filaments arranged transverse to the loading direction, and (3) horizontal

samples with filaments arranged parallel to the loading direction. To understand the adopted approach, a plate layout with the cuts is reported in Fig. 77.

*Table 12 – Main deposition parameters*

| *Process parameter* | *Value* |
|---|---|
| *Nozzle temperature (°C)* | 210 |
| *Building plate temperature (°C)* | 60 |
| *Printing speed (mm/min)* | 3000 |
| *Nozzle diameter (mm)* | 0.4 |
| *Extrusion width (mm)* | 0.5 |
| *Layer thickness (mm)* | 0.2 |
| *Infill percentage (%)* | 100 |
| *Infill strategy* | Rectilinear |
| *Number of external shells* | 1 |
| *Extrusion multiplier* | 100% |

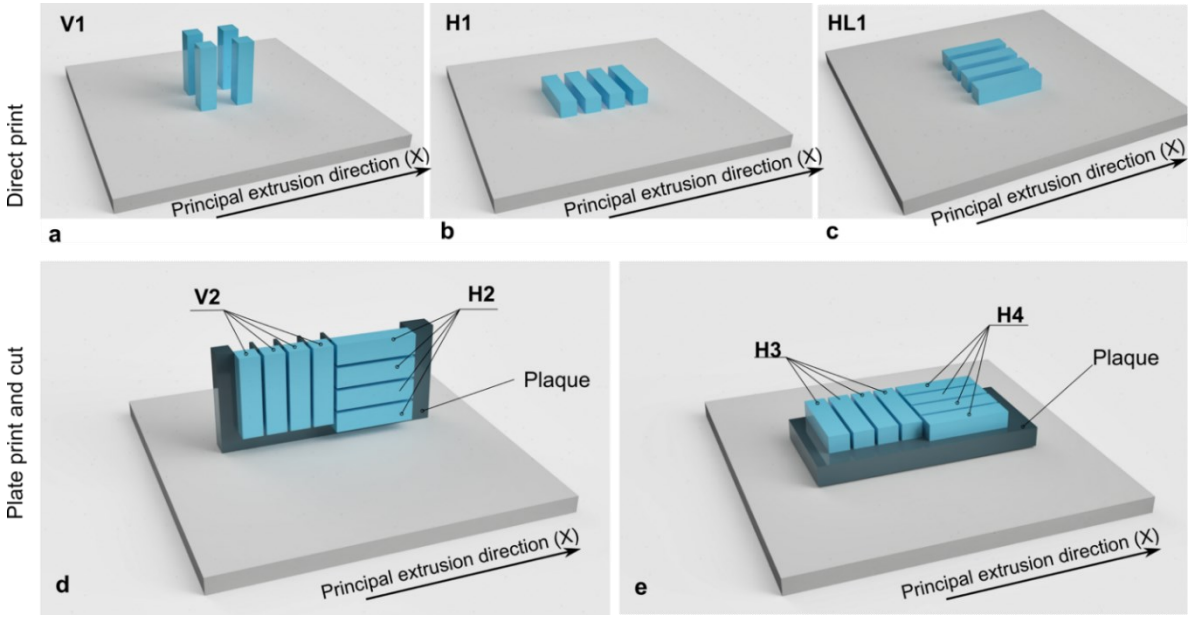



*Fig. 77 – Schematic of the adopted printing strategies: direct print of a) vertical, b) horizontal samples, and c) horizontal with longitudinal filaments. Plaque print and cut of d) vertical plaque and e) horizontal plaque*

The picture shows that configurations V1, H1, and HL1 immediately produce the samples. However, some of these samples (especially those of type H1 and HL1) are in contact with the building platform. Thus, such regions could be affected by prolonged contact with the building platform, which may alter the region's structure and mechanical properties. On the

other hand, V2 and H2 samples are cut from the 3D-printed plaque, taking care to avoid the region coming in contact with the building plate. H3 and H4 samples (shown in Fig. 77d) were produced with benchmarking purposes to determine the influence of the printed part size on the mechanical behavior. Table 13 provides an overview of the final experimental strategy.

*Table 13 – Levels of the first full factorial experimental plan*

| *Sample* | *Manufacturing* | *Sample Direction* |
|---|---|---|
| *V1* | Direct print | Vertical |
| *H1* | Direct Print | Horizontal |
| *HL1* | Direct print | Horizontal |
| *V2* | Extracted from the vertical plate | Vertical |
| *H2* | Extracted from the vertical plate | Horizontal |
| *H3* | Extracted from the horizontal plate | Vertical |
| *H4* | Extracted from the horizontal plate | Horizontal |

The samples of the second experimental campaign were manufactured according to ASTM D638 [94] standards. Particularly, the samples were produced using different processes:

1) Direct printing: the samples were printed at the final dimension; thus, any further post-process was needed before of characterization.

2) Sample extraction: the samples were cut through abrasive waterjet cutting. To this end, a box with side walls of 2.5 mm and 3 mm of thickness was printed. Then the samples were cut from the box by adopting a waterjet cutting. Fig. 78 presents a detailed schematic of the samples.

Additionally, six small sized samples (designed according to ASTM D638 Type V) were also produced using the extraction method to identify possible differences in terms of mechanical behavior. To this end, the samples were extracted from a same box with the same dimensions of that used for production of type I samples (80 mm width and 180 mm height) to preserve the thermal history. The test matrix of the experimental campaign is summarized in Table 14.

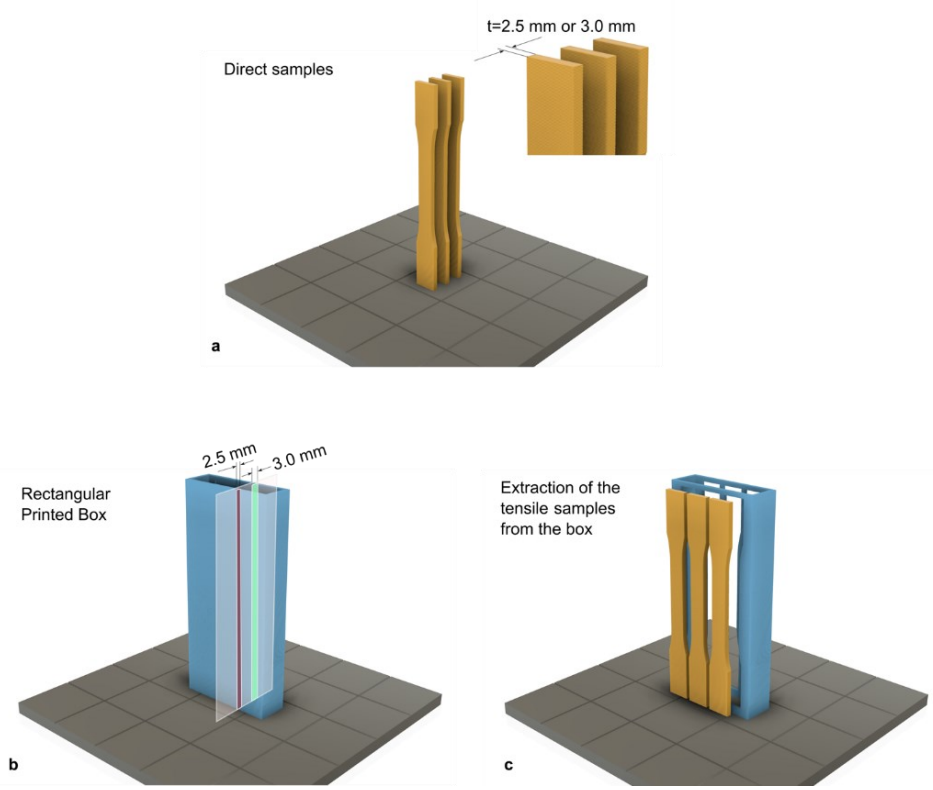



*Fig. 78 – Schematic of the sample produced using different approaches: a) direct sample printing, b) rectangular box printing. c) extraction (through abrasive waterjet cutting) of tensile samples from the rectangular box.*

*Table 14 – Test matrix summarizing the experimental conditions used for the second experimental campaign*

| *Condition* | *Sample geometry* | *Sample manufacturing* | *Thickness (mm)* |
|---|---|---|---|
| *I* | ASTM D638 Type I | Direct sample printing | 2.5 |
| *II* | ASTM D638 Type I | Direct sample printing | 3.0 |
| *III* | ASTM D638 Type I | Plate printing and waterjet cutting | 2.5 |
| *IV* | ASTM D638 Type I | Plate printing and waterjet cutting | 3.0 |
| *V* | ASTM D638 Type V | Plate printing and waterjet cutting | 3.0 |

An infrared camera, the FLIR E60 model, was involved in the MatExt process for real-time temperature distribution monitoring of the specimens of both the first and the second experimental campaign. The acquisition frequency was set to the maximum available (30 Hz) to ensure high-quality data capture. Subsequently, ResearchIR software was employed

to analyze the thermal history. The thermal camera was securely mounted on the machine frame, enabling continuous temperature monitoring throughout the deposition process.

Samples of the latter experimental campaign were produced by using Polyaryletherketone (PAEK), provided by VICTREX, boasting an initial diameter of 1.75 mm ± 0.02 mm. The production of the samples was carried out using an industrial machine model Spectral 30 by 3ntr (from Novara, Italy). The critical deposition parameters are listed in Table 15.

*Table 15 – Main deposition parameters of the third experimental campaign*

| *Process parameter* | *Value* |
|---|---|
| *Printer primary extruder temperature (°C)* | 398 |
| *Printer secondary extruder temperature (°C)* | 280 |
| *Building plate temperature (°C)* | 120 |
| *Printer chamber temperature (°C)* | 120 |
| *Printing speed (mm/min)* | 3600 |
| *Nozzle diameter (mm)* | 0.4 |
| *Extrusion width (mm)* | 0.5 |
| *Layer thickness (mm)* | 0.2 |
| *Infill percentage (%)* | 100 |
| *Infill strategy* | Linear |
| *Number of external shells* | 4 |
| *Volumetric material flow ($mm^3$/min)* | 360 |

The samples were manufactured according to ASTM D638 [94] standards Type I. Particularly, the samples were produced using different protocols:

1. Direct printing: the samples were printed at the final dimension.

2. Sample extraction: the samples were cut through abrasive waterjet cutting. To this end, a box with side walls 4 mm of thickness was printed. Then, the samples were cut from the box. Waterjet cutting was used to cut the samples to avoid any material modification since no heating was produced during the cutting operation.

Fig. 79 presents a detailed schematic of the samples. In both cases, the entire thickness of the sample (of 4 mm) was filled by the external shells. Indeed, each shell was 0.5 mm wide; consequently, at least in the central region, the samples cut from the box and directly printed

were produced with the same strategy. Of course, some differences existed in the side regions. Indeed, the cut samples were characterized by filaments arranged along one direction, while directly printed samples showed a concentric shell strategy, as schematized in Fig. 79.

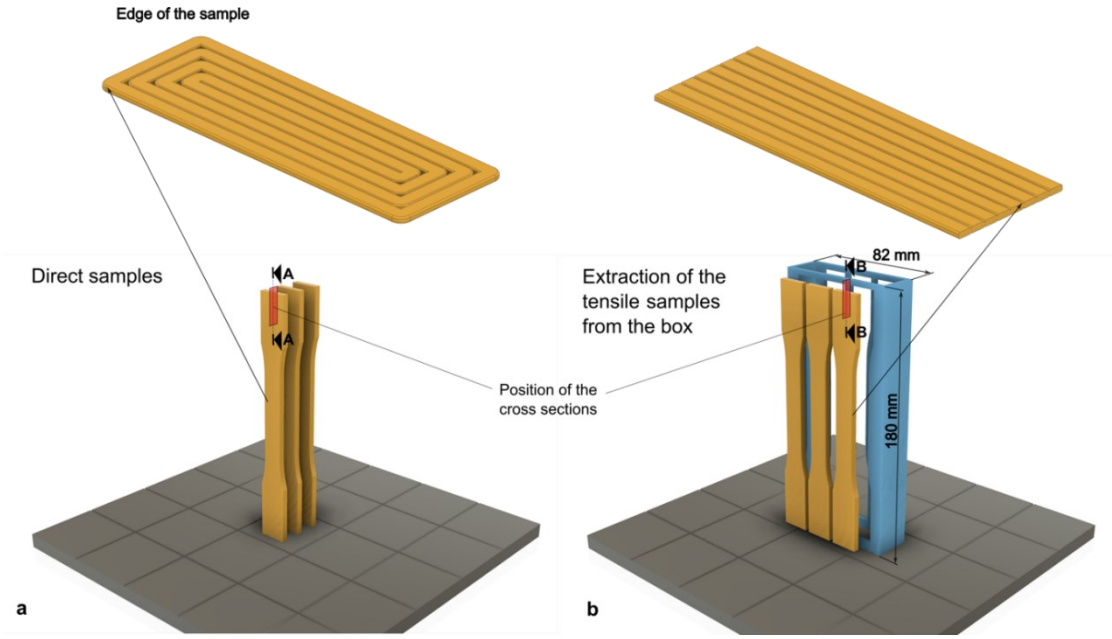



*Fig. 79 – Schematic of the sample produced using different approaches: a) direct sample printing, b) extraction (through abrasive waterjet cutting) of tensile samples from the rectangular box*

Additionally, some specimens were post-processed by annealing; Fig. 80 shows the thermal cycle that the specimens were subjected during the annealing process.

The test matrix of the experimental campaign is summarized in Table 16. For each processing condition, five samples were produced. Thus, the mean value and standard deviation were computed.

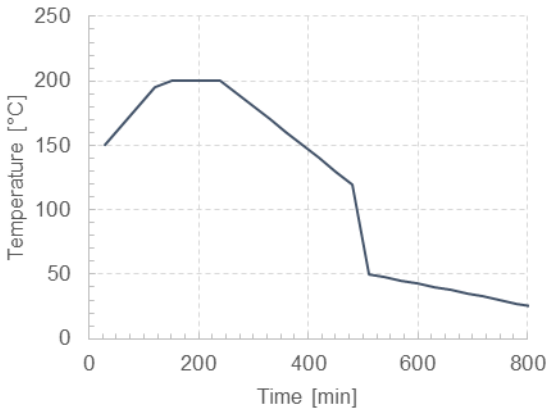



*Fig. 80 – Annealing thermal cycle*

*Table 16 – Test matrix summarizing the experimental conditions used for the experimental investigation*

| *Manufacturing* | *Post-processing* |
|---|---|
| *Direct print – AP* | As printed |
| *Direct print – A* | Annealed |
| *Cut from the box – AP* | As printed |
| *Cut from the box – A* | Annealed |

The samples of the first experimental campaign were geometrically characterized before mechanical tests to establish the component densities. The dimensions were determined using a centesimal micrometer. The weight of the samples was then determined using a Precisa balance model XT1220M. This enabled us to estimate the density of the samples and how the chosen process parameters affected it.

On the other hand, samples of the second and third experimental campaigns, underwent geometrical characterization prior to mechanical testing through microscopy analysis. This enabled to determine the effective cross section (adhesion area) neglecting external defects.

Both compression and tensile tests were performed using a universal testing machine model C43.50 equipped with a 50 kN load cell. The tests were conducted using a traverse speed of 1 mm/min. During the tests, the strain of the sample was measured through an extensometer model 632.24F-50 by MTS. Compression tests were conducted up to a displacement of 2 mm, while tensile tests were carried out until the samples were completely failed. Optical microscopy served as a valuable tool in understanding the material's morphology both pre and post mechanical tests. To this end, a stereoscope model M205 by LEICA was used to determine the real dimension of the cross section, the surface morphology, and the analysis of the fracture surface. Additionally, for the specimens subjected to compression tests, a LEICA DM5000 metallographic microscope was used to comprehend better the microstructural features (interlayer neck and void sizes). Some samples were cross-sectioned and polished using abrasive paper to see better the internal flaws of the samples and the impact of the material flow (up to 2400 grit). Thus, a cooled diamond blade was used to cross-section the samples in the past. The samples were then molded and polished following consolidated metallographic techniques.

Calorimetric analyses were also conducted on PAEK specimens by differential scanning calorimetry (Perkin Elmer DSC 8500) with 20 °C/min heating/cooling rate. Heating was

conducted from 25 to 350 °C. Crystallinity ratio $\chi$ was determined for all the samples from the melting enthalpy $\Delta H_m$ according to eq. 19.

$$\chi(\%) = \frac{\Delta H_m - \Delta H_{cc}}{\Delta H_\infty} \qquad \textit{eq. 19}$$

where $\Delta H_{cc}$ is the cold crystallization enthalpy and $\Delta H_\infty$ is the theoretical melting enthalpy of a 100% crystalline polymer. To this end, the $\Delta H_\infty$ for PEEK was used which equals 130 J/g [211].

### 4.3.3 Mechanical behavior

Fig. 81a summarizes the density measurements performed on the different samples of the first experimental campaign; green bars refer to sample realized by direct printing. As can be inferred, direct sample printing led to underestimating the density in vertical samples. The density of V1 samples was 5.3% lower than that measured on extracted samples V2. On the other hand, negligible differences (lower than 1%) were found while comparing the density of all the samples extracted from the plaque. This indicates good robustness and reproducibility of the procedure adopted while extracting the samples. Directly printed samples HL1 showed a slightly higher density than the other samples. This difference can be ascribed mainly to the inversion of the printing direction (at the edges). On the other hand, the average density was less affected by the distance of the sample from the building plate. The samples V2 and H2 which were extracted far from the plate showed similar density compared to samples H3 and H4, which were extracted from a plaque printed with a large area in contact with the building (heated) plate.

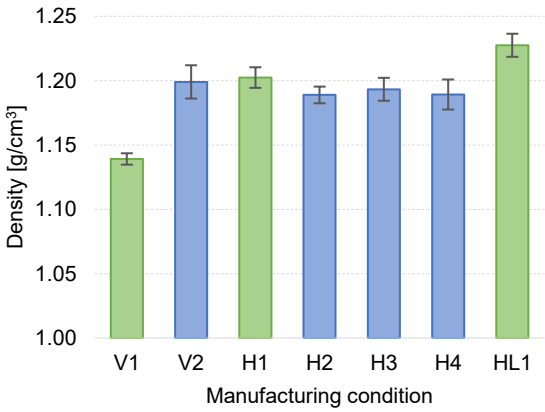



*Fig. 81 – Influence of the deposition conditions on the density of the samples*

Fig. 82a depicts the influence of the printing strategy and direction on Young's modulus, while Fig. 82b depicts the influence on the yield stress. Regarding Young's modulus, directly printed samples V1 and H1 showed lower value than the corresponding "extracted" samples V2 and H3. The measurements using V1 samples underestimated Young's modulus by 10%. Similarly, the difference between Young's modulus measured along the horizontal direction was even more marked; indeed, for H1, the average Young' s modulus was 1380 MPa, while that of the H3 sample was 1780 MPa, corresponding to an underestimation of 29%. Only direct printed samples HL1 showed a similar Young's modulus as compared to the corresponding "extracted" samples H4 and H2 because, during the compression test, filaments are oriented perpendicular to the direction of load application in all three specimens considered. Direct printed samples H1 showed the lowest Young's modulus because, during the compression test, these samples were not compressed in the direction of layer growth; indeed, layers were not compressed with each other, but there was compression of filaments. On the other hand, directly printed samples V1 showed lower yield stress than the corresponding "extracted" samples V2. The measurements performed using V1 samples underestimated the yield stress by 12%. The difference between the yield stress measured along the horizontal direction was not marked; indeed, for H1, the average yield stress was 61 MPa, while that of the H3 sample was 63 MPa. Differences were more marked if compared to H4 and HL1; HL1 depicts an average yield stress of 73 MPa, corresponding to an underestimation with H2 of 18%. The motivation for this difference can be found in the printing mode, which results in a 3% higher density in HL1 than in H2. HL1, having been printed in the horizontal direction, has a greater contact surface with the printing plane than H2, leading to a higher density.

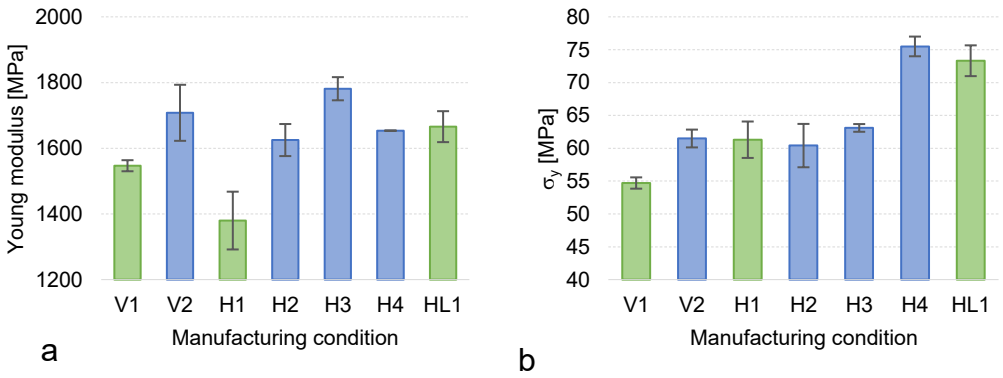



*Fig. 82 – Influence of the deposition conditions on the Young's modulus (a) and on the yield stress (b) of the samples*

Regarding the second experimental campaign, after the tensile tests, the fracture developed in the middle of the samples, except for samples of Type V. In these samples, the fracture developed at the fillet just before the clamping area. Fig. 83 depicts the stress-strain curves recorded during the tensile tests using different sample manufacturing protocols. For each sample manufacturing strategy and thickness, two curves were reported to check the repeatability. Type V samples were not reported since the dimension of the extensometer did not fit with the dimensions of these samples. Thus, for Type V samples, only the strength information was recorded. All the curves showed an initial almost linear increase of stress pertaining to the elastic regime, followed by a peak load, which was followed by a plateau, indicating the onset of plastic strain. After the small plastic deformation, the load suddenly fell to zero, and brittle failure occurred.

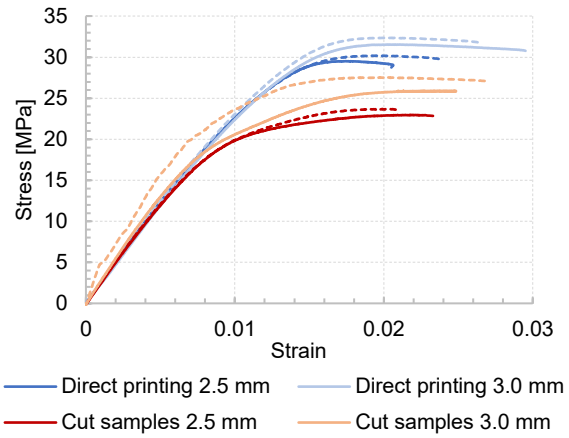



*Fig. 83 – Stress-strain curves of different samples produced with direct sample printing and cutting with two thicknesses*

The main mechanical characteristics were identified from the stress-strain curves, including Young's modulus, the elongation at rupture, and the peak strength; these characteristics are depicted in Fig. 84. For each sample, the average and the standard deviation were calculated. For samples of Type V, only the peak strength was calculated (since the tests were conducted without the extensometer). Fig. 84a compares the Young's modulus of the samples. As can be inferred, the samples produced by direct printing exhibited a similar Young's modulus (with an average value of 2.51 GPa), irrespective of the thickness of the samples. On the other hand, the samples cut from the box had Young's modulus, which was influenced by the thickness of the wall: for samples of 2.5 mm (viz 3.0 mm) of thickness, Young's modulus was 2.4 GPa (viz. 2.8 GPa). This indicated that the elastic properties of the samples were influenced by the interlayer time and the thickness of the samples. Fig. 84b compares the peak strength of the samples: here, a more marked difference among the specimen

manufacturing strategy is noticeable. Direct printed samples showed a peak strength of almost 31 MPa, which was higher than that of cut samples, which was 23 MPa (for cut samples with 2.5 mm of thickness) and 28 MPa (for samples with 3.0 mm of thickness). Finally, the samples cut from the box with Type V dimensions were characterized by even lower peak strength with a mean value of 21 MPa. This was due to the premature fracture of the samples in correspondence with the fillet's regions. Fig. 84c indicates a lower influence of the manufacturing strategy and the thickness of the sample of the elongation at rupture $\varepsilon_{max}$.

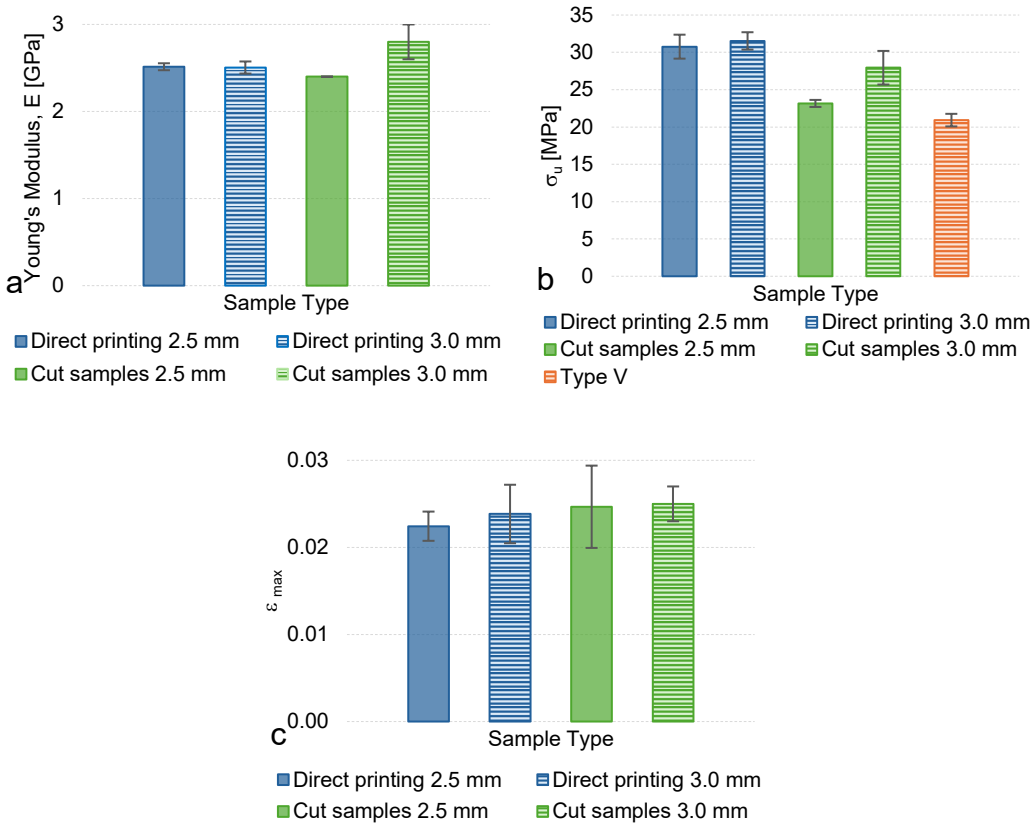



*Fig. 84 – Mechanical characteristics of the samples produced using different manufacturing strategies*

After the tensile tests, specimens of the latter experimental campaign were typically characterized by a fracture that occurred in the middle of the samples, although there were a few exceptions, particularly among some directly printed samples. Conversely, all the cut samples were fractured in the middle of the narrow region. Depending on the adopted sample preparation protocol, the samples exhibited different colors. After annealing, regardless of the production strategy, the samples displayed an opaque beige color, indicating the development of crystalline structures. In contrast, the samples cut from the box under the "as printed" condition exhibited a translucent brown color, suggesting that the material was

mainly in an amorphous state. Directly printed samples showed higher opacity and a lighter color, potentially indicating the onset of crystallization during printing. Fig. 85 shows the side view of the samples from which it is evident the different morphology of the samples in correspondence of the edges. Indeed, directly printed samples showed an irregular shape (typical of the MatEx process) while the samples cut from the box showed a more regular flat surface.

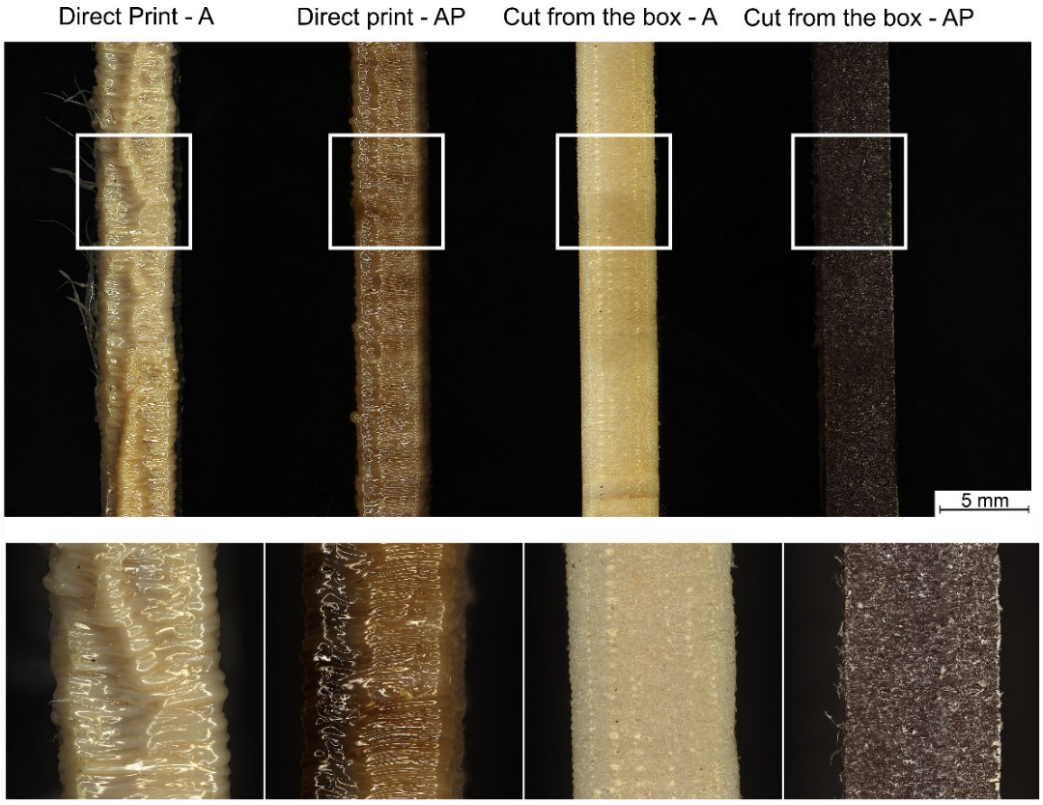



*Fig. 85 – Side view of the samples at low and higher magnifications*

Fig. 86 illustrates the stress-strain curves obtained from the tensile tests conducted using various sample manufacturing methods. Each curve exhibits an initial nearly linear rise in stress associated with the elastic region, followed by a peak load, and then a plateau, signifying the initiation of plastic deformation. In samples fabricated through direct printing, the load abruptly dropped to zero after minimal plastic deformation, resulting in brittle failure. Conversely, specimens cut from the box displayed a prolonged plastic deformation zone, characterized by significantly higher elongation at rupture. The main mechanical characteristics were identified from the stress-strain curves, including the Young's modulus, the elongation at rupture and the peak strength. This enabled a deeper comparison among the samples produced with different protocols.

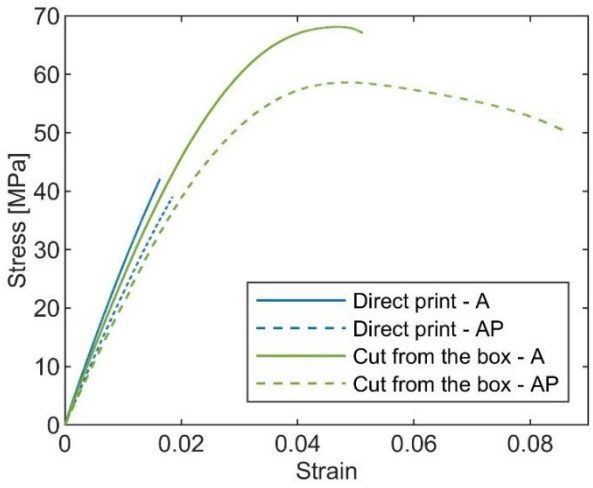



*Fig. 86 – Stress-strain curves of different samples produced with direct sample printing and cutting one*

Fig. 87a compares the Young's modulus. All the samples (except those cut from box under as printed conditions) exhibited a similar Young's modulus (with average value of 2.66 GPa), irrespective of the manufacturing conditions. Fig. 87b indicates that a more marked difference among the specimen manufacturing strategy is noticeable when considering the peak stress. Direct printed samples showed a peak stress of almost 31 MPa, which was lower than that of cut samples which was 69 MPa (for annealed cut samples) and 60 MPa (for cut samples "as printed"). Furthermore, the tensile strength of directly printed samples suffered of higher dispersion while that of samples cut from box was much more repetitive. Fig. 87c compares the elongation at rupture $\varepsilon_{max}$; even for the elongation at rupture there is a remarkable difference between specimen produced with direct printing and cut from the box. Direct printed samples showed a peak of $\varepsilon_{max}$ of about 2%; cut samples, on the other hand, showed higher elongation at rupture and its value is more influenced by annealing post-treatment. For samples cut from the box, annealed samples showed an average elongation at rupture of almost 6%, while as printed samples showed a value of 8%. This further confirms that substantial differences between as printed and annealed samples only occurred on cut samples, while negligible differences were observed in directly printed samples.

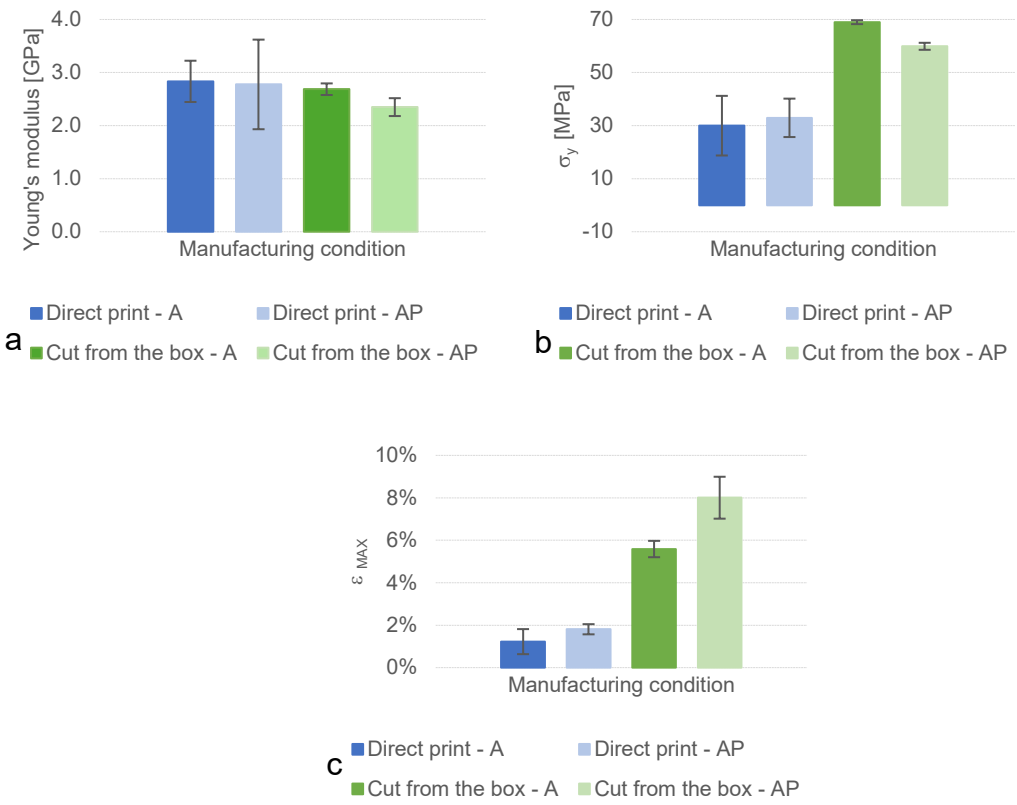



*Fig. 87 – Mechanical characteristics of the samples produced using different manufacturing strategies*

### 4.3.4 Optical analysis

Optical analysis conducted on specimens of the first experimental campaign allows to study the presence of porosities. The specimens with the lowest density are the direct printed vertical samples V1. The average density of the sample V1 is 1.14 g/cm$^3$, while the density of the corresponding "extracted" sample V2 is 1.20 g/cm$^3$, showing an increase for the extracted specimens of 5.3%. Fig. 88 shows the porosities present in the three types of specimens analyzed. Fig. 88a shows the porosities in the V1 specimens, which are much more evident than those in the V2 specimens, shown in Fig. 88b.

Fig. 88c shows the porosities present in the H1 samples, which are those directly printed in the horizontal direction. Observing how the porosities present a gradient in their distribution is possible. The lower area, in contact with the printing plane, shows almost absent porosities; while moving away from the printing plane, the porosities gradually increase.

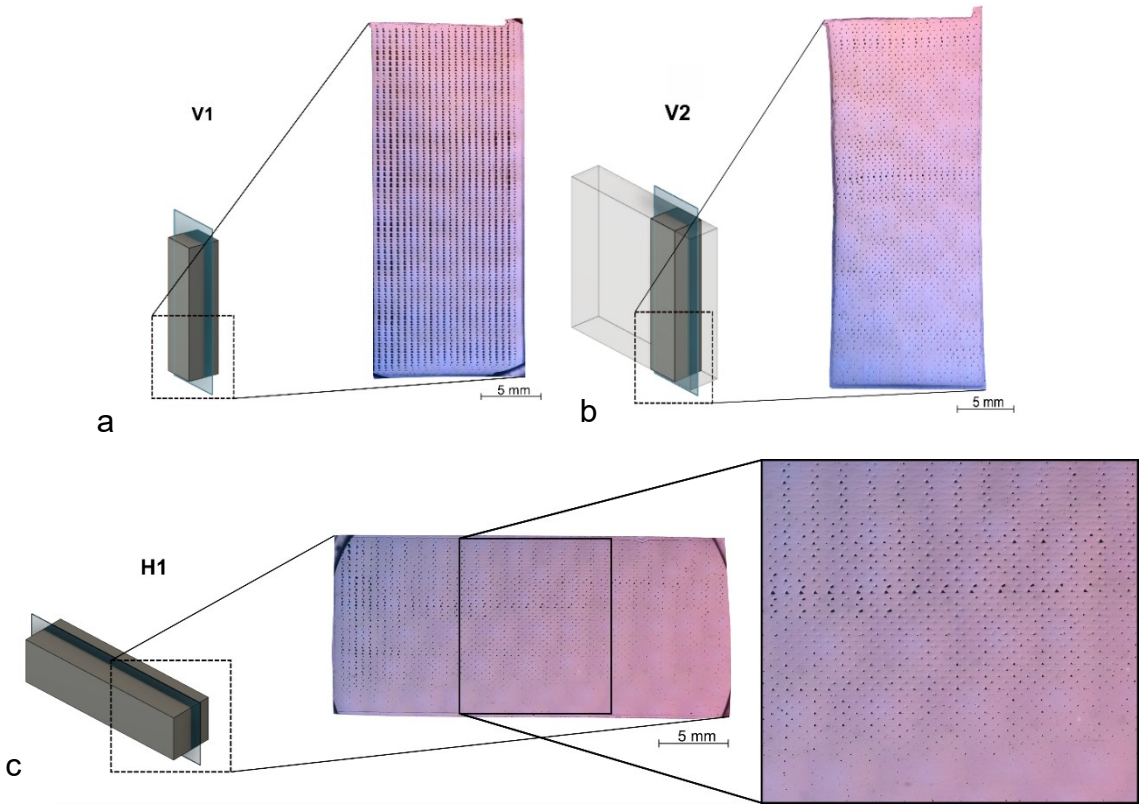



*Fig. 88 Porosities in direct printed vertical samples V1 (a), in corresponding "extracted" samples (b) and in direct printed horizontal samples H1 (c) with a zoom on their distribution*

Optical microscopy of the fracture surfaces was performed on specimens of both second and third experimental campaign to understand the influence of the sample manufacturing strategy on the failure modes.

Regarding the second experimental campaign, two main failures were identified in the samples: intralayer fracture and delamination. Intralayer fracture was observed on samples which showed the highest tensile strength. Herein, the adhesion between consecutive layers was so strong that a crack fractured some filaments (of the same layer). On the other hand, delamination (interlayer) involved the failure of the bonding between consecutive layers. The onset of delamination indicates a weaker adhesion produced during the MatExt process as compared to intrafilamentary fracture. However, even in delaminated samples, the fracture surfaces were different: in some cases, the fracture surface was characterized by irregular morphology indicating higher interlayer adhesion, while in other regions smoother surfaces were found indicating lower adhesion. Intralayer fracture was observed is directly printed samples (irrespective of the thickness) as well as in cut samples with thicker wall (3.0 mm of thickness). This further confirms how the manufacturing strategy, and the thickness of the sample can influence the mechanical behavior and more specifically the

fracture strength of components made by the MatExt process. A higher magnification (SEM) image of intralayer fracture is reported in Fig. 89. From this picture, it is evident the strong adhesion that arises between the layers.

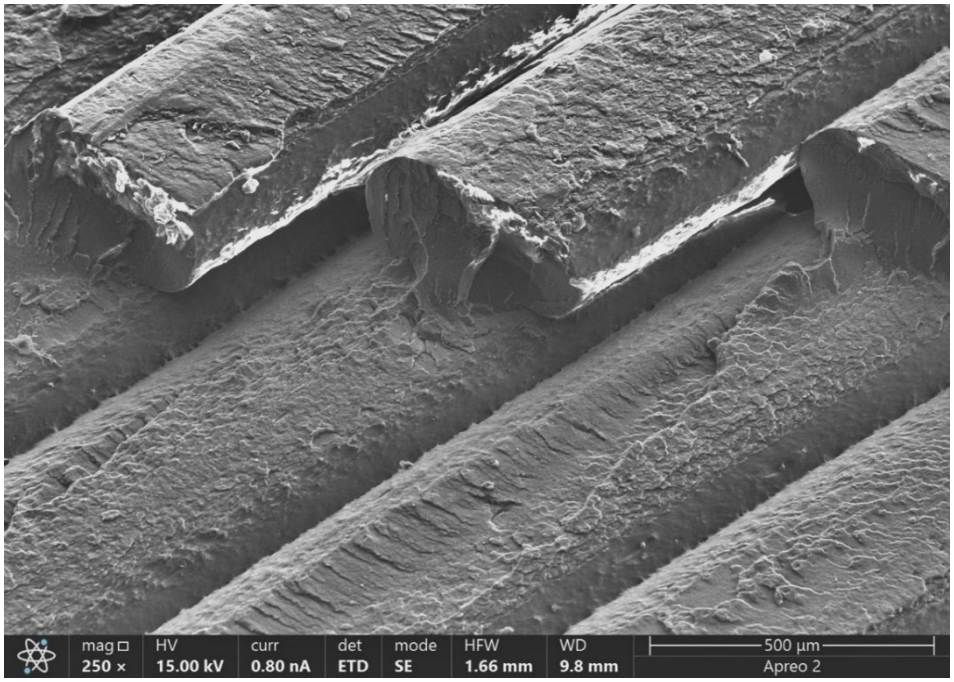



*Fig. 89 – SEM image of the intralayer fracture of a specimen made by direct printing*

Cross sectional analysis was performed on samples produced through direct printing and cutting from the plate, as depicted in Fig. 90. The cross sections show the interfilamentous porosities that develop between adjacent filaments. As can be observed, the porosities in the directly printed samples are larger than those observed in the cut samples, as also confirmed by the histograms reported in Fig. 91.

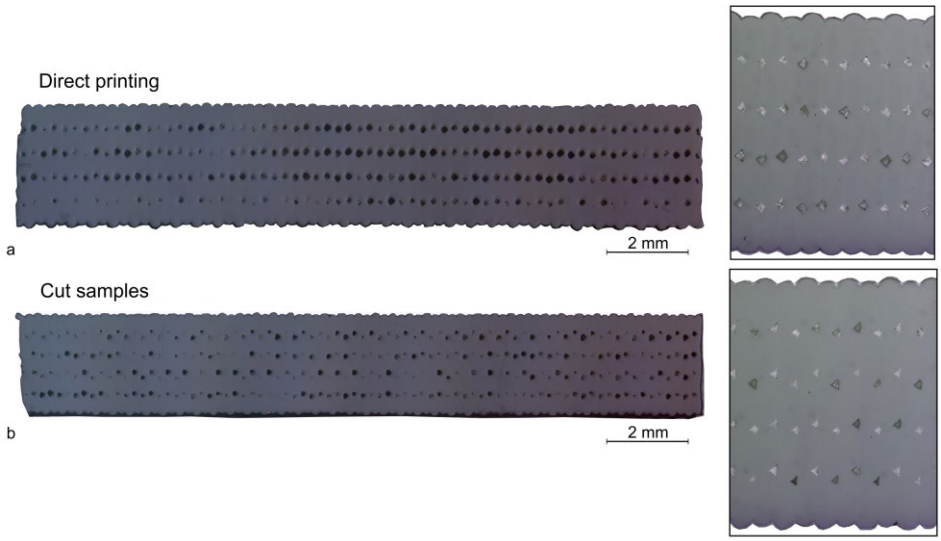



*Fig. 90 – Cross sections of (a) directly printed and (b) cut samples*

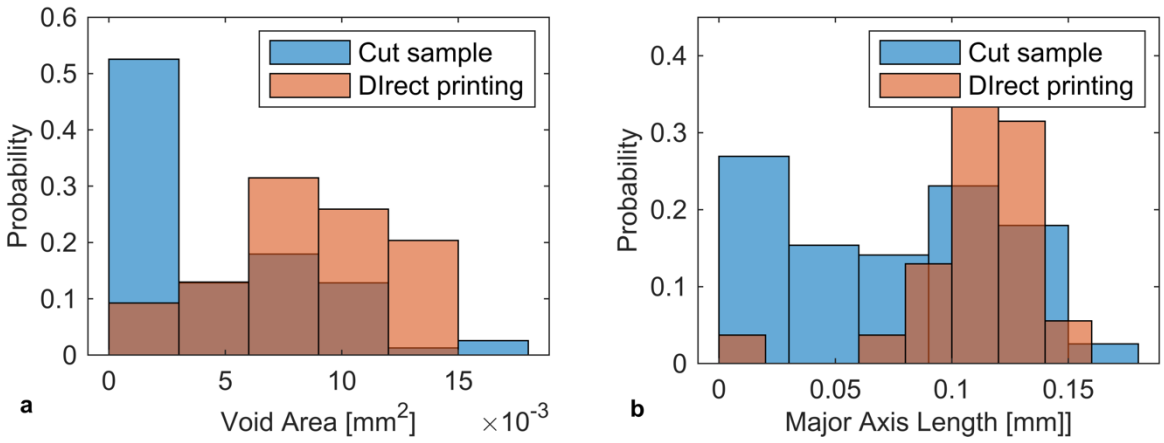



*Fig. 91 – Dimensional characterization if interlayer voids produced on samples made by direct printing and cutting*

On the other hand, specimens of the third experimental campaign, depict an opposite distribution of porosities: as can be inferred from Fig. 92, a higher number of porosities distributed in a more regular pattern is evident on the sample cut from the box.

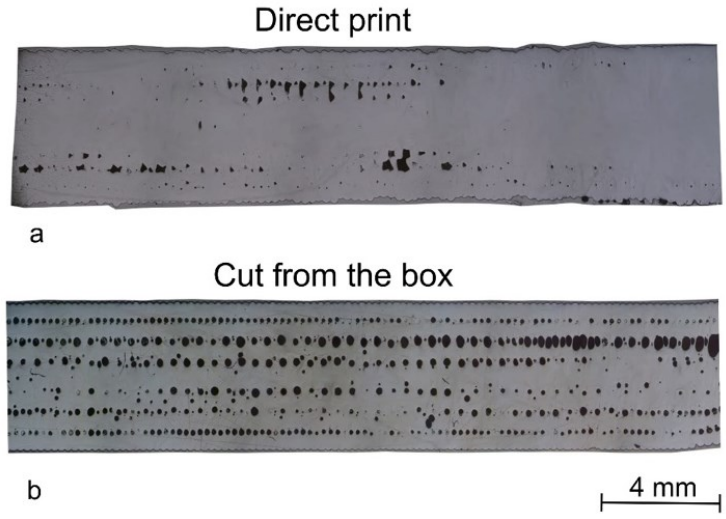



*Fig. 92 – Cross section of (a) directly printed sample and (b) cut sample. (SECT. AA-Direct print and SECT. BB-Cut from the box)*

Directly printed samples failed by interlayer delamination (irrespective of being under "as-printed" or "annealed" state). This failure mode was also observed in cut samples under as printed condition. On the other hand, cut samples under annealing condition failed by intralayer fracture, as shown in Fig. 93a. This failure mode is indicative of a much stronger adhesion between the layers achieved through the annealing post-process. Indeed, the adhesion between consecutive layers was found to be so robust that a crack caused the fracture of several filaments within the same layer. Conversely, delamination, referring to the separation between consecutive layers, demonstrated failure in the bond strength

between these layers. The occurrence of delamination suggests a relatively weaker adhesion resulting from the Material Extrusion (MatEx) process, in comparison to fractures occurring within the filaments themselves.

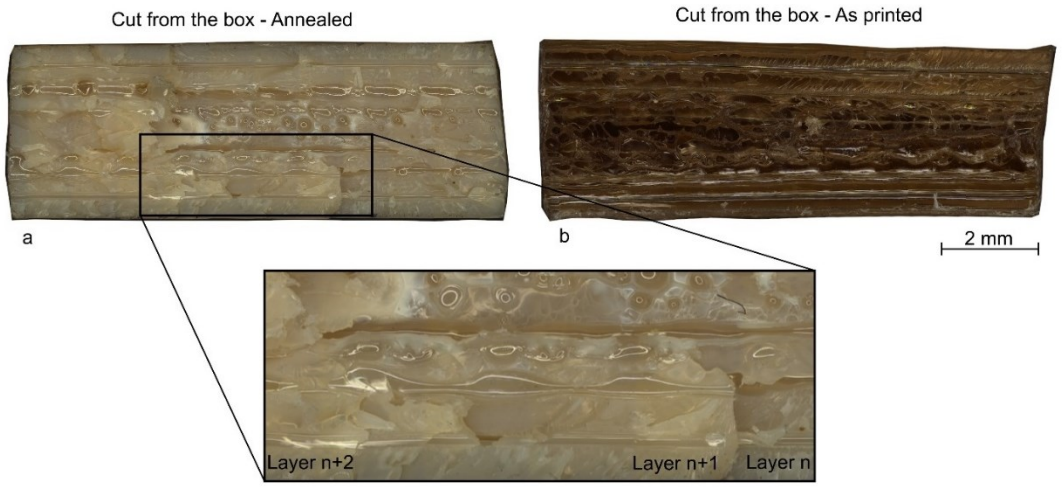



*Fig. 93 – Fracture surfaces of cut samples under (a) annealing and (b) as printed conditions*

### 4.3.5 Geometrical artifacts

During the deposition of relatively small features (as compared to the nozzle diameter), some geometrical artifacts can develop. The main cause is the acceleration/deceleration regions that occur at the directly printed samples edges. Indeed, at the edge, the extruder change in direction leads to an acceleration up to the selected printing speed from zero. Similarly, as the extruder approaches to the edges, it decelerates from the set speed to zero. Hence, in correspondence of the edges the high pressure of the material within the nozzle involves a higher amount of material which is deposited leading to an uneven deposition (edge effect). Although in correspondence of the edges higher adhesion is observed, this clearly alters the mechanical behavior exhibited by the direct printed samples leading to superior mechanical behaviors as compared to a larger component.

Within acceleration and deceleration ramp regions, uneven material flow is produced since the difficulty (for the MatEx machine) to precisely control the material feeding under such speed gradients. This is also due the low viscosity of the material and pressure variations within and underlying the nozzle, which makes very complex the material flow control under unsteady deposition conditions. Fig. 94a depicts a 3D view in false colors of a fractured cross section of a directly printed sample. As can be noted, the fracture surface morphology indicates a different adhesion from the left side (where a smoother surface is observable) from the right side where a more fragmented surface is shown. This indicates an uneven

adhesion within the sample. On the other hand, Fig. 94b shows the fracture surface of a cut sample (after annealing). Here, the picture shows a more regular (and rectangular) shape and more homogeneous conditions of adhesion.

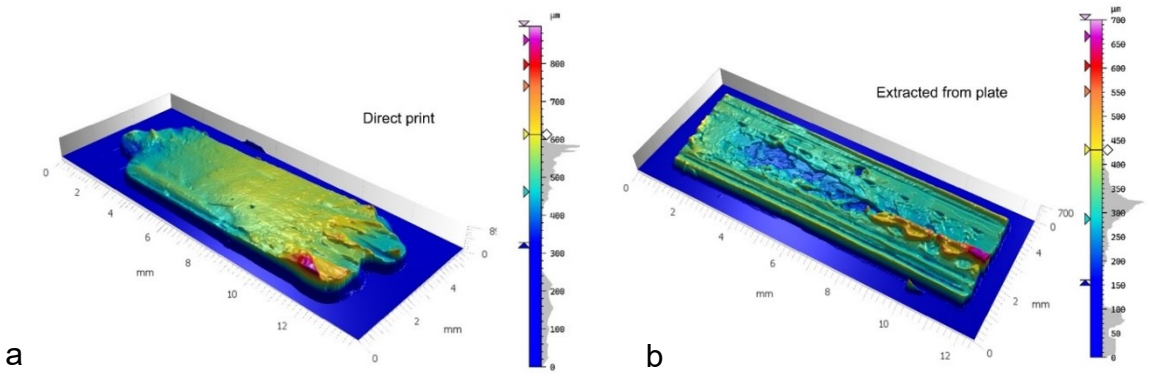



*Fig. 94 – 3D analysis of the fracture surfaces showing (a) directly printed sample and (b) cut sample both under "as printed condition"*

More precise observations of the fracture surfaces were conducted using Scanning Electron Microscopy (SEM). As depicted in Fig. 95a, the fracture surface of a directly printed sample tested after the annealing post-process exhibits an almost monolithic appearance, indicating robust adhesion between paths within the same layer. This was due to the relatively short interlayer time that increased the adhesion of paths within the same layer. However, the surface appears relatively smooth, confirming the comparatively weak interlayer bonding that resulted in delamination of the sample (owing to the incipient crystallization). In contrast, Fig. 95b displays the fracture surface of a sample cut from the box following the annealing post-treatment. The morphology of this fracture surface markedly differs; characterized by a highly fragmented appearance and intralayer fractures. This disparity underscores the significant differences in material deposition between directly printed samples and those obtained via cutting from the box.

To examine the characteristics of the samples produced with different strategies, differential scanning calorimetry tests were performed on all the samples of the third experimental campaign. Fig. 96 depicts the DSC results for samples directly printed and cut from box under as printed and annealed states.

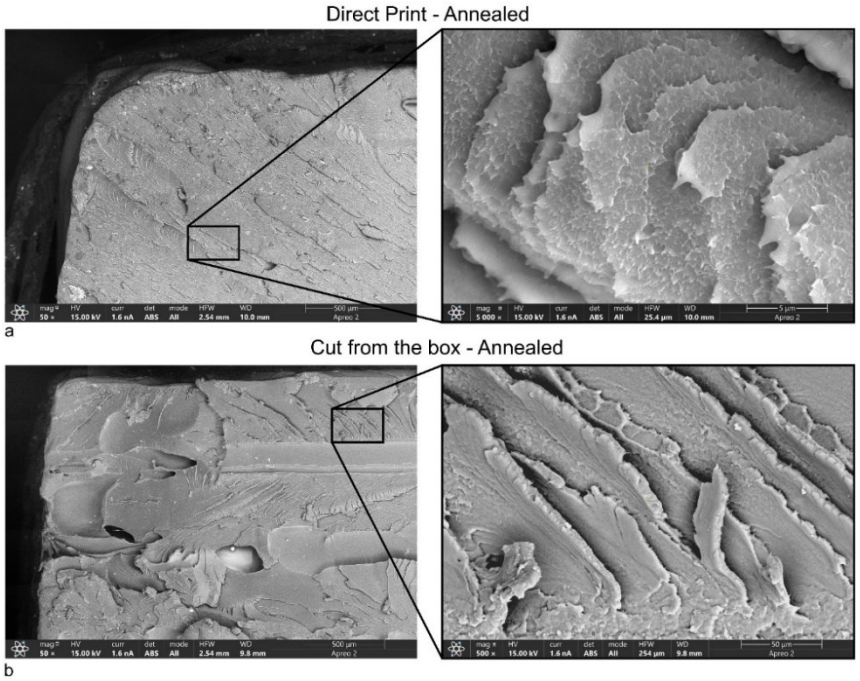



*Fig. 95 – Fracture surfaces observed through SEM of (a) directly printed and (b) cut from the box samples both after annealing*

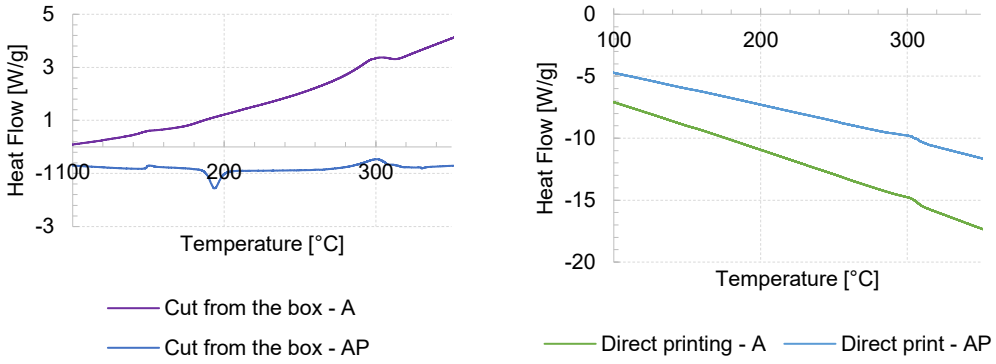



*Fig. 96 – DSC curves of the samples produced through different deposition and post-processes conditions*

The melting enthalpies and the cold crystallization enthalpies were calculated for each condition to determine the crystallization percentages, which are summarized in Table 17.

*Table 17 – Measurement of enthalpies and crystallinity of the samples produced through different deposition and post-processes conditions*

| *Manufacturing Condition* | $\Delta H_{Cryst}$ *(J/g)* | $\Delta H_{Melt}$ *(J/g)* | $\chi$ *(%)* |
|---|---|---|---|
| *Direct print – As Printed* | - | 15.01 | 11.55 |
| *Direct print – Annealed* | - | 15.11 | 11.62 |
| *Cut from the box – As Printed* | -16.66 | 20.91 | 3.27 |
| *Cut from the box – Annealed* | - | 15.31 | 11.77 |

As can be inferred, the percentage of crystallinity of the samples cut from the box under "as printed" condition was 3.27%; such value was much smaller than that achieved after the annealing post-treatment (11.77%). These values confirm the almost amorphous nature of the as printed samples cut from the box and the increase in the crystallization after the annealing process. On the other hand, the directly printed samples under "as printed" condition showed a much higher percentage of crystallinity (12.18%). This confirms the onset of an incipient crystallization achieved during the deposition process owing to the smaller layer dimension which led to shorter interlayer time and higher substrate temperature. This promoted the crystallization observed on the directly printed samples under "as printing" conditions.

### 4.3.6 Thermal analysis

The temperature of the sample during the printing process was monitored with the aim of determining how the different sample dimensions affect the thermal history and, consequently, the polymer chain entanglement that determined the fracture strength of the samples.

Fig. 97 refers to specimens of the first experimental campaign and it illustrates thermal infrared (IR) images captured at various stages during the deposition of directly printed samples. The images vividly display temperature variations within the printed structure. Initially, the upper layers exhibit higher temperatures immediately after deposition, reflecting their recent extrusion. However, the temperatures in these upper layers quickly decrease due to heat diffusion toward the underlying layers and heat dissipation into the surroundings through radiation and convection. This rapid cooling results in a substantial drop of approximately 80‑90 °C in filament temperature. In contrast, the first layers, in direct contact with the build platform, maintain a relatively higher temperature, approximately 60 °C, even after an extended period since deposition. This sustained temperature can be attributed to the continuous heat exchange between these layers and the build platform. The thermal images of the directly printed samples also reveal distinct horizontal temperature gradients. The isotherms exhibit a characteristic parabolic pattern, which arises from increased heat dissipation at the sample corners compared to the sides. This gradient in temperature distribution highlights the complex thermal dynamics within the printed structure.

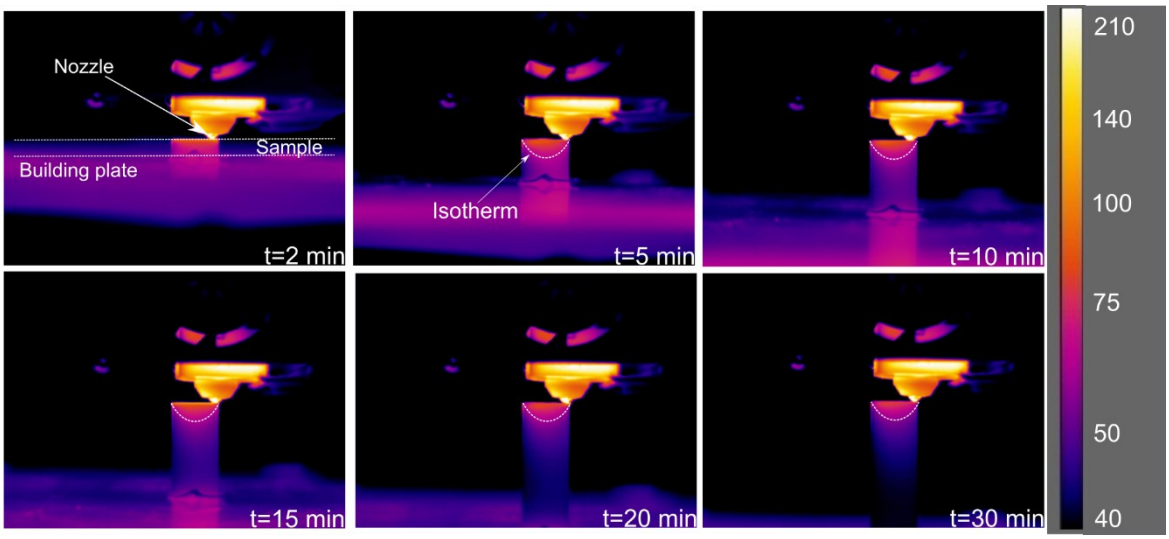



*Fig. 97 – IR maps recorded at different deposition times during 3D printing of a single sample*

The sequence of the IR images of the directly printed samples deposited in parallel (four at a time) has been reported in Fig. 98. The IR map indicates a smoother gradient of temperature as compared to that observed during single-sample printing. In addition, the average temperature was much lower. Both these phenomena were addressed to the longer interlayer time that promoted higher heat diffusion and heat loss when four specimens were printed instead of only one.

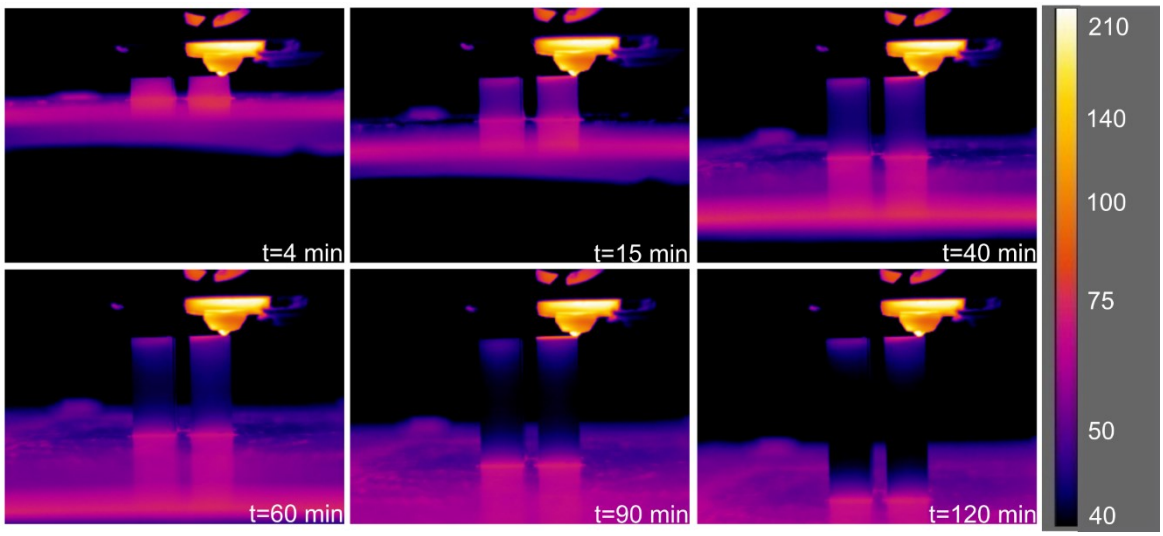



*Fig. 98 – IR maps recorded at different deposition times during 3D printing of four samples (two samples are behind the shown ones)*

The thermal infrared (IR) images, as depicted in Fig. 99, distinctly highlight a contrasting thermal distribution pattern measured on the plate. Notably, a considerably steeper temperature gradient is observed in the vertical direction, particularly just beneath the

deposited layer. This gradient is a consequence of the significantly longer interlayer time, which is directly proportional to the layer's surface area. In contrast, these images reveal negligible horizontal temperature gradients within the printed structure.

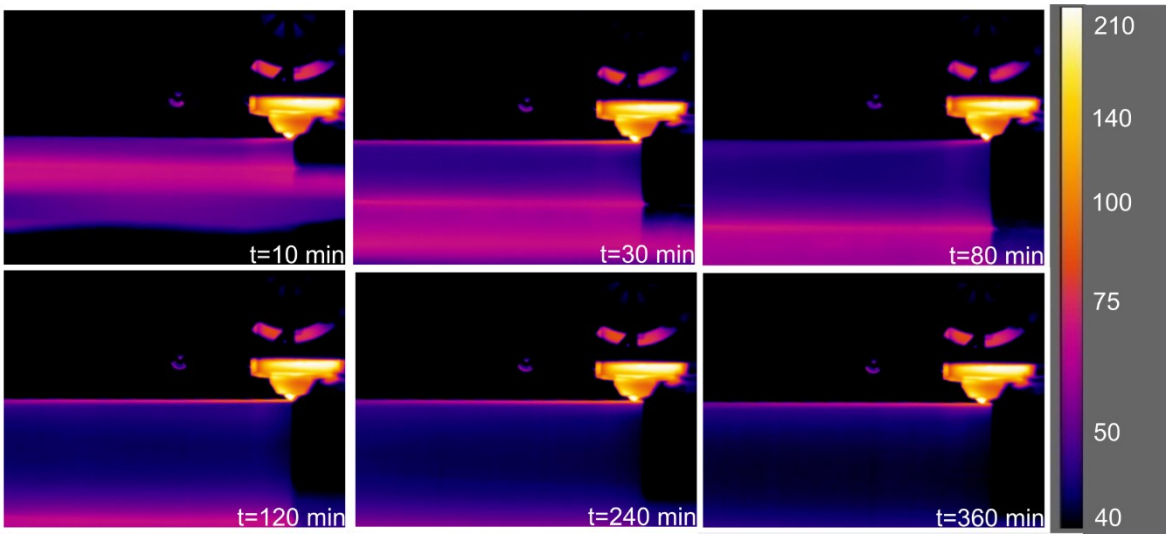



*Fig. 99 – IR maps recorded at different deposition times during 3D printing of the plate*

Further analysis was conducted to assess temperature variations within the actual layer. A fixed point (region of interest) was strategically placed at the center of the layer to monitor temperature fluctuations. As illustrated in Fig. 100, the temperature exhibits a periodic trend corresponding to the nozzle's motion along the layer. Notably, when the nozzle passes through the ROI (Region Of Interest), the temperature reaches a peak and quickly decreases. Comparing the temperature data collected under the three deposition conditions, it is evident that the average temperature of the actual layer varies. The average temperature for direct printing of a single sample was 93 °C, while it was 56 °C for direct printing of four samples in parallel. In contrast, the average temperature for the larger component was 43 °C. This variance can be attributed to the significantly smaller dimensions of the layers in the plate sample, which are nearly six times smaller. Therefore, it is apparent that the direct printing of a single sample, or even four samples in parallel, introduces more significant artifacts compared to plate printing, potentially impacting intermolecular diffusion, entanglement, and crystallinity.

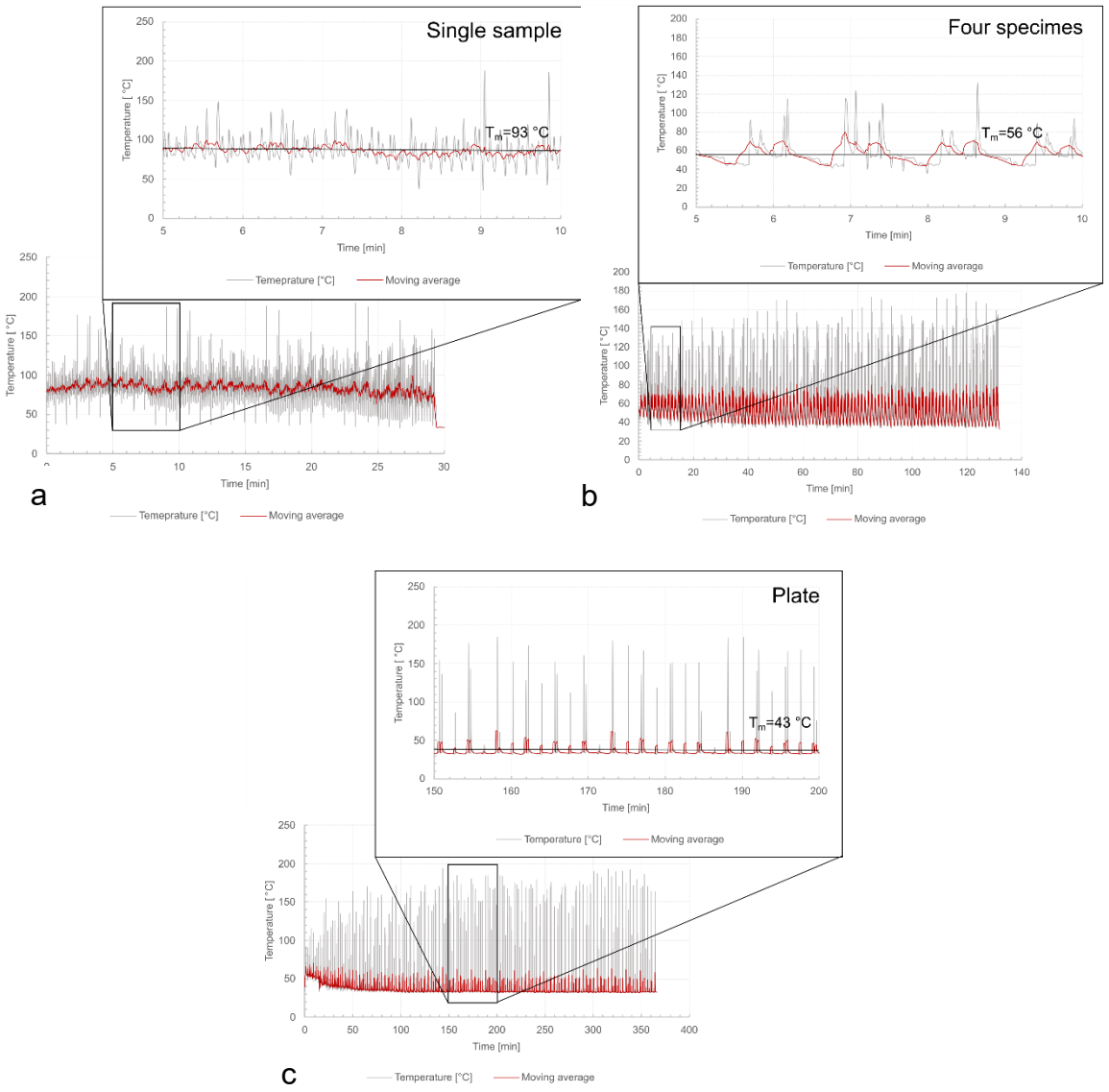



*Fig. 100 – Thermal history measured at the actual printing layer during the sample deposition using three strategies: (a) direct printing of one sample, (b) direct printing of four samples, and (c) printing of a plate*

On the other hand, Fig. 101 refers to specimens of the second experimental campaign and it compares the IR maps recorded during the deposition of directly printed samples and a box (from which the samples will be cut). The temperature maps indicate a sudden cooling of the layer just after it is deposited, irrespective of the type of sample. A deeper analysis of the temperature trend was performed using a measuring point. This enabled the temperature variation to be evaluated during the deposition. As can be inferred, the temperature trends repeat periodically, where the period is the interlayer time. This can be better observed in the zoom-in plot shown in Fig. 101c. As can be observed, during the depositing of directly printed samples, the temperature of the substrate is higher than that measured in larger components. This is due to lower interlayer time for 2.5 mm of thickness (9.3 s) and 3.0 mm

of thickness (10.8 s) as compared to the production of the box whose interlayer time requires 29.9 s. Consequently, when direct samples are produced higher substrate temperature is faced (125°C vs. 79°C) leading to higher intermolecular chain entanglement. This in turns enhances the strength of the samples printed directly leading to an artificial higher strength as compared to samples extracted from a larger component.

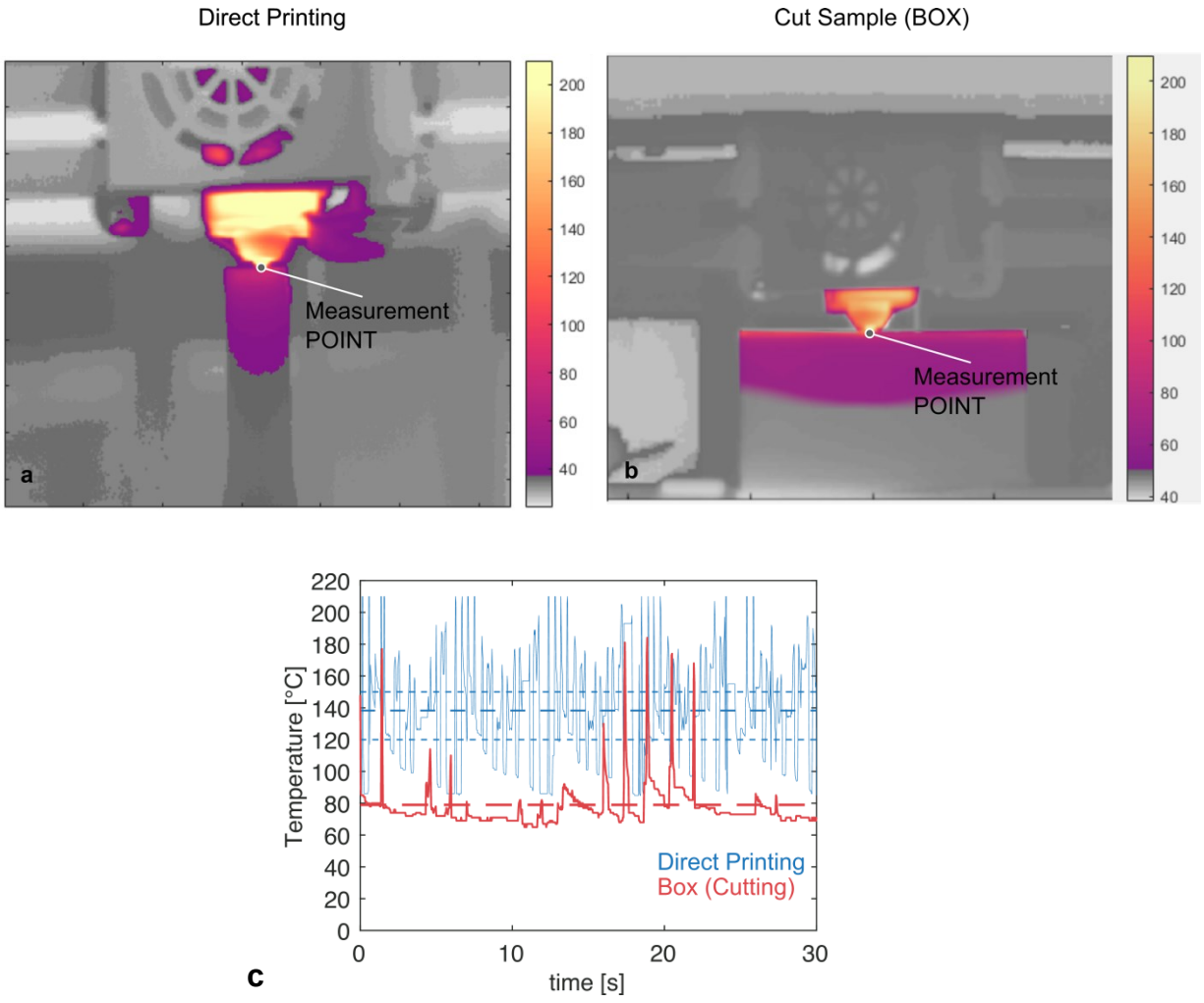



*Fig. 101 – Infrared pictures acquired during deposition of (a) direct sample printing and (b) box printing for sample cutting; (c) Thermal history recorded during deposition of direct samples and box*

# Chapter 5 – Results analysis and Discussion

Additive Manufacturing technologies are rapidly evolving from a rapid prototyping niche to a suitable solution for producing customized components, small batches, and even unique components manufacturing. This is due to several advantages, including the possibility of producing highly customizable products, economic suitability for small batches (even unit batches), extreme geometrical flexibility, distributed production, on-demand production, shortening of the supply chain, and the possibility of continuously improving component performance with real-time feedback. So far, applications of AM processes in fields such as biomedical and aerospace are growing significantly. This demands a deep understanding of the AM components' behavior and physical and mechanical properties.

Among different AM processes, material extrusion is gaining great diffusion since different advantages over other AM processes of plastics, including the more effortless scalability, higher material deposition rate, possibility to produce reinforced plastics even with long fibers, chance to embed electrical circuits or other materials, and the broader availability of raw materials and lower costs. The growing adoption of additive manufacturing components for structural applications is rapidly pushing attention to product qualification and the assessment of mechanical behavior.

To this end, the ability to predict the mechanical behavior of the components and how this is influenced by the parameters of the printing process is crucial. The mechanical behavior depends on different aspects, including the raw material, process parameters, the adopted AM machine, and the geometry of the component. Thus, adopting reference samples, which are often characterized by simpler geometries, may lead to an unreliable prediction of the mechanical behavior of the actual part.

## 5.1 Impact of porosity on mechanical properties

One of the aspects that most limit the mechanical characteristics of the components obtained by additive manufacturing is represented by the internal voids of the components. This is particularly significant in the material extrusion process, due to the high viscosity during the deposition phase. The presence of such voids affects several aspects of a physical nature (e.g. density, thermal conductivity), and of a mechanical nature (stiffness, yield strength, etc.). Even though the weight and volume measurement can be used to determine the density of the components, this approach is not suitable for complex shapes. In addition, as mentioned

above, the density of a component is also highly influenced by geometry; consequently, the average density cannot be representative of the local properties. On the other hand, X-ray computed tomography analysis produces a digital twin of the actual part. However, the application of this method is limited since the cost of the equipment, long scanning time, and the maximum dimension of the part being tested. On the other hand, the cross-sectioning approach of the actual part is unfeasible. Indeed, it is a destructive method, which requires a physical twin of the actual component to be used for cross-sectioning. This would lead to a significant waste of material and production time. In addition, observations of the porosities through optical microscopy are highly time-consuming since it involves different phases, including cutting, molding, lapping, ultrasonic cleaning to remove possible material flowing within the voids, and optical observation. Consequently, also, this approach is not suitable for the needs of production, but it can provide some interesting information about printed parts.

For what has been said so far, a need arises to analyze the porosity present within components made by material extrusion in a different way than procedures performed traditionally. The presence of such porosities has a very high impact on the density of manufactured components. Another important issue of these components is their local characterization instead of global characterization that is usually conducted on specimens. The force-displacement features determined during instrumented indentation tests showed a high correlation with the components' density, regardless of the direction of testing [166]. The test performed on horizontally printed samples indicated a high correlation between the force-displacement curves and the porosity measurements regardless of both the tool diameters used in the indentation tests ($D$ = 2 mm and $D$ = 4 mm). The correlation coefficient on these samples ranged between $R^2$ = 0.93 and $R^2$ = 0.98 depending on the measurement procedure (during the loading and unloading phases) and the tool diameter. On the other hand, when testing the vertically oriented samples, the adoption of the larger tool is mandatory. Indeed, the tests conducted by the smaller indenter ($D$ = 2 mm) resulted in a weak correlation between the characteristic indentation slopes and the density ($R^2$ was lower than 0.6). On the other hand, the correlation between the force-displacement slopes and the porosity using the indenter with $D$ = 4 mm were $R^2$ = 0.94 and $R^2$ = 0.96 (in loading and unloading phases, respectively). This indicates the excellent capability of the proposed methodology to determine the local properties of the components.

The execution of the indentation tests also enabled to investigate the influence of the selected pattern during the printing on mechanical properties. External shells, if they are involved, are typically deposited first during the deposition of a layer; then, the process proceeds towards the inner shells. Thus, different deposition conditions are experienced depending on the position of the distance from the external layer perimeter. Fig. 102 depicts a schematic of the other deposition conditions occurring during the layer formation with different colors. As mentioned above, the outer layers were first deposited.

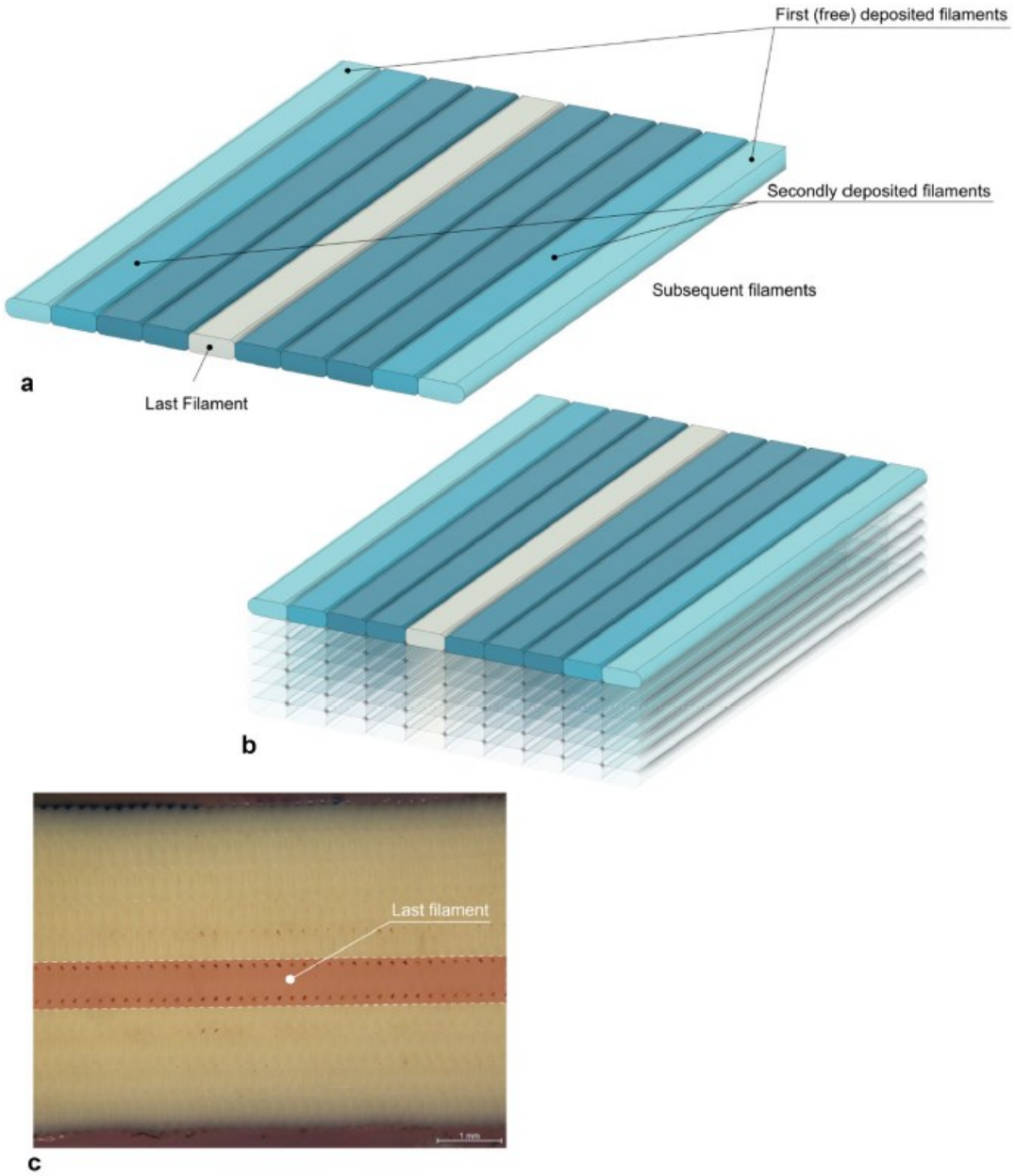



*Fig. 102 – (a) Schematic of the different material flow conditions arising during the deposition of subsequent shells as moving from the outside perimeter shells towards the core of the layer and (b) during the deposition of subsequent layers; (c) uneven porosity distribution in the central zone*

Therefore, during the deposition of the external shells, barreling edges were produced. Inner shells were deposited differently. Indeed, the material flow of the inner shell was partially constrained by the presence of the filaments already deposited. Therefore, barreling was hindered from the side in contact with the already deposited layer. This was perpetrated as going towards the layer core until the last layer was deposited. Here, the last filament was constrained from both sides, leading to a different material flow than previously deposited filaments. The other deposition conditions lead to an uneven porosity distribution, as depicted in Fig. 102c. Such porosities participate differently when testing horizontal and vertical samples. Indeed, as schematized in Fig. 103a, during the indentation tests of vertically printed samples, the tool plunges into the barreled side of the external shells. According to the sample orientation, all types of shells (outer to the inner) were loaded during the indentation. On the other hand, during the indentation of the horizontally printed samples, the tool plunged the top (flat) surface of the sample, and only the inner shells were loaded, as depicted in Fig. 103b. While testing vertically printed samples, the load is spread (vertically) over all "types" of deposition (shells with different colors). On the other hand, during indentation tests of the horizontal specimens, the external shells do not contribute to balancing the load exerted by the indenter.

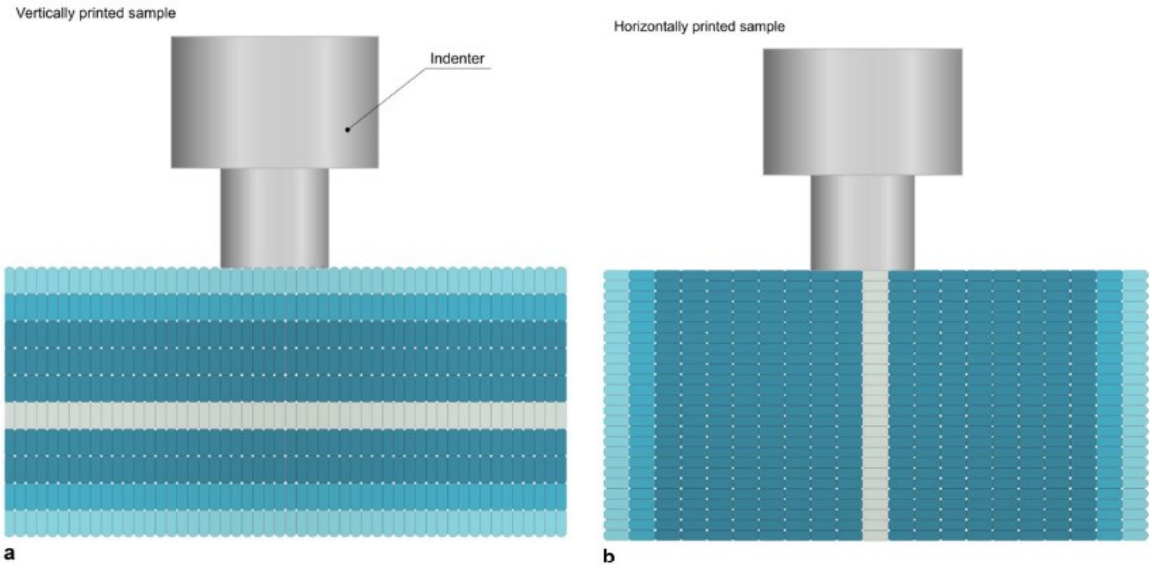



*Fig. 103 – Schematic of the loaded shells tested during indentation tests on (a) vertically and (b) horizontally printed samples*

These different load distribution patterns can explain why in the case of vertically printed samples the adoption of larger indenter (D=4 mm) is mandatory to carry out the tests.

Indentation tests can also determine a component's local yield strength, and this value can be correlated to the compressive yield strength [167]. Since indentation produces compression rather than tension, it can be better correlated to the compressive properties of the component. It is important to note that through the indentation test, it is possible to determine the value of the yield strength by fixing the crosshead displacement to a value smaller than 1 mm. This allows for a negligible imprint on the specimen. An empirical relationship between the yield strength measured through the compression test and the normalized strength determined during the indentation test was determined. The coefficient of determination $R^2$ = 0.92; this indicates that the indentation tests can be successfully employed to determine the local properties of the components made by material extrusion.

To verify the relationship between density, porosities and mechanical characteristics, further analysis was conducted [169]. Some specimens were subjected to a thermomechanical compaction process before the compression test. This process has led to the production of specimens with a density of 1.25 g/cm$^3$, which equals the density of the base material.

The thermomechanical compaction process also eliminated the typical layer-by-layer finish present on all MatExt components. The samples made by MatExt showed characteristics similar to those made by thermal compaction. The yield strength of the specimens was substantially related to the relative density of the component. However, the characteristics of post-yielding are different. While compacted specimens showed marked strain softening, MatExt specimens are characterized by a lower stress drop. This difference was related to the lowest cooling rate during thermal compaction leading to greater aging of the polymer.

Through the realization of compression tests at different deformations and the cross-sectioning, it was possible to qualitatively observe the deformation field. In fact, the samples showed three different regions: (1) shear bands where the deformation localization takes place (and to which strain softening is linked); (2) dead material region−in contact with the compression planes where there are minor deformations; and (3) side region where partial deformation occurs. The increase in the deformation rate led to an increase in yield strength but also to a greater localization of the deformations (as depicted in Fig. 104) and consequently a greater strain softening.

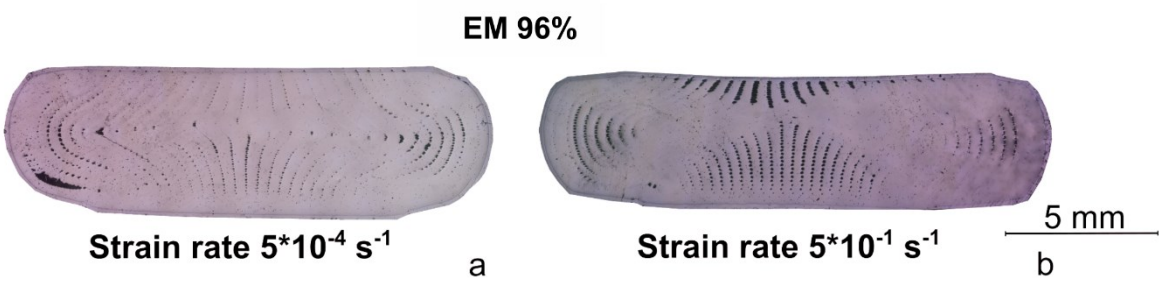



*Fig. 104 – Effect of the strain rate (during the compression tests) on the distribution of the voids*

Furthermore, the cross-sections of the samples revealed an uneven distribution of the porosities along the vertical direction. The bottom of the samples was characterized by smaller voids. As shown in Fig. 105, this region (in contact with the building plate) was approximately 1.5 mm in height. Thus, this region is more compact than the overlying layers. During the deposition process, the temperature of the building plate was set to 60°C. Such value was higher than the $T_g$ of the adopted PLA (55°C). Consequently, the molecular chains within these regions rearranged leading to a much more compact arrangement.

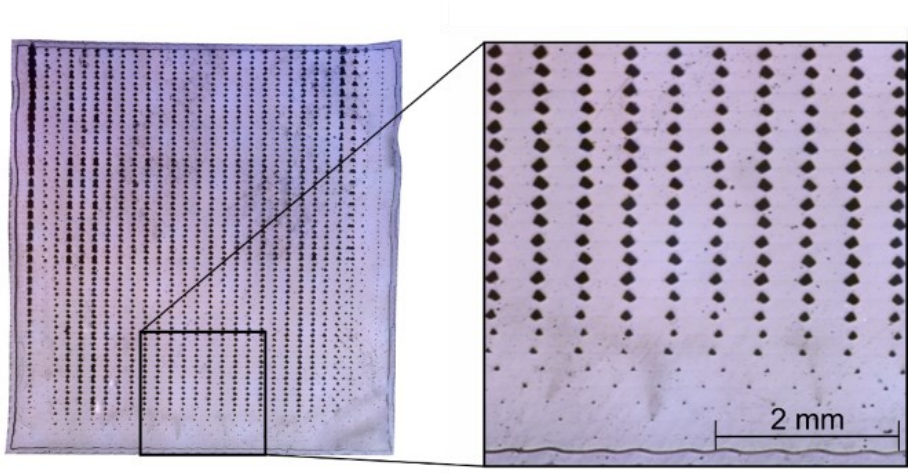



*Fig. 105 – Higher magnification of a printed sample showing smaller voids in contact with the building plate*

## 5.2 Influence of process parameters on the interlayer fracture toughness

The investigation into the impact of deposition strategy, encompassing material flow and travel speed, on interlayer adhesion in the material extrusion (MatEx) process has yielded significant insights. The MatEx process, while celebrated for its efficiency and versatility, hinges on the cohesive strength of interlayer bonds to ensure mechanical integrity. The experimental tests conducted, employing mode I fracture toughness as a pivotal parameter, shed light on the nuanced interplay between deposition parameters and the resultant

interlayer adhesion. The interlayer adhesion of material extrusion parts relies upon inter-diffusion and entanglement of the polymer across the interlayer interface through reptation [164]. Steep temperature drop imposed immediately after the extrusion prevents the complete healing between the two consecutive layers [195]. The healing process proceeds until the temperature is higher than the glass transition temperature. The quality of interlayer healing can be indirectly measured through mechanical tests. A new specimen type that can measure the interlaminar fracture toughness in mode I crack opening for additive manufacturing components was introduced [171]. The new sample was designed to overcome the limitations of the classic DCB specimen when utilized for material extrusion specimens, including manufacturing, human-induced variability, and induced alteration of the thermal cycle owing to the pause time required by the insertion of the tape. The proposed specimen with pre-crack and removable spacers appears to be an effective type of sample for conducting the mode I fracture toughness characterization, delivering almost identical results with the conventional specimen with the release film when the ASTM D5528 test execution is applied. From the analysis of the results, the critical energy release rate of the new specimen type appeared to be slightly higher compared to the conventional sample with the release film. In fact, the crack in the classic specimen with the release film propagated in the midplane, sometimes also unstably, in pure mode I while in the case of the specimen with the slot the filaments interface appeared to be more resistant causing a stable crack propagation but with a crack that exfoliated the adjacent filament layers. This is explained mostly by the different temperature cycles that are applied during the printing process, a fact that is also supported by the different fracture modes obtained by the experimental campaign.

Experimental tests were then aimed at studying the influence of process parameters on failure modes [172]. Specifically, the effect of material flow and printing speed were analyzed. The observed trend indicates a profound influence of material flow rate on interlayer adhesion. Optimal material flow facilitates consistent layer bonding, minimizing the potential for voids or irregularities. The results revealed unanticipated trends. An increase in the extrusion multiplier, which correlates with a reduction in void dimensions, is anticipated to enhance deposition toughness. Conversely, the highest energy release rate was observed at a deposition speed of 1000 mm/min (the minimum deposition speed used) and 100% infill (representing the intermediate infill percentage). Under these conditions, with filaments oriented at ±45°, the energy release rate GIc reached 7.5 kJ/m$^2$. However, the same deposition conditions resulted in significantly weaker deposition when the filaments were

oriented at 0/90° relative to the sample direction. A balanced approach, yielding a high energy release rate for both 0/90° and ±45° loading directions, was achieved with a deposition speed of 2000 mm/min and an intermediate infill percentage of 100%. This finding suggests that the highest infill percentage does not necessarily provide the optimal solution. Fracture surface analysis indicated weaker interlayer adhesion with an extrusion multiplier set at 104% compared to 100%. Temperature analysis during the MatEx process revealed significant differences in mean temperature associated with varying extrusion multipliers. Additionally, higher printing speeds and increased material flow (via higher extrusion multipliers) may result in incomplete filament melting. This incomplete melting can contribute to increased crystallization during deposition, originating from existing crystalline regions in the filament. Such crystallization is detrimental as it can impede molecular chain mobility, thereby reducing interlayer molecular chain entanglement.

The intricate link between travel speed and interlayer adhesion was elucidated. Slower deposition speeds exhibited a positive correlation with enhanced interlayer bonding, aligning with the fundamental principles of the material extrusion process. The travel speed influences the melting degree reached by the polymer inside the extruder through the residence time. The higher the travel speed, the shorter the residence time is. This leads to an incomplete melting that induces faster solidification [196]. On the other hand, higher travel speeds led to diminished interlayer adhesion, emphasizing the significance of finding an equilibrium between efficiency and structural integrity. The material flow, which was varied through the extrusion multiplier, also showed a strong influence on the interlayer adhesion. This effect was more pronounced in sample printed at lower deposition speeds. Under such conditions, the adoption of higher extrusion multiplier yielded to weaker interlayer adhesion even though it yielded higher mean temperatures of the substrate. This effect was addressed to two phenomena: incomplete melting of the crystalline phase within the filament and the possible development of crystalline phase during the deposition owing to different cooling rates.

These findings underscore the significance of meticulous parameter control to achieve optimal interlayer bonding. This understanding contributes to advancing the efficacy and reliability of additive manufacturing processes, fostering enhanced component integrity in various applications.

## 5.3 Impact of manufacturing strategies on mechanical properties

The accurate identification of the mechanical behavior of the components made by material extrusion is mandatory. Besides, unreliable characterization procedures may lead to underestimation or overestimation of the mechanical properties. This may lead to oversized structures in aerospace components, which would tremendously increase the space mission cost (the cost for getting a kilogram of material in orbit is 5‑10 k€). On the other hand, overestimation would lead to under sizing of the component with possible failure without the possibility of maintenance. These events make even more demanding the need for accurate characterization of these components and the definition of a reliable procedure.

Thus, different causes of artifacts produced during direct sample printing were identified. These included different thermal histories, (edge) regions where the deposition direction is inverted, rounded edges of the samples, and contact with the building plate shown in directly printed samples and determine different mechanical behavior from that of a larger component. These artifacts also add to the possible bad adhesion between the internal infill and the external shells, which should be avoided during mechanical characterization.

The main artifacts introduced in the directly printed samples for compression tests [168] are depicted in Fig. 106. The artifacts introduced by direct printing determined significant differences in the measurements performed on directly printed samples and those extracted from a larger component.

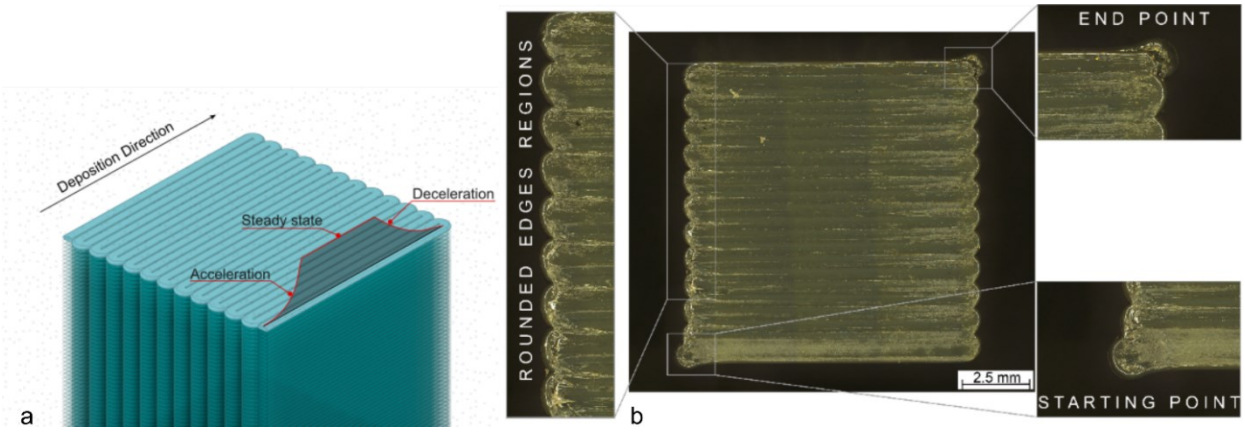



*Fig. 106 – Schematic of the deposition of directly printed vertical samples (V1 type) (a) with a zoom on main artifacts in directly printed samples (b)*

Table 18 summarizes the main differences in the properties measured on directly printed and extracted samples; such differences greatly depend on the direction of the sample.

*Table 18 – Difference of the density and mechanical behavior of samples made by direct printing (V1, H1, and HL1) and extraction method (V2, H3, and H2)*

| | Δ | | |
|---|---|---|---|
| | Density | Youngs Modulus | Yield Strength |
| *Vertical* $(V_1\text{-}V_2)/V_1$ | -5.3% | -10% | -12% |
| *Horizontal-Transverse* $(H_1\text{-}H_3)/H_1$ | 0.6% | -29% | -3% |
| *Horizontal-Longitudinal* $(HL_1\text{-}H_2)/HL_1$ | 3% | 2% | 18% |

As can be inferred in Fig. 77, since the dimensions of the sample along the deposition path are relatively small (the edge is 12 mm long), the deposition conditions and especially the extruder speed are strongly uneven along the deposition path. Indeed, since the need for acceleration and deceleration ramps, only a small part of the path is effectively deposited under predefined steady-state speed. Therefore, the characteristics of the sample are greatly variable along the deposition path. This indicates that V1 samples suffer from edge effects. On the other hand, the samples "extracted" from the plate, as those of V2 type, are cut from an almost homogeneous region where the extruder speed is constant and equal to that prescribed. Consequently, V1 samples showed lower density and mechanical properties as the larger component. Thus, assuming the characteristics retrieved from direct printing sample testing would result in an underestimation of the final weight and oversizing of the component. In the samples printed horizontally with filaments deposited transversely to the loading direction (H1), a negligible density difference was found compared to extracted samples (H3). On the other hand, an extremely lower Young's modulus was measured (29% lower). This difference was due to the shorter deposition path, which led to a different thermal history and a great edge effect. Finally, in samples printed horizontally with filaments arranged along the loading direction, the directly printed samples HL1 showed much higher yield strength values than the extracted samples H2. This was due to the large portion of samples HL1 in contact with the building plate. Such high values of yield strength were also observed in H4 samples. This confirms the strong influence of the densification occurring near the build platform on the yield strength. All the previous comparisons indicate that, although direct printing of the samples by MatExt shows unquestionable advantages in

terms of reduced efforts, time, and cost of manufacturing, it provides results that tend to underestimate or overestimate the mechanical properties of the deposition strategy.

Regarding specimens fabricated for tensile tests [170] also in this case significant differences in the mechanical behavior between directly printed samples and the extracted samples were observed. Specifically, for those specimens made by PLA, directly printed samples exhibited higher tensile strength compared to waterjet-cut samples, attributed to two key phenomena:

1. Enhanced adhesion at side regions: directly printed samples displayed higher adhesion at the side regions, evident from interlayer fractures originating at the sides and the increased irregularity of the fracture surface compared to the smoother central region. This enhanced adhesion was attributed to different deposition conditions at the edge, where tool reversal motions involved deceleration, change of direction, and acceleration (resulting in lower tool speed). This, coupled with a lack of reduction in material flow, led to a higher local material deposition acting as reinforcement, as shown in Fig. 107, altering the mechanical behavior.
2. Different thermal history: the production of direct samples involved a distinct thermal history compared to the box from which the samples were cut. Variances in interlayer time and convection heat exchanges within the building chamber contributed to this difference. Directly printed samples had interlayer times of 9.3 s (for $t$ = 2.5 mm) and 10.8 s (for $t$ = 3.0 mm), while the box's interlayer time was nearly triple (29.9 s). Samples cut from the box experienced lower average temperatures, hindering prolonged interfilamentous polymer chain entanglement and consequently reducing tensile strength.

These results were found on specimens made from PLA, but the differences between directly printed and box-cut samples were pronounced also in PAEK specimens [210]. This indicates that these effects are strongly influenced by both the material properties and deposition conditions. However, the key point lies in the potential discrepancies between the mechanical properties of directly printed test samples and those of larger components in real-world applications, particularly in industries like aerospace where such discrepancies can have critical implications. Many industries, including aerospace, commonly use direct sample printing for quality assessment of mechanical properties, which are then used in simulations and design of larger components.

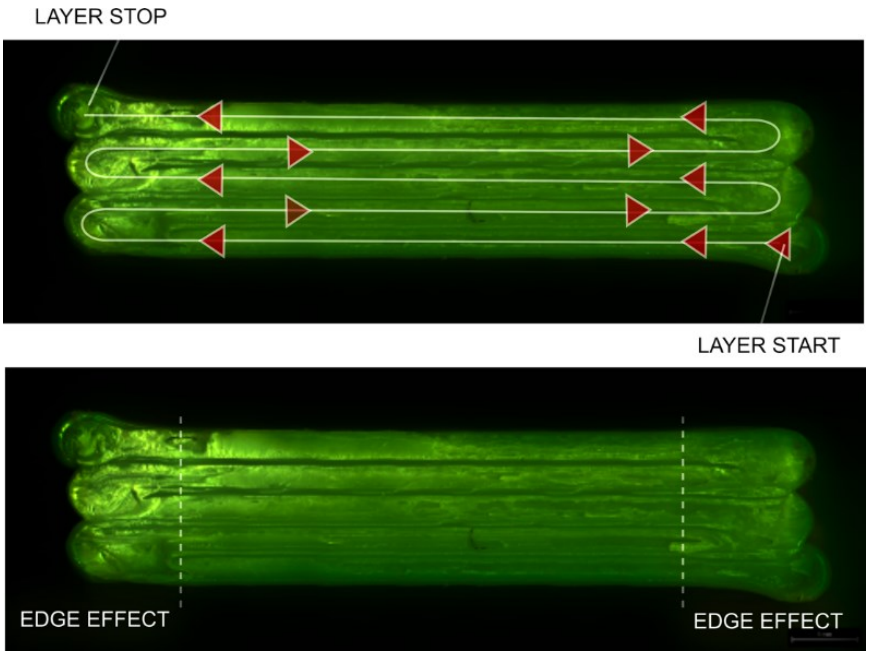



*Fig. 107 – Artifacts affecting the interlayer deposition in directly printed samples*

The campaigns of experiments conducted demonstrate how significantly different these mechanical characteristics can be, due to several factors:

- Thermal history: The thermal cycles experienced during printing differ significantly between small, directly printed samples and larger components. This variation affects the degree of crystallinity, which in turn influences the entanglement of polymeric chains between layers during deposition, ultimately impacting mechanical behavior.
- Flow dynamics: The presence of perimetral shells in directly printed samples indeed influences local deposition flow. The extruder undergoes steep accelerations/ decelerations at the edges, altering the thermal cycle and local pressure. These factors contribute to the differences in mechanical properties observed.
- Scale effects: The size difference between directly printed samples and the larger box from which samples are cut leads to different cooling rates and thermal gradients, further influencing the material's microstructure and properties.

Mechanical characterization tests should accurately reflect the material behavior of real components. Results demonstrate that for PAEK components manufactured via material extrusion (MatEx), the sample preparation method significantly influences the measured mechanical properties. This finding highlights the critical importance of choosing appropriate testing methodologies that align with the intended application and component scale. This research serves as a cautionary note to industries relying on directly printed test

samples. It highlights the potential risks of using data from such samples to predict the behavior of larger, more complex components. By quantifying these differences, valuable insights were provided that can lead to more accurate testing methodologies and improved design processes for PAEK components in critical applications like aerospace.

# Chapter 6 – Conclusions and future works

In today's industrial landscape, advanced manufacturing processes have revolutionized the production of complex components, driving innovation and reshaping traditional manufacturing methods. Among various advanced techniques, additive manufacturing, commonly known as 3D printing, has become a key technology, enabling the efficient and precise creation of intricate structures with unmatched flexibility and customization. This transformative capability has captured significant attention across a variety of sectors, such as aerospace, automotive, biomedical, and electronic, leading to a fundamental change in the way products are designed, developed, and manufactured.

The rapid evolution of additive manufacturing technologies has been fueled by several factors, including advances in material science, computational modeling, and process optimization. Through additive manufacturing, complex designs that were once considered impractical or prohibitively expensive to produce using traditional methods, are now being realized with greater ease and efficiency. This shift has not only expanded the limits of design, but has also accelerated the speed of innovation, making it possible to achieve complex geometries, better functional integration, and the production of lightweight, high-strength components with superior mechanical properties.

Among the various additive manufacturing techniques, Material Extrusion (MatExt), also known as Fused Filament Modeling (FDM) and Fused Filament Fabrication (FFF), has become a leading method for producing intricate components with high structural integrity and precise dimensions. Using a layer-by-layer deposition approach, MatExt technology allows for the creation of robust components from a wide range of thermoplastic materials, providing greater design flexibility and cost-effective manufacturing solutions. As industries continue to demand lightweight and high-performance components, the adoption of MatExt has expanded, with an increasing focus on optimizing the mechanical properties and structural performance of printed parts. The complexity of material extrusion technology highlights the importance of understanding the intricate relationships between process parameters, material properties, and design factors. Effective implementation of material extrusion requires a comprehensive approach that includes careful material selection, precise calibration of process parameters, and the integration of advanced post-processing techniques to achieve the desired mechanical properties and dimensional accuracy. The interdependence between process variables and material behavior has prompted extensive

research into the mechanisms that influence the structural performance and material properties of MatExt-produced components. To improve the mechanical properties and performance of material extrusion components, it is essential to explore the complex factors that affect material behavior, interlayer adhesion, and overall structural integrity. By studying the complexities of the MatExt process, researchers and industry professionals can gain valuable insights into how process parameters, thermal history, and microstructural evolution interact, paving the way for the development of optimized component designs, material choices, and manufacturing protocols. Additionally, the dynamic nature of additive manufacturing requires a thorough evaluation of how different manufacturing strategies affect product quality, structural integrity, and mechanical behavior.

Several articles in the literature have dealt with the mechanical characterization of components made by material extrusion. The relationships between the process parameters chosen during the printing stage and the mechanical properties found in the components after fabrication were investigated. However, to the present, there is no specific standard for the mechanical characterization of components made by this process. Therefore, traditional tests and methodologies are used to determine the mechanical properties of parts produced by material extrusion. Traditional characterization methods, however, do not take into account some peculiar aspects of components made by MatEx. Such components inherently have a production mode that occurs layer by layer, resulting in strong anisotropy, which is affected by adhesion between successive layers. Then, during the printing process, there are several factors that give rise to the occurrence of porosity within the produced parts. Moreover, the mechanical properties do not result uniform in all regions of the printed parts and are highly dependent on the dimensions chosen at the design stage. As a result, the need arises to develop advanced mechanical characterization methodologies aimed at studying the mechanical properties of components made by material extrusion.

In this thesis work, mechanical characterization methodologies developed specifically for components produced by material extrusion were proposed. Three main aspects that impact on mechanical properties were considered:

1. Presence of porosities.
2. Interlayer adhesion.
3. Influence of manufacturing strategies.

Regarding the first issue, all MatEx produced components are characterized by the presence of porosities. These porosities strongly impact on the density of the printed parts and consequently on mechanical properties; porosities, moreover, are not evenly distributed along the height of the considered parts. In order to take them into account, local mechanical characterization tests were performed. Specifically, flat indentation instrumented test was carried out. This test gives the local properties of the tested components, without performing a destructive test, but rather, leaving an imprint on the component with a small size (4 mm in diameter and 1 mm in depth). A high correlation between the results obtained by indentation and compression tests was also found; the correlation between the two yield strengths showed a linear trend, with a coefficient $R^2$ of 0.92. Similarly, the elastic limit (measured by the indentation test) and the yield strength (measured through the compression test) also showed a significant correlation since the coefficient of determination $R^2$ was 0.90. Thus, the established relationship (linear regression coefficients) can be exploited to convert the yielding condition measured through indentation tests to predict the compressive yield strength of the actual component on a specific location. Some specimens were then subjected to a process of thermomechanical compaction with the aim of minimizing the presence of porosity; this process resulted in obtaining specimens with a density equal to that of the filament used during the printing phase (1.25 g/cm$^3$), thus completely nullifying internal voids. Analysis of material flow during the compression test revealed additional peculiarities of components made by material extrusion. Firstly, poor adhesion between the external skin and the infill layers was observed. This resulted in larger porosities with uneven adhesion, which led to considerable separation of the skin from the infill during deformation. Cross sections of the uncompressed samples revealed a non-uniform distribution of porosity along the vertical direction. In fact, the lower part of the samples, in contact with the build plate, was characterized by smaller voids. During the deposition process, the temperature of the printing plate was set at 60 °C. This value was higher than the $T_g$ of the adopted PLA (55 °C). As a result, the molecular chains within these regions rearranged themselves resulting in a much more compact arrangement. During compression tests, this region showed less deformation than the overlying layers. Therefore, the samples did not show a perfectly barrel profile, but rather a barrel with a lower neck. Eventually, the influence of material extrusion and strain rate on the presence and the distribution of porosities was analyzed. For Extrusion Multiplier (EM) of 96%, many voids were already vertically connected. This defect disappeared almost completely for EM =100% and EM = 104%. The distribution of voids for strain values of 33% and 66% is indicative of the internal deformation of the samples.

For relatively low strain (33%), the filaments shifted radially (except for the central one). At higher deformations, the characteristic regions of the compressed specimens, that are the shear bands, dead material zone and lateral regions, are clearly visible. During compression of the specimens, the shear bands are a narrow zone where intense plastic deformation occurs. Here the size of the voids is drastically reduced due to the intense shear deformation. In the dead material zone, the region in contact with the compression plates and surrounded by the shear bands, reduced deformation occurred, leading to a smaller reduction in voids. Moderate deformation occurred in the lateral regions, leading to less void closure. Also, in the central region, a macroscopic void is visible resulting from the coalescence of the voids in the dead metal zone. These four characteristic regions are clearly visible on specimens made with the EM=96%, whereas for higher density specimens, the porosities within the dead metal zone are almost undetectable.

Interlaminar adhesion also has been found to be an influential theme in the study of the mechanical properties of MatEx components. A campaign of experimental tests with different thickness was conducted according to ASTM D5568 standard. In addition, a new type of specimen that does not require the implementation of an insert to produce the pre-crack was proposed. The proposed specimen with pre-crack and removable spacers appears to be an effective type of sample for conducting the mode I fracture toughness characterization, delivering almost identical results with the conventional specimen with the release film when the ASTM D5528 test execution is applied. From the analysis of the results, the critical energy release rate of the new specimen type appeared to be slightly higher compared to the conventional sample with the release film. In fact, the crack in the classic specimen with the release film propagated in the midplane, sometimes also unstably, in pure mode I, while in the case of the specimen with the slot the filaments interface appeared to be more resistant causing a stable crack propagation, but with a crack that exfoliated the adjacent filament layers. This is explained mostly by the different temperature cycles that are applied during the printing process, a fact that is also supported by the different fracture modes obtained by the experimental campaign. The interplay between deposition strategy, including material flow and travel speed, and its impact on interlayer adhesion was also investigated through mode I fracture toughness tests. The findings underscore the significance of meticulous parameter control to achieve optimal interlayer bonding. The alternate deposition strategy of ±45° resulted to be more reliable than the 0°/90°; in average, the values of the fracture toughness are higher for all the different

analyzed cases. Moreover, the adoption of filaments with crystalline phase may be harmful especially when printing at high material flow rates; the incomplete melting of the filament and the presence of the crystalline phase during the material deposition, in fact, may hinder the molecular chain mobility, and consequently, it may reduce the interlayer chain entanglement and interlayer adhesion.

Finally, the implications of varying manufacturing procedures on the characterization of components produced through material extrusion were explored. Two distinct approaches were investigated: direct sample printing and sample extraction from larger components. The findings underscore how critical the manufacturing procedure is since it may significantly alter the mechanical behavior of the sample. To gather deeper insights into such differences, IR thermography and fracture surface analysis were performed; thermal history during the printing phase has been shown to be crucial in the study of mechanical characteristics. This study has highlighted some crucial points. First, the direct printing of the test specimens has led to the creation of various artifacts; these artifacts include alterations in thermal history, regions with inverted deposition directions, the formation of rounded sample edges, and interactions with the building platform. These differences in deposition paths under direct sample printing had a profound impact on the mechanical behavior of the components, whether specimens were characterized under compression or tensile test. Furthermore, thermal history has a high impact on mechanical properties, due to different interlayer time during printing. Samples extract from a larger part, in fact, experienced lower average temperatures, hindering prolonged interfilamentous polymer chain entanglement, thus giving rise to weaker intermolecular bonds. The study provides a critical examination of how different manufacturing procedures can significantly impact the characterization of material extrusion components. This exploration of deposition strategies contributes to a deeper understanding of the complexities involved in additive manufacturing.

Although the main objective of the thesis has been achieved, some limitations need to be pointed out:

- Expanded testing: future studies will aim to extend the experimental characterization procedure to include additional mechanical tests, providing a more comprehensive understanding of how manufacturing strategy affects various mechanical properties. Additional characterization methods such as bending tests and impact tests could

provide a more comprehensive understanding of the differences between manufacturing strategies.

- Material range: it could be investigated whether these findings extend to other thermoplastics materials or other types of high-performance polymers used in aerospace applications, such as PEI or PEKK.
- Process parameter optimization: further research could focus on optimizing printing parameters to minimize the differences between directly printed samples and larger components, potentially improving the reliability of small-scale testing for predicting large-component behavior.
- In situ monitoring: development of in situ monitoring techniques during printing could provide valuable insights into the real-time development of material properties.

The analysis conducted so far delve deeper into the specific influence of manufacturing protocols, expanding on the existing body of knowledge. To address the limitation of fixed process parameters, future studies should encompass a broader spectrum of process parameters. This includes variations in nozzle temperature, and layer height. Understanding how these parameters interact, and influence mechanical properties is essential for advancing the field. Developing more comprehensive qualification protocols that consider sample dimensions as a critical factor will contribute to more accurate representations of MatExt components. This is particularly crucial as the technology finds broader industrial applications. Exploring the influence of different loading conditions, such as tensile, bending, and shearing, on components manufactured with various protocols, can provide insights into the versatility and limitations of material extrusion parts in real-world applications. Such investigations will be vital for tailoring MatExt components to specific industry needs.

# List of symbols

*ASTM D638 Standanrd*

| Symbol | *Unit* | *Caption* |
|---|---|---|
| $D$ | - | Dilution |
| $d$ | mm | Depth of melt pool |
| $h$ | mm | Height of deposited material |
| $\sigma$ | MPa | Tensile stress |
| $W$ | N | Load |
| $A_0$ | $mm^2$ | Original cross-sectional area |
| $\%El$ | % | Percent elongation |
| $\varepsilon$ | mm/mm | Strain |
| $\Delta L$ | mm | Increment of distance between gage marks |
| $L$ | mm | Distance between gage marks |
| $L_0$ | mm | Original distance between gage marks |
| $\varepsilon_U$ | mm/mm | Total strain at break |
| $L_U$ | mm | Distance between gage marks at moment of rupture |

*ASTM D790 Standard*

| Symbol | *Unit* | *Caption* |
|---|---|---|
| $\sigma_f$ | MPa | Flexural stress |
| $P$ | N | Load at a given point on the load-deflection curve |
| $L$ | mm | Support span |
| $b$ | mm | Width of beam tested |
| $d$ | mm | Depth of beam tested |
| $\in_f$ | mm/mm | Flexural strain maximum |
| $D$ | mm | Deflection of the center of the beam |
| $E_f$ | MPa | Chord modulus |

| Symbol | *Unit* | *Caption* |
|---|---|---|
| $T_g$ | °C | Glass transition temperature |
| $T_m$ | °C | Melting temperature |
| $T_c$ | °C | Crystallization temperature |
| $\Delta H_m$ | J | Melting enthalpy |
| $\Delta H_c$ | J | Crystallization enthalpy |
| $\chi_c$ | % | Degree of crystallinity |
| $\lambda$ | W/(mK) | Thermal conductivity |
| $C_p$ | J/(kgK) | Specific heat at constant pressure |
| $\Delta H_m^0$ | J | Melting enthalpy of a perfect crystal |
| $E'$ | MPa | Storage modulus |
| $E''$ | MPa | Loss modulus |
| $tan\delta$ | - | Loss tangent |

# List of acronyms

| | |
|---|---|
| AM: | Additive Manufacturing |
| PBF: | Powder Bed Fusion |
| SLS: | Selective Laser Sintering |
| SLM: | Selective Laser Melting |
| EBM: | Electron Beam Melting |
| DED: | Directed Energy Deposition |
| LOM: | Laminated Object Manufacturing |
| UAM: | Ultrasonic Additive Manufacturing |
| SLA: | Stereolithography |
| DLP: | Digital Light Processing |
| MJ: | Material Jetting |
| MatEx: | Material Extrusion |
| FDM: | Fused Deposition Modeling |
| FFF: | Fused Filament Fabrication |
| PLA: | Polylactic Acid |
| ABS: | Acrylonitrile Butadiene Styrene |
| ASA: | Acrylonitrile Styrene Acrylate |
| PETG: | Polyethylene Terephthalate Glycol |
| PC: | Polycarbonate |
| TPES: | Thermoplastic Elastomers |
| TPU: | Thermoplastic Polyurethane |
| PEEK: | Polyetheretherketone |
| PEKK: | Polyetherketoneketone |
| PAEK: | Polyaryletherketone |
| PEI: | Polyetherimide |
| DSC: | Differential Scanning Calorimetry |
| TGA: | Thermogravimetric Analysis |
| DMA: | Dynamic Mechanical Analysis |
| TTS: | Time Temperature Superposition Principle |

# References


1. *ISO (2015). ASTM 52900:2015 Additive manufacturing—general principles—terminology*.
2. Bourell, D., et al., *Materials for additive manufacturing*. CIRP Annals, 2017. **66**(2): p. 659-681.
3. Abdulhameed, O., et al., *Additive manufacturing: Challenges, trends, and applications*. Advances in Mechanical Engineering, 2019. **11**(2).
4. Gibson, I., D.W. Rosen, and B. Stucker, *Additive Manufacturing Technologies*. 2021.
5. Bandyopadhyay, A. and B. Heer, *Additive manufacturing of multi-material structures*. Materials Science and Engineering: R: Reports, 2018. **129**: p. 1-16.
6. Rajaguru, K., T. Karthikeyan, and V. Vijayan, *Additive manufacturing – State of art*. Materials Today: Proceedings, 2020. **21**: p. 628-633.
7. Prakash, K.S., T. Nancharaih, and V.V.S. Rao, *Additive Manufacturing Techniques in Manufacturing -An Overview*. Materials Today: Proceedings, 2018. **5**(2): p. 3873-3882.
8. Singh, S., C. Prakash, and S. Ramakrishna, *3D printing of polyether-ether-ketone for biomedical applications*. European Polymer Journal, 2019. **114**: p. 234-248.
9. González-Henríquez, C.M., M.A. Sarabia-Vallejos, and J. Rodriguez-Hernandez, *Polymers for additive manufacturing and 4D-printing: Materials, methodologies, and biomedical applications*. Progress in Polymer Science, 2019. **94**: p. 57-116.
10. Sun, S., et al., *Topology optimization, additive manufacturing and thermohydraulic testing of heat sinks*. International Journal of Heat and Mass Transfer, 2024. **224**.
11. Zhu, J., et al., *A review of topology optimization for additive manufacturing: Status and challenges*. Chinese Journal of Aeronautics, 2021. **34**(1): p. 91-110.
12. Meng, L., et al., *From Topology Optimization Design to Additive Manufacturing: Today's Success and Tomorrow's Roadmap*. Archives of Computational Methods in Engineering, 2019. **27**(3): p. 805-830.
13. Armstrong, M., H. Mehrabi, and N. Naveed, *An overview of modern metal additive manufacturing technology*. Journal of Manufacturing Processes, 2022. **84**: p. 1001-1029.
14. Bernard, A., G. Taillandier, and K. Karunakaran, *Evolutions of rapid product development with rapid manufacturing: concepts and applications*. International Journal of Rapid Manufacturing, 2009. **1**(1): p. 3-18.
15. Liu, Y., W. Wang, and L.-C. Zhang, *Additive manufacturing techniques and their biomedical applications*. Family Medicine and Community Health, 2017. **5**(4): p. 286-298.
16. Bryła, J. and A. Martowicz, *Study on the Importance of a Slicer Selection for the 3D Printing Process Parameters via the Investigation of G-Code Readings*. Machines, 2021. **9**(8).
17. Jiang, J., X. Xu, and J. Stringer, *Support Structures for Additive Manufacturing: A Review*. Journal of Manufacturing and Materials Processing, 2018. **2**(4).
18. Peng, X., et al., *A Review of Post-Processing Technologies in Additive Manufacturing*. Journal of Manufacturing and Materials Processing, 2021. **5**(2).
19. Bahnini, I., et al., *Additive manufacturing technology: the status, applications, and prospects*. The International Journal of Advanced Manufacturing Technology, 2018. **97**(1-4): p. 147-161.
20. Ferraris, E., et al., *Shaping of engineering ceramics by electro, chemical and physical processes*. CIRP Annals, 2016. **65**(2): p. 761-784.
21. Bikas, H., P. Stavropoulos, and G. Chryssolouris, *Additive manufacturing methods and modelling approaches: a critical review*. The International Journal of Advanced Manufacturing Technology, 2015. **83**(1-4): p. 389-405.

22. Ziaee, M. and N.B. Crane, *Binder jetting: A review of process, materials, and methods*. Additive Manufacturing, 2019. **28**: p. 781-801.
23. Zhang, Y., et al., *Additive Manufacturing of Metallic Materials: A Review*. Journal of Materials Engineering and Performance, 2017. **27**(1): p. 1-13.
24. Park, S., et al., *3D printing of polymer composites: Materials, processes, and applications*. Matter, 2022. **5**(1): p. 43-76.
25. Vock, S., et al., *Powders for powder bed fusion: a review*. Progress in Additive Manufacturing, 2019. **4**(4): p. 383-397.
26. Mirzababaei, S. and S. Pasebani, *A Review on Binder Jet Additive Manufacturing of 316L Stainless Steel*. Journal of Manufacturing and Materials Processing, 2019. **3**(3).
27. Mostafaei, A., et al., *Binder jet 3D printing—Process parameters, materials, properties, modeling, and challenges*. Progress in Materials Science, 2021. **119**.
28. Trombetta, R., et al., *3D Printing of Calcium Phosphate Ceramics for Bone Tissue Engineering and Drug Delivery*. Ann Biomed Eng, 2017. **45**(1): p. 23-44.
29. Mostafaei, A., et al., *Binder jetting of a complex-shaped metal partial denture framework*. Additive Manufacturing, 2018. **21**: p. 63-68.
30. Rojas-Nastrucci, E.A., et al., *Ka-Band Characterization of Binder Jetting for 3-D Printing of Metallic Rectangular Waveguide Circuits and Antennas*. IEEE Transactions on Microwave Theory and Techniques, 2017. **65**(9): p. 3099-3108.
31. Huang, G.-L., S.-G. Zhou, and T. Yuan, *Development of a Wideband and High-Efficiency Waveguide-Based Compact Antenna Radiator With Binder-Jetting Technique*. IEEE Transactions on Components, Packaging and Manufacturing Technology, 2017: p. 1-7.
32. Marrey, M., et al., *A framework for optimiziang process parameters in powder bed fusion (PBF) process using artificial neural network (ANN)*. Procedia Manufacturing, 2019.
33. Herzog, D., et al., *Additive manufacturing of metals*. Acta Materialia, 2016. **117**: p. 371-392.
34. Schmidt, M., et al., *Laser based additive manufacturing in industry and academia*. CIRP Annals, 2017. **66**(2): p. 561-583.
35. Ladani, L. and M. Sadeghilaridjani, *Review of Powder Bed Fusion Additive Manufacturing for Metals*. Metals, 2021. **11**(9).
36. Han, W., L. Kong, and M. Xu, *Advances in selective laser sintering of polymers*. International Journal of Extreme Manufacturing, 2022. **4**(4).
37. Florio, K., et al., *Process characterization and analysis of ceramic powder bed fusion*. The International Journal of Advanced Manufacturing Technology, 2021. **117**(7-8): p. 2105-2116.
38. Strondl, A., et al., *Characterization and Control of Powder Properties for Additive Manufacturing*. Jom, 2015. **67**(3): p. 549-554.
39. Caulfield, B., P.E. McHugh, and S. Lohfeld, *Dependence of mechanical properties of polyamide components on build parameters in the SLS process*. Journal of Materials Processing Technology, 2007. **182**(1-3): p. 477-488.
40. Appleyard, D., *Powering up on powder technology*. Metal Powder Report, 2015. **70**(6): p. 285-289.
41. Oliveira, J.P., A.D. LaLonde, and J. Ma, *Processing parameters in laser powder bed fusion metal additive manufacturing*. Materials & Design, 2020. **193**: p. 108762.
42. Jiménez, A., et al., *Powder-based laser hybrid additive manufacturing of metals: a review*. The International Journal of Advanced Manufacturing Technology, 2021. **114**(1-2): p. 63-96.
43. Dilberoglu, U.M., et al., *Current trends and research opportunities in hybrid additive manufacturing*. The International Journal of Advanced Manufacturing Technology, 2021. **113**(3-4): p. 623-648.

44. Ahn, D.-G., *Directed Energy Deposition (DED) Process: State of the Art*. International Journal of Precision Engineering and Manufacturing-Green Technology, 2021. **8**(2): p. 703-742.
45. Dass, A. and A. Moridi, *State of the Art in Directed Energy Deposition: From Additive Manufacturing to Materials Design*. Coatings, 2019. **9**(7).
46. Lambiase, F., S.I. Scipioni, and A. Paoletti, *Accurate prediction of the bead geometry in wire arc additive manufacturing process*. The International Journal of Advanced Manufacturing Technology, 2022. **119**(11-12): p. 7629-7639.
47. Shamsaei, N., et al., *An overview of Direct Laser Deposition for additive manufacturing; Part II: Mechanical behavior, process parameter optimization and control*. Additive Manufacturing, 2015. **8**: p. 12-35.
48. Kistler, N.A., et al., *Effect of processing conditions on the microstructure, porosity, and mechanical properties of Ti-6Al-4V repair fabricated by directed energy deposition*. Journal of Materials Processing Technology, 2019. **264**: p. 172-181.
49. Zuback, J.S. and T. DebRoy, *The Hardness of Additively Manufactured Alloys*. Materials (Basel), 2018. **11**(11).
50. Saboori, A., et al., *Application of Directed Energy Deposition-Based Additive Manufacturing in Repair*. Applied Sciences, 2019. **9**(16).
51. Kassym, K. and A. Perveen, *Atomization processes of metal powders for 3D printing*. Materials Today: Proceedings, 2020. **26**: p. 1727-1733.
52. Nikolić, N.D., V.M. Maksimović, and L. Avramović, *Correlation of Morphology and Crystal Structure of Metal Powders Produced by Electrolysis Processes*. Metals, 2021. **11**(6).
53. Antony, L.V.M. and R.G. Reddy, *Processes for Production of High-Purity Metal Powders*. JOM, 2003. **55**: p. 14-18.
54. Divakaran, N., et al., *Comprehensive review on various additive manufacturing techniques and its implementation in electronic devices*. Journal of Manufacturing Systems, 2022. **62**: p. 477-502.
55. Gao, W., et al., *The status, challenges, and future of additive manufacturing in engineering*. Computer-Aided Design, 2015. **69**: p. 65-89.
56. Al Rashid, A., et al., *Vat photopolymerization of polymers and polymer composites: Processes and applications*. Additive Manufacturing, 2021. **47**.
57. Pazhamannil, R.V. and P. Govindan, *Current state and future scope of additive manufacturing technologies via vat photopolymerization*. Materials Today: Proceedings, 2021. **43**: p. 130-136.
58. Piedra-Cascon, W., et al., *3D printing parameters, supporting structures, slicing, and post-processing procedures of vat-polymerization additive manufacturing technologies: A narrative review*. J Dent, 2021. **109**: p. 103630.
59. Cullen, A.T. and A.D. Price, *Fabrication of 3D conjugated polymer structures via vat polymerization additive manufacturing*. Smart Materials and Structures, 2019. **28**(10).
60. Sampson, K.L., et al., *Multimaterial Vat Polymerization Additive Manufacturing*. ACS Applied Polymer Materials, 2021. **3**(9): p. 4304-4324.
61. An, J., et al., *Design and 3D Printing of Scaffolds and Tissues*. Engineering, 2015. **1**(2): p. 261-268.
62. Moon, S.K., et al., *Application of 3D printing technology for designing light-weight unmanned aerial vehicle wing structures*. International Journal of Precision Engineering and Manufacturing-Green Technology, 2015. **1**(3): p. 223-228.
63. Saleh Alghamdi, S., et al., *Additive Manufacturing of Polymer Materials: Progress, Promise and Challenges*. Polymers (Basel), 2021. **13**(5).
64. Li, N., et al., *Progress in additive manufacturing on new materials: A review*. Journal of Materials Science & Technology, 2019. **35**(2): p. 242-269.

65. Das, A., et al., *Current understanding and challenges in high temperature additive manufacturing of engineering thermoplastic polymers*. Additive Manufacturing, 2020. **34**.
66. Zanjanijam, A.R., et al., *Fused Filament Fabrication of PEEK: A Review of Process-Structure-Property Relationships*. Polymers (Basel), 2020. **12**(8).
67. Zhang, X., W. Fan, and T. Liu, *Fused deposition modeling 3D printing of polyamide-based composites and its applications*. Composites Communications, 2020. **21**.
68. Singh, S. and S. Ramakrishna, *Biomedical applications of additive manufacturing: Present and future*. Current Opinion in Biomedical Engineering, 2017. **2**: p. 105-115.
69. Feroz Ali, L., et al., *Evaluation of the polyamide's mechanical properties for varying infill percentage in FDM process*. Materials Today: Proceedings, 2022. **68**: p. 2509-2514.
70. Singh, S., et al., *Current status and future directions of fused filament fabrication*. Journal of Manufacturing Processes, 2020. **55**: p. 288-306.
71. Berretta, S., K. Evans, and O. Ghita, *Additive manufacture of PEEK cranial implants: Manufacturing considerations versus accuracy and mechanical performance*. Materials & Design, 2018. **139**: p. 141-152.
72. Vakharia, V.S., et al., *Multi-Material Additive Manufacturing of High Temperature Polyetherimide (PEI)–Based Polymer Systems for Lightweight Aerospace Applications*. polymers, 2023.
73. Abderrafai, Y., et al., *Additive manufacturing and characterization of high temperature thermoplastic blends for potential aerospace applications*. Composites Science and Technology, 2023. **231**: p. 109839.
74. Quan, D., et al., *Effect of interlaying UV-irradiated PEEK fibres on the mechanical, impact and fracture response of aerospace-grade carbon fibre/epoxy composites*. Composites Part B: Engineering, 2020. **191**: p. 107923.
75. Costa, J.M., E.W. Sequeiros, and M.F. Vieira, *Fused Filament Fabrication for Metallic Materials: A Brief Review*. Materials (Basel), 2023. **16**(24).
76. Leal, R., et al., *Additive manufacturing tooling for the automotive industry*. The International Journal of Advanced Manufacturing Technology, 2017. **92**: p. 1671-1676.
77. Oladapo, B.I., et al., *3D printing of PEEK and its composite to increase biointerfaces as a biomedical material- A review*. Colloids Surf B Biointerfaces, 2021. **203**: p. 111726.
78. Liao, C., Y. Li, and S.C. Tjong, *Polyetheretherketone and Its Composites for Bone Replacement and Regeneration*. Polymers (Basel), 2020. **12**(12).
79. Dizon, J.R.C., et al., *Mechanical characterization of 3D-printed polymers*. Additive Manufacturing, 2018. **20**: p. 44-67.
80. Garzon-Hernandez, S., et al., *Design of FDM 3D printed polymers: An experimental-modelling methodology for the prediction of mechanical properties*. Materials & Design, 2020. **188**.
81. Algarni, M. and S. Ghazali, *Comparative Study of the Sensitivity of PLA, ABS, PEEK, and PETG's Mechanical Properties to FDM Printing Process Parameters*. Crystals, 2021. **11**(8): p. 995.
82. Gonabadi, H., A. Yadav, and S.J. Bull, *The effect of processing parameters on the mechanical characteristics of PLA produced by a 3D FFF printer*. The International Journal of Advanced Manufacturing Technology, 2020. **111**(3-4): p. 695-709.
83. Geng, P., et al., *Effects of extrusion speed and printing speed on the 3D printing stability of extruded PEEK filament*. Journal of Manufacturing Processes, 2019. **37**: p. 266-273.
84. Zaldivar, R.J., et al., *Influence of processing and orientation print effects on the mechanical and thermal behavior of 3D-Printed ULTEM® 9085 Material*. Additive Manufacturing, 2017. **13**: p. 71-80.
85. Kaplun, B.W., et al., *Influence of orientation on mechanical properties for high-performance fused filament fabricated ultem 9085 and electro-statically dissipative polyetherketoneketone*. Additive Manufacturing, 2020. **36**.

86. A. C. de Bruijn, G. Gomez-Gras, and M.A. Perez, *Thermal annealing as a post-process for additively manufactured Ultem 9085 parts*. Procedia computer science, 2022.
87. A. W. Gebisa and H.G. Lemu, *Influence of 3D Printing FDM Process Parameters on Tensile property of ULTEM 9085*. Procedia Manufacturing, 2019.
88. Li, Q., et al., *Porous polyether ether ketone: A candidate for hard tissue implant materials*. Materials & Design, 2017. **116**: p. 171-175.
89. Fischer, M. and V. Schöppner, *Fatigue Behavior of FDM Parts Manufactured with Ultem 9085*. Jom, 2016. **69**(3): p. 563-568.
90. Kok, Y., et al., *Anisotropy and heterogeneity of microstructure and mechanical properties in metal additive manufacturing: A critical review*. Materials & Design, 2018. **139**: p. 565-586.
91. Zheng, J., et al., *Effects of printing path and material components on mechanical properties of 3D-printed polyether-ether-ketone/hydroxyapatite composites*. J Mech Behav Biomed Mater, 2021. **118**: p. 104475.
92. Shekar, R.I., et al., *Properties of high modulus PEEK yarns for aerospace applications*. Journal of Applied Polymer Science, 2009. **112**(4): p. 2497-2510.
93. Wang, Y., et al., *Mechanical properties of fused filament fabricated PEEK for biomedical applications depending on additive manufacturing parameters*. J Mech Behav Biomed Mater, 2021. **115**: p. 104250.
94. ASTM, *ASTM D638 - Standard Test Method for Tensile Properties of Plastics*.
95. ASTM, *ASTM D695 - Standard Test Method for Compressive Properties of Rigid Plastics*.
96. ASTM, *ASTM D790 - Standard Test Methods for Flexural Properties of Unreinforced and Reinforced Plastics and Electrical Insulating Materials*.
97. ASTM, *ASTM D6272 - Standard Test Method for Flexural Properties of Unreinforced and Reinforced Plastics and Electrical Insulating Materials by Four-Point Be*.
98. ASTM, *ASTM D732 - Standard Test Method for Shear Strength of Plastics by Punch Tool*.
99. Kazemi, M., S. Faisal Kabir, and E.H. Fini, *State of the art in recycling waste thermoplastics and thermosets and their applications in construction*. Resources, Conservation and Recycling, 2021. **174**.
100. Rajan, K., et al., *Fused deposition modeling: process, materials, parameters, properties, and applications*. The International Journal of Advanced Manufacturing Technology, 2022. **120**(3-4): p. 1531-1570.
101. Ferry, J., *Viscoelastic properties of polymers*. Vol. 264. 1980: Wiley.
102. Gao, X., et al., *Fused filament fabrication of polymer materials: A review of interlayer bond*. Additive Manufacturing, 2021. **37**: p. 101658.
103. Yan, C., Y. Shi, and L. Hao, *Investigation into the differences in the selective laser sintering between amorphous and semi-crystalline polymers*. International polymer processing, 2011. **26**(4): p. 416-423.
104. Liu, X., et al., *A Study of the Pressure-Induced Solidification of Polymers*. Polymers (Basel), 2018. **10**(8).
105. Lu, C., et al., *Effects of Molecular Structure and Packing Order on the Stretchability of Semicrystalline Conjugated Poly(Tetrathienoacene-diketopyrrolopyrrole) Polymers*. Advanced Electronic Materials, 2016. **3**(2).
106. Fukuoka, M., et al., *Role of Amorphous Region on the Deformation Behavior of Crystalline Polymers*. Polymer Journal, 2006. **38**(6): p. 542-547.
107. Meng, J., et al., *Non-symmetric Half-Fused B<--N Coordinated Diketopyrrolopyrrole Building Block for n-type Semiconducting Polymers*. Angew Chem Int Ed Engl, 2023. **62**(23): p. e202301863.
108. Perez, A., et al., *Mechanical Properties and Blocking Resistance of Films Cast from Core–Shell Latex Particles*. Macromolecular Reaction Engineering, 2023. **17**(5).
109. Xie, R., et al., *Glass transition temperature from the chemical structure of conjugated polymers*. Nat Commun, 2020. **11**(1): p. 893.

110. Yoon, K.-B., et al., *Electrical Properties of Non-Crosslinked Polyethylene/Syndiotactic Polystyrene Composites Filled with Carbon Black*. Polymer Journal, 2007. **39**(11): p. 1143-1149.
111. Kim, D., et al., *Low-Temperature Alignment of Conjugated Polymers by Plasticizer-Aided Physical Rubbing*. Small Methods, 2023. **7**(10): p. e2300256.
112. Zhao, H., et al., *Study of the Dual Amorphous Phases in Semicrystalline Poly(ethylene terephthalate) Using the Heat Capacity Increment at the Glass Transition*. Macromuolecules, 2003.
113. Hardon, S., et al., *Influence of Nanoparticles on the Dielectric Response of a Single Component Resin Based on Polyesterimide*. Polymers (Basel), 2022. **14**(11).
114. Martínez-Tong, D.E., et al., *Crystallization of Poly(l-lactide) Confined in Ultrathin Films: Competition between Finite Size Effects and Irreversible Chain Adsorption*. Macromolecules, 2014. **47**(7): p. 2354-2360.
115. ASTM, *ASTM D3418 - Standard Test Method for Transition Temperatures and Enthalpies of Fusion and Crystallization of Polymers by Differential Scanning Calorimetry*.
116. ASTM, *ASTM E1131 - Standard Test Method for Compositional Analysis by Thermogravimetry*.
117. Saadatkhah, N., et al., *Experimental methods in chemical engineering: Thermogravimetric analysis—TGA*. The Canadian Journal of Chemical Engineering, 2019. **98**(1): p. 34-43.
118. Dunson, D., *Characterization of Polymers using Dynamic Mechanical Analysis (DMA)*. EAG Laboratories, 2017.
119. Menard, K.P. and N.R. Menard, *Dynamic Mechanical Analysis in the Analysis of Polymers and Rubbers*, in *Encyclopedia of Polymer Science and Technology*. 2015. p. 1-33.
120. Foreman, J., *Dynamic mechanical analysis of polymers*. American laboratory, 1997.
121. Singh, S., S. Ramakrishna, and R. Singh, *Material issues in additive manufacturing: A review*. Journal of Manufacturing Processes, 2017. **25**: p. 185-200.
122. Jafferson, J.M. and D. Chatterjee, *A review on polymeric materials in additive manufacturing*. Materials Today: Proceedings, 2021. **46**: p. 1349-1365.
123. El Magri, A., S.E. Ouassil, and S. Vaudreuil, *Effects of printing parameters on the tensile behavior of 3D-printed acrylonitrile styrene acrylate (ASA) material in Z direction*. Polymer Engineering & Science, 2022. **62**(3): p. 848-860.
124. Hsueh, M.H., et al., *Effect of Printing Parameters on the Thermal and Mechanical Properties of 3D-Printed PLA and PETG, Using Fused Deposition Modeling*. Polymers (Basel), 2021. **13**(11).
125. Tanikella, N.G., B. Wittbrodt, and J.M. Pearce, *Tensile strength of commercial polymer materials for fused filament fabrication 3D printing*. Additive Manufacturing, 2017. **15**: p. 40-47.
126. Xiao, J. and Y. Gao, *The manufacture of 3D printing of medical grade TPU*. Progress in Additive Manufacturing, 2017. **2**(3): p. 117-123.
127. Yap, T., et al., *Additive Manufacturing of Polyaryletherketone (PAEK) polymers and their composites*. Composites Part B: Engineering, 2023.
128. Byberg, K.I., A.W. Gebisa, and H.G. Lemu, *Mechanical properties of ULTEM 9085 material processed by fused deposition modeling*. Polymer Testing, 2018. **72**: p. 335-347.
129. Doshi, M., et al., *Printing parameters and materials affecting mechanical properties of FDM-3D printed Parts: Perspective and prospects*. Materials Today: Proceedings, 2022. **50**: p. 2269-2275.
130. Deng, X., et al., *Mechanical Properties Optimization of Poly-Ether-Ether-Ketone via Fused Deposition Modeling*. Materials (Basel), 2018. **11**(2).

131. Brischetto, S. and R. Torre, *Tensile and Compressive Behavior in the Experimental Tests for PLA Specimens Produced via Fused Deposition Modelling Technique*. Journal of Composites Science, 2020. **4**(3).
132. Forés-Garriga, A., et al., *Role of infill parameters on the mechanical performance and weight reduction of PEI Ultem processed by FFF*. Materials & Design, 2020. **193**: p. 108810.
133. Cojocaru, V., et al., *The Influence of the Process Parameters on the Mechanical Properties of PLA Specimens Produced by Fused Filament Fabrication-A Review*. Polymers (Basel), 2022. **14**(5).
134. Arif, M.F., et al., *Performance of biocompatible PEEK processed by fused deposition additive manufacturing*. Materials and Design, 2018. **146**: p. 249-259.
135. Gao, S., et al., *The Surface Characteristics, Microstructure and Mechanical*

*Properties of PEEK Printed by Fused Deposition Modeling with Different Raster Angles*. polymers, 2021.
136. Zhao, Y., et al., *Mechanical characterization of biocompatible PEEK by FDM*. Journal of Manufacturing Processes, 2020. **56**: p. 28-42.
137. Padovano, E., et al., *Mechanical and Thermal Behavior of Ultem® 9085 Fabricated by Fused-Deposition Modeling*. Applied Sciences, 2020. **10**(9): p. 3170.
138. Shelton, T.E., et al., *Effects of thermal process parameters on mechanical interlayer strength for additively manufactured Ultem 9085*. Polymer Testing, 2020. **81**: p. 106255.
139. Ding, S., et al., *Effects of nozzle temperature and building orientation on mechanical properties and microstructure of PEEK and PEI printed by 3D-FDM*. Polymer Testing, 2019. **78**.
140. Morettini, G., et al., *Comprehensive characterization of mechanical and physical properties of PLA structures printed by FFF-3D-printing process in different directions*. Progress in Additive Manufacturing, 2022. **7**(5): p. 1111-1122.
141. Kozior, T. and C. Kundera, *Evaluation of the Influence of Parameters of FDM Technology on the Selected Mechanical Properties of Models*. Procedia Engineering, 2017. **192**: p. 463-468.
142. Chalgham, A., A. Ehrmann, and I. Wickenkamp, *Mechanical Properties of FDM Printed PLA Parts before and after Thermal Treatment*. Polymers (Basel), 2021. **13**(8).
143. Pulipaka, A., et al., *Effect of 3D printing process parameters on surface and mechanical properties of FFF-printed PEEK*. Journal of Manufacturing Processes, 2023. **85**: p. 368-386.
144. Wang, P., et al., *Effects of printing parameters of fused deposition modeling on mechanical properties, surface quality, and microstructure of PEEK*. Journal of Materials Processing Technology, 2019. **271**: p. 62-74.
145. Basgul, C., et al., *Structure-Property Relationships for 3D printed PEEK Intervertebral Lumbar Cages Produced using Fused Filament Fabrication*. J Mater Res, 2018. **33**(14): p. 2040-2051.
146. Zohdi, N. and R.C. Yang, *Material Anisotropy in Additively Manufactured Polymers and Polymer Composites: A Review*. Polymers (Basel), 2021. **13**(19).
147. Cao, D., et al., *Bending and shear improvements in 3D-printed core sandwich composites through modification of resin uptake in the skin/core interphase region*. Composites Part B: Engineering, 2023. **264**: p. 110912.
148. Somireddy, M., C.V. Singh, and A. Czekanski, *Analysis of the Material Behavior of 3D Printed Laminates Via FFF*. Experimental Mechanics, 2019. **59**(6): p. 871-881.
149. Gebisa, A.W. and H.G. Lemu, *Investigating Effects of Fused-Deposition Modeling (FDM) Processing Parameters on Flexural Properties of ULTEM 9085 using Designed Experiment*. Materials (Basel), 2018. **11**(4).

150. Han, P., et al., *An approach to improve interface healing in FFF 3D printed Ultem 1010 using laser pre-deposition heating*. Procedia Manufacturing, 2019.
151. Abdullah, F., et al., *Effects of Thermal Cycle and Ultraviolet Radiation on 3D Printed Carbon Fiber/Polyether Ether Ketone Ablator*. Aerospace, 2020. **7**(7): p. 95.
152. Zhang, Y. and S.K. Moon, *The Effect of Annealing on Additive Manufactured ULTEM() 9085 Mechanical Properties*. Materials (Basel), 2021. **14**(11).
153. Han, X., et al., *Carbon Fiber Reinforced PEEK Composites Based on 3D-Printing Technology for Orthopedic and Dental Applications*. J Clin Med, 2019. **8**(2).
154. Garcia-Gonzalez, D., et al., *Investigation of mechanical impact behavior of short carbon-fiber-reinforced PEEK composites*. Composite Structures, 2015. **133**: p. 1116-1126.
155. Benfriha, K., et al., *Effect of process parameters on thermal and mechanical properties of polymer-based composites using fused filament fabrication*. Polymer Composites, 2021. **42**(11): p. 6025-6037.
156. Faes, M., E. Ferraris, and D. Moens, *Influence of Inter-layer Cooling time on the Quasi-static Properties of ABS Components Produced via Fused Deposition Modelling*. Procedia CIRP, 2016. **42**: p. 748-753.
157. Bragaglia, M., et al., *Modeling the fracture behavior of 3D-printed PLA as a laminate composite: Influence of printing parameters on failure and mechanical properties*. Composite Structures, 2023. **322**.
158. Deshpande, A., et al., *Interlayer thermal history modification for interface strength in fused filament fabricated parts*. Progress in Additive Manufacturing, 2018. **4**(1): p. 63-70.
159. Formisano, A., L. Boccarusso, and A. Langella, *Surface Optimization of Components Obtained by Fused Deposition Modeling for Air-Plasma-Sprayed Ceramic Coatings*. Journal of Composites Science, 2023. **7**(4): p. 158.
160. Dinita, A., et al., *Additive Manufacturing Post-Processing Treatments, a Review with Emphasis on Mechanical Characteristics*. Materials (Basel), 2023. **16**(13).
161. Tofangchi, A., et al., *Effect of Ultrasonic Vibration on Interlayer Adhesion in Fused Filament Fabrication 3D Printed ABS*. Polymers (Basel), 2019. **11**(2).
162. Pu Han, A.T., Anagh Deshpande, Sihan Zhang, Keng Hsu, *An approach to imrpove interface healing in FFF-3D printed Ultem 1010 using laser pre-deposition heating*. Procedia Manufacturing, 2019.
163. Kechagias, J. and S. Zaoutsos, *Effects of 3D-printing processing parameters on FFF parts' porosity: outlook and trends*. Materials and Manufacturing Processes, 2024: p. 1-11.
164. McIlroy, C. and R.S. Graham, *Modelling flow-enhanced crystallisation during fused filament fabrication of semi-crystalline polymer melts*. Additive Manufacturing, 2018. **24**: p. 323-340.
165. Hassanifard, S. and S.M. Hashemi, *On the strain-life fatigue parameters of additive manufactured plastic materials through fused filament fabrication process*. Additive Manufacturing, 2020. **32**.
166. Lambiase, F., S.I. Scipioni, and A. Paoletti, *Determination of local density in components made by fused deposition modeling through indentation test*. The International Journal of Advanced Manufacturing Technology, 2022. **122**(3-4): p. 1467-1478.
167. Lambiase, F., S.I. Scipioni, and A. Paoletti, *Mechanical characterization of FDM parts through instrumented flat indentation*. The International Journal of Advanced Manufacturing Technology, 2023. **125**(9-10): p. 4201-4211.
168. Scipioni, S.I. and F. Lambiase, *Error introduced by direct 3D printing of compression samples of PLA made by FDM process*. The International Journal of Advanced Manufacturing Technology, 2023. **129**(9-10): p. 4355-4368.

169. Scipioni, S.I. and F. Lambiase, *Yielding and post-yielding behavior of FDM parts under compression stress at different strain rates*. The International Journal of Advanced Manufacturing Technology, 2023. **128**(3-4): p. 1199-1211.
170. Lambiase, F., et al., *Unraveling the main issues of direct sample printing and sample cutting from a sheet of tensile test samples for characterization of Material Extrusion components*. The International Journal of Advanced Manufacturing Technology, 2024. **132**(5-6): p. 2991-3003.
171. Stamopoulos, A.G., S. Ilaria Scipioni, and F. Lambiase, *Experimental characterization of the interlayer fracture toughness of FDM components*. Composite Structures, 2023. **320**.
172. Lambiase, F., et al., *A multidisciplinary approach to investigate the influence of process parameters on interlayer adhesion in material extrusion additive manufacturing*. The International Journal of Advanced Manufacturing Technology, 2024. **133**(11-12): p. 5553-5570.
173. Cao, D., et al., *Nanoindentation measurement of core–skin interphase viscoelastic properties in a sandwich glass composite*. Mechanics of Time-Dependent Materials, 2020. **25**(3): p. 353-363.
174. Cao, D., et al., *The effect of resin uptake on the flexural properties of compression molded sandwich composites*. Wind Energy, 2021. **25**(1): p. 71-93.
175. Liao, Y., et al., *Effect of Porosity and Crystallinity on 3D Printed PLA Properties*. Polymers (Basel), 2019. **11**(9).
176. Wang, X., et al., *Effect of Porosity on Mechanical Properties of 3D Printed Polymers: Experiments and Micromechanical Modeling Based on X-ray Computed Tomography Analysis*. Polymers (Basel), 2019. **11**(7).
177. Alisafaei, F. and C.-S. Han, *Indentation Depth Dependent Mechanical Behavior in Polymers*. Advances in Condensed Matter Physics, 2015. **2015**: p. 1-20.
178. Schneider-Maunoury, C., et al., *On the use of instrumented indentation to characterize the mechanical properties of functionally graded binary alloys manufactured by additive manufacturing*. Materials Today Communications, 2020. **25**.
179. Zhou, Y., et al., *The Verification of the Mechanical Properties of Binder Jetting Manufactured Parts by Instrumented Indentation Testing*. Procedia Manufacturing, 2015. **1**: p. 327-342.
180. Jin, Y., et al., *Nondestructive ultrasonic evaluation of fused deposition modeling based additively manufactured 3D-printed structures*. Smart Materials and Structures, 2020. **29**(4).
181. Butt, J., R. Bhaskar, and V. Mohaghegh, *Non-Destructive and Destructive Testing to Analyse the Effects of Processing Parameters on the Tensile and Flexural Properties of FFF-Printed Graphene-Enhanced PLA*. Journal of Composites Science, 2022. **6**(5).
182. Riccardi, B. and R. Montanari, *Indentation of metals by a flat-ended cylindrical punch*. Materials Science and Engineering: A, 2004. **381**(1-2): p. 281-291.
183. Bernard, C., et al., *Numerical implementation of an elastic-viscoplastic constitutive model to simulate the mechanical behaviour of amorphous polymers*. International Journal of Material Forming, 2017. **10**: p. 607-621.
184. Kumar, S., S.S. Singh, and P. Rozycki, *Numerical simulation of strain-softening behavior of glass-filled polymer composites: Comparison of two-dimensional and three-dimensional analyses using Arruda-Boyce and Three-Network viscoplastic models*. Mechanics of Materials, 2022. **175**.
185. Pulak M. Pandey, N. Venkata Reddy, and S.G. Dhande, *Improvement of surface ®nish by staircase machining in fused deposition modeling*. Journal of Materials Processing Technology, 2003.
186. Lambiase, F., S. Genna, and C. Leone, *Laser finishing of 3D printed parts produced by material extrusion*. Optics and Lasers in Engineering, 2020. **124**.

187. Barile, C., C. Casavola, and A. Cazzato, *Acoustic Emissions in 3D Printed Parts under Mode I Delamination Test*. Materials (Basel), 2018. **11**(9).
188. Fonseca, J., et al., *Study of the interlaminar fracture under mode I loading on FFF printed parts*. Composite Structures, 2019. **214**: p. 316-324.
189. Khudiakova, A., et al., *Inter-layer bonding characterisation between materials with different degrees of stiffness processed by fused filament fabrication*. Additive Manufacturing, 2019. **28**: p. 184-193.
190. Marșavina, L., D.I. Stoia, and L. Emanoil, *Fracture toughness in additive manufacturing by selective laser sintering: an overview*. Material Design & Processing Communications, 2021. **3**(6).
191. Santos, J.D., et al., *Experimental Characterization and Analysis of the In-Plane Elastic Properties and Interlaminar Fracture Toughness of a 3D-Printed Continuous Carbon Fiber-Reinforced Composite*. Polymers (Basel), 2022. **14**(3).
192. Young, D., N. Wetmore, and M. Czabaj, *Interlayer fracture toughness of additively manufactured unreinforced and carbon-fiber-reinforced acrylonitrile butadiene styrene*. Additive Manufacturing, 2018. **22**: p. 508-515.
193. Farah, S., D.G. Anderson, and R. Langer, *Physical and mechanical properties of PLA, and their functions in widespread applications - A comprehensive review*. Adv Drug Deliv Rev, 2016. **107**: p. 367-392.
194. Irwin, G.R. and J. Kies, *Critical energy rate analysis of fracture strength*. Spie Milestone series MS, 1997. **137**: p. 136-141.
195. Bartolai, J., T.W. Simpson, and R. Xie, *Predicting strength of additively manufactured thermoplastic polymer parts produced using material extrusion*. Rapid Prototyping Journal, 2018. **24**(2): p. 321-332.
196. Northcutt, L.A., et al., *Effect of processing conditions on crystallization kinetics during materials extrusion additive manufacturing*. Polymer (Guildf), 2018. **154**.
197. Peng, F., B.D. Vogt, and M. Cakmak, *Complex flow and temperature history during melt extrusion in material extrusion additive manufacturing*. Additive Manufacturing, 2018. **22**: p. 197-206.
198. ASTM, *ASTM D5528 - Standard Test Method for Mode I Interlaminar Fracture Toughness of Unidirectional Fiber-Reinforced Polymer Matrix Composites*.
199. I.A. Ashcroft, D.J. Hughes, and S.J. Shaw, *Mode I fracture of epoxy bonded composite joints: 1. Quasi-static loading*. International Journal of Adhesion & Adhesives, 2001.
200. EN, D., *DIN EN 1465*.
201. Lambiase, F., et al., *Influence of the deposition pattern on the interlayer fracture toughness of FDM components*. The International Journal of Advanced Manufacturing Technology, 2023. **128**(9-10): p. 4269-4281.
202. Foglia, F., et al., *Isothermal crystallization of PLA: Nucleation density and growth rates of α and α′ phases*. The Canadian Journal of Chemical Engineering, 2020. **98**(9): p. 1998-2007.
203. Volpe, V., F. Foglia, and R. Pantani, *Effect of the application of low shear rates on the crystallization kinetics of PLA*. Polymer Crystallization, 2020. **3**(6).
204. Cao, D., et al., *Bending and shear improvements in 3D-printed core sandwich composites through modification of resin uptake in the skin/core interphase region*. Composites Part B: Engineering, 2023. **264**.
205. Srinivas, V., et al., *Promotion of molecular diffusion and/or crystallization in fused deposition modeled poly(lactide) welds*. Polymer, 2020. **202**.
206. Yin, J., et al., *Interfacial bonding during multi-material fused deposition modeling (FDM) process due to inter-molecular diffusion*. Materials & Design, 2018. **150**: p. 104-112.

207. Özen, A., et al., *Exploring the Role of Manufacturing Parameters on Microstructure and Mechanical Properties in Fused Deposition Modeling (FDM) Using PETG*. Applied Composite Materials, 2021. **28**(6): p. 1799-1828.
208. Zhang, R., et al., *Aging-dependent strain localization in amorphous glassy polymers: From necking to shear banding*. International Journal of Solids and Structures, 2018. **146**: p. 203-213.
209. Dua, R., et al., *Applications of 3D-Printed PEEK via Fused Filament Fabrication: A Systematic Review*. Polymers (Basel), 2021. **13**(22).
210. Scipioni, S.I., et al., *Mechanical characterization of FDM components made of polyaryletherketone (PAEK) for aerospace applications: a comparison of direct printing and box-cut sample manufacturing strategies*. The International Journal of Advanced Manufacturing Technology, 2024.
211. Blundell, D.J. and B. Osborn, *The morphology of poly (aryl-ether-ether-ketone)*. Polymer, 1983. **24**(8): p. 953-958.